# Tuning Magnetism and Superconductivity in Layered Chalcogenides and Pnictides

Ludmila Taskesen

A thesis submitted in part fulfilment of the requirements for the degree
of *Doctor of Philosophy*

*The Queen's College*

*University of Oxford*

*October 2025*

*To Ata*

# Declaration

The work described in this thesis was carried out in the Inorganic Chemistry Laboratory, South Parks Road, Oxford from September 2020 to October 2025 under the supervision of Prof. Simon J. Clarke. All the work described is my own unless stated to the contrary, and has not been submitted for any degree at this or any other university.

Ludmila Taskesen

October 2025

# Abstract


## Tuning Magnetism and Superconductivity in Layered Chalcogenides and Pnictides

DPhil Thesis Ludmila Taskesen October 2025

This thesis reports the synthesis and characterisation of various layered mixed transition metal chalcogenide and pnictide materials. The commonality between the studied systems is that they exhibit exotic magnetic phenomena, such as high- and low-$T_c$ superconductivity and long-range magnetic order of the 3d transition metal moments.

Chapter 3 details the effect of Ni substitution in $A$Co$_2$$Ch_2$ phases, where $A$ = K, Rb, Cs, and $Ch$ = S, Se. All of the Co-based phases show ferromagnetism, with the sole exception of antiferromagnetic CsCo$_2$Se$_2$, suggesting that larger interlayer separation favours antiferromagnetic order. On the other hand, all $A$Ni$_2$$Ch_2$ phases show paramagnetism with a low-$T_c$ superconducting transition below 2 K. Upon substitution of Ni for Co, a solid solution forms, which is evident from Synchrotron PXRD, and magnetometry measurements reveal a region of antiferromagnetic ordering, before the onset of paramagnetism at high substitution levels. These drastic changes in magnetism arise from the addition of an electron to the 3d band of the metallic $A$Co$_2$$Ch_2$ phases. The antiferromagnetic members of the KCo$_{2-x}$Ni$_x$$Ch_2$ ($Ch$ = S, Se) series were studied by neutron powder diffraction, revealing A-type antiferromagnetism in $x$ = 0.5 and 1 members, while the long-range magnetic order was not detected in $x$ = 1.5 member. The refined magnetic model is highly anisotropic and is characterised by ferromagnetic coupling between Co/Ni ions within the (Co/Ni)$_2$Se$_2$ sheets and an antiferromagnetic interaction between the adjacent (Co/Ni)$_2$Se$_2$ sheets along the stacking axis. The mechanisms responsible for the different types of magnetic coupling are direct ferromagnetic interactions between transition metal ions within the plane, while the RKKY mechanism is responsible for the between-the-plane antiferromagnetic coupling, as the distance between the planes is too large (~5 Å) for any kind of direct interaction. PND of the CsCo$_{2-x}$Ni$_x$Se$_2$ solid solution also showed A-type antiferromagnetism in its $x$ = 1 member, and an intriguing structural distortion was found from Synchrotron PXRD for a small region of compositions between $1.1 \leq x \leq 1.4$. The tetragonal symmetry of the parent phase is lowered to orthorhombic in these compositions.

Chapters 4 and 5 detail the effect of chemical disorder and pressure, respectively, on the 1144 family of iron-based superconductors. CaKFe$_4$As$_4$ is subject to chemical doping with small amounts of Ca to introduce chemical disorder on one of its sublattices, however, the phase behaves as a line phase and its structural features do not allow any disorder on any of the sublattices. On the other hand, SrRbFe$_4$As$_4$ is subject to elevated pressures in a high-pressure Synchrotron PXRD experiment. It is found that no lattice collapse, driven by formation of As-As bonds, occurs between 0-26 GPa, as was reported in the case in related compounds.

Chapter 6 details the high-pressure synthesis of LaNi$_x$Bi$_2$, a low-$T_c$ superconductor with a very small superconducting volume fraction. It is found that superconductivity likely has an extrinsic origin, as even a highly pure LaNi$_x$Bi$_2$ shows minimal superconducting volume fraction and its superconducting features, including $T_c$ and $H_{c1}$ are coincidental with that of Ni-Bi secondary phases.

# Acknowledgements

First of all, I want to thank God for guiding me on this path.

I owe a lot to my supervisor, Prof. Simon Clarke, for his guidance and for the many different ways he supported me during this DPhil, and from whom I learned a lot throughout the years. I am thankful for being able to be a part of the Clarke group, which has been a wonderful and stimulating learning environment mainly thanks to Simon's leadership.

I have been fortunate to work alongside many people who have taught me a great deal not only about chemistry: Dr Victoria Falkowski for introducing me to the ways of the group and treating me to nice meals of various roast vegetables, Dr Shunsuke Sasaki for sharing his encyclopaedia-like wisdom, Dr Nicola Kelly for being an inspiration to me and all the women in STEM and for the many helpful chats about chemistry and motherhood, and Dr Robert Smyth for all the help, encouragement, and magnetic refinements without which this thesis would not see the light of day. I thank Dr Simon Cassidy not only for his help with all things Topas, but also for reaching out to me in those early days of motherhood and getting me out of the house for a much-needed library rhymetime session. A big thank you goes to Dr Tong Zhu for his help at SPring-8 and beyond, Dr Suraj Mahato for introducing me to the ways of the Bamboo press, and to Prof. Hiroshi Kageyama for allowing me to join his group for a month of chemistry fun, which has truly been a highlight of this DPhil. I would also like to mention Dr Maitane Fernandez Chento of the OxICFM CDT, who always had my back and helped me in numerous ways throughout this DPhil.

I would like to thank the other DPhil students with whom I crossed paths and shared many great memories that truly cannot be summed up on one page: Souvik, for being an older DPhil brother I didn't know I needed, Lexy - my Clarkie bestie - for being a constant source of support and kindness, Lemuel, for being a genius while never making me feel bad for not being one (and for all the hours spent trying to get a single-crystal XRD pattern of my bad crystals), Penny, for her humour and advice on baking strategies (both in the kitchen and in the S3 lab), Bradley, for kindly running all my X-rays during pregnancy due to my irrational fear of the Bruker, Mags, for being my badminton partner in those early days when we couldn't even beat old Michael, Katie, for her capillary expertise and being a good friend, Kasamol, for being a lovely presence in the office, and Georgia and Annabel for being the new CDT cool girls. Thank you goes to the lovely Part IIs who brought a lot of fun to the group each year, namely Ella and Henry who both contributed to the $ThCr_2Si_2$ work.

I would like to thank Dr Pascal Manuel (WISH) and Dr Emmanuelle Suard (D2B) for their assistance with the neutron powder diffraction experiments, and Dr Satoshi Nakano and Dr Yuki Shibazaki (University of Nagoya) for their help with DAC assembly. Also, I am grateful to Dr James Murrell and Kantaro Murayama (University of Kyoto) for their help with resistivity measurements.

Last but not least, I want to thank my family and friends: my parents Alena and Ondrej for their support and encouragement, and most notably, for helping me with childcare responsibilities. Dad, thank you for taking care of me and Ata when we most needed it even with your aching back. Mom, I will always be thankful for making me feel that I can do it, even when I did not believe it myself. To my sisters, Zuzana and Katarina, who are a source of inspiration to me since day 1: there are no words to describe my gratitude for all the ways you showed up for me in this time. Zuzka, thank you for sacrificing many vacation days to care for Ata so that I could enjoy conferences abroad. To Teo, I could have never done it without you, and I am thankful for all the sacrifices you made for our family. To Ata, thank you for your shining smile, and I hope I made you proud.

To Maya, I would give up my life's earnings for one more pricey oat latte with you pondering the reasons why we joined the CDT. To Amberle, Hunter, Atlas & Aiden, your friendship has given me so much joy in times when I most needed it. To all the moms I met at Alan Bullock Close, I am thankful for all the lovely memories we shared in the garden and beyond.

# Table of Contents

# Chapter 1. Introduction

## 1.1 Solid-state Chemistry

The solid state encompasses a great range of materials with diverse chemical and physical properties that make them suitable for technological and commercial use. This area of study is a subsection of chemistry and has close links to solid-state physics and materials chemistry. The design and synthesis of new functional materials and the optimisation of known compounds are two areas that are at the forefront of solid-state chemistry and have significantly contributed to the technological advancements that transformed our societies in the past century. The physical properties of solids are vast and include superconductivity, semiconductor properties, various types of magnetic order, such as ferromagnetism, and various optical and thermoelectric properties. Solids with a long-range order of their atomic array are classed as crystalline, while those that lack a long-range order are amorphous. The focus of this thesis will be on the former of the two. The study of crystalline solids has been enabled by the discovery and development of X-ray diffraction, a technique which probes the average structure of solids at the atomic scale, by W.H. and W.L. Bragg in the early 20$^{th}$ century.

There are many classes of solids with useful properties exploited in industrial and technological applications. The solid-state technology that has revolutionised energy storage is the rechargeable lithium ion-battery used in small consumer electronics and is now being scaled up. Here, reversible (de)intercalation of lithium ions is used to store electrical energy as chemical energy. Commercialised technologies in small consumer electronics have in the past included $LiCoO_2$,[1] $LiMn_2O_4$,[2] and $LiFePO_4$.[3] Properties of new crystalline solids are often difficult to predict, which has led to serendipitous, ground-breaking discoveries, such as high-temperature superconductivity. The discovery of high-$T_c$ cuprates earned its researchers an immediate Nobel Prize in Physics in 1987. The researchers that discovered another class of high-$T_c$ superconductors – the iron-based superconductors (IBSCs) – had originally been investigating optically transparent p-type semiconductors, and the superconductivity was unexpected; these examples shows that important

properties can emerge without warning and that subtle tuning of the composition, oxidation states, and electron count have strong impact on the resulting properties. Superconducting materials with $T_c$ above 77 K can exploit the use of liquid $N_2$ as a coolant and are industrially important as generators of large magnetic fields in medical imaging instruments including MRI systems, and could potentially find use in long-range DC power transmission, as cooling with liquid $N_2$ is considerably cheaper than with liquid He.

Magnetically-ordered materials, such as the alloy CoPtCr,[4] are used in data storage technologies, where a magnetic head is used to magnetise or demagnetise specific sections to store data in binary form. Similarly, giant magnetoresistance is achieved by layering ferromagnetic and non-ferromagnetic materials, and used in magnetoresistive random-access memories (MRAM).[5] Other examples of widespread industrial applications of solid-state materials are semiconductors; here, tuning of the bandgap is crucial to absorb and emit light of specific wavelengths and production of solid state transistors is sharply dependent on their purity, as impurities negatively affect carrier mobility and overall device efficiency. Multitudes of semiconducting materials offer promising properties for industrial use in solar cells, including Si, GaAs and other 'III-V' semiconductors, and most recently the halide perovskite-type $CH_3NH_3PbX_3$ ($X$ = Br, I)[6] have garnered considerable attention as light absorbers in solar cells. Similarly, light-emitting diodes (LEDs) based on the wide-band-gap semiconductor GaN used in lighting and displays offer much greater efficiency and lower cost than other energy-intensive sources. Zeolites and porous materials, such as metal-organic-frameworks (MOFs) offer a new potential route for $H_2$ and $CO_2$ storage and have been widely used in catalysis.[7]

Much research interest in the area of solid-state chemistry has been placed on oxides due to their inherent stability and availability, with many of the aforementioned examples of functional materials belonging to this class of compounds. Non-oxides, on the other hand, offer intriguing and exotic properties that complement those of oxides, but suffer from difficulties in avoiding oxidation and hydrolysis during formation and long-term storage. They are less explored than oxides mainly due to their lower natural abundance and complicated synthesis routes where care must be taken to

exclude atmospheric oxygen and moisture. This thesis will explore a range of non-oxide solid-state materials with magnetic and superconducting properties, including chalcogenides, pnictides, and intermetallics.

## 1.2 Chemistry of layered chalcogenides and pnictides

Among the vast array of solid-state materials, most elements prefer to build a 3D crystal structure, which is often the case in oxides; this is due to the presence of strong ionic or covalent bonds between a metal and oxygen ('hard' interactions), which extend in all dimensions. Ionic bonding also maximises the Coulombic potential, which represents the electrostatic interaction between charged ions. On the other hand, a 2D atomic array in a solid-state material often gives rise to an ideal playground for exotic magnetic and electronic phenomena. This is due to the weaker interactions between individual layers in a 2D materials, which are held together by van der Waals forces ('soft' interactions), although strong bonds between the atoms are present within the layers. The weaker interlayer interactions give rise to reduced electronic coupling along the stacking axis (between the layers), which renders the electronic structure 2-dimensional. It is worth noting that a 2-dimensional structure can be achieved in phases where bonding is strong in all directions, and the reduced dimensionality arises from cationic/anionic order or stacking of the constituent 'blocks'. Non-oxides (*i.e.* chalcogenides and pnictides) are a newly emerging classes of materials often with novel crystal structures and exotic properties and will be explored further in this work.

### *1.2.1 Common layered crystal structures*

Chalcogenides and pnictides form in a variety of layered crystal structures. The layered arrangement of chalcogenide- and pnictide-based compounds arises from the high polarizability of these anions.[8] The large size of chalcogenide and pnictide anions often gives preference for a tetrahedral coordination around a transition metal, but it is not a rule: in the case of $TiS_2$ and $TiO_2$, the former has a layered structure while in the latter bonding extends in all directions, but Ti is octahedral in each case (Figure 1.1). The layered structure of $TiS_2$ is the result of strong polarisation of the bonding between $Ti^{\delta+}$-$S^{\delta-}$ due to their difference in electronegativities, with van der Waals forces between the individual layers, which are much weaker than the polar covalent bonds within them.

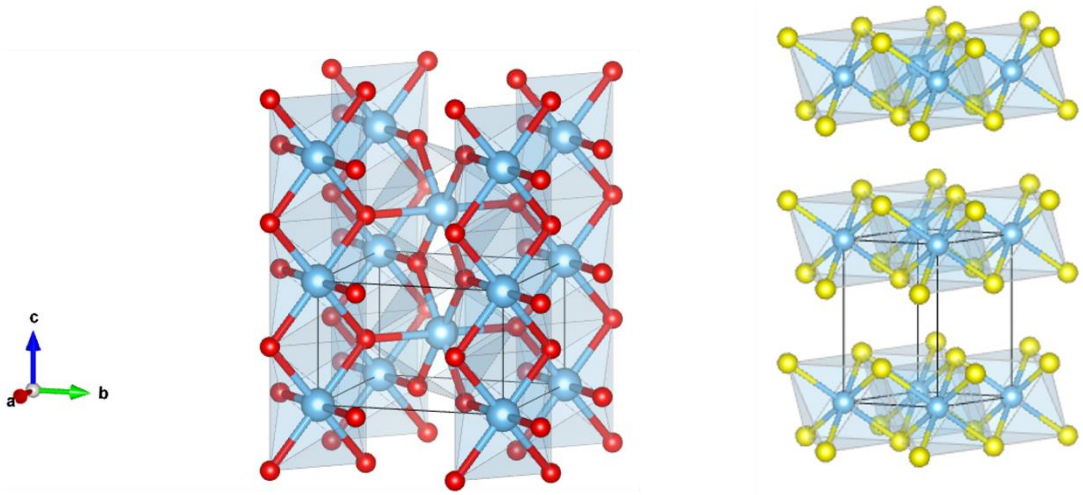


**Figure 1.1** Differences in structures of $TiO_2$ and $TiS_2$.

Other rarer coordination environments are known, too, such as square nets made entirely of pnictide anions containing unpaired electrons. Edge-sharing tetrahedra which are stacked above each other with no cations filling tetrahedral holes are classed as the PbO structure type (Figure 1.2); a famous example is the superconducting FeSe.[9] The PbFCl-structure type (also reported as $Cu_2Sb$) consists of $PbF^+$ layers (same as PbO) separated by a double layer of $Cl^-$ ions in 5-coordinate square pyramidal sites. It is known for both binary and ternary chalcogenides and pnictides. The anti-type of this structure is equally common. This structure crystallises in a primitive cell. The $ThCr_2Si_2$-type structure consists of edge-sharing $[Cr_2Si_2]^{4-}$ tetrahedral layers separated by 8-coordinated electropositive $Th^{4+}$ ions. This structure has body centring so is shifted relative to PbO. It is closely related to $BaZn_2P_2$-type structure in that there is interlayer bonding between anions present in $ThCr_2Si_2$-type, but not in $BaZn_2P_2$. There also exists an anti-type of this structure, but these compounds are much rarer; $La_2O_2Bi$ and $Nd_2O_2Te$ are examples.[10,11] The ZrCuSiAs-type structure is formed by filling the tetrahedral holes (between the double layer of $Cl^-$) of the PbFCl-type structure; here, Cu filles the tetrahedral holes between As layers. There are vast numbers of compounds reported in the ICSD with these four structure types, (~3000 for the $ThCr_2Si_2$-type).

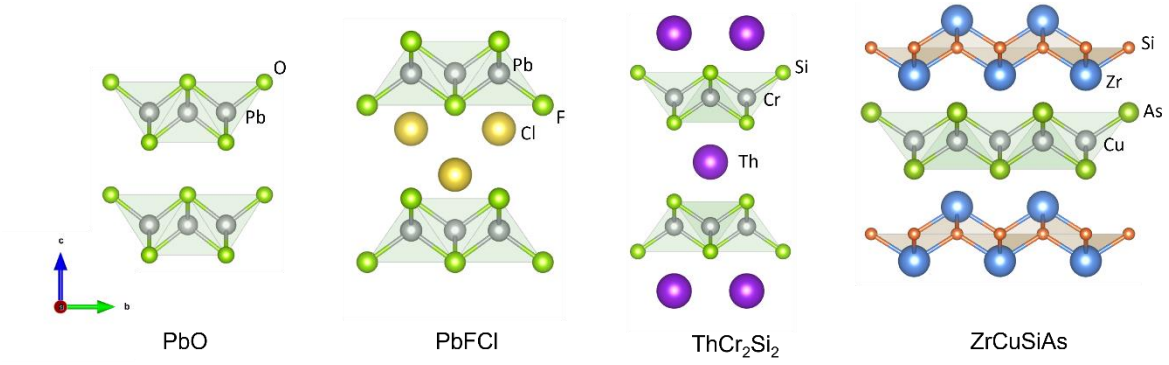


**Figure 1.2** Four common structure types of layered solid-state materials that are related to each other.

### *1.2.2 Ternary compounds with the $ThCr_2Si_2$-type structure (122 type)*

The $ThCr_2Si_2$-type structure was labelled the 'perovskite of intermetallics' due to its versatility;[12] a large range of element combinations can lead to this structure type. The notation $AT_2X_2$ described the structure containing an 8-coordinate electropositive metal *A* (*A* = alkali metal, alkaline earth, or rare earth metal), *T* = transition metal, and *X* = main group anion. The combination of $4^-$- and $8^-$-coordinate environments results in two different bonding regimes (ionic and covalent bonding) being present in these compounds,[12] which allows for a large number of elements to form ternary compounds. It has several isostructural analogues: $BaAl_4$ (*I*4/*mmm*), $CaBe_2Ge_2$ (*P*4/*nmm*), and $BaZn_2P_2$ (*I*4/*mmm*) (Figure 1.3). $BaAl_4$ is the only binary structure type related to $ThCr_2Si_2$-type and $ThCr_2Si_2$ can be obtained from $BaAl_4$-type by replacing two crystallographically unique Al sites (*4d* and *4e* Wyckoff positions) with chemically different atoms (Cr in *4d* and Si in *4e* positions). $CaBe_2Ge_2$-type is much rarer, as the metal site (*4d*) and anion site (*4e*) are switched compared to $ThCr_2Si_2$, but was observed for $RNi_2As_2$ and $RIr_2Si_2$ (R = rare earth metal).[13,14] Here thermal quenching from high-temperature conditions traps the metastable polymorph. $BaZn_2P_2$ is a structural analogue of $ThCr_2Si_2$-type in that although all crystallographic positions remain unchanged, $ThCr_2Si_2$-type are classed as those with smaller interlayer spacing and are often described as 'collapsed tetragonal' structure, while $BaZn_2P_2$-type has a larger interlayer distance and is described as 'normal (uncollapsed) tetragonal' structure.[12] The collapsed structures can undergo a structural phase transition upon application of external temperature and/or pressure, where interlayer *X*-*X* bonds form across the *A* layer.[15] This will be further discussed in Chapter 5.

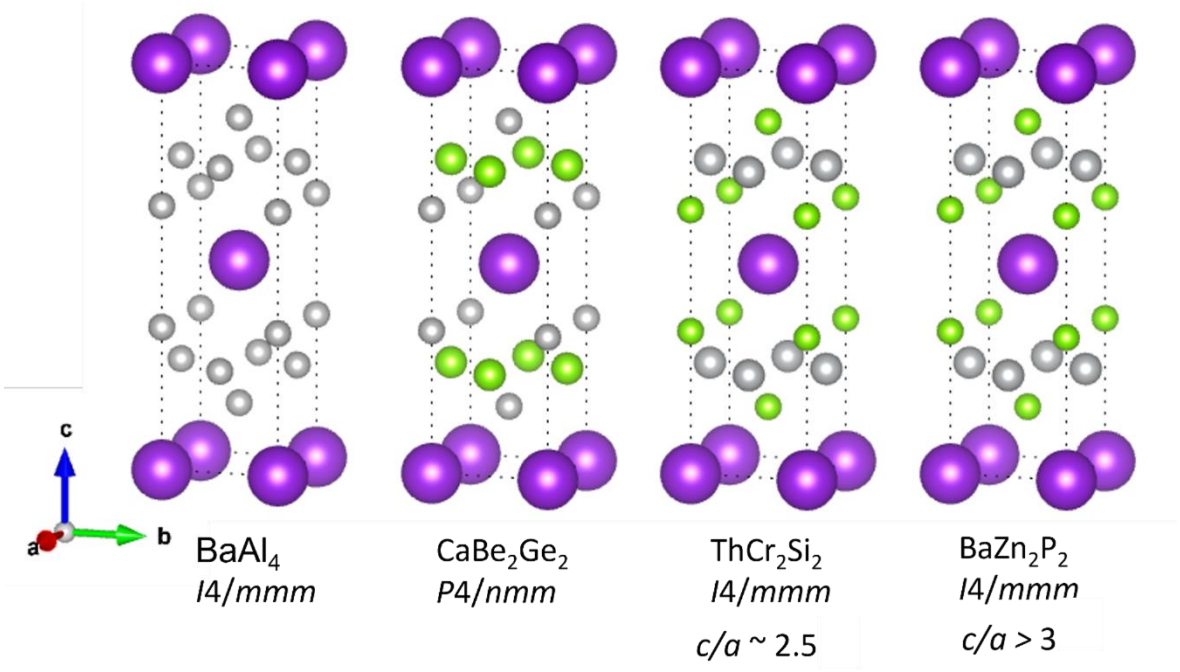


**Figure 1.3** The relationship between $BaAl_4$ and its ternary structural variants $CaBe_2Ge_2$-type, $ThCr_2Si_2$-type, and $BaZn_2P_2$-type structures. The electropositive metal, transition metal, and main group anion are shown in purple, green, and grey, respectively.

Non-stoichiometry was reported on metal and anion sites (*4e* and *4d*) in Ni- and Cu-containing pnictides, namely $ACu_{1.75}P_2$ (*A* = Ca, Sr, Eu)[16] and $RNi_{1.88}P_{1.9}$ (*R* = La, Ce)[17] and a region of homogeneity was established for $SrNi_{1.72\text{-}1.85}Sb_2$,[18] but is not as pronounced for Fe- and Co-based pnictides, such as in the case of $RT_2P_2$ (*R* = Fe, Co) family, where the upper deficiency limit was established at 3% on the transition metal site.[19,20] The reason for this is that vacancy formation allows for structural stabilisation due to the decrease in the number of valence electrons and strengthening the interlayer bonding.[20] This reasoning is thought to be proven by the fact that non-stoichiometry is not reported for $ThCr_2Si_2$-type compounds with a Group 14 element occupying the anion site (tetrelides).

Many $ThCr_2Si_2$-type phases exhibit ferromagnetic or antiferromagnetic order. High temperature superconductivity is reported for Fe-containing compounds with this structure type, and in the context of iron-based superconductors it is often talked about as the 122-type (denoting the stoichiometry); $Ba_{1-x}K_xFe_2As_2$ [21] and $Sr_{1-x}Na_xFe_2As_2$ [22] are well-investigated examples, while $K_xFe_{2-y}Se_2$ adopts a superstructure in the FeSe sheets due to ordering of Fe vacancies.[23] Heavy-

fermion behaviour is observed in $CeCu_2Si_2$,[24] $YPd_2Si_2$,[25] and $CeRu_2Si_2$,[26] with the former being the first example of a heavy-fermion superconductor; here, conduction electrons interact with localised magnetic moments to create quasiparticles that behave as if they have an extremely large effective mass, leading to enhanced correlation. Changes in magnetic properties upon substitution with nickel in $ACo_2Ch_2$ (*A* = alkali metal, *Ch* = S, Se) phases of the $ThCr_2Si_2$-type will be the topic of study in Chapter 3.

### *1.2.3 Quaternary pnictides with the 1144-type*

The 1144 structure type was first discovered by Iyo *et al.* in 2016 as a new type of iron-based superconductor with the general formula $AeAFe_4As_4$ (Ae = alkaline earth metal, A = alkali metal, shown in Figure 1.4),[27] where the difference in ionic radii between the two metals is larger than 0.35 Å. It can be thought of as a superstructure of the 122 structure type, as *Ae* and *A* order along the stacking (*c*) axis. No disorder is allowed in any of the sublattices, and the line nature of these compounds was reported. The superconducting transition temperatures, $T_c$s, are in the 30-40 K range and very high $J_c$ (critical current density) renders them suitable for technological applications (*e.g.* superconducting wires).[27] Their microstructure has been a subject of study due to an intrinsic defect structure characterised by intergrown planar defects of 122 secondary phases in the nanoscale.[28] Pure polycrystalline 1144 and single crystals are challenging to obtain, but defects were found to be desirable for obtaining superior $J_c$ performance.[28] Chapter 4 will explore the effect of chemical disorder on $CaKFe_4As_4$, and Chapter 5 will discuss the effect of applied pressure on $SrRbFe_4As_4$.

### *1.2.4 Ternary pnictides with the 112-type structure*

An intriguing feature of the 112-type compounds, which crystallise in the $HfCuSi_2$-type structure, is the metallic square net made of pnictide ions. BCS superconductivity is observed in a variety of compounds, and this structure type offers a large range of possible chemical substitutions. High-$T_c$ superconductivity is reported only in *R*-substituted $CaFeAs_2$,[29] and further substitution on As site increases superconductivity to 45 K (for P-substitution)[30] and 47 K (Sb-substitution).[31] The pnictide anion is here present in two coordination environments: $Pn(1)^{3-}$ in tetrahedral coordination with a transition metal, and $Pn(2)^{1-}$ forms a charged metallic square net, which possesses unpaired electrons and stabilises due to the Coulomb attraction-driven relaxation between the *R* ions (in $RTPn_2$, *R* = rare

earth metal, *T* = transition metal, *Pn* = pnictogen, Figure 1.4). Similar to the aforementioned structure types, the 112-type crystal structure is also quasi-two-dimensional with reduced electronic coupling along the *c*-axis, and the appearance of superconductivity is tied to the suppression of antiferromagnetic order.[9] Synthesis is hindered by difficulty of obtaining good-quality large-sized single crystals, and research is focused on polycrystalline samples made via ceramic high-temperature or high-pressure syntheses.[32] These are promising materials for emergence of intriguing electronic properties, including Kondo-lattice antiferromagnetism (Kondo effect – the interaction of conduction electrons with localised magnetic moments – coexists with antiferromagnetic order) in $CePd_xBi_2$,[33] type-II superconductivity in $CeNi_xBi_2$,[34] and high-$T_c$ superconductivity in $Ca_{1-x}RFeAs_2$ ($R$ = La ($T_c$ = 34 K), Pr ($T_c$ = 47 K)).[29] Chapter 6 will explore the effect of Ni vacancies on superconductivity in $LaNi_xBi_2$ (Figure 1.4).

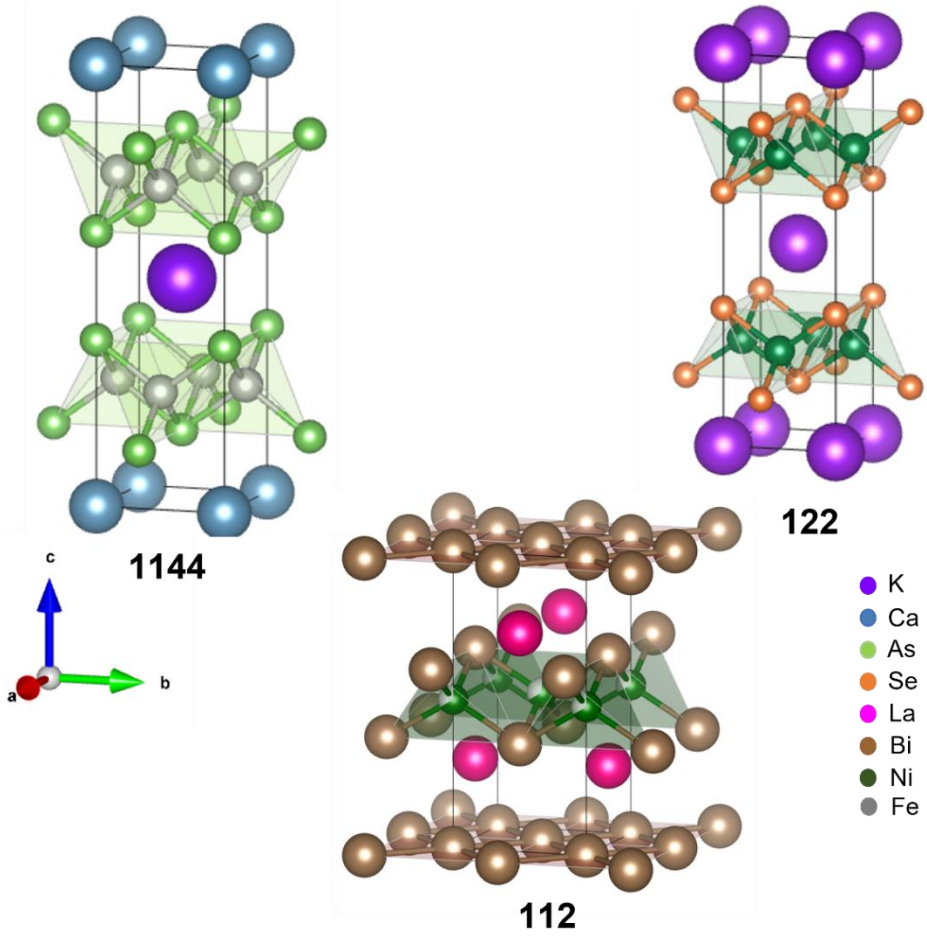


**Figure 1.4** Crystal structures of various layered pnictides and chalcogenides explored in this thesis.

## 1.3 Band theory

In a free atom, electrons occupy atomic orbitals of defined energy levels. In a solid, many atoms come together to form a crystal lattice, and their orbitals overlap: each energy level then splits into *n* levels with differing energies, and as *n* is very large, the energies are very closely spaced, resulting in a continuous energy band. The width of the bands depends on the degree of overlap of the orbitals. A good overlap results in broad bands, and density of states is small, while poor overlap of orbitals (such as core electrons) results in narrow bands, and density of states is large. As valence electrons are involved in bonding and conductivity, the energy bands are particularly relevant, while for core electrons can be disregarded due to very poor overlap of orbitals and their low energy as they are always filled. Bands have finite width, and whether the Fermi level (mean of the highest filled and lowest empty orbital) lies in a band gap or not dictates the compounds' electronic properties. The bonding of atoms and their spacing determines the allowed energy levels for electrons, separating them into valence and conduction bands; the valence band is the highest occupied energy band that contains valence electrons, while conduction band is the lowest unoccupied energy band that contains conduction electrons. The energy region between the two bands is called the band gap and determines whether a material is an insulator, semiconductor, or a conductor (Figure 1.5).

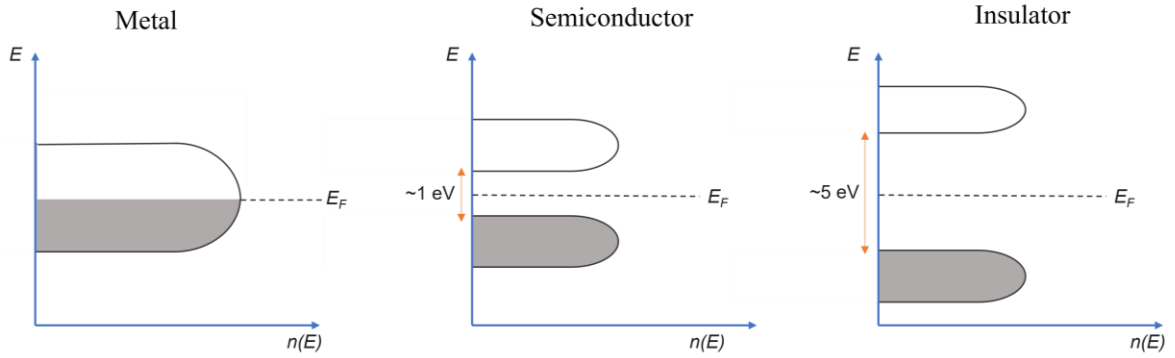


**Figure 1.5** Band structures of a metal, semiconductor, and insulator.

Therefore, a material's band gap is determined by its crystalline atomic structure, which creates the electronic band structure; the band gap is influenced by the number of electrons and the occupancy of electron shells in the atoms, and also by the strength and nature of the bonds between atoms in the crystal structure impacting the overlap of electron clouds.

## 1.4 Common Magnetic Phenomena

This section will provide an overview of some common magnetic phenomena observed in solids. Magnetic properties of solids are closely related to the crystal and electronic structure of the material; for instance, the oxidation state of an ion and magnetic spins are interconnected properties in solids, so altering the electron count of the system can have dramatic effects on properties. The oxidation state of an ion in a solid, which is determined by the number of electrons gained or lost, influences the number of unpaired electrons (electronic configuration) of the ion. Each electron has a quantum mechanical property called magnetic spin ($m_s$), which can take two values: +1/2 (spin-up) or −1/2 (spin-down). If electrons of an ion are paired – that is one spin-up, one spin-down – their magnetic moments cancel out. However, when a solid contains ions with unpaired electrons, their magnetic moments do not cancel out, which results in a material with magnetic properties where the type of the property depends on the arrangement of the spins. These will be described in the following sections. Atoms and ions also carry an orbital moment, which has high importance in lanthanide-containing systems, but it is often 'quenched' (its contribution to the total magnetic moment is minimal) by the ligand field in 1st row transition metals due to covalency, leading to only the spin component contributing to the overall magnetic moment.

### *1.4.1 Diamagnetism*

Diamagnetism is a magnetic property of materials with paired electrons, which weakly repel an applied magnetic field. This is explained by the action of a magnetic field on the orbital circulation of an electron around the nucleus, which induces a small current and produces an opposing magnetic field. This effect is described by Lenz's law. The dimensionless magnetic susceptibility $\chi_{vol}$ is a measure of how strongly a material is attracted to a magnetic field. Therefore, a diamagnetic material will have a largely temperature-independent and negative magnetic susceptibility, which is defined in terms of magnetisation $M$ and applied magnetic field $H$:

$$\chi_{vol} = \frac{M}{H} \qquad \text{Equation 1.1}$$

Diamagnetism is generally dominant in non-metallic materials with no unpaired electrons, and is typically several orders of magnitude weaker ($\chi_{vol} \sim 10^{-5}$) than Curie and Curie-Weiss type

paramagnetism (described below) and is overpowered in these types of magnetic materials. Examples include $Cu_2O$, graphite, and all closed-shell semiconductors. [35,36]

### *1.4.2 Paramagnetism*

In contrast to diamagnetism comes paramagnetism, which is a magnetic property of solids with unpaired electrons (which contain unpaired magnetic spins). These spins align parallel to applied magnetic field, resulting in positive magnetisation. A variety of molecular compounds and extended solids are paramagnets. Paramagnetic materials are divided further depending on whether electrons are localised or itinerant (*i.e.* in a metallic band).

Paramagnetism in materials with itinerant electrons, such as in metals, is referred to as Pauli paramagnetism and it is temperature-independent. This type of paramagnetism arises in the conduction band as the spin-up and spin-down electron states lose their degeneracy in an applied magnetic field. This results in the spin state which aligns parallel with the field to become energetically favoured, while the other spin state is aligned anti-parallel. The spin state that lies lower in energy becomes preferentially occupied. This causes the spin-up and spin-down electron populations to be non-equal, leaving a positive net magnetisation proportional to the density of states at the Fermi level ($E_F$) and the applied field. Pauli paramagnetism is usually of similar magnitude to diamagnetism as only electrons near the Fermi energy can contribute, and examples include $KNi_2S_2$[37] and $KNi_2Se_2$,[38,39] which will be discussed in Chapter 3.

On the other hand, when spins are localised and non-interacting, magnetic susceptibility obeys the Curie Law, where magnetic susceptibility is inversely proportional to temperature, as the thermal energy, $k_BT$, of the system, will randomise the spins away from their alignment to magnetic field:

$$\chi_{mol} = \frac{C_{mol}}{T} \qquad \text{Equation 1.2}$$

Where $C$ is the Curie constant, defined below in Equation 1.3, where $N_A$ is Avogadro's constant, $\mu_{eff}$ is the effective magnetic moment, and $k_B$ is the Boltzmann constant. This can be further simplified to Equation 1.4.

$$C_{mol} = \frac{N_A \, \mu_{eff}^2 \, \mu_B^2}{3k_B} \qquad \text{Equation 1.3}$$

$$\mu_{eff} \approx 2.84\sqrt{C} \qquad \text{Equation 1.4}$$

Using Equation 1.4, the effective magnetic moment, $\mu_{eff}$, can be calculated for a given paramagnetic material by plotting $1/\chi$ against $T$, which gives a gradient $C$ (this is graphically represented for paramagnetic, ferromagnetic, and antiferromagnetic coupling of spins in Section 1.4.3).

Solids that obey Curie law, *i.e.* exhibit paramagnetism and their spins are non-interacting, are quite rare. It is much more common that spins are localised and interact with each other. Here, the Curie Law has to be adjusted to account for these additional interactions; the Curie-Weiss law is used the describe the behaviour of paramagnetic materials with interacting spins:

$$\chi_{mol} = \frac{C_{mol}}{T - \theta} \qquad \text{Equation 1.5}$$

These tend to exhibit ferromagnetism or antiferromagnetism at low temperatures. In Curie-Weiss law, $T$ is replaced by an effective temperature ($T - \theta$), where $\theta$ is the empirical 'Weiss temperature'. The magnitude and sign of $\theta$ is dependent on the spin interactions; if $\theta > 0$, the interactions are ferromagnetic. For Curie-Weiss paramagnets with low-temperature ferromagnetic order, the value of Weiss temperature is close to $T_c$. On the other hand, when $\theta < 0$, the interactions are predominantly antiferromagnetic, and the value of Weiss temperature is close to $T_N$, the Néel temperature. The Weiss temperature gives an indication of the average strength of all the interactions between magnetic moments.

### *1.4.3 Curie-Weiss fitting*

The previously described Weiss temperature, $\theta$, can be experimentally determined by plotting inverse susceptibility, $1/\chi$, against temperature, $T$. The intercept of the plot with x axis is equal to $\theta$, which is visually represented in Figure 1.6.

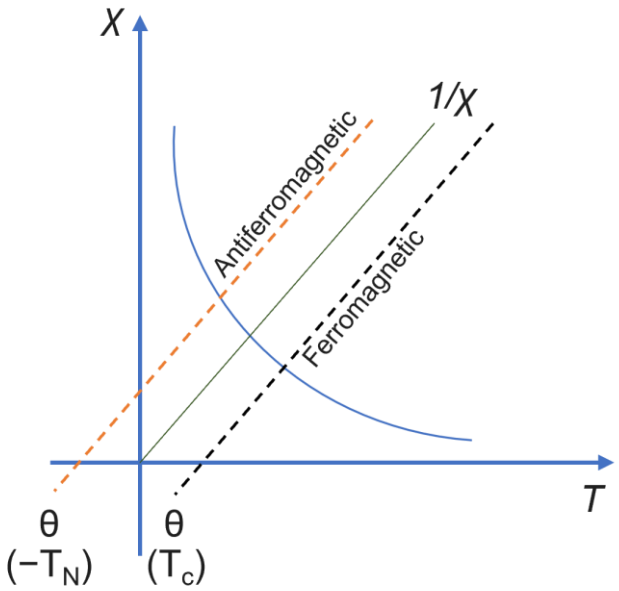


**Figure 1.6** Curie-Weiss plot of *1/χ vs T* for Curie paramagnets (solid grey line) and Curie-Weiss paramagnets (orange and black dashed lines).

Another parameter which can be extracted from the plot of *1/χ vs T* is the effective magnetic moment, $\mu_{eff}$, as described by Equation 1.4. Here, the Curie constant, C, can be extracted from the determined from extraction of the Curie constant, *C*, from a plot of *1/χ vs T* by taking the inverse of the slope. As this plot may often deviate from linearity, a Curie-Weiss plot can be modified to include a constant contribution to the susceptibility – a temperature-independent paramagnetic contribution, $\chi_0$:

$$\chi_{mol} \approx \chi_0 + \frac{C_{mol}}{T - \theta} \qquad \text{Equation 1.6}$$

### *1.4.4 Ferromagnetism*

Ferromagnetism is a magnetic property od solids similar to paramagnetism in that the unpaired electrons' spins within the material tend to align parallel to an applied field. However, in ferromagnets, the spin coupling is so strong that they align parallel even in the absence of applied field. This occurs above a certain critical temperature, known as Curie temperature, $T_C$ (Figure 1.7). Above $T_C$, the coupling is disrupted and paramagnetism is observed. As the alignment of spins occurs in domains, which do not align with each other spontaneously, an applied field is necessary to give a net positive magnetisation. The magnetisation will then persist even upon removing of field. At

strong enough fields, more of the domains are aligned until all are co-aligned, which results in saturation. This type of magnetic coupling is several orders of magnitudes greater than that of a paramagnet. An important differentiation arises between localised-electron ferromagnets and itinerant metallic ferromagnets, where there is spin polarisation (these are all of the iron triad elements).

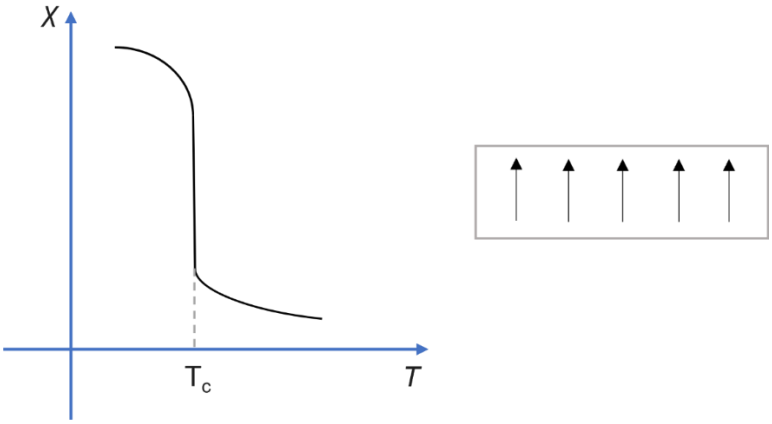


**Figure 1.7** General plot of magnetic susceptibility ($\chi$) *vs* temperature, $T$, in a ferromagnet. Right: Alignment of spins in a ferromagnet at $T < T_C$.

### *1.4.5 Antiferromagnetism*

Similar to a ferromagnet, an antiferromagnet has unpaired electrons whose spins interact strongly with each other. However, antiferromagnetic coupling is such that the magnetic spins align anti-parallel to each other. Above a critical temperature, known as Néel temperature, $T_N$, there is enough thermal energy to randomise the directions of coupled spins and paramagnetism is observed. Below $T_N$, the magnetic susceptibility will decrease towards zero with temperature, as shown in Figure 1.8.

An unusual form of antiferromagnetism arises when the magnitude of coupling is not uniform, which causes an increase in magnetic susceptibility below $T_N$, resembling ferromagnetism. This type of magnetic order is called ferrimagnetism and an example of such compound is $Fe_3O_4$.[40]

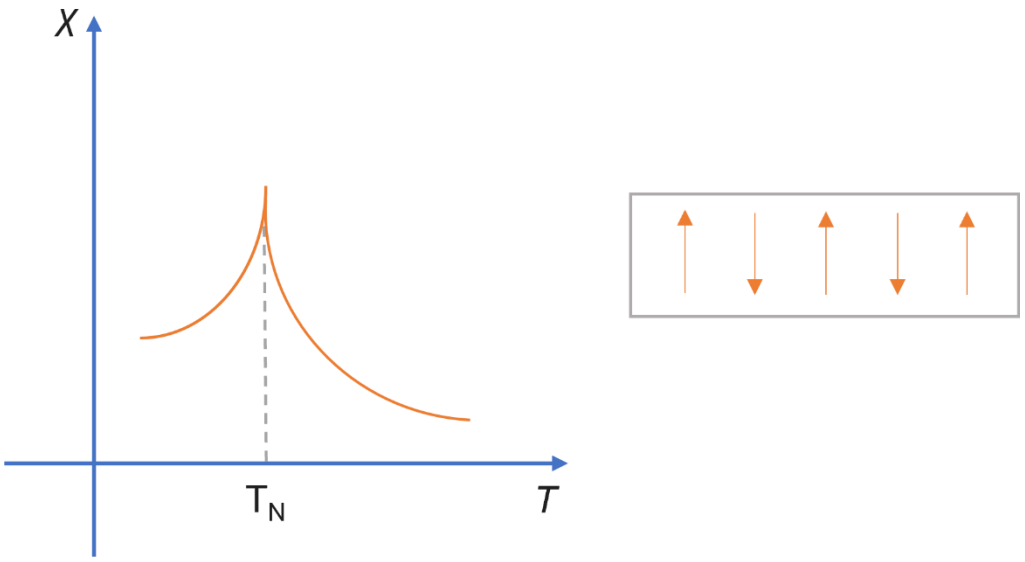


**Figure 1.8** Left: General plot of magnetic susceptibility ($\chi$) *vs* temperature, $T$, in an antiferromagnet. Right: Alignment of spins in an antiferromagnet at $T < T_N$.

## 1.5 Models of magnetic exchange

Different mechanisms of magnetic interactions exist in solid materials. Long-range interactions occur through space and are typically weak. On the other hand, magnetic interactions that occur through bonds are generally stronger and require an orbital overlap. The resulting magnetic coupling is here stronger but depends on factors such as local geometry.

### *1.5.1 Direct exchange*

Direct exchange occurs through overlapping orbitals of neighbouring magnetic ions and is very short-range. For a direct exchange to occur, an ion must have unpaired electrons.

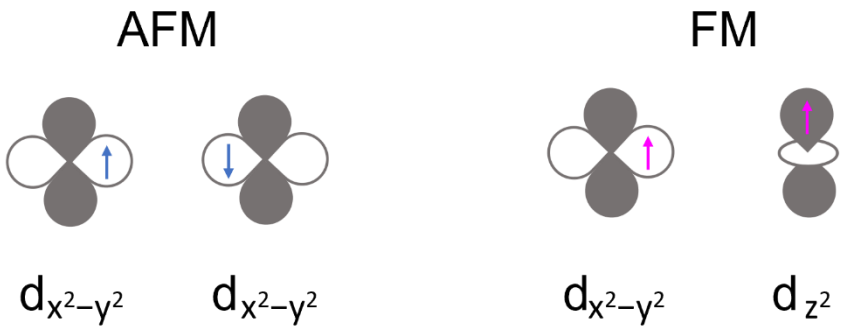


**Figure 1.9** Direct exchange for left: antiferromagnetic coupling of magnetic moments, and right: ferromagnetic coupling.

### *1.5.2 Superexchange*

Superexchange occurs when two non-neighbouring magnetic ions interact through a non-magnetic ion – a mediating ion such as oxide or fluoride– between them. When this exchange occurs in a linear arrangement of ions (and their orbitals) arranged at 180° in space, the resulting magnetic interaction is antiferromagnetism, as shown in Figure 1.10.

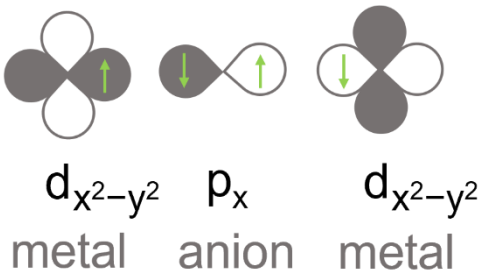


**Figure 1.10** Superexchange with antiferromagnetic coupling.

Superexchange can result in ferromagnetic coupling, too, and this often happens when the geometry of the orbital overlap is 90° for two similar metal ions interacting over a connecting p-orbital (although this case can also result in antiferromagnetism).

### *1.5.3 The Ruderman–Kittel–Kasuya–Yosida (RKKY) interaction*

The RKKY interaction is an important indirect long-range interaction in metallic compounds which also contain localised electrons; it is the dominant magnetic interaction in metals where there is little or no overlap of neighbouring magnetic electrons. It was first proposed by Ruderman and Kittel in 1954 and further elaborated on by Kasuya and Yosida. Localised magnetic moments here couple via polarisation of conduction electrons, which serve as intermediaries. A magnetic ion induces a spin polarisation in the conduction electrons in its vicinity. This spin polarisation in the itinerant electrons is felt by the moments of other magnetic ions within range, leading to an indirect coupling. The interaction is characterised by a coupling coefficient, *j*, which oscillates from positive to negative as the separation of the ions changes; therefore, depending on the distance between the magnetic moments, this interaction can result in ferromagnetic or antiferromagnetic coupling. The coupling coefficient, *j*, is given by:

$$j\,(R_l - R_{l'}) = 9\pi(\frac{j^2}{E_F})F(2k_F|R_l - R_{l'}|) \qquad \text{Equation 1.7}$$

Where $R_l$ is the lattice position of the point moment, $E_F$ is the Fermi energy, and $k_F$ is the radius of the conduction electron Fermi surface. The oscillating nature of $j$ is shown in Figure 1.11.

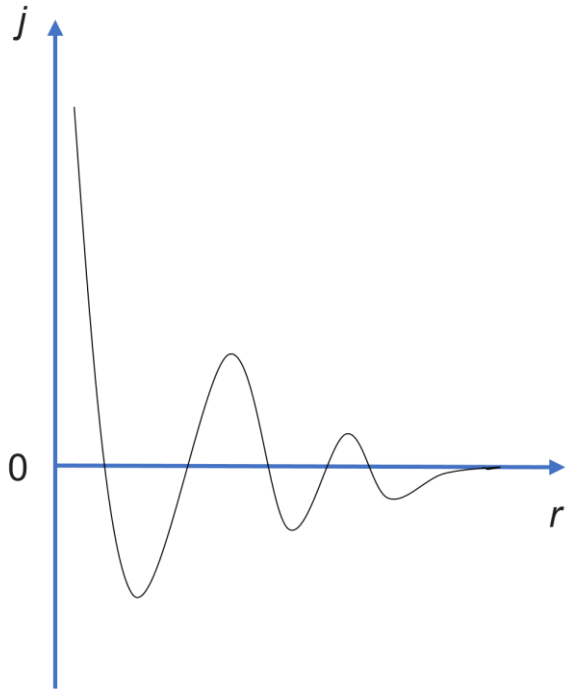


**Figure 1.11** The oscillatory nature of the exchange coupling constant, *j*, of a free electron gas in the vicinity of a point magnetic moment at the origin r = 0.

## 1.6 Superconducting materials

### *1.6.1 Discovery and Conventional superconductivity*

The discovery of superconductivity dates back to 1911, when a Dutch physicist Heike Kamerlingh Onnes used liquid helium to conduct resistivity measurements on a sample of solid mercury, and observed that its resistance fell rapidly to zero below 4.2 K.[42] His resistivity experiments were made possible by previously designing a cryogenic refrigeration technique, which allowed him to cool various substances to extremely low temperature using liquid helium. Later on, the phenomenon of zero resistance was found in other systems, and by creating a superconducting circuit from tin or lead, current continued to flow even without an external power supply had been removed. No current theory of conduction could explain Kamerlingh Onnes' findings. Later, in 1933, German physicists Fritz Meissner and Robert Ochsenfeld discovered that the superconducting transition coincides with

the expulsion of external magnetic flux from the volume of the superconductor.[43] This is caused by zero-resistance current near the surface of the superconductor, which generates an equal and opposite field to the applied field, rendering the inside of the sample 'shielded' from external magnetic field. This means that a sample in a superconducting state is a perfect diamagnet (of orders of magnitude more diamagnetic than core electrons). Like the zero resistivity, the Meissner-Ochsenfeld effect was found to be an intrinsic property of all superconductors. However, no contemporary theory of conduction could explain these findings. In 1950, Maxwell and Reynolds found that superconducting critical temperature depends on the isotopes of the elements used in a superconducting sample, which suggested that electrons interact with lattice vibrations (phonons), which leads to the observation of the phenomenon.[44,45] These findings provided the groundwork for the Baarden-Cooper-Schrieffer theory of superconductivity, published in 1957 (and was awarded the Nobel Prize in Physics in 1972),[46] which accounted for all three observed properties of known superconductors: zero resistivity, the Meissner-Ochsenfeld effect, and the isotope effect.

### *1.6.2 Baarden-Cooper Schrieffer (BCS) Theory*

According to the BCS theory, vibrations of the crystal lattice facilitate a small attractive interaction between the electrons near the Fermi level. In the superconducting state, the electrons condense into 'Cooper pairs' due to the attraction, leaving an energy gap opening at $E_F$, which is equal to the energy necessary to break a Cooper pair. The gap formation stabilises the superconducting state relative to the normal state. The superconducting energy gap ($\Delta_0$) can be related to $T_c$ and $T$ as the energy ($E$) needed to break up a Cooper pair and can be expressed as:

$$E = 2\Delta_0 = 3.52 k_B T_c \sqrt{1 - \frac{T}{T_c}} \qquad \text{Equation 1.8}$$

The energy required to break up a Cooper pair is equal to twice the energy gap as an electron excited out of the superconducting state must also pull its pair out of the ground state. From Equation 1.8, the $T_c$ can be expressed in terms of the electron-phonon coupling constant ($\lambda$) and the theoretical maximum phonon energy of the crystal, known as the Debye energy ($\hbar\omega_D$):

$$k_B T_c = 1.13\ \hbar\omega_D e - (\tfrac{1}{\lambda}) \qquad \text{Equation 1.9}$$

The relationship in Equation 1.9 shows that $T_c$ correlates positively with the Debye energy and with $\lambda$. For a material to exhibit high $T_c$, its crystal structure should have strong electron-phonon coupling and possess phonons with high frequency. According to BCS theory, superconductivity arising from electron-phonon interaction should yield $T_c$s below 30-40 K. The highest ambient pressure BCS superconductor is agreed to be $MgB_2$ with a $T_c$ of 39 K.[47] Recent studies have shown that under extreme pressures, $H_2S$ can exhibit $T_c$ of 203 K.[48] The commonality of the two phases have in common are their light constituent elements, which give rise to high frequency phonons.

Cooper pair alignment can be broken by thermal energy and by an applied external field; superconductivity is destroyed when the magnitude of the field passes a critical point ($H_c$). This can happen in two ways: Type I superconductors exclude the field entirely up to $H_c$, after which point the material ceases to exclude the field very sharply (and superconductivity is destroyed, Figure 1.12a). Type II superconductors will behave in a similar way to type I until $H_{c1}$, at which point they will gradually reduce their field expulsion until $H_{c2}$, at which point superconductivity is destroyed (Figure 1.12b).

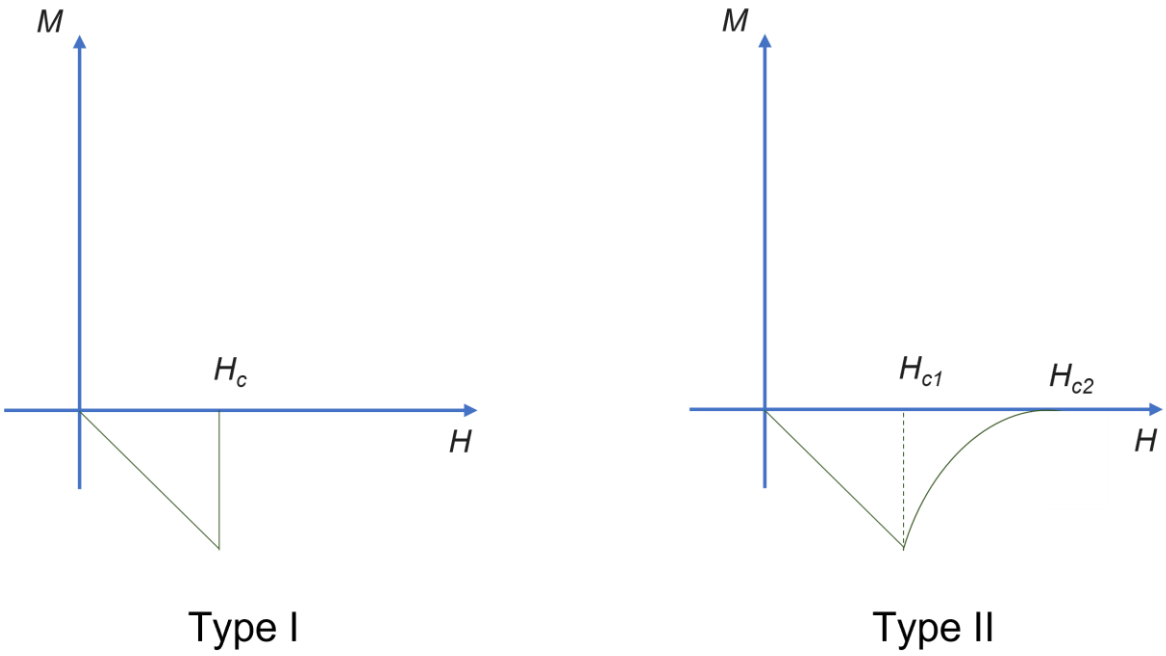


**Figure 1.12** Type I (left) and type II (right) superconductivity.

Superconductivity continues to be discovered in various systems thanks to availability of cryogenic techniques which can reach temperatures close to absolute zero. Superconductors which obey BCS theory include all elements and alloys, including a frontrunner for industrial applications in superconducting magnets - $Nb_3Sn$, with a $T_c$ of 10 K and very high $H_{c2}$ of 30 T.[49] However, since the publication of the BCS theory, a number of superconductors have been discovered that greatly exceed the upper $T_c$ limit predicted by the theory. Two main classes of these systems will be discussed in the following sections.

### *1.6.3 High temperature superconductivity*

#### 1.6.3.1 High-temperature cuprates

After 1957, it was believed that the phenomenon of superconductivity was well understood with the quantifiable limits on the properties of superconducting materials. However, in 1986, IBM researchers J.G. Bednorz and K.A. Muller discovered an unusually high $T_c$ of 30 K in a ceramic materials $La_{2-x}Ba_xCuO_4$ and $La_{2-x}Sr_xCuO_4$, which have the layered $K_2NiF_4$ structure (Figure 1.13) and $Cu^{2+}$ is Jahn-Teller distorted which leads to the 2-dimensional behaviour.[50] Several other Cu-based superconductors followed, namely $YBa_2Cu_3O_{6+x}$ with a $T_c$ of ~93 K (Figure 1.13),[51] $Bi_2Sr_2CaCu_2O_8$ ($T_c$ = 85 K),[52] and the "2223" compound $Bi_2Sr_2Ca_2Cu_3O_{10}$ ($T_c$ = 110 K).[53] The Cu-based system with the highest $T_c$ is the $HgBa_2Ca_2Cu_3O_{8+\delta}$ ($T_c$ = 133 K).[54] Overall, the important finding was that electron count needs to be controlled to evade the Mott-Hubbard state and produce the metallic state, which becomes superconducting. These discoveries sparked a huge level of interest in the area, especially since these systems do not require liquid helium as coolant, but instead can be cooled with liquid nitrogen, reducing the cost of the technology, however their industrial application has been hindered by the difficulty of turning these ceramic compounds into materials which are application-ready, such as wires.

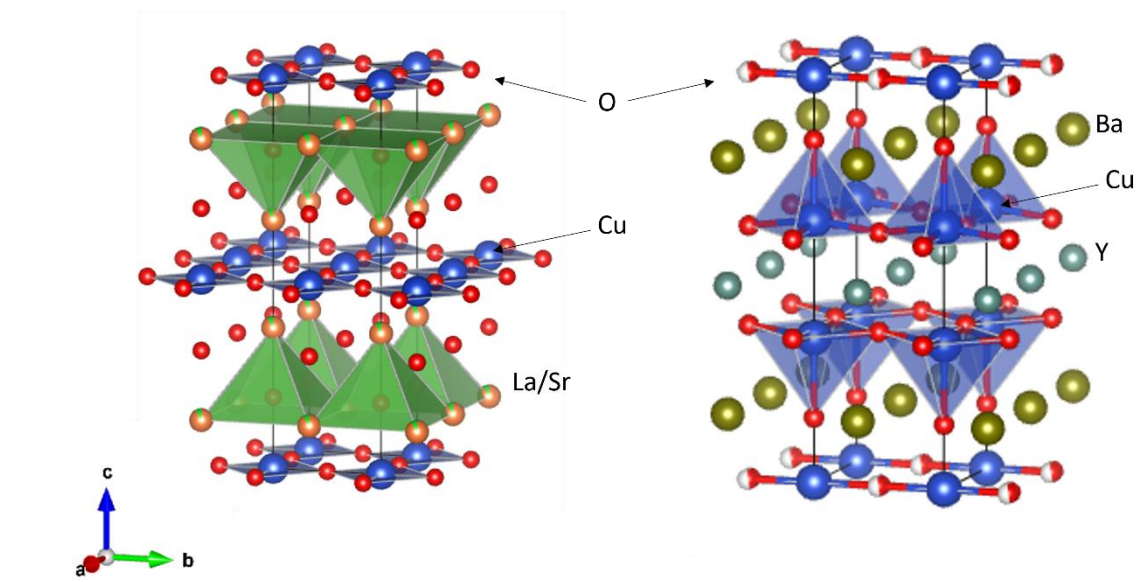


**Figure 1.13** Left: Structure of $La_{2-x}Sr_xCuO_4$ and right: structure of $YBa_2Cu_3O_{6+x}$, with their 2-dimensional sheets highlighted in blue.

The high $T_c$s of cuprate superconductors cannot be explained by BCS theory, as they show no phonon dependence. A common structural feature of these systems is the 2-dimensional $CuO_2$ block, formed by corner-sharing square planar $CuO_4$ units, and separated by different spacing layers; in $La_{2-x}Sr_xCuO_4$, the lanthanum/strontium oxide layer separates the $CuO_2$ sheets, while in $YBa_2Cu_3O_{6+x}$, the structure is a bit more complicated and contains 1-dimensional chains of corner-linked $CuO_4$ squares along the crystallographic *b*-direction, in addition to 2-dimensional $CuO_2$ sheets separated by yttrium ions. Although the Cooper pairing mechanism in cuprate superconductors is yet to be fully explained by theory, it is understood that it is based on Cooper pairs formed by coupling to magnetic fluctuations, rather than BCS-type electron-phonon coupling; magnetic "spin wave" interactions between the electron and the magnetic lattice may play a role in the coupling of Cooper pairs.[55] The surge in research after the discovery of these compounds declined in the 1990s, however, a new superconducting surprise arose in 2008 with the iron-based superconductors, which will be described in the following sections.

### 1.6.3.1 Iron-based superconductors (IBSCs)

#### *1.6.3.1.1 Structure types of iron pnictide superconductors*

In 2008, Kamihara *et al.* of the Hosono group in Japan discovered that superconductivity emerges below 26 K in F-doped LaFeAsO,[56] which takes the ZrCuSiAs structure type and contains anti-PbO-type layers of FeAs, described in Figure 1.1. Substitution of smaller lanthanide ions and tuning the fluoride content led to increased $T_c$ of 55 K in $SmFeAsO_{1-x}F_x$,[57] and Tb- and Dy-substituted *Ln*FeAs(O,F) were achieved by Bos *et al*. using high-pressure synthesis and reaching $T_c$s of 46 and 45 K, respectively,[58] far above the BCS theory's predicted limit of $T_c$. This marked the discovery of a new superconducting family of compounds – the iron-based superconductors (IBSCs) – similar to cuprates in their high $T_c$s and layered structures.

McQueen *et al*. studied the stoichiometric LaFePO phase, which was the initial focus of the research in Hosono's group; Kamihara *et al.* found that LaFePO had a $T_c$ of 3.2 K,[59] which was later increased to 7 K upon doping with fluoride ions. However, McQueen *et al.* showed that stoichiometric LaFePO phase does not show any superconducting features in its resistivity measurements, and therefore concluded that superconductivity arises from oxygen vacancies in $LaFePO_{1-x}$.[60]

As the anti-PbO-type layer is a common structural feature of a variety of systems, and superconductivity was and still is believed to originate in the anti-PbO-type $[Fe_2As_2)^{2-}$ layer when the electron count and structural parameters are optimised, this exciting discovery sparked a new surge in research into superconducting materials. Since 2008, a variety of iron pnictide-based superconductors have been found, along with a smaller number of iron chalcogenides, which will be described below.

In *Ln*OFeAs (*Ln* = La-Dy), also known as the 1111 structure type of IBSCs (space group *P*4/*nmm*), superconductivity can be tuned by doping on various sites; substitution of another rare earth ion for La can induce superconducting regime in the parent compound, and when Th is substituted for Gd in GdFeAsO, $T_c$ is raised to 56 K,[61] one of the highest transition temperatures of IBSC reported. Similarly, hydride substitution for oxide introduces superconductivity in LaFeAsO with a $T_c$ of 36 K, and upon application of pressure of 6 GPa, $T_c$ is raised to 52 K.[62] Cobalt doping on the Fe site in

LaFeAsO was also found to introduce superconductivity, however $T_c$ reached a maximum of moderate 17 K.[63] It would be reasonable to speculate that this is because the layer responsible for superconductivity is being chemically disrupted. A contrasting behaviour to the 1111 IBCSs is seen in the 111-type (space group *P*4/*nmm*): bulk superconductivity is observed in the stoichiometric LiFeAs ($T_c$ = 18 K)[64] and NaFeAs ($T_c$ = 9 K),[65] and even 2% Li-deficiency was found to supress superconductivity.[66]

All previous examples of substitution into LaFeAsO were electron-doping. Hole-doping – i.e. oxidative substitution – was carried out in the case of aliovalent of K for Ba in $BaFe_2As_2$ with the $ThCr_2Si_2$-type structure (space group *I*4/*mmm*), where $T_c$ of 38 K is observed in composition $Ba_{0.6}K_{0.4}Fe_2As_2$.[21] Other 122 IBSC include $Sr_{0.6}Na_{0.4}Fe_2As_2$ ($T_c$ = 26 K),[22] $Sr_{0.6}K_{0.4}Fe_2As_2$ ($T_c$ = 32 K),[67] and $Ca_{0.6}Na_{0.4}Fe_2As_2$ ($T_c$ = 21 K).[68] Onset of the superconducting state can be induced by substitution on Fe and pnictogen site in 122-type IBSCs, too; P-substitution into non-superconducting stoichiometric $BaFe_2As_2$ has the same effect as chemical pressure. Here, at ambient pressures, smaller P takes place of As and this alters the bond distances and angles of the structure in a very similar way to application of external pressure, resulting in a $T_c$ of 30 K for $BaFe_2(As_{1-x}P_x)_2$ with x = 0.24-0.6.[69] Another structure type of IBCS closely related to the 122-type is the 12442-type (space group *I*4/*mmm*), shown on the left-hand side of Figure 1.14. Here, a tetrahedral layer of $[Ca_2F_2]^{2+}$ is inserted between the layers of $[Fe_2As_2]^{2-}$, while K retains its crystallographic position. $KCa_2Fe_4As_4F_2$ was found to be superconducting below 33.5 K and was found to have a particularly high $H_{c2}$ of 50 T,[70] several times higher than for other IBSCs. A related structure type to 12442, previously shown in Figure 1.4, is the 1144-structure type of IBSC; here, the only difference from the 12442-type is that the $[Ca_2F_2]^{2+}$ layer has been replaced by a layer of 8-coordinate Ca ions only, and the alternation of Ca and K ions is strict, *i.e.* no disorder is allowed on any of the sublattices, lowering its symmetry from body centred to primitive tetragonal (space group *P*4/*mmm*). Fe is here found in the ideal valence for observation of superconductivity: $Fe^{+2.25}$.[27] $T_c$ of $CaKFe_4As_4$ is 33.2 K and for other phases of this structure type $T_c$ ranges between 30-35 K.[27] Other structurally complex IBSCs include $Sr_2VO_3FeAs$ with a $T_c$ of 37 K,[71] where perovskite-type oxide spacing layers are

inserted between iron arsenide layers, and $Sr_4Sc_2Fe_2P_2O_6$ (space group *P*4/n*mm*) with a moderate $T_c$ of 17 K.[72] Figure 1.14 shows a selection of superconducting iron-based pnictides.

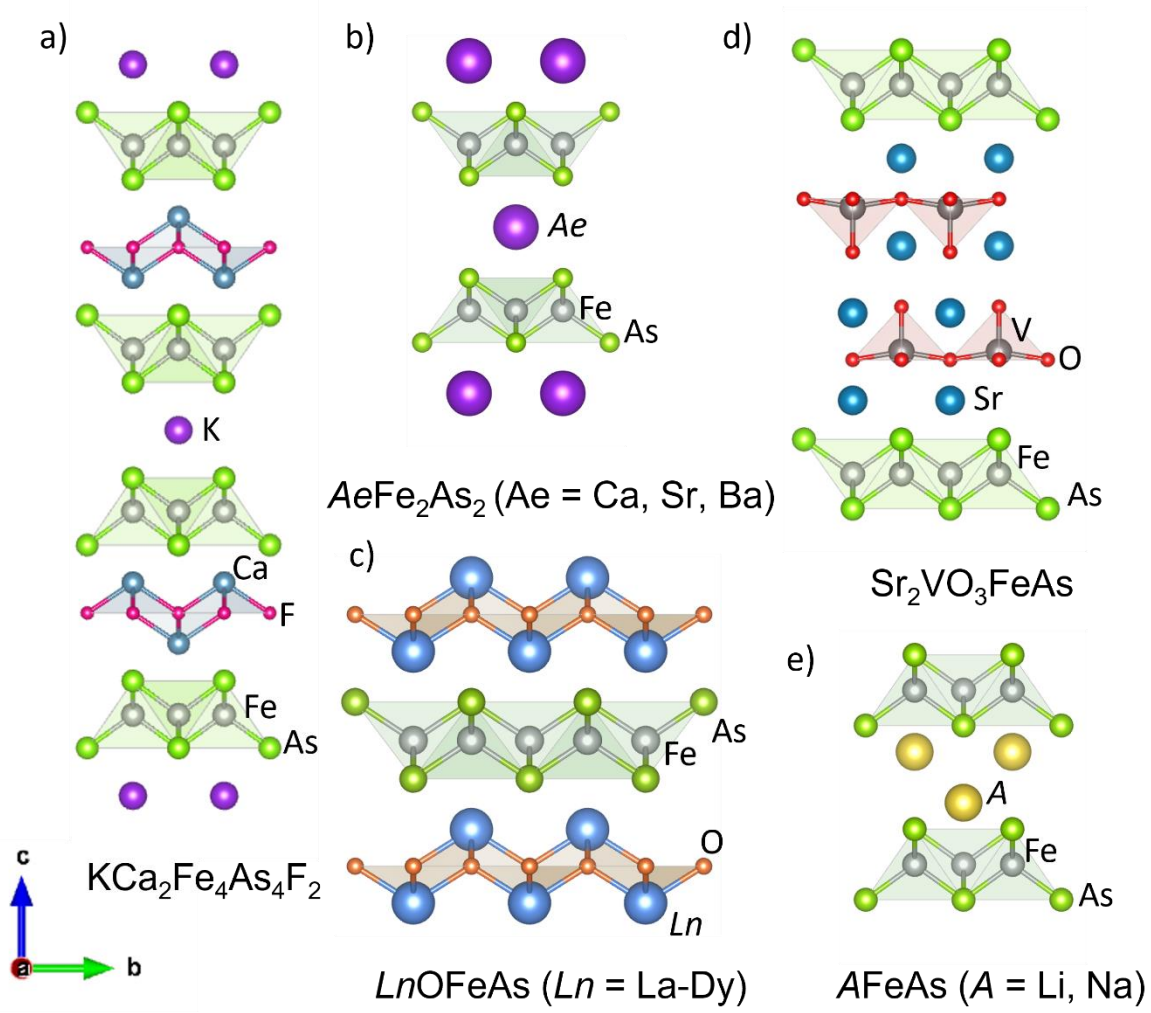


**Figure 1.14** Several iron arsenide-based layered structures that exhibit superconductivity: a) $KCa_2Fe_4As_4F_2$,[70] b) *Ae*$Fe_2As_2$,[21,22,68] c) *Ln*OFeAs,[61-63] d) $Sr_2VO_3FeAs$,[71] e) *A*FeAs.[64-66]

### *1.6.3.1.2 Superconducting and magnetic properties of iron pnictide superconductors*

The phase diagrams of different IBSCs reveal differences among the magnetic properties of various structural types; LiFeAs and FeSe (the only example of the 11-type of IBSCs) are superconducting when undoped,[8,66] while LaFe*Pn*O (*Pn* = P, As), and *Ae*$Fe_2As_2$ (*Ae* = Ca, Sr, Ba) are antiferromagnetic non-superconducting metals, where electron- and hole-doping, respectively, suppresses the magnetic order and induces superconductivity.[62,63,67-69] Application of external pressure has also been found to induce superconductivity in some IBSCs; $CaFe_2As_2$ transitions from

its antiferromagnetic state at ambient pressures to superconducting state at just 0.69 GPa.[73] A commonly occurring feature in the iron pnictide superconductor family is the existence of an antiferromagnetic state that closely neighbours the superconducting state, and the two are often found to overlap. Phase diagrams of several systems show that upon electron/hole doping, the structural and antiferromagnetic transition temperatures are reduced and eventually supressed whilst a superconducting state is induced simultaneously. This type of behaviour has been identified for several unconventional superconductors.[74-76] Antiferromagnetic order and superconductivity sometimes overlap before the system enters a fully superconducting state (Figure 1.15a), which is a feature not seen in cuprate superconductors (Figure 1.15b); this could be because in IBSCs there are multiple bands crossing $E_F$, while in cuprates only one. Parallels can be drawn between the phase diagram of IBSCs and the cuprate superconductors, shown in Figure 1.15a and b, respectively, on examples of $BaFe_2As_2$ and $YBa_2Cu_3O_{6+x}$, taken from References 74 and 77. The difference is that the undoped parent of the cuprate superconductor is an antiferromagnetic Mott insulator.[77]

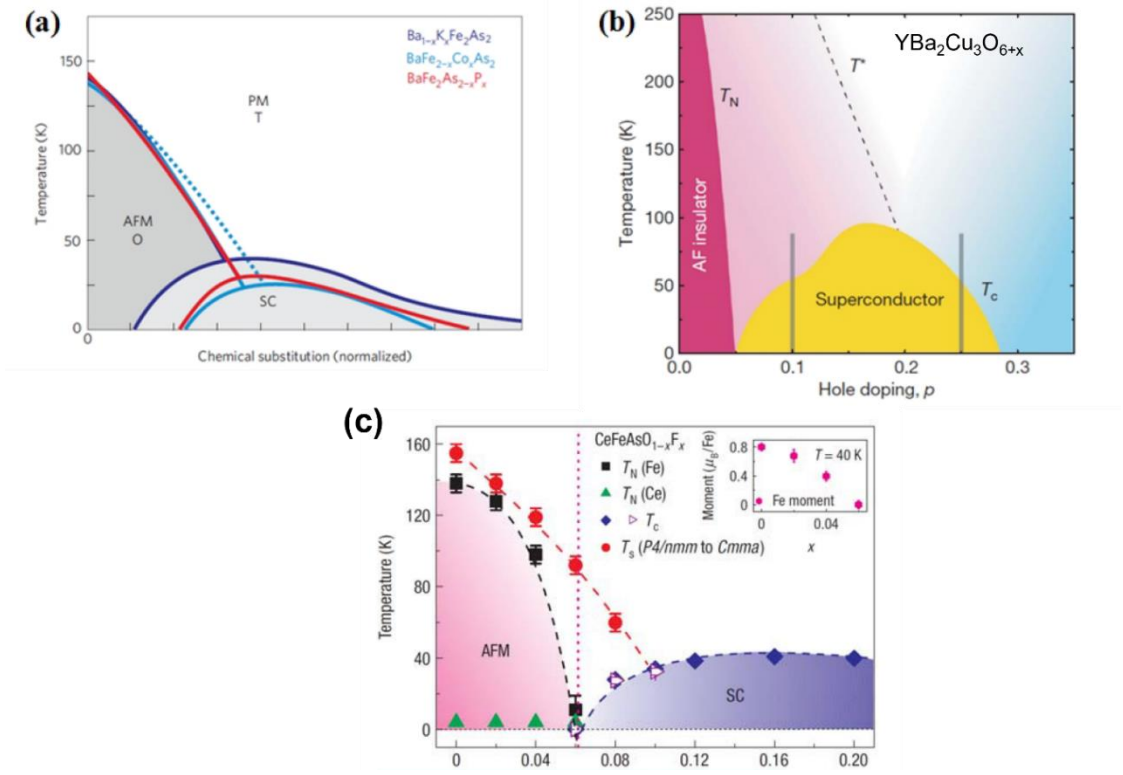


**Figure 1.15** Magnetic phase diagrams of a) $BaFe_2As_2$ system (taken from Reference 74), b) $YBa_2Cu_3O_{6+x}$ system (from Reference 77), and c) $CeFeAsO_{1-x}F_x$ system (from Reference 78), showing the effect of electron and hole doping against the magnetic and superconducting properties of three high temperature superconductors.

*1.6.3.1.3 Iron chalcogenide superconductors*

The iron-based superconducting compound with the simplest structure is the FeSe with only anti-PbO-type layers of $FeSe_4$ tetrahedra stacked above each other and separated by a van der Waals gap. This β polymorph of FeSe has a $T_c$ = 8 K,[79] and application of external pressure raises $T_c$ to 37 K at ~9 GPa.[80] Also, isovalent substitution with Te raises the $T_c$ to 14 K for x = 0.5 in $FeSe_{1-x}Te_x$.[81] Incorporation of alkali metals into the spacer layers results in a formation of the 122 class of IBSC; a notable example is the $K_{1-x}Fe_{2-y}Se_2$ system, which was found to exhibit iron vacancy ordering at y = 0.4 and x = 0.2.[23] A fivefold expansion of the parent $ThCr_2Si_2$ cell along the *ab* plane was identified and is reported to accommodate 20% vacancy on a single site within the square FeSe layer.[23] $K_{1-x}Fe_{2-y}Se_2$ and its Rb-analogue were both found to intrinsically phase separate into a superconducting phase with $T_c$~30 K coexisting with extremely high Néel temperature (>500 K) antiferromagnetic phase with ordered iron vacancies.[82-84] Speller *et al.* used a number of powerful scanning microscopy techniques, namely High-resolution Electron Backscatter Diffraction, Energy Dispersive X-ray analysis, and Scanning Transmission Electron Microscopy, to analyse a single crystal of $Rb_{1-x}Fe_{2-y}Se_2$ system[83,84] and found that two different compositions can be located in different domains: Fe-poor $Rb_{0.8}Fe_{1.6}Se_2$ matrix and Fe-rich $Rb_{0.5}Fe_2Se_2$ plate-like filaments shown in Figure 1.16.

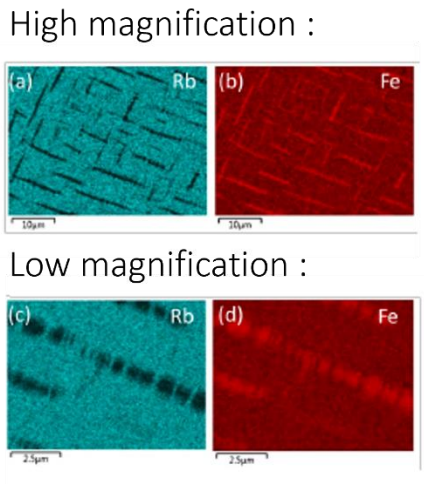


**Figure 1.16** Elemental Rb and Fe EDX maps with high (a,b) and low (c,d) magnification of regions of Fe-poor and Fe-rich $Rb_{1-x}Fe_{2-y}Se_2$ crystal from Rerefence 83.

The plate-like filaments in Figure 1.16 are seen to be rich in Fe and poor in Rb relative to the matrix and Se is distributed uniformly. Later, Texier *et al.* studied the $Rb_{1-x}Fe_{2-y}Se_2$ system using solid state NMR and showed that the Fe-poor matrix is the superconducting phase, while the Fe-rich filaments are antiferromagnetic and non-superconducting.[82]

Another important study where $T_c$ was substantially increased from 8 K in an FeSe was conducted using intercalation of lithium metal in liquid $NH_3$ solution. $T_c$ is raised to 43K, and Neutron Powder Diffraction identified ammonia and amide moieties co-intercalated into the structure with Li on a deuterated sample (Figure 1.17).[85]

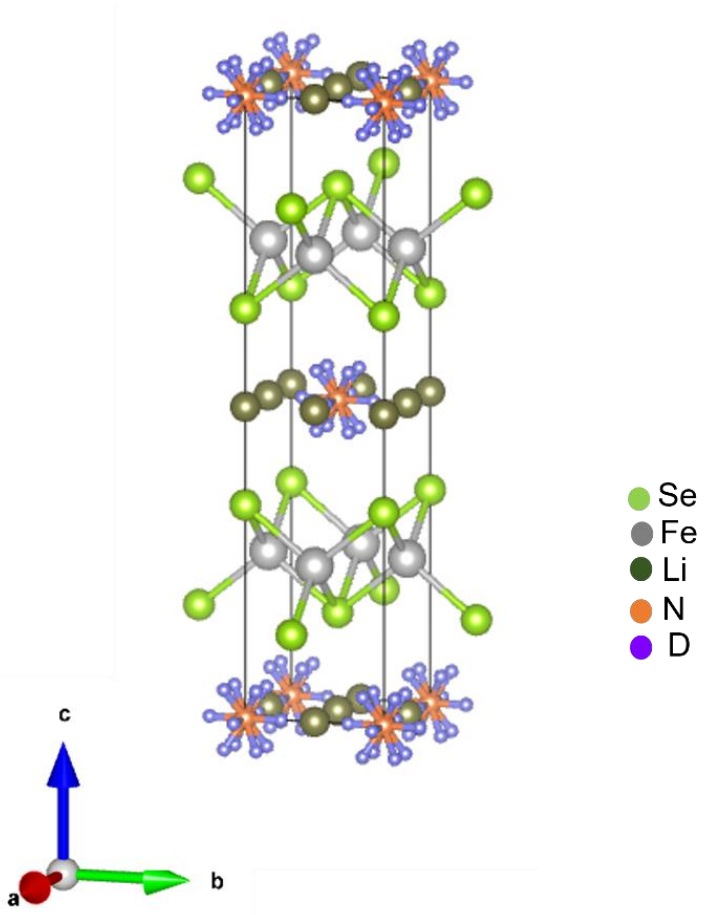


**Figure 1.17** Structure of lithium and ammonia co-intercalated into FeSe, yielding a $Li_{0.6(1)}(ND_2)_{0.2(1)}(ND_3)_{0.8(1)}$ $Fe_2Se_2$ (from PND).[85]

## 1.7 Thesis aims

The research described in this thesis will focus on tuning magnetic and superconducting properties of layered chalcogenides and pnictides with composition; the close relationship between structure, composition, and properties of three structure types of layered non-oxide materials with a 2-dimensional electronic structure will be explored. The three investigated structure types are:

- 122-type ($A$Ni$_2$$Ch_2$ and $A$Co$_2$$Ch_2$, with $A$ = K, Rb, Cs, and $Ch$ = S, Se, and the solid solutions that form when these nickel- and cobalt-based phases mix),
- the 1144-type ($CaKFe_4As_4$ and $SrRbFe_4As_4$), and
- the 112-type ($LaNi_xBi_2$).

Although structurally related, they have drastically different properties, and show varying responses to chemical substitution, and effect of chemical/external pressure.

Chapter 3 will explore the phase space between $A$Ni$_2$$Ch_2$ and $A$Co$_2$$Ch_2$, with $A$ = K, Rb, Cs, and $Ch$ = S, Se which take the $ThCr_2Si_2$ structure type. The end members of the $A$Co$_{2-x}$Ni$_x$$Ch_2$ solid solutions have varying properties; the nickel-containing chalcogenides are Pauli paramagnetic with a low-temperature superconducting transition (>1 K), while the cobalt-containing chalcogenides are ferromagnets, with the sole exception of $CsCo_2Se_2$ which is antiferromagnetic below 66 K. In the series $A$ = Tl, K, Rb, Cs, of $A$Co$_2$Se$_2$, it is suggested that increasing the interlayer spacing favours antiferromagnetic coupling. A number of literature reports demonstrate antiferromagnetic coupling in 122 phases occurs via the long-range RKKY mechanism, as interlayer spacing of the tetrahedral $[T_2X_2]^{2-}$ layers is in the order of ~5 Å. Chapter 3 will focus on mapping out the magnetic regions of the $A$Co$_{2-x}$Ni$_x$$Ch_2$ solid solutions using SQUID magnetometry and Neutron Powder Diffraction. An anomalous structural behaviour, not reported before in the $ThCr_2Si_2$-type structure, is shown to occur in a small range of $x$ in $CsCo_{2-x}Ni_xSe_2$, where a lowering of symmetry from body-centred tetragonal to orthorhombic is demonstrated using high resolution powder X-ray diffraction.

Chapter 4 focuses on investigating the effects of chemical disorder on the structure of $CaKFe_4As_4$. Iyo *et al.* reported that the 1144-type phases are line phases, meaning that no disorder is allowed as that would result in formation of side phases instead. However, several studies suggest that doping is possible on the Fe site with Co or Ni and a report of (La, Na)$A$Fe$_4$As$_4$ (A = Rb, Cs)[86] shows that

the structure can accommodate a degree of disorder on at least one of the sublattices. This chapter will evaluate the effect of non-stoichiometry between Ca : K cations in $CaKFe_4As_4$, and relate the changes in structure to its superconducting properties. Chapter 5 will focus on another member of the 1144 class of IBSCs: $SrRbFe_4As_4$. Following reports of half-collapse and eventual full collapse of the 1144 structure upon application of external pressure (< 10 GPa) on $CaAFe_4As_4$ (*A* = K, Rb),[87,88] this investigation focuses on the response of a larger 1144 phase $SrRbFe_4As_4$ to increased pressures of up to 26 GPa using high pressure powder X-ray diffraction.

Lastly, Chapter 6 will explore the effect of nickel vacancies on superconductivity in $LaNi_xBi_2$. Several literature reports state the $T_c$ of Ni-deficient $LaNi_xBi_2$ at ~4 K,[89,90] however the superconducting volume fraction of the phase is reported below 1%, raising questions as to the origin of the superconducting feature, as a number of Bi-containing impurities have coincidental $T_c$, and it was reported that highly pure $LaNi_xBi_2$ is difficult to obtain. A related phase, $CeNi_xBi_2$ shows an identical $T_c$,[90,91] yet its superconducting volume fraction is that of a bulk superconductor (superconducting volume fraction of 96%). Our investigations use an alternative synthesis route – high-pressure ceramic method – to achieve a 99% pure $LaNi_xBi_2$ from powder X-ray diffraction, and use magnetometry and resistivity measurements to characterise the superconducting features of the compound.

## References

[1] Mizushima, K., Jones, P. C., Wiseman, P. J., Goodenough, J. B. (1980) LixCoO2 (0<x~l): A New cathode material for batteries of high energy density. *Mat. Res. Bull.*, *15*(6), 783-789. https://doi.org/10.1016/0025-5408(80)90012-4.

[2] Thackeray, M. M., Johnson, P. J., de Picciotto, L. A., Africa, S., Bruce, P. G., Goodenough, J. B. (1984). Electrochemical extraction of lithium from LiMn2O. *Mat. Res. Bull*, *19*(2), 179-187. https://doi.org/10.1016/0025-5408(84)90088-6.

[3] Padhi, A. K., Goodenough, J. B. (1997). Phospho-olivines as Positive-Electrode Materials for Rechargeable Lithium Batteries. *J. Electrochem. Soc.*, *144*(4), 1188, https://doi.org/10.1149/1.1837571.

[4] Judy, J. H. (2005). Advancements in PMR thin-film media. *Journal of Magnetism and Magnetic Materials*, *287*, 16–26. https://doi.org/10.1016/j.jmmm.2004.10.004

[5] Spaldin, N.A. (2013). *Magnetic materials fundamentals and device applications*. Cambridge Cambridge Univ. Press, 16-19.

[6] Wehrenfennig, C., Liu, M., Snaith, H. J., Johnston, M. B., & Herz, L. M. (2014). Charge-carrier dynamics in vapour-deposited films of the organolead halide perovskite CH3NH3PbI3-xClx. *Energy and Environmental Science*, *7*(7), 2269–2275. https://doi.org/10.1039/c4ee01358a

[7] Saha, D., Bao, Z., Jia, F., & Deng, S. (2010). Adsorption of CO2, CH4, N2O, and N 2 on MOF-5, MOF-177, and zeolite 5A. *Environmental Science and Technology*, *44*(5), 1820–1826. https://doi.org/10.1021/es9032309

[8] Madden, P. A., Wilson, M. (1996). 'Covalent' Effects in 'Ionic' Systems. *Chem. Soc. Rev*., *25*, 339-350. https://doi.org/10.1039/CS9962500339.

[9] Yamasaki, A., Matsui, Y., Imada, S., Takase, K., Azuma, H., Muro, T., Kato, Y., Higashiya, A., Sekiyama, A., Suga, S., Yabashi, M., Tamasaku, K., Ishikawa, T., Terashima, K., Kobori, H., Sugimura, A., Umeyama, N., Sato, H., Hara, Y, Ikeda, S. I. (2010). Electron correlation in the FeSe superconductor studied by bulk-sensitive photoemission spectroscopy. *Physical Review B - Condensed Matter and Materials Physics*, *82*(18). https://doi.org/10.1103/PhysRevB.82.184511

[10] Mizoguchi, H., Kamiya, T., Hosono, H. (2012). Superconducting compounds with metallic square net. *Solid State Communications*, *152*(8), 666–670. https://doi.org/10.1016/j.ssc.2011.12.016

[11] Raccah, M., Longo, J. M., Eick, A., Length, B. (1967). The Crystal Structure of Neodymium Monotellurooxide—Nd2O2Te, *Acta Cryst*, *6*(8), 1471-1473.https://doi.org/10.1021/ic50054a008.

[12] Shatruk, M. (2019). ThCr 2 Si 2 structure type: The "perovskite" of intermetallics. *Journal of Solid State Chemistry*, 272, 198–209. https://doi.org/10.1016/j.jssc.2019.02.012

[13] Ghadraoui, E. H., Pivan, J. Y., Gudrin, R., Pena, O., Padiou, J., Sergent, M. (1988). Polymorphism and Physical Porperties of LnNi2As2 Compounds (Ln = La - Gd). *Mat. Res. Bull*, *23*(9), 1345-1354. https://doi.org/10.1016/0025-5408(88)90123-7.

[14] Mihalik, M., Pospíšil, J., Rudajevová, A., Marti, X., Wallacher, D., Hoser, A., Hofmann, T., Diviš, M., Sechovský, V. (2011). Structure phase transitions of polymorphic compounds with layered crystal structures: The REIr2Si2 case. *Intermetallics*, *19*(10), 1622–1626. https://doi.org/10.1016/j.intermet.2011.06.011

[15] Johrendt, D., Felser, C., Jepsen, O., Andersen, O. K., Mewis, A., Rouxel, J. (1997). LMTO Band Structure Calculations of ThCr2Si2-Type Transition Metal Compounds. *Journal of Solid State Chemistry*, *130*(2), 254-265. https://doi.org/10.1006/jssc.1997.7300.

[16] Mewis, A. (1980). Ternäre Phosphide mit $ThCr_2Si_2$ -Struktur / Ternary Phosphides with the $ThCr_2Si_2$ Structure. *Zeitschrift für Naturforschung B*, 35(2), 1980, 141-145. https://doi.org/10.1515/znb-1980-0205.

[17] Hofmann, W.K., W. Jeitschko (1984). Structural investigations of ternary lanthanoid and uranium nickel phosphides. *Journal of Solid State Chemistry*, 51(2), 152–158. doi:https://doi.org/10.1016/0022-4596(84)90328-1.

[18] Gvozdetskyi, V., Hlukhyy, V., Gladyshevskii, R. Fässler, T.F. (2015). Crystal Structure and Magnetic Properties of $SrNi_{2-x}Sb_2$. *Zeitschrift für anorganische und allgemeine Chemie*, 641(11), 1859–1862. doi:https://doi.org/10.1002/zaac.201500518.

[19] Jeitschko, W., Meisen, U., Möller, M. H., Reehuis, M. (1985). Über LaCo2P2 und andere Neue Verbindungen mit ThCr2Si2- und CaBe2Ge2-Struktur. *ZAAC - Journal of Inorganic and General Chemistry*, *527*(8), 73–84. https://doi.org/10.1002/zaac.19855270807

[20] Reehuis, M., Jeitschko, W. (1990) Structure and Magnetic Properties of the Phosphides CaCo2P2 and LnT2P2 with ThCr2Si2 Structure and LnT2P2 with PbFCl Structure (Ln = Lanthanoids, T = Fe, Co, Ni). *J. Phys. Chem. Solids*, *51*(8), 961–968. https://doi.org/10.1016/0022-3697(90)90039-I.

[21] Rotter, M., Tegel, M., Johrendt, D. (2008). Superconductivity at 38 K in the iron arsenide (Ba1-xKx)Fe2As2. *Physical Review Letters*, *101*(10). https://doi.org/10.1103/PhysRevLett.101.107006

[22] Cortes-Gil, R., Clarke, S. J. (2011). Structure, magnetism, and superconductivity of the layered iron arsenides Sr1- xNaxFe2As2. *Chemistry of Materials*, *23*(4), 1009–1016. https://doi.org/10.1021/cm1028244

[23] Bacsa, J., Ganin, A. Y., Takabayashi, Y., Christensen, K. E., Prassides, K., Rosseinsky, M. J., & Claridge, J. B. (2011). Cation vacancy order in the K0.8+xFe1.6-ySe2 system: Five-fold cell expansion accommodates 20% tetrahedral vacancies. *Chemical Science*, *2*(6), 1054–1058. https://doi.org/10.1039/c1sc00070e.

[24] Stewart, G. R. (1989). Heavy-fermion systems. *Reviews of Modern Physics*, *56*(4), 755. https://doi.org/10.1103/RevModPhys.56.755.

[25] Jeong, T., Pickett, W. E. (2006). First-principles study of the electronic structure of heavy fermion YbRh2Si2. *Journal of Physics Condensed Matter*, *18*(27), 6289–6297. https://doi.org/10.1088/0953-8984/18/27/012.

[26] Haen, P., Flouquet, J., Lapierre, F., Lejay, P., Mignot, J. M., Ponchet, A., Voiron, J. (1987). A polarized heavy fermion system: CeRu2Si2. *Journal of Magnetism and Magnetic Materials*, *63–64*, 320–322. https://doi.org/10.1016/0304-8853(87)90598-1.

[27] Iyo, A., Kawashima, K., Kinjo, T., Nishio, T., Ishida, S., Fujihisa, H., Gotoh, Y., Kihou, K., Eisaki, H., & Yoshida, Y. (2016). New-Structure-Type Fe-Based Superconductors: CaAFe4As4 (A = K, Rb, Cs) and SrAFe4As4 (A = Rb, Cs). *Journal of the American Chemical Society*, *138*(10), 3410–3415. https://doi.org/10.1021/jacs.5b12571.

[28] Ishida, S., Iyo, A., Ogino, H., Eisaki, H., Takeshita, N., Kawashima, K., Yanagisawa, K., Kobayashi, Y., Kimoto, K., Abe, H., Imai, M., Shimoyama, J. I., & Eisterer, M. (2019). Unique defect structure and advantageous vortex pinning properties in superconducting CaKFe4As4. *Npj Quantum Materials*, *4*(1). https://doi.org/10.1038/s41535-019-0165-0

[29] Katayama, N., Kudo, K., Onari, S., Mizukami, T., Sugawara, K., Sugiyama, Y., Kitahama, Y., Iba, K., Fujimura, K., Nishimoto, N., Nohara, M., & Sawa, H. (2013). Superconductivity in Ca1-xLaxFeAs2: A novel 112-type iron pnictide with arsenic zigzag bonds. *Journal of the Physical Society of Japan*, *82*(12). https://doi.org/10.7566/JPSJ.82.123702

[30] Kudo, K., Iba, K., Takasuga, M., Kitahama, Y., Matsumura, J. I., Danura, M., Nogami, Y., & Nohara, M. (2013). Emergence of superconductivity at 45 K by lanthanum and phosphorus co-doping of CaFe2 As2. *Scientific Reports*, *3*. https://doi.org/10.1038/srep01478

[31] Ota, H., Kudo, K., Kimura, T., Kitahama, Y., Mizukami, T., Ioka, S., & Nohara, M. (2017). Site-selective antimony doping in arsenic zigzag chains of 112-type Ca1-xLaxFeAs2. *Journal of the Physical Society of Japan*, *86*(2). https://doi.org/10.7566/JPSJ.86.025002

[32] Ray, S. J., & Alff, L. (2017). Superconductivity and Dirac fermions in 112-phase pnictides. *Physica Status Solidi (B) Basic Research*, *254*(1). https://doi.org/10.1002/pssb.201600163

[33] Han, F., Wan, X., Phelan, D., Stoumpos, C. C., Sturza, M., Malliakas, C. D., Li, Q., Han, T. H., Zhao, Q., Chung, D. Y., & Kanatzidis, M. G. (2015). Antiferromagnetic Kondo lattice in the layered compound CePd1-x Bi2 and comparison to the superconductor LaPd1-x Bi2. *Physical Review B - Condensed Matter and Materials Physics*, *92*(4). https://doi.org/10.1103/PhysRevB.92.045112

[34] Mizoguchi, H., Matsuishi, S., Hirano, M., Tachibana, M., Takayama-Muromachi, E., Kawaji, H., & Hosono, H. (2011). Coexistence of light and heavy carriers associated with superconductivity and antiferromagnetism in CeNi0.8Bi2 with a Bi square net. *Physical Review Letters*, *106*(5). https://doi.org/10.1103/PhysRevLett.106.057002

[35] Bogenrieder, S. E., Beßner, J., Engstfeld, A. K., & Jacob, T. (2024). First-Principles Study on the Structural and Magnetic Properties of Low-Index Cu2O and CuO Surfaces. *Journal of Physical Chemistry C*, *128*(23), 9693–9704. https://doi.org/10.1021/acs.jpcc.4c01102

[36] McClure, J.W. (1956). Diamagnetism of Graphite. *Physical Review*, 104(3), pp.666–671. https://doi.org/10.1103/physrev.104.666.

[37] Neilson, J. R.; McQueen, T. M.; Llobet, A.; Wen, J.; Suchomel, M. R. (2013) Charge Density Wave Fluctuations, Heavy Electrons, and Superconductivity in $KNi_2S_2$. *Phys. Rev. B*, *87*, 045124. https://doi.org/10.1103/PhysRevB.87.045124.

[38] Lei, H., Abeykoon, M., Wang, K., Bozin, E. S., Ryu, H., Graf, D., Warren, J. B., & Petrovic, C. (2014). Physical properties of KxNi2-ySe2 single crystals. *Journal of Physics Condensed Matter*, *26*(1). https://doi.org/10.1088/0953-8984/26/1/015701

[39] Neilson, J. R., & McQueen, T. M. (2012). Bonding, ion mobility, and rate-limiting steps in deintercalation reactions with ThCr 2Si 2-type KNi 2Se 2. *Journal of the American Chemical Society*, *134*(18), 7750–7757. https://doi.org/10.1021/ja212012k

[40] Kato, K., Iida, S., Yanai, K., Mizushima, K. (1983). Ferrimagnetic Ferroelectricity of Fe3O4. *Journal of Magnetism and Magnetic Materials*, *31-34*(2), 783-784. https://doi.org/10.1016/0304-8853(83)90683-2.

[41] Ruderman, M.A. and Kittel, C. (1954). Indirect Exchange Coupling of Nuclear Magnetic Moments by Conduction Electrons. *Physical Review*, *96*(1), 99–102. https://doi.org/10.1103/physrev.96.99.

[42] Kamerlingh Onnes. H. (1911). The superconductivity of mercury. *Commun. from Phys. Lab. Univ. Leiden Suppl. Mater. 29*, 122-124. https://doi.org/10.1103/physreva.86.023405.

[43] Meissner, W. and Ochsenfeld, R. (1933). Ein neuer Effekt bei Eintritt der Supraleitfähigkeit *Naturwissenschaften, 21*, 787-788. https://doi.org/10.1007/BF01504252.

[44] Maxwell, E. (1950). Isotope effect in the superconductivity of mercury. *Phys. Rev. 78*, 477. https://doi.org/10.1103/PhysRev.78.477.

[45] Reynolds, C., Serin, B., Wright, W., Nesbitt, L. (1950). Superconductivity of isotopes of mercury. *Phys. Rev. 78*, 487. https://doi.org/10.1103/PhysRev.78.487.

[46] Bardeen, J., Cooper, L.N., Schrieffer, J.R. (1957). Theory of superconductivity. *Phys. Rev. 108*, 1175. https://doi.org/10.1103/PhysRev.108.1175.

[47] Nagamatsu, J., Nakagawa, N., Muranaka, T., Zenitani, Y., Akimitsu, J. (2001). Superconductivity at 39 K in Mg2B. *Nature, 410*, 63-64. https://doi.org/10.1038/35065039.

[48] Drozdov, A. P., Eremets, M. I., & Troyan, I. A. (2014). Conventional superconductivity at 190 K at high pressures. *IEEE/CSC & ESAS Superconductivity News Forum*, https://doi.org/10.48550/arXiv.1412.0460.

[49] Matthias, B., Geballe, T., Geller, S., Corenzwit, E. (1954). Superconductivity of $Nb_3Sn$. *Phys. Rev. 95*, 1435. https://doi.org/10.1103/PhysRev.95.1435.

[50] Bednorz, J. G., Miiller, K. A. (1986). Condensed Possible High Tc Superconductivity in the Ba-La-Cu-O System. *Z. Physik B - Condensed Matter, 64*, 189–193. https://doi.org/10.1007/BF01303701.

[51] Wu, M. K., Ashburn, J. R., Torng, C. J., Hor, P. H., Meng, R. L., Gao, L., Huang, Z. J., Wang, Y. Q., & Chu ', C. W. (1987). Superconductivity at 93 K in a New Mixed-Phase Y-Ba-Cu-0 Compound System at Ambient Pressure, *Physical Review Letters, 58*(9), 908. https://doi.org/10.1103/PhysRevLett.58.908.

[52] Parkin, S. S. P., Engler, E. M., Lee, V. Y., Nazzal, A. I., Tokura, Y., Torrance, J. B., & Grant, P. M. (1988). Magnetic Seld dependence of the resistivity and susceptibility of the above-100-K BiSr-Ca-Cu superconductor, *Phys. Rev. B, 38*, 7101. https://doi.org/10.1103/PhysRevB.38.7101.

[53] Lipps, I., Tolhoek, F. W., Blume, H. A., Lovesey, M., Platzman, S. W., Tzoar, P., Debergevin, N., Brunel, F., Blume, M., Gibbs, M., Gibbs, D., Moncton, D., Amico, D. E., & Vettier, K. L. (1988). High-Tc superconducting phases in the series Bi2.1(Ca, Sr)(n+1)Cu(n)O(2n+4+δ). *Nature, 333*, 153-156. https://doi.org/10.1038/333153a0.

[54] Radaelli, P. G., Marezioa, M., Tholence, J. L., de Brion, S., Loureiro, S., Santoro, A., Huang, Q., Capponi, J. J., Alario-Franco, M., & Chaillout, C. (1994). Synthesis, crystal structure and properties of Hg2Ba2(Y,Ca)Cu2O8-δ: the first cuprate superconductor containing a double mercury-oxygen layer, *Physica C, 235*, 925-926. https://doi.org/10.1016/0921-4534(94)91687-X.

[55] Lee, P. A., Nagaosa, N., & Wen, X. G. (2006). Doping a Mott insulator: Physics of high-temperature superconductivity. *Reviews of Modern Physics*, *78*(1), 17–85. https://doi.org/10.1103/RevModPhys.78.17

[56] Kamihara, Y., Watanabe, T., Hirano, M., & Hosono, H. (2008). Iron-based layered superconductor La[O1-xFx]FeAs (x= 0.05-0.12) with Tc = 26 K. *Journal of the American Chemical Society*, *130*(11), 3296–3297. https://doi.org/10.1021/ja800073m.

[57] Chen, X. H., Wu, T., Wu, G., Liu, R. H., Chen, H., & Fang, D. F. (2008). Superconductivity at 43 K in SmFeAsO1-xFx. *Nature*, *453*(7196), 761–762. https://doi.org/10.1038/nature07045

[58] Bos, J.-W.G., George, Rodgers, J.A., Sokolov, D.A., Huxley, A.D. and J. Paul Attfield (2008). High pressure synthesis of late rare earth RFeAs(O,F) superconductors; R = Tb and Dy. *Chemical Communications*, (31), pp.3634–3634. doi:https://doi.org/10.1039/b808474b.

[59] Kamihara, Y., Hiramatsu, H., Hirano, M., Kawamura, R., Yanagi, H., Kamiya, T., & Hosono, H. (2006). Iron-based layered superconductor: LaOFeP. *Journal of the American Chemical Society*, *128*(31), 10012–10013. https://doi.org/10.1021/ja063355c.

[60] McQueen, T. M., Regulacio, M., Williams, A. J., Huang, Q., Lynn, J. W., Hor, Y. S., West, D. v., Green, M. A., & Cava, R. J. (2008). Intrinsic properties of stoichiometric LaFePO. *Physical Review B - Condensed Matter and Materials Physics*, *78*(2). https://doi.org/10.1103/PhysRevB.78.024521.

[61] Wang, C., Li, L., Chi, S., Zhu, Z., Ren, Z., Li, Y., Wang, Y., Lin, X., Luo, Y., Jiang, S., Xu, X., Cao, G., & Xu, Z. (2008). Thorium-doping induced superconductivity up to 56 K in Gd1-xThxFeAsO. *Europhysics Letters*, *83(6)*. https://doi.org/10.1209/0295-5075/83/67006.

[62] Takahashi, H., Soeda, H., Nukii, M., Kawashima, C., Nakanishi, T., Iimura, S., Muraba, Y., Matsuishi, S., & Hosono, H. (2015). Superconductivity at 52 K in hydrogen-substituted LaFeAsO1-xHx under high pressure. *Scientific Reports*, *5*. https://doi.org/10.1038/srep07829.

[63] Li, G., Grissonnanche, G., Yan, J. Q., McCallum, R. W., Lograsso, T. A., Zhou, H. D., & Balicas, L. (2012). High superconducting anisotropy and weak vortex pinning in Co-doped LaFeAsO. *Physical Review B - Condensed Matter and Materials Physics*, *86*(5). https://doi.org/10.1103/PhysRevB.86.054517.

[64] Wang, X. C., Liu, Q. Q., Lv, Y. X., Gao, W. B., Yang, L. X., Yu, R. C., Li, F. Y., & Jin, C. Q. (2008). The superconductivity at 18 K in LiFeAs system. *Solid State Communications*, *148*(11–12), 538–540. https://doi.org/10.1016/j.ssc.2008.09.057.

[65] Parker, D. R., Pitcher, M. J., Baker, P. J., Franke, I., Lancaster, T., Blundell, S. J., & Clarke, S. J. (2009). Structure, antiferromagnetism and superconductivity of the layered iron arsenide NaFeAs. *Chemical Communications*, *16*, 2189–2191. https://doi.org/10.1039/b818911k.

[66] Pitcher, M. J., Parker, D. R., Adamson, P., Herkelrath, S. J. C., Boothroyd, A. T., Ibberson, R. M., Brunelli, M., & Clarke, S. J. (2008). Structure and superconductivity of LiFeAs. *Chemical Communications*, *45*, 5918–5920. https://doi.org/10.1039/b813153h.

[67] Qi, Y., Zhang, X., Gao, Z., Zhang, Z., Wang, L., Wang, D., & Ma, Y. (2009). Superconductivity of powder-in-tube Sr0.6K0.4Fe2As2 wires. *Physica C: Superconductivity and Its Applications*, *469*(13), 717–720. https://doi.org/10.1016/j.physc.2009.03.008.

[68] Kreyssig, A., Green, M. A., Lee, Y., Samolyuk, G. D., Zajdel, P., Lynn, J. W., Bud'ko, S. L., Torikachvili, M. S., Ni, N., Nandi, S., Leão, J. B., Poulton, S. J., Argyriou, D. N., Harmon, B. N., McQueeney, R. J., Canfield, P. C., & Goldman, A. I. (2008). Pressure-induced volume-collapsed tetragonal phase of CaFe 2As2 as seen via neutron scattering. *Physical Review B - Condensed Matter and Materials Physics*, *78*(18). https://doi.org/10.1103/PhysRevB.78.184517.

[69] Allred, J. M., Taddei, K. M., Bugaris, D. E., Avci, S., Chung, D. Y., Claus, H., dela Cruz, C., Kanatzidis, M. G., Rosenkranz, S., Osborn, R., & Chmaissem, O. (2014). Coincident structural and magnetic order in BaFe2(As1-x Px)2 revealed by high-resolution neutron diffraction. *Physical Review B - Condensed Matter and Materials Physics*, *90*(10). https://doi.org/10.1103/PhysRevB.90.104513.

[70] Wang, T., Chu, J., Jin, H., Feng, J., Wang, L., Song, Y., Zhang, C., Xu, X., Li, W., Li, Z., Hu, T., Jiang, D., Peng, W., Liu, X., & Mu, G. (2019). Single-Crystal Growth and Extremely High Hc2 of 12442-Type Fe-Based Superconductor KCa2Fe4As4F2. *Journal of Physical Chemistry C*, *123*(22), 13925–13929. https://doi.org/10.1021/acs.jpcc.9b04624.

[71] Zhu, X., Han, F., Mu, G., Cheng, P., Shen, B., Zeng, B., & Wen, H. H. (2009). Transition of stoichiometric Sr2VO3FeAs to a superconducting state at 37.2 K. *Physical Review B - Condensed Matter and Materials Physics*, *79*(22). https://doi.org/10.1103/PhysRevB.79.220512.

[72] Ivanovskii, A.L. (2010). New superconductors based on five-component transition metal oxypnictides. *Russian Chemical Reviews*, *79*(1), 1–11. https://doi.org/10.1070/rc2010v079n01abeh004088.

[73] Torikachvili, M. S., Bud'ko, S. L., Ni, N., & Canfield, P. C. (2008). Pressure induced superconductivity in CaFe2As2. *Physical Review Letters*, *101*(5). https://doi.org/10.1103/PhysRevLett.101.057006.

[74] Rotter, M., Pangerl, M., Tegel, M., & Johrendt, D. (2008). Superconductivity and Crystal Structures of (Ba 1−x K x )Fe 2 As 2 (x = 0-1). *Angewandte Chemie International Edition*, *47*, 7949-7952. https://doi.org/10.1002/anie.200803641.

[75] Iida, K., Grinenko, V., Kurth, F., Ichinose, A., Tsukada, I., Ahrens, E., Pukenas, A., Chekhonin, P., Skrotzki, W., Teresiak, A., Hühne, R., Aswartham, S., Wurmehl, S., Mönch, I., Erbe, M., Hänisch, J., Holzapfel, B., Drechsler, S. L., & Efremov, D. (2016). Hall-plot of the phase diagram for Ba(Fe1-xCox)2As2. *Scientific Reports*, *6*. https://doi.org/10.1038/srep28390

[76] Jiang, S., Xing, H., Xuan, G., Wang, C., Ren, Z., Feng, C., Dai, J., Xu, Z., & Cao, G. (2009). Superconductivity up to 30 K in the vicinity of the quantum critical point in BaFe2(As1-xPx)2. *Journal of Physics Condensed Matter*, *21*(38). https://doi.org/10.1088/0953-8984/21/38/382203

[77] Doiron-Leyraud, N., Proust, C., LeBoeuf, D., Levallois, J., Bonnemaison, J.-B., Liang, R., Bonn, D.A., Hardy, W.N. and Taillefer, L. (2007). Quantum oscillations and the Fermi surface in an underdoped high-Tc superconductor. *Nature*, 447(7144), 565–568. https://doi.org/10.1038/nature05872.

[78] Zhao, J., Huang, Q., de la Cruz, C., Li, S., Lynn, J.W., Chen, Y., Green, M.A., Chen, G.F., Li, G., Li, Z., Luo, J.L., Wang, N.L. and Dai, P. (2008). Structural and magnetic phase diagram of CeFeAsO1− xFx and its relation to high-temperature superconductivity. *Nature Materials*, 7(12), 953–959. https://doi.org/10.1038/nmat2315.

[79] Hsu, F.-C., Luo, J.-Y., Yeh, K.-W., Chen, T.-K., Huang, T.-W., Wu, P.M., Lee, Y.-C., Huang, Y.-L., Chu, Y.-Y., Yan, D.-C. and Wu, M.-K. (2008). Superconductivity in the PbO-type structure alpha-FeSe. *Proceedings of the National Academy of Sciences of the United States of America*, [online] 105(38), 14262–4. https://doi.org/10.1073/pnas.0807325105.

[80] S. Yu. Medvedev, McQueen, T.M., Troyan, I.A., Taras Palasyuk, Mikhail Eremets, Cava, R.J., S.M. Hossein Naghavi, Casper, F., Vadim Ksenofontov, Wortmann, G. and Felser, C. (2009). Electronic and magnetic phase diagram of β-Fe1.01Se with superconductivity at 36.7 K under pressure. *Nat Mater*, 8(8), 630–633. https://doi.org/10.1038/nmat2491.

[81] Kumar, A., Tandon, R. P., & Awana, V. P. S. (2012). Effect of 3d metal (Co and Ni) doping on the superconductivity of FeSe 0.5Te 0.5. *IEEE Transactions on Magnetics*, *48*(11), 4239–4242. https://doi.org/10.1109/TMAG.2012.2201215

[82] Texier, Y., Deisenhofer, J., Tsurkan, V., Loidl, A., Inosov, D. S., Friemel, G., & Bobroff, J. (2012). NMR study in the iron-selenide Rb 0.74Fe 1.6Se 2: Determination of the superconducting phase as iron vacancy-free Rb 0.3Fe 2Se 2. *Physical Review Letters*, *108*(23). https://doi.org/10.1103/PhysRevLett.108.237002

[83] Speller, S. C., Mousavi, T., & Dudin, P. (2015). Analytical microscopy of iron-based superconducting materials. *Novel Superconducting Materials*, *1*(1). https://doi.org/10.1515/nsm-2015-0004

[84] Hazi, J., Mousavi, T., Dudin, P., van der Laan, G., MacCherozzi, F., Krzton-Maziopa, A., Pomjakushina, E., Conder, K., & Speller, S. C. (2018). Magnetic imaging of antiferromagnetic and superconducting phases in R bx F e2-y S e2 crystals. *Physical Review B*, *97*(5). https://doi.org/10.1103/PhysRevB.97.054509

[85] Burrard-Lucas, M., Free, D.G., Sedlmaier, S.J., Wright, J.D., Cassidy, S.J., Hara, Y., Corkett, A.J., Lancaster, T., Baker, P.J., Blundell, S.J. and Clarke, S.J. (2012). Enhancement of the superconducting transition temperature of FeSe by intercalation of a molecular spacer layer. *Nature Materials*, 12(1), 15–19. doi:https://doi.org/10.1038/nmat3464.

[86] Kawashima, K., Ishida, S., Fujihisa, H., Gotoh, Y., Kihou, K., Yoshida, Y., Eisaki, H., Ogino, H., & Iyo, A. (2018). Superconductivity in a New 1144-Type Family of (La,Na)AFe4As4 (A = Rb or Cs). *Journal of Physical Chemistry Letters*, *9*(4), 868–873. https://doi.org/10.1021/acs.jpclett.8b00162

[87] Kaluarachchi, U.S. *et al.* (2017) 'Pressure-induced half-collapsed-tetragonal phase in CaKFe4As4', *Physical Review B*, 96(14). https://doi.org/10.1103/physrevb.96.140501.

[88] Stillwell, R.L. *et al.* (2019) 'Observation of two collapsed phases in CaRbFe4As4', *Physical Review B*, 100(4). https://doi.org/10.1103/physrevb.100.045152.

[89] Lin, X., Straszheim, W. E., Bud'Ko, S. L., & Canfield, P. C. (2013). Anisotropic magnetization and resistivity of single crystalline RNi 1-xBi2±y (R = La-Nd, Sm, Gd-Dy). *Journal of Alloys and Compounds*, *554*, 304–311. https://doi.org/10.1016/j.jallcom.2012.11.138

[90] Rosa, P. F. S., Jesus, C. B. R., Adriano, C., Fisk, Z., & Pagliuso, P. G. (2014). The role of Ni vacancies on the physical properties of CeNixBi2-y single crystals. *Journal of Physics: Conference Series*, *592*(1). https://doi.org/10.1088/1742-6596/592/1/012063

[91] Mizoguchi, H., Matsuishi, S., Hirano, M., Tachibana, M., Takayama-Muromachi, E., Kawaji, H., & Hosono, H. (2011). Coexistence of light and heavy carriers associated with superconductivity and antiferromagnetism in CeNi0.8Bi2 with a Bi square net. *Physical Review Letters*, *106*(5). https://doi.org/10.1103/PhysRevLett.106.057002

# Chapter 2. Experimental techniques

## 2.1 Synthetic methods

### 2.1.1 Ceramic synthesis

The most used synthetic method in solid state chemistry is the ceramic method, which uses high temperatures (500-1500ºC) to overcome the large barrier to reaction caused by low ion mobility in the solid state. It involves grinding together stoichiometric amounts of starting reagents with a mortar and pestle in order to achieve good distribution of grain boundaries and a homogeneous mixture of reactants. To further increase the chance of reactants coming into contact with each other at elevated temperatures, the powders of starting reactants are pressed into a pellet to maximise contact of grains using a force of < 5 tonnes. The powder or a pellet of starting reagents is usually placed in a crucible made of an inert material, such as alumina, and heated to elevated temperatures for anything between a couple of hours to multiple weeks. Subsequent re-grinding may be necessary to re-introduce the crystallites to one another and increase the likelihood of reacting together. Cooling methods have an effect on the final reaction product, too; slow-cooling from high temperatures often favours the formation of single crystals, while quenching can trap a polymorph/metastable phase which is only stable at elevated temperatures.

### 2.1.2 High-pressure synthesis

High-pressure ceramic synthesis is a powerful solid state chemistry technique which uses extremely high pressures (in the range of tens of thousands of atmospheres) to access phases not accessible via more traditional routes under standard conditions, such as metastable phases. These materials often exhibit drastically different properties from their low-pressure analogues, including exotic magnetic and electronic phenomena. High-pressure synthesis is typically performed in specialised equipment. The high-pressure experiments described in this thesis were performed at the University of Kyoto using a cubic anvil high-pressure device – the ‘Bamboo’ press – equipped with a hydraulic pump, capable of generating ultra-high hydrostatic pressure at its centre by isotropically pressing a sample inside a pyrophyllite cell from six directions using tungsten carbide alloy anvils. Four anvils on the sides move simultaneously toward the centre, where the cell is located, in conjunction with two other

anvils pressing from the top and bottom axial directions (Figure 2.1). As a result, this press can generate a maximum pressure of 8 GPa (~80,000 atmospheres) at the centre from six directions using an anvil. The cell used for this type of synthesis employs pyrophyllite – a hydrous aluminium silicate mineral known for its heat resistance and excellent pressure transmission – as the pressure medium, carbon as the heater, and boron nitride (BN) to prevent sample contamination and provide insulation. When heating, a constant current is passed through the top and bottom anvils to conduct electricity through the internal carbon component, causing it to generate heat. This enables heating and synthesis at a maximum temperature of 1700 °C. The molybdenum sheet is used to improve the contact between the SUS (stainless steel) ring and the carbon component. The assembly of a pyrophyllite cell is illustrated in Figure 2.1.

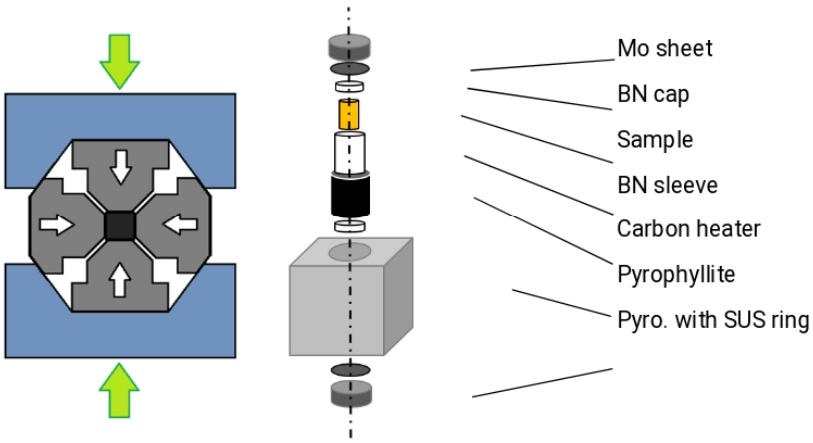


**Figure 2.1** Left: High-pressure cell (black square) inside of press (green arrows illustrate that pressure is also being applied isotropically from top and bottom directions). Right: Assembly of a pyrophyllite cell used in high-pressure synthesis.

### 2.1.3 Handling of air-sensitive materials

All phases described in this thesis are air-sensitive to various degrees, *i.e.* some oxidise within a couple of minutes and other within a number of hours. Using inert atmosphere to prevent oxidation of air-sensitive materials is necessary during appropriate stages of synthesis. All samples were prepared and handled inside of an argon-filled dry glovebox. Argon is re-circulated through a copper catalyst and a molecular bed sieve to remove any contaminating $O_2$ and $H_2O$, respectively. The concentration of $O_2$ is monitored by an integrated $O_2$ sensor and was kept under 5ppm under normal

working conditions. For these inert conditions to be maintained at all times, all equipment is dried in an oven prior to transfer to glovebox via an antechamber. When pelletisation of loose air-sensitive powders was required outside of the glovebox, the inert atmosphere was maintained by sealing the pellet die inside two polyethylene bags (by tying a knot in them), then quickly removing it from the glovebox for transport to the press, applying pressure, and again transferring back into the glovebox via an antechamber. The pellet was then extracted from the pellet die inside of the glovebox, and placed inside an alumina crucible in a silica tube (or directly in a silica tube when side-reaction with silica was unlikely to occur). The silica tubes are dried in a drying oven prior to being brought into glovebox, and for reactions involving the use of elemental alkali metals, the silica tube was flame-heated with a blow torch to eliminate adsorbed $H_2O$ and prevent faster oxidation of reactants. The silica tube containing the samples/starting reagents is closed with a brass end cap fitted with a Young's tap, which is closed until the attachment of the tube to a vacuum line outside of the glovebox. The evacuated tube is then sealed close using a methane-oxygen blowtorch under dynamic vacuum, with the pressure maintained in the order of $10^{-2}$ bar. Silica tubes are then placed directly into an oven and can be heated up to 1200ºC, before their integrity becomes compromised.

When a high-temperature reaction involves volatile elements (such as P or As), a corrosive metal vapour is produced which renders the use of silica tube as reaction vessels unsuitable. Therefore, a metal ampoule with a high melting point is used for such reactions, such as Nb- or Ta-based tubes, which are well-suited for making weld-sealed ampoules due to their ductility (provided they have been annealed in manufacture). It is also important that the metal tube is inert to the reaction mixture, and in the syntheses described in this thesis, a Ta tube was used. Ta tubes were firstly crimped closed and then sealed under argon atmosphere using an arc-welding apparatus. The Ta tube must be also sealed inside a silica tube to prevent degradation caused by reaction with atmospheric oxygen at elevated temperatures.

### 2.1.4 Handling ammonia as solvent

The ceramic method might not be suitable for some synthetic targets, and in some of these cases an intercalation reaction, or a reaction between elements using liquid ammonia as a solvent, may be

suitable. In this thesis, the synthesis of alkali chalcogenides ($K_2S$ and $K_2Se$) was performed using this technique to offer a better control of reaction conditions. The reaction is carried out in a Schlenk tube and ammonia condenses onto the reactants at −78 °C in a dry ice/isopropanol bath. This temperature is maintained for a number of hours while the reactants are left stirring on a stirrer plate. Once reaction was complete at low temperatures (marked by colour change from blue solution to bright suspensions), ammonia is allowed to evaporate by removing the dry ice/isopropanol bath and warming the reaction mixture. After the solid residue had reached room temperature, dynamic vacuum is applied to remove any $NH_3$ vapour or adsorbed $NH_3$ before transferring the sample to the glovebox. The synthesis is performed in a fume hood and at all times the liquid-ammonia-containing vessel has to stay open to a mercury bubbler to avoid the possibility of pressures exceeding 50 mmHg above atmospheric pressure in the reaction vessel. This reaction was performed to synthesise $K_2S$ and $K_2Se$ precursors from elemental K and Se/S starting reagents.

## 2.2 Characterisation techniques

### 2.2.1 Crystal symmetry and Diffraction

A crystalline solid is made up of an infinite periodic array of atoms which result from a translational repetition of a structural motif (an atom or an entire molecule) on a 3-dimensional lattice. The crystal structure of any solid (other than amorphous) can be described by a unit cell, which generates said crystal structure in all three dimensions by translation alone; it is a parallelpiped with edges of length $a$, $b$, and $c$, and angles of $\alpha$, $\beta$, and $\gamma$ between them, and these are known as lattice parameters. In the case of $a = b = c$, and $\alpha = \beta = \gamma$, the symmetry can be described as cubic, with four 3-fold axes running along the long diagonals, and has the highest number of non-translational symmetry elements (*i.e.* mirror planes and rotation axes) and has only two defining lattice parameters: $a$ and $\alpha$. When we imagine the other extreme, where $a \neq b \neq c$, and $\alpha \neq \beta \neq \gamma$, the symmetry can be described as triclinic and has six defining lattice parameters and the only symmetry elements allowed are the identity and inversion. There are overall seven crystal systems, namely cubic, tetragonal, orthorhombic, rhombohedral, hexagonal, monoclinic, and triclinic.[1]

A unit cell contains at least one or more lattice points. In systems with only one lattice point, the unit cell is described as primitive (space group symbol *P*). When a unit cell contains more than one lattice point, it is called centred: there are several types of centred cells, including body-centred (space group symbol *I*), where two lattice points are related by a translation of $x + \frac{1}{2}$, $y + \frac{1}{2}$, and $z + \frac{1}{2}$. Face-centred lattices have an additional lattice point at the centre of each face of the unit cell, but this type of symmetry can also arise when a unit cell has lattice points on only two opposing faces, and these space groups are labelled *A*, *B*, or *C*. As some of these centring types are incompatible with certain crystal systems (*i.e.* only orthorhombic, tetragonal, and cubic systems can be have *I*-Bravais lattices), we arrive at 14 Bravais lattices which are formed after combination of the six centring types and seven crystal systems. When these 14 lattices are combined with all possible symmetry operations inside the unit cell, we arrive at 230 possible space groups.

It is due to this feature of crystalline solids – the periodic array of atoms – that renders them suitable for interaction with radiation. The diffraction of radiation by a crystal is the basis of crystallography. When a crystal is irradiated and the incident radiation has a wavelength similar to the spacing of the atoms within the crystal, the scattering shows many features, with various intensities at different angles, due to constructive interference in a few special directions. The resultant diffraction pattern can then be indexed according to one of the abovementioned 230 space groups. Suitable types of radiation include X-rays, neutrons, and electrons.

### 2.2.2 X-ray Diffraction

Interaction of X-rays with a crystalline solid results in a number of processes: photons are scattered by the electrons of an atom through a Coulombic interaction due to the oscillating electric field of an X-ray, giving either elastic or inelastic scattering.[2] An elastic scattering event emits an electromagnetic wave with the same energy as the incident photon, and results in Bragg scattering – the core of crystallography. Secondly, fluorescence results from the emitting of a second photon by an excited electron in a random direction, contributing to the background signal and should be minimised in a diffraction experiment.

Max von Laue developed the first theory of X-ray diffraction by crystals; the 3-dimensional scattering of X-rays from a crystal of copper sulfate hydrate was explained from a 1-dimensional hypothetical crystal, where atoms are arranged in rows of regular spacing along each axis. This theory can be illustrated on a 1-dimensional lattice (Figure 2.2).

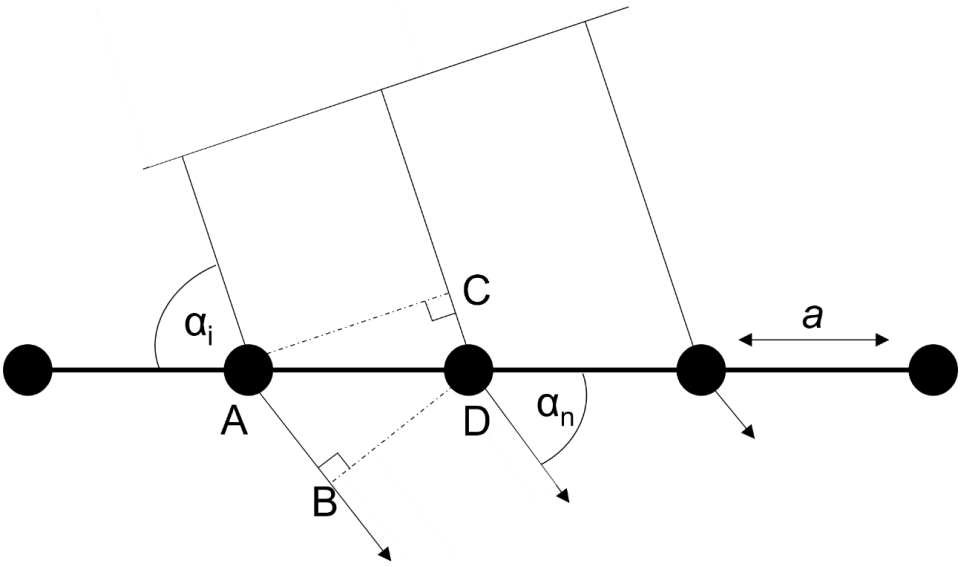


**Figure 2.2** Laue scattering of monochromatic radiation by a 1-dimensional lattice (black spheres represent atoms).

When incident X-rays hit the lattice at an angle $\alpha_i$, each atom acts as a point scatterer, and X-rays are diffracted at an angle $\alpha_n$. The constructive interference between waves occurs if the difference between their paths is a whole number, *n*, of wavelengths, $\lambda$:

$$AB - CD = a(cos\alpha_n - cos\alpha_i) = n\lambda \qquad \text{Equation 2.1}$$

For a 3-dimensional system, we can consider the additional axes as *y* and *z* to derive second and third Laue equations:

$$b(cos\beta_n - cos\beta_i) = n_y\lambda \qquad \text{Equation 2.2}$$

$$c(cos\gamma_n - cos\gamma_i) = n_z\lambda \qquad \text{Equation 2.3}$$

As this model requires the determination of the 12 variables to solve a crystal structure, it is not widely used in crystallography. Instead, the Bragg's law, developed by father and son W.L.Bragg

and W.H.Bragg, is used in practice,[3] which gives a simpler solution; rows of atoms are treated as planes, called Miller planes, each defined by a set of Miller indices *h*, *k*, and *l*, which intercept the unit cell axes at $\frac{a}{h}$, $\frac{b}{k}$, and $\frac{c}{l}$, respectively. Constructive interference will occur when the additional distance travelled by a beam of X-rays scattered by different Miller planes is equal to an integer number of wavelengths, $n\lambda$. This is illustrated in Figure 2.3, where the distance between the planes, $d_{hkl}$, is related to the angle of incident X-rays, $\theta$.

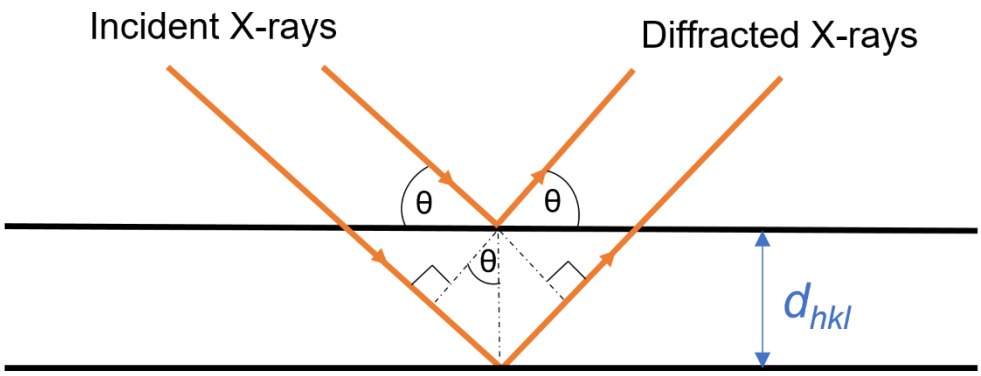


**Figure 2.3** Bragg scattering of X-rays by Miller planes in one direction.

The diffraction angle, $\theta$, can be related to the radiation wavelength and the spacing of Miller planes, $d_{hkl}$, by Bragg's law:

$$n\lambda = 2d_{hkl}\sin\theta \qquad \text{Equation 2.4}$$

This relationship forms the basis of diffraction experiments, where a sample is illuminated by monochromatic radiation and the diffracted intensity is measured as a function of $2\theta$. As d-spacing is directly correlated to the distance between atomic planes in a crystal, and only the diffraction intensities are observed at $\theta$ values that satisfy Bragg's law. The different *hkl* values can then be assigned to the various reflections observed in a process called indexing which allows for crystal structure determination (*i.e.* lattice parameters of the unit cell and space group candidates) by characterising the conditions for allowed reflections, however it does not solve the structure directly, as that requires also intensities of reflections. An important clue for assigning the correct Bravais lattice is the presence of systematic absences of certain reflections, which are indicative of the

presence of symmetries, such as glide planes, within the unit cell. The intensities of allowed reflections give information about the arrangement of atoms inside the unit cell. The intensities are directly related to the structure factor, $F_{hkl}$, as shown by Equation 2.5.

$$I_{hkl} \propto |F_{hkl}|^2 \qquad \text{Equation 2.5}$$

The structure factor is defined by the positions and identities of all atoms in the unit cell and describes both the amplitude and phase wave diffracted by the Miller planes with indices *h k l* and is given by:

$$F_{hkl} = \sum_{j=1}^{n} f_j \left( cos2\pi\left(hx_j + ky_j + lz_j\right)q + i\, sin2\pi\left(hx_j + ky_j + lz_j\right)\right) q \qquad \text{Equation 2.6}$$

In Equation 2.6, $f_j$ is the atomic form factor which defines the contribution of the *j*th atom to the overall structure factor, and its coordinates are expressed as $x_j$, $y_j$, *and* $z_j$, and $q$ is the scattering vector. The atomic form factor defines the scattering strength of the atom, and is proportional to the number of electrons of the *j*th atom. Therefore, heavier atoms dominate the intensities of an X-ray diffraction pattern. The relationship between the atomic number, Z, and the atomic form factor is expressed as follows:

$$f_j(\theta) \propto \frac{Z}{2}(1 + \cos 2\theta) \qquad \text{Equation 2.7}$$

This relationship has important implications on the X-ray data obtained from a diffraction experiment; firstly, the proportional relationship between $f_j$ and $Z$ results in an increased difficulty to extract information about light atoms from an X-ray diffraction pattern. Secondly, atoms of similar atomic numbers are difficult to distinguish, which has a particular relevance to this thesis Chapter 4. Thirdly, the angular dependence of diffraction intensity results in reflections at higher angles with inherently more reduced intensities. This is due to the large separation of the electrons within the scattering atom, comparable to the wavelength of X-ray radiation (in the order of 1 Å), as the electron cloud is not a point scatterer. In the scenario where two photons are scattered from different regions of the same atom (*i.e.* core *vs* outer electrons), the created path difference will produce successively greater destructive interference with $\theta$.

The Debye-Waller factor, $q$, contributes to the peak intensities, too; as atoms are found to be non-stationary due to thermal motion, the electron density is dispersed via atomic vibrations. The thermal displacement results in a decrease in intensities of reflections with $2\theta$, as the greater phase difference of scattered waves leads to destructive interference. The isotropic thermal displacement parameter, $q_{iso}$, is given by:

$$q_{iso} = exp^{(\frac{-8\pi^2 U_{iso} sin^2(\theta)}{\lambda^2})} \qquad \text{Equation 2.8}$$

where $U_{iso}$ is an experimentally-determined isotropic temperature factor.

Solution of structure factors from Equation 2.6 allows for determination of the contents of the unit cell, however only the amplitude and not the phase of $F_{hkl}$ can be determined directly from intensities of reflections; this is known as the 'phase problem' and it arises from the proportional relationship between intensity and the square of the modulus of the structure factor shown in Equation 2.5. This makes the structure solution from diffraction data much more complex, and is addressed by the 'direct methods',[4] Patterson method',[5] and 'charge flipping',[6] all of which rely on computational techniques, and allow for structure solution *ab initio*. After the use of a structural solution method, or when an approximate model is available, fingerprinting can be performed, which can be used to refine structural parameters via the least-squares minimisation, and the X-ray diffraction pattern serves as a fingerprint of a phase that can be compared to a known pattern; this is the Rietveld refinement.

In a single crystal diffraction experiment, a monochromatic X-ray beam irradiates the crystal as it is rotated to satisfy Bragg's law for a set of Miller planes, and in this way, the diffraction event occurs at an absolute angle according to the chosen $d_{hkl}$ values; the different Miller planes give scattering intensity that does not overlap with that of any other. However, in a powder diffraction experiment on a polycrystalline sample, which contains a large number of randomly oriented crystallites, the beam hits all Miller planes of the powder simultaneously and the diffraction event occurs at all angles. The result is a Debye-Scherrer cone of diffracted intensity detected as rings as opposed to

spots (Figure 2.4), which is then visualised as a 2-dimensional diffractogram of diffracted intensity *vs* $2\theta$, generated after integrating the intensities of the whole ring or of an intercepted part of the ring, depending on the experimental setup.

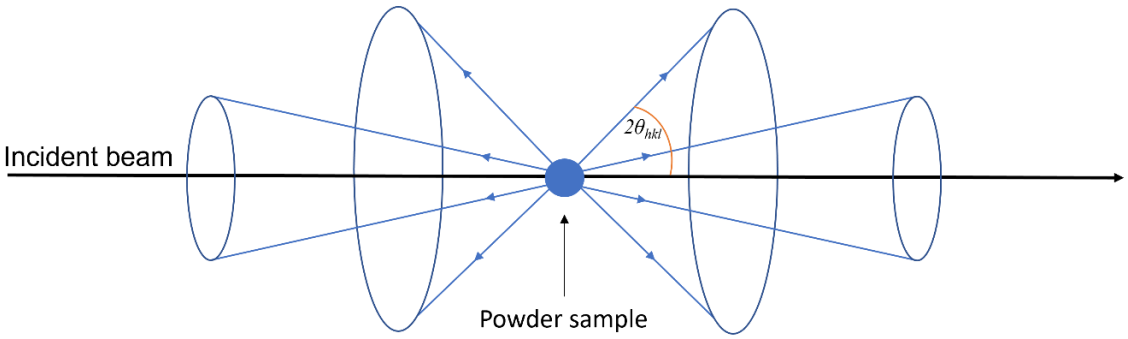


**Figure 2.4** Debye-Scherrer rings generated by diffraction from a powder sample.

There is, however, a loss of information between a single crystal and a powder diffraction experiment, as in the latter, all reflections that have the same $d_{hkl}$ are coincident (*i.e.* 001 and $00\bar{1}$), which would not happen in a single crystal diffraction pattern on a three-axis plot. This inherent characteristic of a powder diffraction experiment renders the structure solution complex and more difficult.

### 2.2.3 Neutron Diffraction

Similar to X-rays, if appropriate energy is used in a diffraction experiment, neutrons have a wavelength that is in the order of spacing of atoms in a crystal lattice, and can serve as an alternative radiation type for diffraction. There are a number of differences in which X-rays and neutrons are scattered in a diffraction experiment: firstly, neutrons are scattered by atomic nuclei, while in an X-ray diffraction event, photons are scattered from the electron cloud (core or outer electrons). This has several implications on the type of data that can be extracted from a neutron diffraction experiment; as the atomic nucleus is much smaller than the electron cloud, the neutrons interact with the entire point scatterer (nucleus), which diminishes the angular dependence of the atomic scattering factor for neutrons, allowing for obtaining more structural data from high $2\theta$ angles. Instead of depending

on the number of electrons like in the X-ray case, the neutron scattering form factor is proportional to the coherent scattering length of the atom, which unsystematically varies between different elements and their isotopes. This inherent characteristic of neutrons allows for facile location of light atoms, like oxygen, and sometimes differentiation between two atoms of similar atomic numbers from neutron diffraction experiment, which will be exploited in Chapter 3 of this thesis because this variation is particularly pronounced for the 1st row transition metals. The scattering lengths of elements used in this thesis are shown in Table 2.1. Another difference between neutrons and X-rays arises from the fact that neutrons are spin−½ particles, *i.e.* they carry a magnetic dipole moment, which means that in a neutron diffraction event, neutron beam is scattered by not only the atomic nuclei, but also by the unpaired electron's magnetic moments. That means that the magnetic component is superimposed on the structural one in a neutron diffraction pattern. Similar to X-ray diffraction, the intensities of magnetic Bragg peaks fall off with $\theta$, and the angular dependence is even more pronounced for magnetic scattering than for X-ray scattering, since the scattering only occurs from outer electrons causing even greater destructive interference than in X-rays. Both techniques are important in structure determination and are complementary in extraction of additional information, such as the position of light elements or distinguishing between two elements with similar *Z*.

**Table 2.1** Bound coherent scattering length (fm) of elements which were subject to neutron powder diffraction experiments in this thesis. Values taken from Neutron News.[7]

| Element | Atomic number, *Z* | Scattering length (fm) |
|---|---|---|
| S | 16 | 2.847(1) |
| K | 19 | 3.67(2) |
| Co | 27 | 2.49(2) |
| Ni | 28 | 10.3(1) |
| Se | 34 | 7.970(9) |
| Cs | 55 | 5.42(2) |

### 2.2.6 X-ray sources

#### *2.2.6.1 Laboratory powder X-ray diffractometers*

In a laboratory powder X-ray diffraction experiment, X-rays are generated by heating a tungsten filament, which produces electrons. These are then accelerated by a 40 kV voltage under vacuum towards a metal anode. Both instruments described in this thesis which were used for laboratory

diffraction experiments use a Cu target, although other sources (such as Mo) can be used. The electrons produced from the heated tungsten filament have enough energy to ionise the core (K-shell) electrons (1s) from the Cu atom resulting in an excited ion. The hole that forms in the core orbital is filled by a 2p or a 3p electron dropping down from higher energy orbitals during the relaxation process, and the energy difference results in the emission of an X-ray photon with the same energy with a characteristic wavelength, $\lambda$. The 2p→1p transition produces Cu $K_\alpha$ radiation with a characteristic wavelength of 1.54 Å, while the 3p→1p transition produces Cu $K_\beta$ radiation ($\lambda$ = 1.39 Å). For X-ray powder diffraction experiments described in this thesis, a monochromator is used which only allows Cu $K_\alpha$ radiation to pass through ($K_\beta$ is eliminated). Due to the spin-orbit coupling, the $K_\alpha$ is a doublet with two slightly different wavelengths: 1.54051 and 1.54433 Å, referring to $K_{\alpha1}$ and $K_{\alpha2}$, respectively. The schematic in Figure 2.5 describes this process visually.

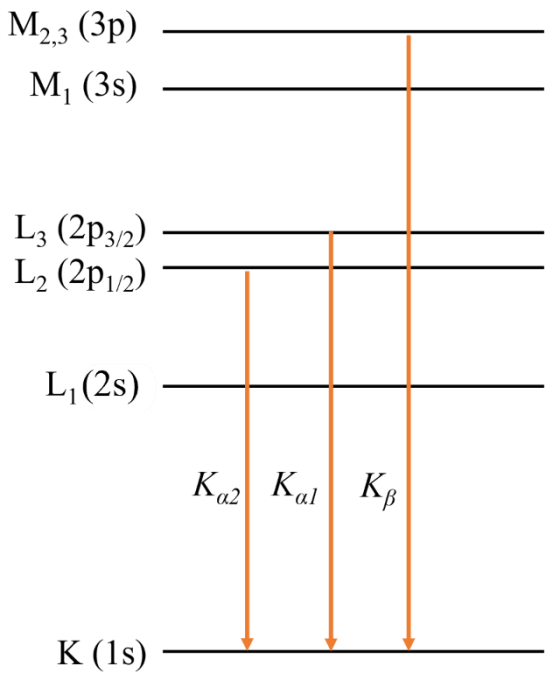


**Figure 2.5** The three X-ray emissions from a Cu source.

In cases where there is no monochromator before the sample, both $K_{\alpha1}$ and $K_{\alpha2}$ will be observed, and $K_\beta$ can be eliminated using a Ni filter. A monochromator is usually a Si or Ge crystal, and this process results in isolation of $K_{\alpha1}$ radiation at the expense of intensity.

Samples analysed on laboratory diffractometers were ground and scattered evenly on a glass slide, which was very thinly greased prior to sample deposition. Air-stable samples were allowed to spin to reduce preferred orientation (inherent to powder samples) and improve powder averaging, but most samples in this thesis were air-sensitive and therefore a lid had to be fixed on top of the slide, and a non-spinning (static) measurements were collected. These airtight lids have Mylar windows that allow for incident X-rays to pass through them.

Laboratory X-ray sources were used for phase checking, obtaining lattice parameters, and checking purity of the sample, while for more precise X-ray analysis, a synchrotron source was used, described in Section 2.2.6.2. This was particularly important for observation of subtle structural distortions described in Chapter 3 that could not be resolved via laboratory X-ray diffractometers.

#### 2.2.6.1.1 Bruker D8 ADVANCE ECO Diffractometer

The Bruker D8 Advance Eco Diffractometer is a laboratory X-ray instrument which operates in Bragg-Brentano geometry; here, sample position is fixed, while the X-ray source and detector rotate on the 2θ axis. The X-ray beam is not monochromated, resulting in both Cu $K_{\alpha 1}$ and $K_{\alpha 2}$ radiation hitting the sample, which reduces the resolution but increases the intensity. The detector is energy-discriminating to reduce $K_{\beta}$ radiation and decrease sample fluorescence, which is useful for samples containing Cr-Co transition metals. The time scale of the diffraction experiment which yields data with good signal-to-noise ratio is ~30 minutes.

#### 2.2.6.1.2. PANalytical Empyrean Diffractometer

As opposed to Bruker, the PANalytical Empyrean Diffractometer operates in a Bragg-Bretano geometry with a fixed X-ray source, and the sample platform and detector rotate. The incident beam is monochromated by a Ge-crystal cut along the *hkl = 111* reflection, resulting in lower intensity but greater resolution. The biggest drawback is that the PANalytical instrument does not filter out fluorescence. A diffraction experiment that results in the best quality data collected takes between 1-2 hours. Most samples described in this thesis were air-sensitive, and therefore the flat-plate mode was selected for data collection; the powder sample was scattered on a glass slide inside an air-tight cell.

### *2.2.6.2 Synchrotron radiation sources*

Synchrotrons can produce highly intense and collimated radiation beams that can be tuned to a specific wavelength. This allows for collection of highly precise data in a fraction of the time compared to laboratory diffractometers. Generation of X-rays begins by heating a tungsten element in the electron gun (source), which emits electrons. These electrons are then accelerated in a linear accelerator (linac), before being further energised in a booster synchrotron to GigaelectronVolt (GeV) scale of energy by bending magnets. When these electrons are then made to travel at speeds close to the speed of light in the storage ring, they are forced to change direction by magnetic fields. In addition to bending magnets, insertion devices are used, which produce a high flux of radiation by forcing electrons through an oscillating magnetic field. It is the change in the electrons' momenta that causes emission of radiation that spans the whole electromagnetic spectrum. A schematic of a synchrotron is shown in Figure 2.6.

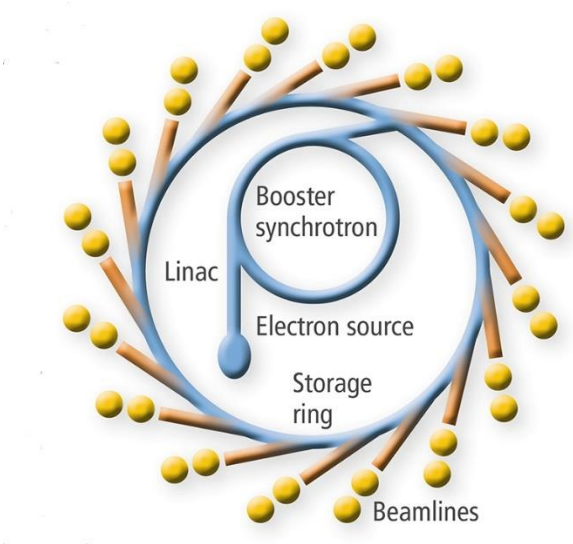


**Figure 2.6** Simplified schematic of a synchrotron (Adapted from Copyright © 2025 • LEAPS - League of European Accelerator-based Photon Sources).[8]

In order to tune the wavelength of the generated X-rays, radiation is directed to individual beamlines where the optics hutch selects a wavelength for the experiment. The experimental hutch is where the irradiation of a sample by synchrotron light occurs in a diffraction/spectroscopy/microscopy/imaging measurement.

A synchrotron X-ray source has many advantages compared to a laboratory diffractometer: the rapid collection times and higher data quality in terms of both resolution in $2\theta$ and signal-to-noise ratio. Secondly, as a wide range of wavelengths is available, allowing for selection of an adequate wavelength; short wavelengths lead to higher quality data and are also more penetrating, while it is possible to make use of anomalous scattering by tuning to a particular absorption edge.

#### 2.2.6.2.1 I11 High-resolution Diffractometer (Diamond Light Source, U.K.)

I11 is the high-resolution powder X-ray diffraction beamline at Diamond Light Source.[9] Here, an undulator-source generates highest beam flux at energies 11-20 keV, placing the wavelength in the range of 0.6-1.1 Å. The white light is strongly monochromated using a cryogenically cooled double-crystal of Si (111) and harmonic rejection mirrors (to remove contribution of higher-energy harmonic photons). The instrument operates in a Debye-Scherrer geometry and has two detectors: the Mythen Position Sensitive Detector (PSD) and the Multi-analyser crystal (MAC) detector. The PSD detector with its 90º aperture can measure an entire diffraction pattern between 5-145º in a matter of seconds, with a very good signal-to-noise ratio. Typically, two patterns are collected with the detector moved slightly (by 0.25º) between measurements and 'summed' to account for small gaps between Si detection modules. On the other hand, the MAC detector consists of 9 detectors on each of 5 detection arms, each detector served by an analyser crystal to only allow X-rays with the chosen incident wavelength to reach the detector, allowing for simultaneous measurement of 45 individual $2\theta$ values, resulting in very high resolution, low background contribution from flourescence and reduced sample misalignment issues. These benefits come at a cost of increased measurement time from PSD's seconds to ~30 minutes for 1 measurement on the MAC.

All measurements on I11 were carried out at the peak flux wavelength of about 0.82 Å (calibrated before each session of beam time using a silicon standard) and the sample was prepared by filling a 0.5mm borosilicate capillary with ground powder of the sample together with ground glass to lower the effect of absorption.

#### 2.2.6.2.2 BL10XU High Pressure and Low Temperature X-ray Powder Diffraction (SPring-8, Japan)

BL10XU is a beamline at the SPring-8 Synchrotron in Hyogo, Japan, dedicated to high-pressure powder X-ray diffraction. A wide range of temperatures is available from cryogenics (via a cryostat) up to 3000 K (via a double-sided laser heating system), but neither were utilised in the experiment that is the subject of Chapter 5, which was carried out at room temperature. SPring-8 uses an in-vacuum undulator to generate X-ray beam at energies 6-61 keV. BL10XU measures the diffraction of a white beam of X-rays through a fixed scattering angle. The X-ray beam is highly monochromated by a Si (*111*) double crystal, resulting in highly intense X-rays with sufficient resolution. . The design of the instrument was optimized to accommodate a diamond anvil cell (DAC), which contains the sample studied at elevated pressures. Flat imaging plate and X-ray CCD are used as area detectors with optics devices. On the detector stage, a microscope unit is equipped to observe samples in DACs and to align the sample to X-ray beam; the position of the sample can be adjusted to the X-ray beam position with a high precision (0.001mm). The microscope unit can also be used as Raman probe head for on-line pressure measurements and Raman spectroscopy measurement. Schematic of the diffractometer setup is illustrated in Figure 2.7a.

The collection of diffraction patterns as a function of pressure during a high-pressure experiment is preceded by a Raman spectroscopy measurement of the exact applied pressure inside the DAC; the generated X-rays irradiate a sample inside of DAC, which is responsible for exerting pressure over the sample as it is connected to a gas (He) membrane with which pressure is controlled remotely (without the need for taking the DAC out of the diffractometer at each pressure step). As the applied pressure via the gas membrane is inequivalent to the pressure inside the DAC, the ruby chip co-loaded with the sample inside the DAC is used for measuring exact pressure in a spectroscopy measurement. The exact value of ruby fluorescence is determined at target pressure by a pressure calculator software (Teledyne Princeton Instruments LightField software) and pressure of He gas is increased until observed ruby fluorescence peak fits to the calculated position for the target amount of pressure. Also, the exact position of the sample needs to be adjusted at each pressure step, as it changes slightly upon application of pressure: sample radius is ~2 μm, while the radius of the beam

is ~10 µm (Figure 2.7b). Failure to do this results in anomalies in the behaviour of the lattice parameters.

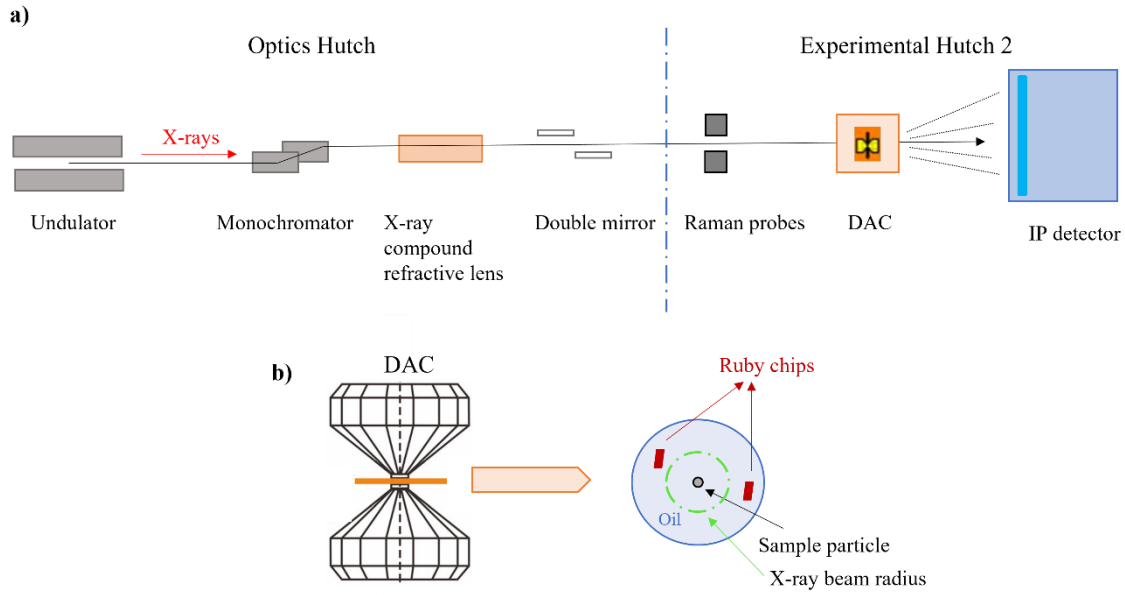


**Figure 2.7** a) Schematic of the BL10XU beamline for high-pressure and ambient temperature measurements, b) Schematic of a diamond anvil cell.

## 2.2.7 Neutron sources

### *2.2.7.1 Generation of Neutrons*

Neutrons exhibit wave-particle duality which is defined by the de Broglie equation:

$$\lambda = \frac{h}{p} = \frac{h\,t}{m_n v} \qquad \text{Equation 2.9}$$

Where $h$ is the Planck constant, $p$ is the momentum, $m_n$ is the mass of the neutron, and $v$ is velocity. Therefore, neutrons can interact with the atoms of the crystal lattice in a diffraction event as their wavelengths at appropriate energies used in a diffraction experiment are comparable to the spacing of atoms in a crystal.

There are two different types of neutron sources used at central facilities across the world: reactor source and spallation source. A reactor source, such as the ILL in Grenoble, France, generates high intensity neutrons from a fission process of the radioactive decay of $^{235}$U. The generated neutrons have wavelengths associated with the nuclear reaction, and their energies are modified via a heavy-water moderator before being monochromated and directed at a sample. For a single-wavelength

neutron source, such as the D2B diffractometer at ILL, the resolution is described by the Cagliotti function of the variation of FWHM (full width at half maximum) of a Bragg reflection with scattering angle, $\theta$:

$$\sigma^2 = \frac{FWHM}{8ln2} = Utan^2\theta + Vtan\theta + W \qquad \text{Equation 2.10}$$

Here, various instrumental and analytical factors influence the values of *U*, *V*, and *W* parameters, including monochromator geometry.

In a spallation source, such as the ISIS pulsed neutron and muon source, Harwell, UK, neutrons are generated by accelerating high energy protons at a tungsten target; hydride ions are firstly accelerated in a linear accelerator, and upon entry to a synchrotron they get ionised to protons (by stripping away the electrons) before colliding them into the target to generate an intense neutron pulse. The neutrons are then moderated and directed to the various neutron instruments. This process is known as spallation. Pulses are generated at 50 Hz and at ISIS four proton pulses in five are directed to target station 1 (TS1), and the other pulse to target station 2 (TS2).

As the distribution of wavelengths is large, and the flux at a particular wavelength is lower than at a reactor source, it is not efficient to monochromate the "white" beam of neutrons after they are generated. Therefore, unlike reactor sources, which often monochromate the beam and measure intensity as a function of $2\theta$, the intensity at ISIS is measured as a function of time of flight (ToF), the arrival of scattered neutrons at detectors. In a time-of-flight diffractometer, such as WISH at ISIS located on TS2, the neutron path length is fixed, and so are the detectors at various scattering lengths around the sample. The time of flight (ToF) over a known distance is therefore directly proportional to the *d*-spacing, equating the Bragg's law to the de Broglie equation (Equation 2.11):

$$\lambda = \frac{h}{p} = \frac{h\,t}{m_n v} = 2d_{hkl}sin\theta \qquad \text{Equation 2.11}$$

This allows for measurement of the *d*-spacing, when the scattering angle, $\theta$, is fixed and incident $\lambda$ is the variable parameter, making maximum use of the white beam; this means that more generated neutrons of varying velocities can be used for the diffraction experiment (as the beam does not need

to be monochromated). Multiple detectors are usually grouped into banks, which cover a fixed range of $\theta$. Velocity, $v$, in Equation 2.9, is replaced with $L/t$ where $L$ is distance and $t$ is time relates the time to the wavelength. The resolution in a ToF diffractometer is described as the uncertainty in $d$-spacing ($\Delta d$) as a function of $d$ according to Equation 2.12:

$$R(d) = \frac{\Delta d}{d} = \sqrt{\Delta\theta^2 cot^2\theta + (\frac{\Delta t}{t})^2 + (\frac{\Delta L}{L})^2} \qquad \text{Equation 2.12}$$

Here, $\Delta d$/d is dependent on the uncertainty in time of flight ($\Delta t$), in path length ($\Delta L$), and in the diffracted angle ($\Delta\theta$). As $2\theta$ approaches 180º, the $\cot^2\theta$ becomes infinitely small, therefore an instrument with a high-angle detector with a long path length will provide the best resolution. Low-angle detector banks are primarily used for investigating magnetic structures, where the magnetic Bragg peaks are observed at highest $d$-spacing, as their intensities drop quickly with decreasing d-spacing. High-angle banks, on the other hand, are used to collect the data with highest resolution, albeit at small $d$-spacing.

#### *2.2.7.2 D2B (ILL)*

The D2B is a high intensity diffractometer at ILL, Grenoble, France, and uses neutrons from a high flux reactor source.[10] The instrument operates in Debye-Scherrer geometry (in the sense that it uses a cylindrical sample with transmission geometry) and uses a Ge (*115*) monochromator to give a single wavelength, either $\lambda$ = 1.594 Å, which is the wavelength used in the experiments reported in this thesis, or 2.398 Å, which is used for studying higher $d$-spacings. The detector setup measures the diffraction pattern of a sample across an angular range of $5 \leq 2\theta\ (°) \leq 165$ and is comprised of 128 $^3$He tubes which are placed at intervals of 1.25°. A schematic of the D2B diffractometer is shown in Figure 2.8.

The sample is placed in a cylindrical vanadium can as the coherent scattering of vanadium is very small compared to the Bragg scattering of other elements (although it does have a non-negligible incoherent scattering that contributes to the background). Approximately 2 g of sample was then added to the vanadium can and sealed with an indium wire under the lid of the can, which is stable down to cryogenic temperatures as the metal does not become brittle.

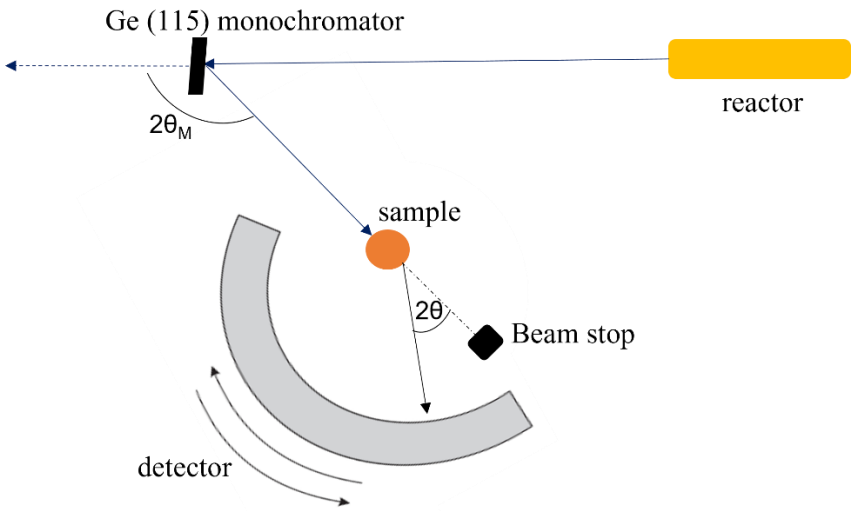


**Figure 2.8** Schematic of D2B diffractometer, a constant-wavelength neutron diffractometer with angle-dispersive detectors.

### *2.2.7.3 WISH (ISIS-TS2)*

WISH (WIde angle in a Single Histogram) is a long-wavelength diffractometer optimised for high resolution at medium-to-high *d*-spacing in the range of 0.7-17 Å.[11] It is suitable for magnetic structure characterisation. Its $^{3}$He detectors cover scattering angles between 10-170º. WISH uses a solid methane moderator at 50 K that generates neutrons with wavelengths of up to 15 Å. As WISH is a time-of-flight diffractometer, it does not have a monochromator. However, since resolution changes as a function of θ, it is divided into 10 banks, 5 on either side, such that banks 1 and 10, 2 and 9, etc., are at equivalent angles and the combined scattering from the two sides has an improved the signal-to-noise ratio. A schematic of the WISH diffractometer is shown in Figure 2.9.

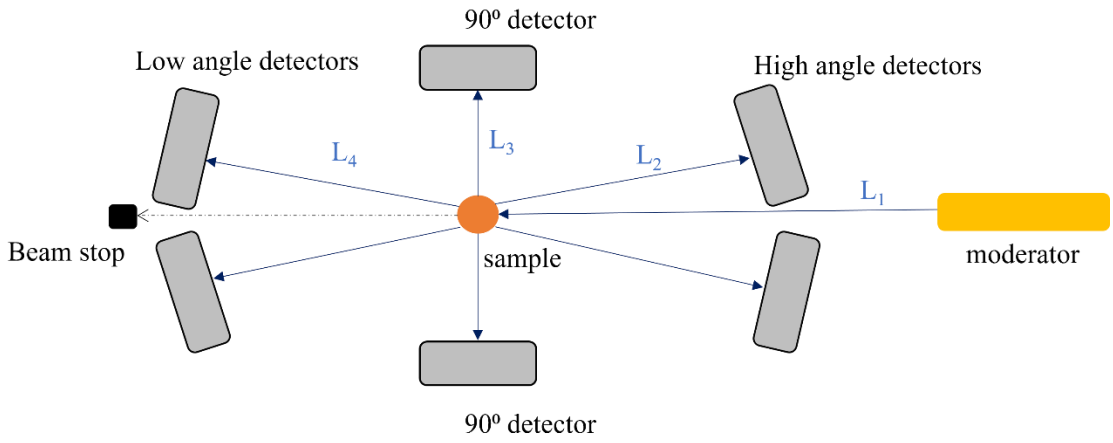


**Figure 2.9** Schematic of WISH diffractometer, a time-of-flight diffractometer with fixed-angle detectors (not all shown for clarity), where total path length $L = L_1 + L_n$.

### 2.2.8 SQUID magnetometry

All magnetometry measurements in this thesis were performed on the Quantum design MPMS instrument, which uses a Superconducing QUantum Interference Device (SQUID) as an extremely sensitive probe of a sample's magnetic moment in an externally applied field.[12] Here, a superconducting loop is separated into two by thin insulating strips to form two parallel Josephson junctions (Figure 2.10). Upon application of a small amount of current, Cooper pairs can tunnel through the insulating strips, and the entire loop conducts without resistance. However, if a critical current is reached, resistivity becomes finite and voltage is generated across the SQUID. The resulting output voltage is related to the magnitude of the externally applied field.

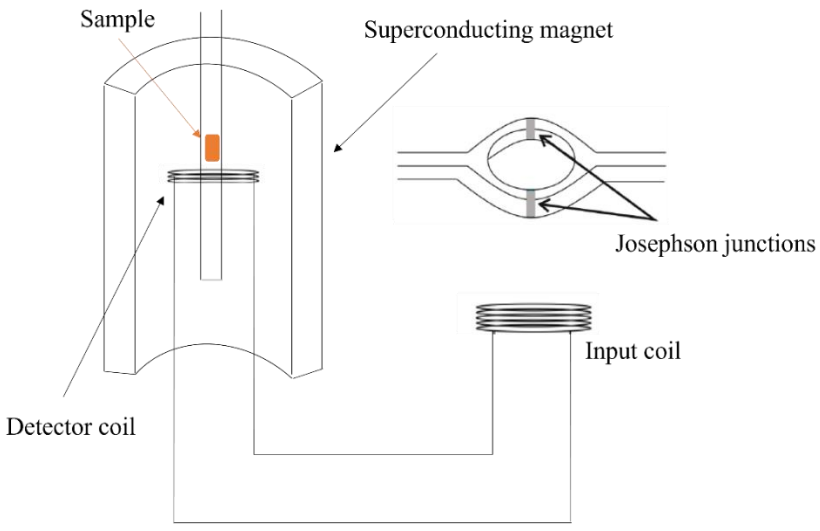


**Figure 2.10** Schematic of the SQUID set-up used in magnetometry experiments.

For an accurate operation of the SQUID, it must be housed away from the sample to protect it from external magnetic fields using a superconducting shield. The sample is mounted on a long stick and lowered onto the induction coils where it is magnetised using a helium-cooled superconducting magnet. When the sample is magnetised, a vertical translation causes the generation of a small current in this coil, coupled to an input coil, which in turn is coupled to the SQUID; therefore, the sample's magnetic moment is proportional to the output SQUID voltage.

The powder sample is weighed out inside of a gelatin capsule, which is then placed in a plastic drinking straw. The straw is lowered into the sample chamber, which is kept under an atmosphere of helium, and can be cooled down to 1.8 K. Generated fields range between ± 7 Tesla (70,000 Oe). The magnetic moment of a sample can therefore be measured as a function of temperature or field.

#### *2.2.8.1 DC magnetometry*

Direct-current magnetometry measurements were performed to extract various magnetic properties of the studied materials, such as magnetic moment, $\mu_B$, superconducting transition temperature, $T_c$, and magnetic susceptibility, $\chi_{mol}$.

For every sample, a scan of magnetisation (*M*) *vs* field (*H*) was performed first to determine sample purity. The gradient of this usually linear plot is the magnetic susceptibly, $\chi$, which describes how easily an applied field may align sample's magnetic moments. A negative gradient is indicative of diamagnetism, whereas a positive gradient shows paramagnetism. For a ferromagnet, the *M vs H* plot starts approximately linear but becomes flat as the field increases. This is due to saturation of magnetic moments (all domains are aligned with field). As the SQUID is more sensitive than PXRD, a ferromagnetic impurity below the detection levels of PXRD would be revealed in a non-linear relationship between *M* and *H* between 0-7 T at room temperature, especially at low fields (<0.1 T) where ferromagnetism dominates until saturation point, $M_{sat}$ (Figure 2.11).

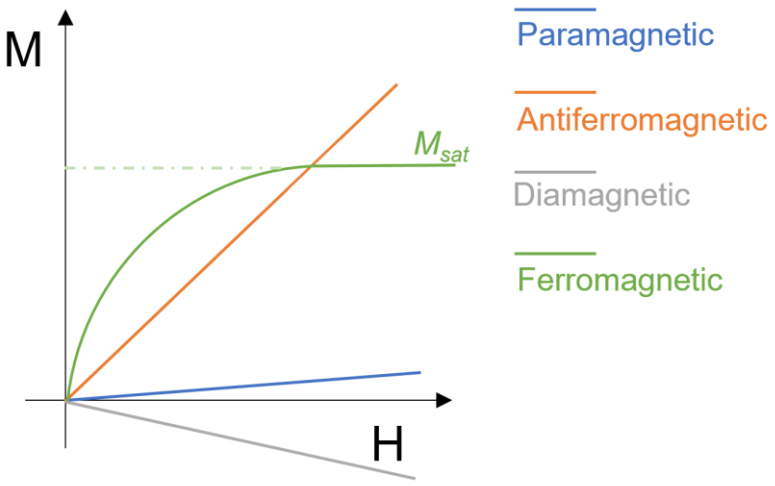


**Figure 2.11** Representation of a typical *M vs H* plot for various types of magnetic orders observed in solids.

In this case, to measure the real magnetic susceptibility of the sample, measurements can be made at two higher applied fields *H*2 and *H*1 that lie in the linear region above the ferromagnetic saturation field, effectively 'removing' the contribution of the impurity to the magnetisation signal. A sample's intrinsic magnetic susceptibility, $\chi_{mol}$, is then calculated from molar magnetisation values using equation 2.13:

$$\chi_{mol} = \frac{M_{H2} - M_{H1}}{H2 - H1} \qquad \text{Equation 2.13}$$

After establishing the *M vs H* relationship, the sample's magnetisation was measured in low field as a function of temperature between 2-300 K in a *M vs T* measurement, firstly upon cooling with no field (zero-field-cooled, ZFC), then upon cooling with a small applied field (field-cooled, FC) of 1000 Oe (0.1 T). The data was collected on warming in both ZFC and FC measurements, and the behaviour of the two curves was indicative of the type of magnetism present in the sample; ferromagnetism, antiferromagnetism, or spin-glass behaviour are distinguishable from their ZFC-FC curves.

Magnetisation isotherms (hysteresis loops) were performed at room temperature and at low temperature (2K or 5K) in the range $-7 \leq H\ (\mathrm{T}) \leq 7$ to further probe magnetic coupling in the

ferromagnetic samples and extract the value of Bohr magneton per magnetic ion, $\mu_B/ion$, indicative of the saturation moment of the ion, with the conversion given in Equation 2.14:

$$\mu_B / ion = \frac{\mu}{n_{ion} N_A \mu_B} \qquad \text{Equation 2.14}$$

Where $\mu_B$ is Bohr magneton, $\mu$ is observed magnetic moment, $n$ is the number of moles, $H$ is the applied field, and $N_A$ is Avogadro's constant.

#### *2.2.8.2 Magnetic measurements of superconducting samples*

A superconducting signal in a magnetometry measurement is distinguished by the onset of diamagnetism below the superconducting transition temperature, $T_c$, due to Meissner effect (*i.e.* the expulsion of all magnetic flux until perfect diamagnetism is achieved). The magnitude of the signal is used to determine the superconducting volume fraction, *SVF*, which is the amount of sample that is superconducting. This is often used in plotting the superconducting signal, as the dimensionless magnetic susceptibility, $\chi$, can be related to the *SVF* by Equation 2.15:

$$\chi = \frac{\rho \Delta_M}{mH} = \frac{SVF}{4\pi} \qquad \text{Equation 2.15}$$

where $\rho$ is the crystallographic density, $\Delta_M$ is the measured difference in magnetic moments of the superconducting and normal state, $m$ is the sample mass, $H$ is the applied field, and $4\pi$ represents the sample exhibiting perfect diamagnetism throughout its entire volume. For a perfect superconductor, $4\chi\pi = -1$, equivalent to an *SVF* of 100%.

For the superconducting compounds in this thesis, magnetisation was measured as a function of temperature in ZFC and FC measurements down to 1.8 K at a small applied field (usually 20 Oe) below the lower critical field, $H_{c1}$, of the superconductor. $H_{c1}$ was estimated from a *M vs H* plot between 0-7 T carried out at small field steps.

### 2.2.9 DC Resistivity

Resistivity measurements were performed to characterise the electrical conductivity of new materials presented in Chapter 3 and to analyse the response of a superconducting sample to field in Chapter 5. The band theory, described in Section 1.3, characterises metals (*i.e.* conductors), semiconductors,

and insulators, based on the size of the band gap that forms between valence and conduction bands at Fermi level, $E_F$ (the mean of the highest filled and lowest empty orbitals), as a result of atomic energy orbitals broadening into continuous energy bands when atom's atomic orbitals are brought close together (which is the case in a crystal lattice). The underlying differences in the band structures of conductors, semiconductors, and insulators, allow them to be easily distinguished in an electrical resistivity measurement, which is a property indicating how strongly a material opposes the flow of electric current.

A four-probe method is a collinear technique often used in resistance measurements (Figure 2.12). Current is passed through a sample via two current leads (outer probes of Figure 2.12), and two separate voltage leads measure the potential difference across the sample (inner probes), greatly reducing errors from contact resistance. Therefore, by using the four-probe method, it is possible to know, to a high degree of certainty, both the current and the voltage drop across the sample and thus calculate the resistance with Ohm's law:

$$R\ [\Omega] = \frac{V}{I} \qquad \text{Equation 2.16}$$

where voltage ($V$) is measured in Volts (V) and current ($I$) in Amperes (A). This resistance value is then used with the known geometry of the sample and the probe spacing to determine the material's resistivity. The sample's length ($L$) and cross-sectional area ($A$) must also be measured, and the resistivity is then determined by Equation 2.17:

$$\rho = \frac{R \times A}{L} \qquad \text{Equation 2.17}$$

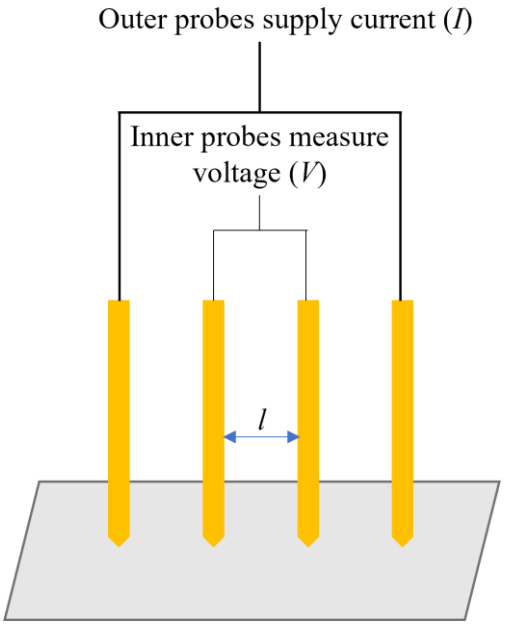


**Figure 2.12** Schematic of the four-probe method, commonly used to measure resistivity, where *l* is the spacing length between individual wires.

In a DC resistivity measurement, resistivity, $\rho$, is measured as a function of temperature. For metals, resistivity increases with temperature because increased atomic vibrations and subsequent electron collisions impede electron flow, resulting in a positive, often near-linear, relationship on the graph (Figure 2.13a). Unlike conductors, a semiconductor's resistivity decreases as temperature increases; at higher temperatures, there are more electron-hole pairs, increasing the number of available charge carriers (Figure 2.13b). For superconductors, the resistivity exhibits a sharp drop at critical temperature, $T_c$ (Figure 2.13c).

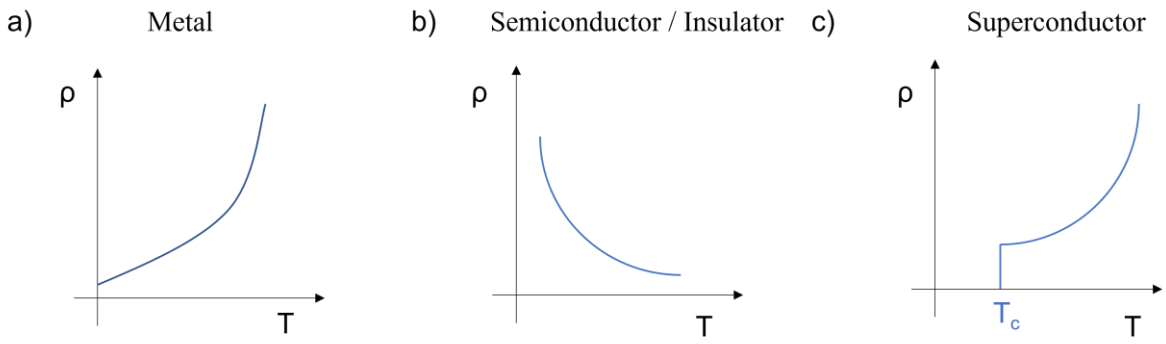


**Figure 2.13** Comparison of the resistivity behaviour as a function of temperature for a) metal, b) semiconductor or insulator, and c) superconductor.

The measurements described in Chapter 3 were performed on a custom-made in-house setup that uses the four-probe method firstly upon cooling and then upon heating (30-300 K). The equipment provided a constant predetermined current to the sample, whilst measuring the voltage every 20 seconds. The resistivity measurements were performed on a small piece of a sintered pellet (sintered to minimise the effect of grain boundaries) connected to four copper wires using silver paint. The wires were soldered to an IC socket, which was mounted on a custom-made probe (Figure 2.14a). The equipment is only suitable for analysis of air-stable materials.

The resistivity measurements described in Chapter 6 were performed on a Physical Property Measurement System (PPMS) instrument at the University of Kyoto, which also uses the four-probe method and can be used for highly air-sensitive samples, as the air exposure occurs only during a short transfer (<5s) of the sample to the instrument. The assembly of the probe is carried out inside the glovebox to prevent air exposure. The sintered pellet is positioned in the centre of the probe which is gold-plated, and four gold wires are attached to a sintered pellet using silver paste diluted with diethyl succinate. Resistivity probes have four contacts – one positive and one negative contact for current ($I$) and voltage ($V$) – to which a sample may be conventionally wired (Figure 2.14b). The probe was placed in a PPMS instrument for an AC resistivity measurement between 20-2 K at a fixed current of 1mA upon cooling as a function of field (0-6 T), as the sample under investigation was superconducting at $T_c$ of 4 K.

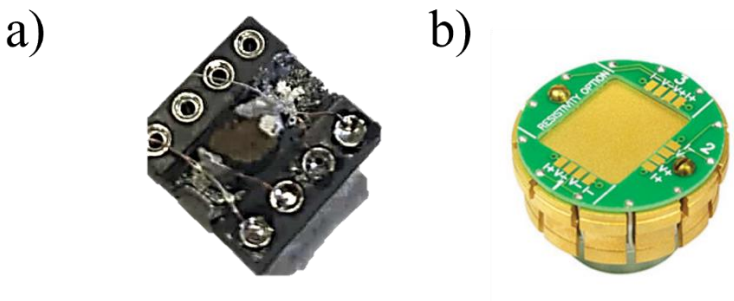


**Figure 2.14** a) Custom-made probe containing a pelletised sample for resistivity measurement, b) PPMS four-probe system puck used in resistivity measurement.

### 2.2.10 SEM-EDX

Scanning electron microscopy (SEM) with energy dispersive X-ray spectroscopy (EDX) is an analytical technique used in a variety of chemistry disciplines to study the topography and surfaces of materials. It combines high-resolution imaging with elemental analysis of a sample's surface by analysing the characteristic X-rays emitted when an electron beam interacts with the sample. The technique uses a finely focused beam of electrons which causes the emission of X-rays, secondary electrons, and backscattered electrons. The energy of the emitted X-rays is unique to the element whose atom's inner shell electron was displaced by the incident electron beam of the EDX; the number and energy of the emitted X-rays can be measured, providing information on the elemental composition. Secondary electrons, which originate from the atoms in the sample due to inelastic scattering, produce high-resolution images of the sample's surface, whereas backscattered electrons, which originate from deeper areas of the sample, give qualitative information in the form of intensities. These intensities can be correlated to the atomic number, hence allowing us to distinguish areas of sample where different elements are distributed. Therefore, SEM-EDX is a fast, inexpensive and non-destructive technique which allows for qualitative and quantitative analysis of the sample's surface.

SEM measurements were carried out in the in the David Cockayne centre for Electron Microscopy, University of Oxford using a Zeiss EVO MA10 microscope with an operating voltage of 20 kV and probe current of 4.0 nA equipped with an Oxford Instruments X-act EDX system with Aztec software to enable semi-quantitative chemical analysis to establish compositions and homogeneity. A small amount of powder sample was sprinkled on adhesive carbon tape mounted on a sample holder for insertion into the SEM instrument. This was done under inert atmosphere within the glovebox and the samples were sealed in a polyethylene bag for transport to the SEM instrument so that there was minimum air exposure from the time of loading the samples until mounting them in the SEM. Mapping measurements for particle homogeneity were carried out and compositions were estimated by averaging point measurements over 3-5 sites per particle for each of several particles. EDS maps were processed using the Oxford Instruments Aztec software.

## References

[1] Glazer, A.M. and Burns, G. (2013). *Space groups for solid state scientists*. Amsterdam; Boston: Elsevier.

[2] Clegg, W.; Blake, A. J.; Gould, R. O.; Main, P. (2001) *Crystal Structure Analysis;* Oxford University Press.

[3] Bragg, W.H. and Bragg, W.L. Proceedings of the Royal Society of London. (1913) *Series A, Containing Papers of a Mathematical and Physical Character*, *88*, 428–438.

[4] Altomare, A.; Cascarano, G.; Giacovazzo, C.; Guagliardi, A.; Burla, M.C.; Polidori, G.; Camalli, M. *J Appl Crystallogr* (1994), *27*, 435–435.

[5] Patterson, L. *Physical Review* (1934**)**, *46*, 372–376.

[6] Oszlányi, G. and Sütő, A. *Acta Crystallogr A* (2004), *60*, 134–141.

[7] Sears, V.F. *Neutron News* (1992**)**, *3*, 26–37.

[8] LEAPS. (2025). *Synchrotrons - LEAPS*. [online] Available at: https://www.leaps-initiative.eu/synchrotrons/.

[9] Thompson, S.P.; Parker, J.E.; Potter, J.; Hill, T.P.; Birt,A.; Cobb, T.M.; Yuan, F.; Tang, C.C. *Rev. Sci. Instrum.* 2009, *80*, 075107. https://doi.org/10.1063/1.3167217.

[10] Suard, E.; Hewat, A. The Super-D2B Project at the ILL. *Neutron News* (2001), *12* (4), 30–33. https://doi.org/10.1080/10448630108245006.

[11] Chapon, L. C.; Manuel, P.; Radaelli, P. G.; Benson, C.; Perrott, L.; Ansell, S.; Rhodes, N. J.; Raspino, D.; Duxbury, D.; Spill, E.; Norris, J.*Neutron News* (2011**)**, *22*, 22–25. https://doi.org/10.1080/10448632.2011.569650.

[12] Fagaly, R.L. *Review of Scientific Instruments* (2006), *77*, 101101.

# Chapter 3. Competing magnetism in layered mixed transition metal chalcogenides with the *ThCr$_2$Si$_2$*-type structure

## 3.1 Introduction

The $ThCr_2Si_2$ structure (Figure 3.1) is a versatile one in solid state chemistry where layers of edge-shared tetrahedra formed of transition metals surrounded by main group anions are separated by 8-coordinate electropositive metals.[1] These layered transition metal compounds, with general formula $AT_2X_2$ ($A$ = electropositive metal; $T$ = transition metal; $X$ = chalcogenide or pnictide), have been investigated in detail in recent years due to their versatile electronic and magnetic properties, including, but not confined to, unconventional superconductivity in the Fe-based pnictides and chalcogenides,[2] metamagnetic behaviour in Co-based selenides,[3] and heavy-fermion behaviour in the Ni-based system $KNi_2Se_2$.[4] A large number of chemical substitutions are possible in this structure and properties are diverse depending on structural details and electron count. The structure consists of covalently bonded transition metal-chalcogenide $T_2X_2$ layers, where the transition metal, $T$, is coordinated tetrahedrally in $TX_4$. The shape of the edge-sharing tetrahedra determines the $T$–$T$ distances and the details of the electronic structure, which in turn determines the electronic and magnetic properties.[1,3,5,6] This gives rise to a sensitive dependence of properties on structure and composition. In the $ThCr_2Si_2$ structure, there is $X$–$X$ bonding parallel to the stacking direction between adjacent $T_2X_2$ layers. However, in the $ACo_{2-x}Ni_xCh_2$ phases to be investigated here, with $A$ = K, Rb, Cs, and $Ch$ = S, Se, there is no bonding between adjacent chalcogenide layers and so this arrangement is often described as the $BaZn_2P_2$ structure.[1]

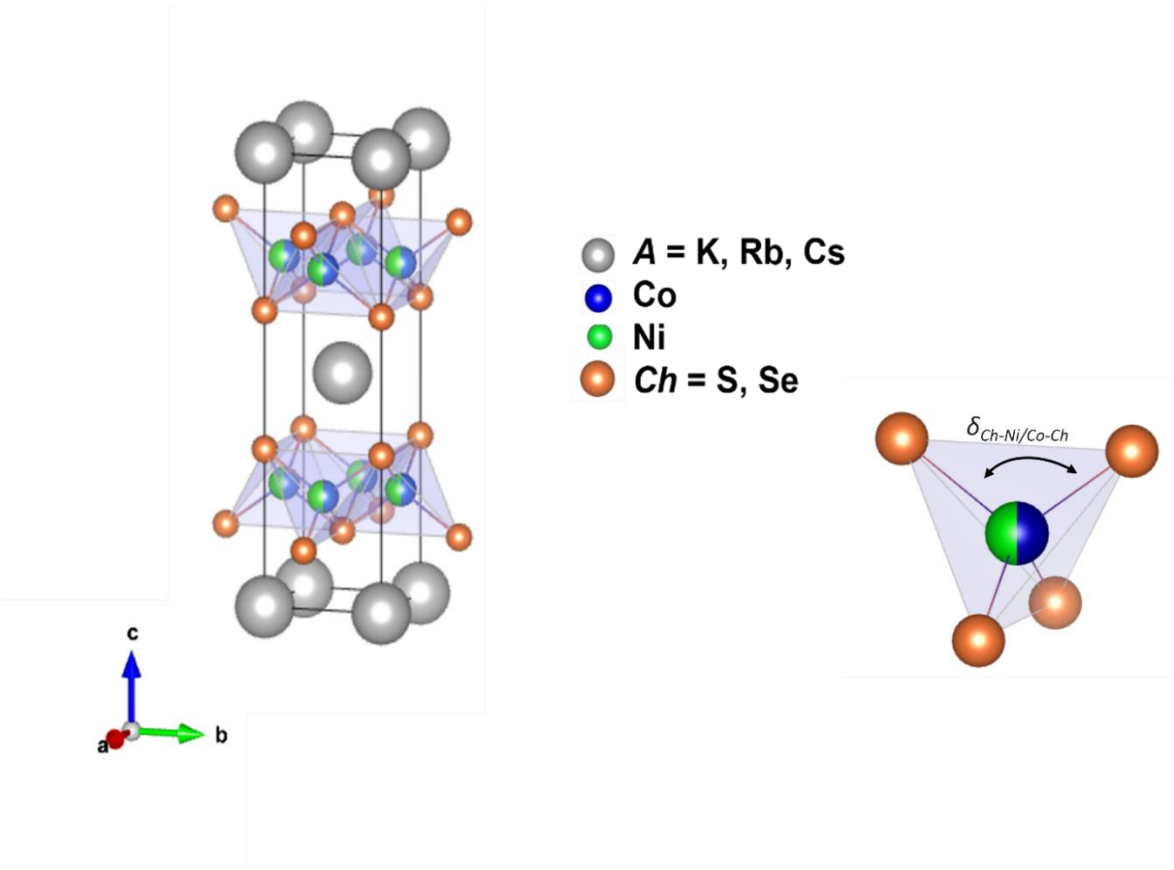


**Figure 3.1** Left: The $ThCr_2Si_2$/$BaZn_2P_2$ type structure of the $ACo_{2-x}Ni_xCh_2$ phases, with no bonding between chalcogenide layers. Grey atoms are electropositive metal (*A* = K, Rb, Cs), green and blue are transition metals – Ni and Co in the case of $ACo_{2-x}Ni_xCh_2$ phases - mixed on the same site, and orange atoms are chalcogenide anions (S, Se), Right: 2-fold tetrahedral angle, $\delta_{Ch\text{-}Ni/Co\text{-}Ch}$, which is bisected by *c*, the stacking axis. This angle will be referred to as simply the 'tetrahedral angle' in this Chapter.

For $AT_2X_2$ compounds with *T* = Co in the chalcogenide layers,[3,6,7] ferromagnetism within the layers is observed (intraplanar), but the interplanar (between-plane) ordering is sensitive to composition and structural features. In the series $TlCo_2(Se_{1-x}S_x)_2$, neutron powder diffraction shows that $TlCo_2S_2$ is fully ferromagnetic (intra- and interplanar) while $TlCo_2Se_2$ is an antiferromagnet with a helical arrangement of the orientation of the ferromagnetic planes that is incommensurate along the stacking direction with a turning angle of 121° at 1.4 K, and the magnetic moment directions are therefore almost commensurate after three layers.[6] While magnetometry shows that $RbCo_2Se_2$ and $KCo_2Se_2$ are ferromagnetic,[3,7] in $CsCo_2Se_2$, single crystal neutron diffraction reveals A-type antiferromagnetic order below 100 K and magnetometry reveals metamagnetism and a transition to a presumably fully ferromagnetic state above 3 T.[3,8] The pure Ni analogues are Pauli paramagnets and superconductivity

emerges at low temperatures,[4,9] showing that increasing the electron count has a dramatic effect on the physical properties.

The structure can accommodate defects; previous literature on $KNi_2Se_2$ single crystals and other Ni- and Fe-based $ThCr_2Si_2$-type compounds found the *A* and *T* content lower than stoichiometric, even when the 1:2:2 stoichiometry was targeted. Examples include $K_{0.64(4)}Fe_{1.44(4)}Se_2$[10,11] and $K_{0.95(1)}Ni_{1.86(2)}Se_2$,[12] while in the Fe systems, the highly deficient phases have Fe/vacancy order and are antiferromagnetic and insulating, but they sometimes coexist with $A_xFe_2Se_2$ compositions which are metallic and show high-temperature superconductivity.[13] Similar Ni-containing systems, including $LaNi_{1.88}P_{1.9}$[14] and $EuNi_{1.88}As_{1.92}$,[15] are also reported as non-stoichiometric, and a homogeneity range was established for $SrNi_xSb_2$ with $1.72 < x < 1.85$.[16] It was proposed that the Ni deficiency could be caused by the necessity to stabilize the electronic structure by removing an excess of valence electrons.[17] Similarly, non-stoichiometry is also reported in Co-containing $ThCr_2Si_2$-type pnictides, including $ACo_{2-x}As_2$ (*A* = Ca, La, Ce, Pr, Nd).[18]

With *A* = Tl, Ni/Co mixing in the $T_2X_2$ transition metal chalcogenide layers[19] results in A-type antiferromagnetism: ferromagnetic coupling within the plane as the result of direct magnetic interactions between the metal moments coexists with antiferromagnetic ordering along the stacking (*c*) axis, which is assumed to operate via the Ruderman-Kittel-Kasuya-Yosida (RKKY) mechanism.[6,19,20] In addition to work on crystal structures and magnetic properties of $ACo_{2-x}Ni_xCh_2$ phases (*A* = K, Rb, Cs; *Ch* = S, Se), this chapter will also explore their alkali metal deficiencies, using PND, SEM-EDX, and SC XRD characterisation techniques.

## 3.2 Synthesis and characterisation of $ACo_{2-x}Ni_xSe_2$ (*A* = K, Rb, Cs)

### *3.2.1 Synthesis of $ACo_{2-x}Ni_xSe_2$ (A = K, Rb, Cs)*

#### 3.2.1.1 Synthesis of $KCo_{2-x}Ni_xSe_2$ and $RbCo_{2-x}Ni_xSe_2$

Samples of $KCo_{2-x}Ni_xSe_2$ and $RbCo_{2-x}Ni_xSe_2$ ($0 \leq x \leq 2$) were prepared with 0.25 increments in *x* from stoichiometric amounts of Se (99.99%, Alfa Aesar), Ni (99.99%, Alfa Aesar) and Co powders (99.99%, Alfa Aesar) and potassium selenide ($K_2Se$) or rubidium selenide ($Rb_2Se$) powders prepared in-house (see below). The mixtures were ground, placed in alumina crucibles covered with loose-

fitting alumina lids and flame-sealed in evacuated silica tubes under vacuum (~ $10^{-2}$ mbar) with the end of the tube submerged in liquid nitrogen during the sealing process to prevent vaporization of elemental Se. The sealed tubes were placed in a furnace for a pre-treatment, to enable the relatively volatile chalcogen to react, ensuring the vapour pressure within the sealed ampoules did not become too great which could lead to the sealed ampoule exploding and result in loss of the sample, which involved slow heating at a rate of 1 °C $min^{-1}$ to 400 °C followed by a 4-hour dwell and then cooling at the natural rate of the furnace. The powders were then reground and reheated to 700 °C for 72 hours, followed by slow cooling at a rate of 0.1 °C $min^{-1}$ to room temperature. Products were dark red-brown polycrystalline powders. It is important to note that pure $KNi_2Se_2$ and $RbNi_2Se_2$ could not be synthesised pure via the above-mentioned route, as competing impurities, including $KNi_3Se_3$/$RbNi_3Se_3$, NiSe and $Ni_3Se_2$, were present in the PXRD patterns. Other synthesis routes were employed in these cases (see below).

#### 3.2.1.2 Synthesis of $KNi_2Se_2$

Single crystal growth using a so-called "self-flux" method was employed to obtain high purity samples of these compounds. Stoichiometric amounts of K ingot (99.95%, Alfa Aesar) and NiSe powder precursors (made previously from the elements, ground and pelletized and heated at 900°C/12hrs in a silica tube) were placed in an alumina crucible, covered with an alumina lid, and sealed in an evacuated silica tube under vacuum (~ $10^{-2}$ mbar) with the end of the tube submerged in liquid nitrogen to prevent vaporization of elemental K during the sealing process. The sealed tubes were placed in a furnace and heated slowly to 1000 °C at a rate of 1 °C $min^{-1}$, held at 1000 °C for 3 hours, and then slowly cooled to 700 °C at 0.1 °C $min^{-1}$, after which the furnace was shut off and allowed to cool at its natural rate over a few hours. Bronze-coloured crystals were obtained (typically 0.2×0.2×0.3 mm in size). A small amount of $KNi_3Se_3$ impurity (2.5 wt %) was detected by PXRD in the ground bulk product.

#### 3.2.1.3 Synthesis of $RbNi_2Se_2$

Neither of the synthesis methods employed for $RbCo_{2-x}Ni_xSe_2$ nor for $KNi_2Se_2$ yielded pure $RbNi_2Se_2$. $RbNi_2Se_2$ was instead synthesized at high purity using $Rb_2Se$, Ni, and Se reagents. These were mixed in an agate mortar and placed as loose powder in an alumina crucible with a loose-fitting

lid, flame-sealed under vacuum (~ $10^{-2}$ mbar) with the end of the tube submerged in liquid nitrogen to prevent vaporization of elemental Se during the sealing process. The sealed tubes were placed in a furnace and heated slowly to 400 °C at a rate of 1 °C $min^{-1}$ for 12 hours, and then cooled to room temperature at the furnace's natural rate over a few hours. The products of this pre-treatment were reground and pelletized and reheated to 650°C for 48hrs, followed by a furnace cool.

#### 3.2.1.4 Preparation of $K_2Se$ precursor

$K_2Se$ precursor was prepared from K ingot (99.95%, Alfa Aesar) and Se powder on a Schlenk line. The elements were placed in a Schlenk tube and ammonia was condensed onto them at −78 °C in a dry ice/isopropanol bath and this temperature was maintained for ~3 hours while stirring on a stirrer plate. Once reaction was complete at low temperatures (marked by colour change from blue solution to orange suspensions), ammonia was allowed to boil off through a mercury manometer by allowing the solution to warm slowly to room temperature by removing the dry ice/isopropanol bath. After the solid residue had reached room temperature the Schlenk tube was evacuated to remove any adsorbed $NH_3$. Orange powder was the products of the reactions and their purity was confirmed by PXRD, where no other phases were detected. (Caution: ammonia is volatile and toxic. The synthesis was performed in a fume hood and at all times the liquid-ammonia-containing vessel was open to a mercury bubbler to avoid the possibility of pressures exceeding 50 mmHg above atmospheric pressure in the reaction vessel). This reaction is further described in Chapter 2.1.4.

#### 3.2.1.5 Preparation of $Rb_2Se$ precursor

The $Rb_2Se$ precursor was prepared from Rb ingot (99.95%, Alfa Aesar) and Se powder in a solid-state reaction. A stoichiometric amount of Se was placed at the bottom of an alumina crucible, and Rb ingot was then carefully added to the crucible so as not to come into contact with the Se powders, as this potentially initiates the reaction in a vigorous way leading to loss of Se to atmosphere. A loose-fitting alumina lid was then placed on top of the crucible, which was placed in a silica tube and flame-sealed under vacuum (~ $10^{-2}$ mbar) with the end of the tube submerged in liquid nitrogen during the sealing process to prevent vaporization of elemental Se. The sealed tube was then placed in a furnace and heated slowly at 1 °C $min^{-1}$ to 175 °C followed by a 24-hour dwell and then cooling at the natural rate of the furnace. The product was an orange powder.

#### 3.2.1.6 Synthesis of $CsCo_{2-x}Ni_xSe_2$

Samples of $CsCo_{2-x}Ni_xSe_2$ with $0.25 \leq x \leq 1.75$ were synthesised from elemental Cs (99.98%, Alfa Aesar), and previously prepared nickel selenide (NiSe) and cobalt selenide (CoSe). These precursors of composition NiSe and CoSe were made by heating pressed pellets of the elements at 900°C (NiSe) or 600 °C (CoSe) for 12 hours in evacuated silica tubes. To synthesise the ternary phases, a stoichiometric amount of Cs was placed in an alumina crucible with a loose-fitting lid with the powdered NiSe and CoSe precursors and sealed in evacuated silica tubes under vacuum (~ $10^{-2}$ mbar) with the end of the tube submerged in liquid nitrogen to prevent vaporization of elemental Cs during the sealing process. The sealed tubes were slowly heated to 450 °C at a rate of 1 °C $min^{-1}$ and the temperature was maintained for 6 hours, followed by furnace cooling. The powders were reground and reheated to 750 °C for 72 hours, followed by quenching the tubes in an ice bath to room temperature. Products were dark brown polycrystalline powders. It is worth noting that end members of the solid solution - $CsNi_2Se_2$ and $CsCo_2Se_2$ - could not be synthesised in this study. Attempts included synthesis methods employed for the synthesis of $KNi_2Se_2$ and $RbNi_2Se_2$, but the resulting product was of poor crystallinity and therefore could not be indexed to any binary or ternary secondary phase, while it also lacked the signature (002) peak of the $ThCr_2Si_2$-type structure. We have also attempted the synthesis of $Cs_2Se$ using the same method as in the case of $Rb_2Se$ but we were unable to prevent the explosive contact between Cs and Se, which has resulted in loss of Se to the atmosphere. $Cs_2Se$ could have been synthesised on the Schlenk line using ammonia.

### *3.2.3 Crystal structure determination of $ACo_{2-x}Ni_xSe_2$ (A = K, Rb, Cs)*

#### 3.2.3.1 Room temperature SPXRD of $KCo_{2-x}Ni_xSe_2$

The entire solid solution $KCo_{2-x}Ni_xSe_2$ with $0 \leq x \leq 2$ was synthesised with good purity (>95%) according to Synchrotron PXRD. Crystalline secondary phases present are small amounts of either NiSe or CoSe, depending on composition. PXRD patterns of all 7 measured samples in the $KCo_{2-x}Ni_xSe_2$ series (Figure 3.2 left), were indexed according to the tetragonal $ThCr_2Si_2$-type structure (Space group: *I*4/*mmm*, no.139) of the parent stoichiometric phases using Rietveld refinement, indicating the formation of a solid solution across the whole $0 \leq x \leq 2$ range.

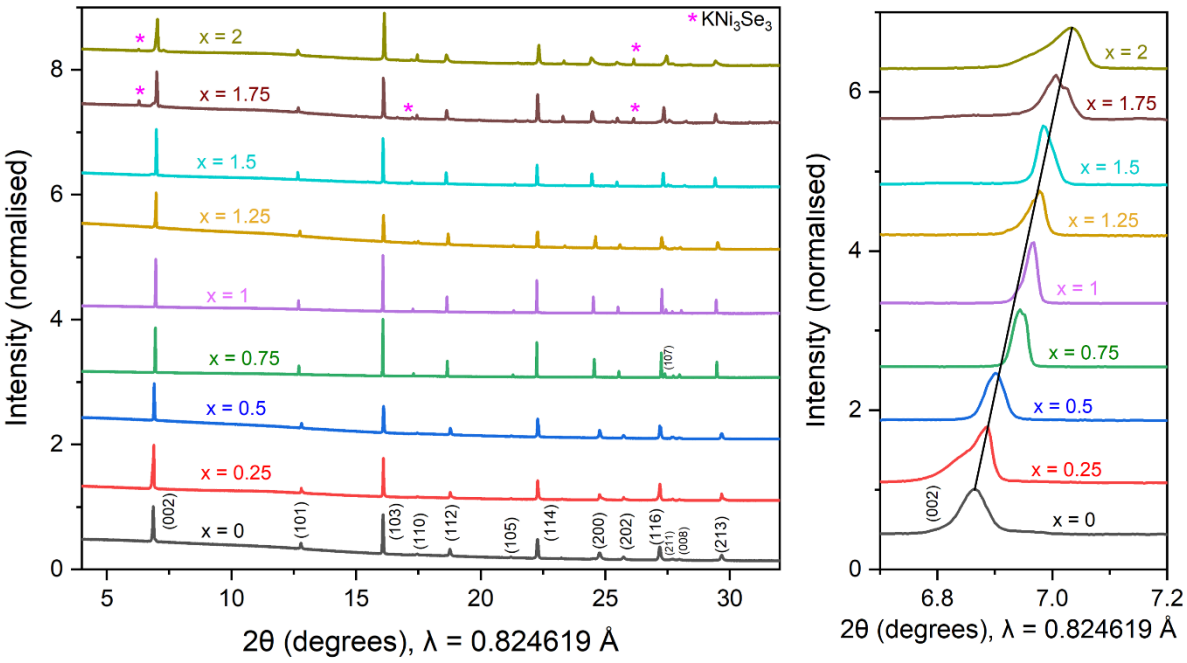


**Figure 3.2** Left: Synchrotron PXRD patterns of $KCo_{2-x}Ni_xSe_2$ with $0 \leq x \leq 2$. Right: (002) peak shifting to higher angles across $KCo_{2-x}Ni_xSe_2$ with increasing Ni content.

Figure 3.2 (right) shows the main (002) peak of the body-centred cell which shifts to higher angles with increasing Ni content, indicating a contraction of the *c* lattice parameter across the solid solution (by 2.6%). However, due to an increase in the dimension of the basal lattice parameter *a* (by 1.6%), the overall unit cell volume (*V*) shows a general increase – by 0.72% – with increasing Ni content from $x = 0$ to 2 in $KCo_{2-x}Ni_xSe_2$. The variations of the unit cell parameters *a* and *c*, unit cell volume, and the *c*/*a* ratio with *x* in $KCo_{2-x}Ni_xSe_2$ are shown in Figure 3.3. It is worth pointing out that some of the (002) peak shapes in Figure 3.2 are somewhat unusual, namely for composition with x = 0.25 and 1.75. Other peaks, namely (112), (200), and (213), exhibit a shoulder on side of the peak for these compositions. As these are near the compositions of the end members, it is possible that the phases separate between the end member and the non-stoichiometric member. Annealing these phases (a single heat treatment at 500°C/72hrs) has helped even out the peak shapes, but further annealing may be necessary. For pure $KCo_2Se_2$, $a = 3.841(3)$ Å, and $c = 13.8020(2)$ Å, which is in good agreement with previous work on this phase.[3] The trends agree with the work of Newmark *et*

*al*. on the related solid solution $TlCo_{2-x}Ni_xSe_2$, where lattice parameter *a* increases and lattice parameter *c* decreases with Ni content, and the *c/a* raio.[19]

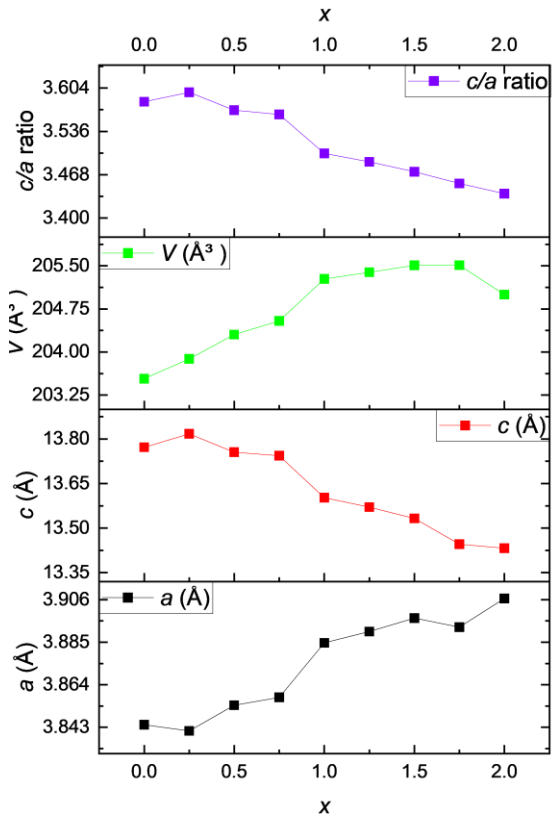


**Figure 3.3** Change in lattice parameters *a*, *c*, and unit cell volume with *x* in $KCo_{2-x}Ni_xSe_2$ series obtained from SXRD measurements on MAC detector at I11 (Diamond Light Source).

The Rietveld refinement of room temperature Synchrotron PXRD pattern of $KCoNiSe_2$ (middle member of the series) is shown in Figure 3.4. It is worth noting that the tetrahedral angle, $\delta_{Se\text{-}Ni/Co\text{-}Se}$, is distorted from ideal at 107.87(4)º. Further structural details on $KCoNiSe_2$ are listed in Appendix A.1.

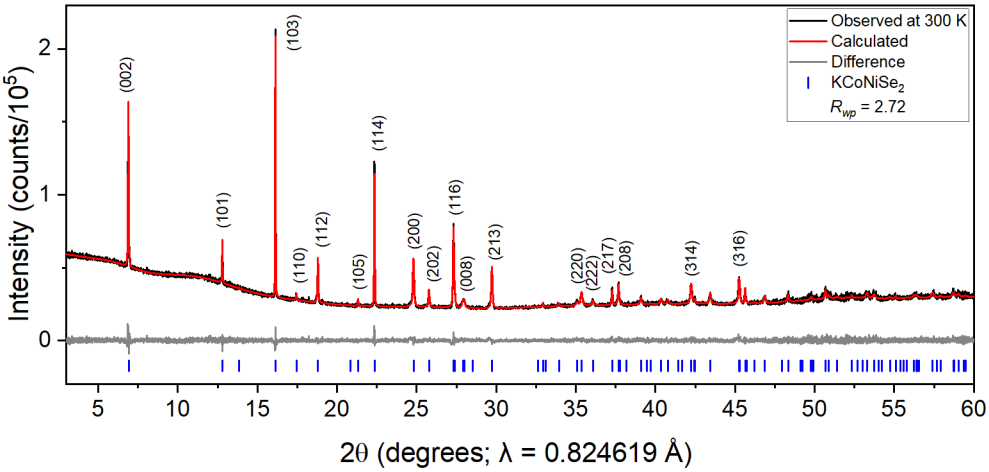


**Figure 3.4** Room-temperature Rietveld refinement of $KCoNiSe_2$ against Synchrotron PXRD.

The interatomic distances and tetrahedral angles across the series are shown in Figure 3.5. The tetrahedral angle, $\delta_{X\text{-}T\text{-}X}$, and the metal-metal distance, *T*-*T*, show a general increase with increasing Ni content. The trend in the regularity of the tetrahedral angle $\delta_{Se\text{-}Ni/Co\text{-}Se}$ is such that the angle increases with increasing Ni content and is closest to the ideal value of 109.5º at x = 2, even though it is still less than ideal. The metal-chalcogen distance, *T*-*X*, increases up to $x = 1.75$, where it shows a slight decrease before increasing again at $x = 2$, showing a non-linear trend, although this could be an artefact of the refinement as the change is small. The chalcogen-chalcogen distance, *X*-*X*, decreases steadily with increasing Ni content from $x = 0$ to 2. The increase in overall unit cell volume from $KCo_2Se_2$ to $KNi_2Se_2$ is demonstrated in an increase in the basal lattice parameter *a*, *T*-*T* distance, and the tetrahedral angle $\delta_{X\text{-}T\text{-}X}$. On the other hand, lattice parameter *c* decreases with increasing Ni content, and so does the *c*/*a* ratio, which is consistent with the work of Newmark *et al*. on the $TlCo_{2-x}Ni_xSe_2$ series.[19] All unit cell parameters, interatomic distances and angles in $KCo_{2-x}Ni_xSe_2$ series are shown in Table A.1.2 in Appendix A.1.

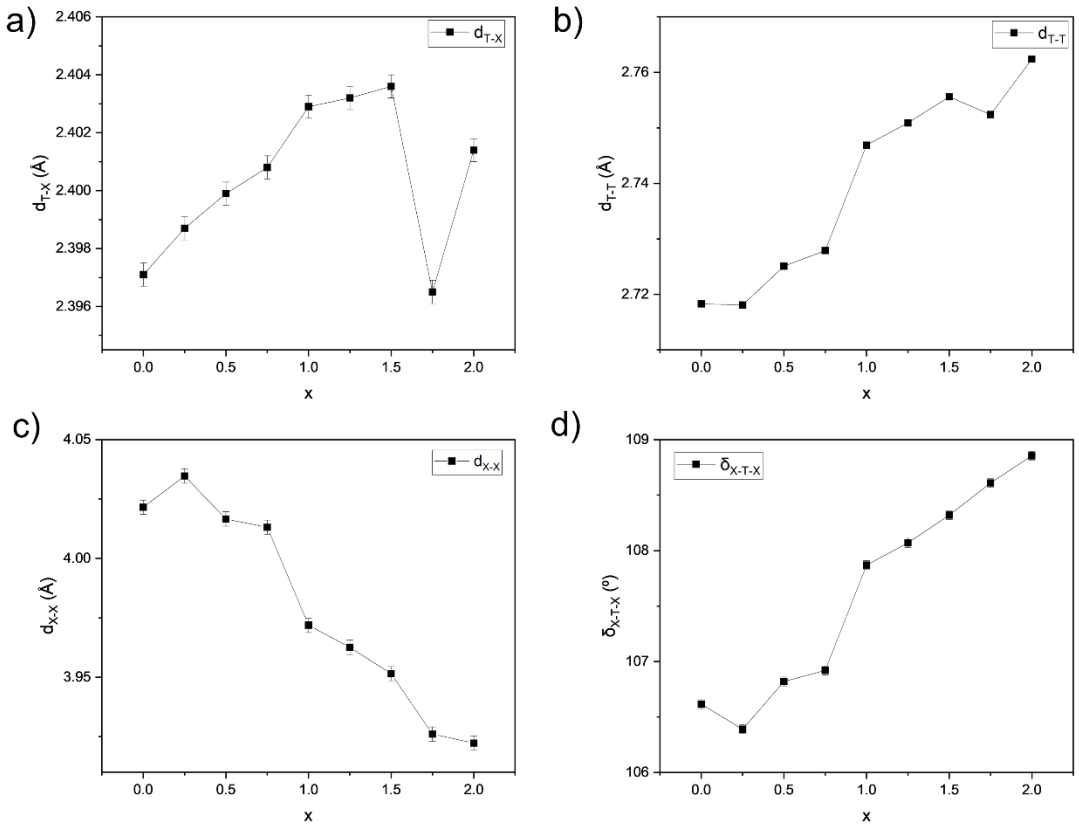


**Figure 3.5** Plots of changes in atomic distances and angles in in $KCo_{2-x}Ni_xSe_2$ series as a function of composition; a) Co/Ni-Se distance, b) Co/Ni-Co/Ni distance, c) Se-Se distance, d) tetrahedral angle Se-Co/Ni-Se.

### 3.2.3.2 Variable temperature SXRD of $KCoNiSe_2$

$KCoNiSe_2$ was also measured as a function of temperature using Synchrotron PXRD from 100 K to 300 K using the cryostream on the I11 beamline (Figure 3.6a). There were no extra peaks forming or peak splitting in the low temperature datasets, which would be indicative of a lowering of the cell symmetry. At $T_N$ = 175 K, there is a sharp change in the gradients of the plots of the *a* and *c* lattice parameters; the *a* parameter increases between 100-175 K, and then the increase is less pronounced between 175-300 K. On the other hand, *c* lattice parameter shows very little change between 100-175 K, and then the increase is much sharper until 300 K (Figure 3.6b). The overall unit cell volume increases linearly between 100-300 K. The *c/a* ratio has a highly non-linear gradient, where at first it decreases between 100-175 K and then remains constant up to room temperature. The reason for

this behaviour is related to the magnetostriction caused by the long-range magnetic properties of the phase and will be discussed in Section 3.2.4.2.

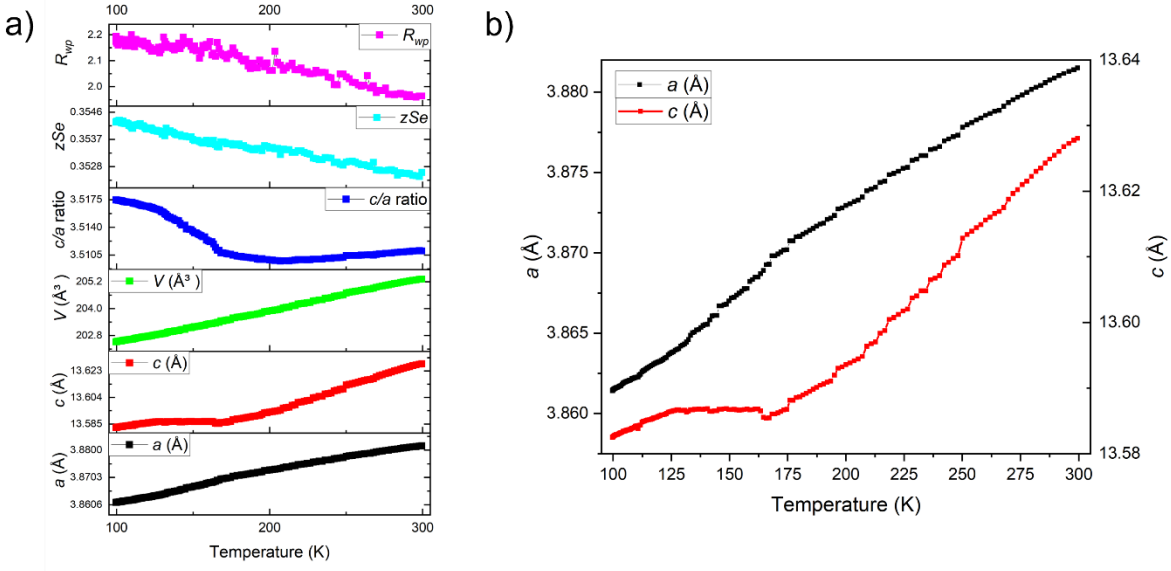


**Figure 3.6** a) Variable temperature SXRD for $KCoNiSe_2$, b) Changes in *a* and *c* lattice parameters between 100-300K.

### 3.2.3.3 Room temperature SPXRD of $RbCo_{2-x}Ni_xSe_2$

The entire solid solution $RbCo_{2-x}Ni_xSe_2$ with $0 \leq x \leq 2$ was synthesised with good purity (>90%) according to Synchrotron PXRD. Crystalline secondary phases present are small amounts of either CoSe or Se, depending on composition. PXRD patterns of all 7 measured samples in the $RbCo_{2-x}Ni_xSe_2$ series (Figure 3.7a), were indexed according to the tetragonal $ThCr_2Si_2$-type structure (Space group: *I*4/*mmm*, no.139) of the parent stoichiometric phases using Rietveld refinement, indicating the formation of a solid solution across the whole $0 \leq x \leq 2$ range.

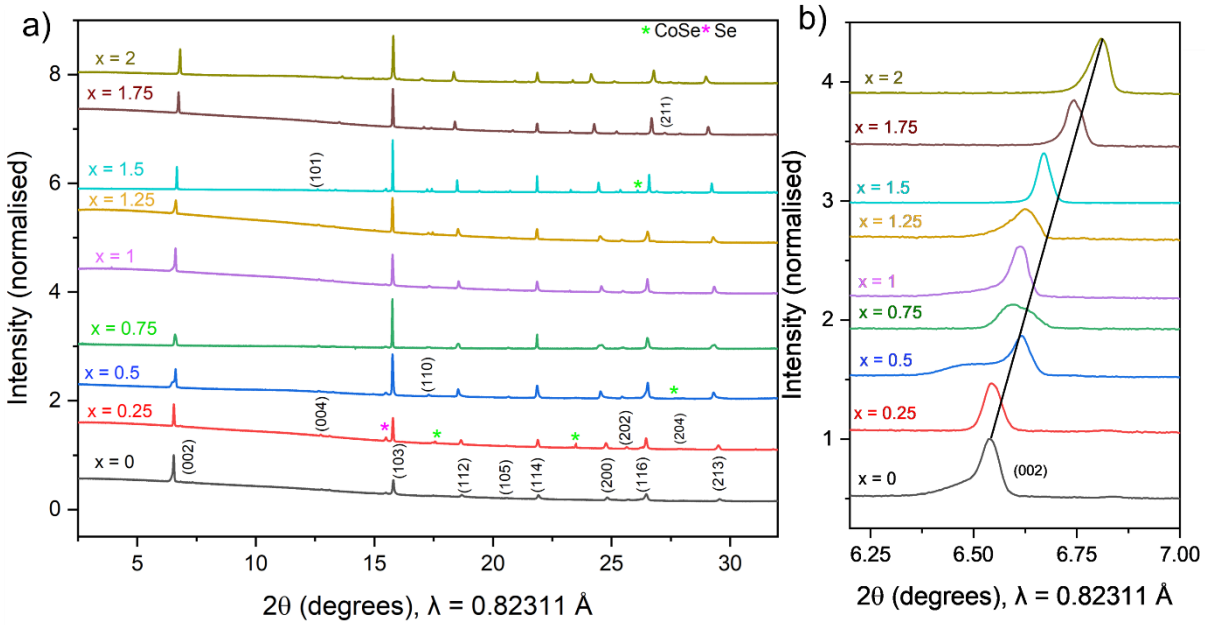


**Figure 3.7** a) Synchrotron PXRD patterns of $RbCo_{2-x}Ni_xSe_2$ with $0 \leq x \leq 2$. b) (002) peak shifting to higher angles across $RbCo_{2-x}Ni_xSe_2$ with increasing Ni content.

Just like in the case of $KCo_{2-x}Ni_xSe_2$, the main (002) peak of the body-centred cell shifts to higher angles with increasing Ni content (Figure 3.7b), indicating a contraction of the *c* lattice parameter across the solid solution (by 3.9%). As the basal lattice parameter *a* increases by 2.7%, the overall unit cell volume (*V*) shows a general increase – by 1.36% – with increasing Ni content from $x = 0$ to 2 in $RbCo_{2-x}Ni_xSe_2$. The variations of the unit cell parameters *a* and *c*, unit cell volume, and the *c*/*a* ratio with *x* in $RbCo_{2-x}Ni_xSe_2$ are shown in Figure 3.8. The (002) peak shapes in Figure 3.7b are again unusual for certain compositions, namely $x = 0.5$, 0.75, and 1.25. However, rest of the solid solution maintains a normal peak profile, and odd peak shapes are an exception rather than a rule. Phase separation between the stoichiometric and non-stoichiometric members is a possible explanation for the varied peak shapes. The Ni-end member – $RbNi_2Se_2$ ($x = 2$) – is a previously unreported phase, synthesised at high purity in this work (at 99%). Its Rietveld refinement is shown in Figure 3.9.

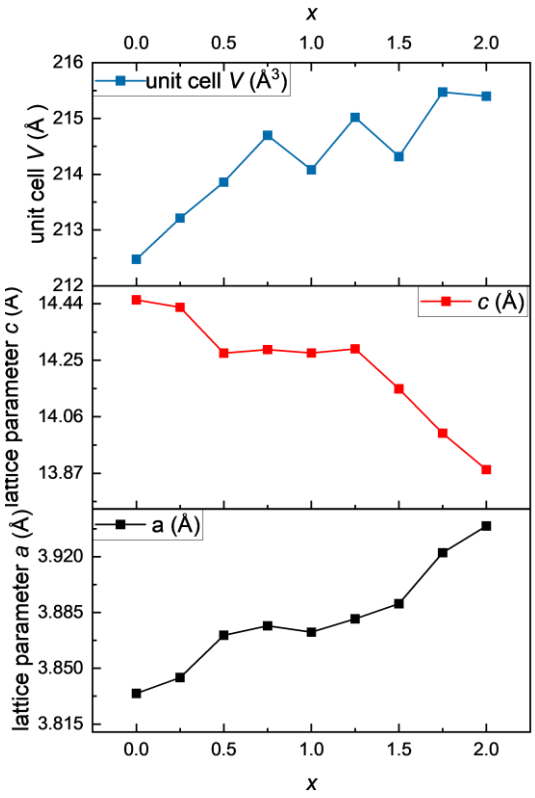


**Figure 3.8** Change in lattice parameters *a*, *c*, and unit cell volume with *x* in $RbCo_{2-x}Ni_xSe_2$ series obtained from XRD measurements on the PSD detector at I11 (Diamond Light Source).

The Rietveld refinement of room temperature Synchrotron PXRD pattern of $RbNi_2Se_2$ is shown in Fig 3.9. The tetrahedral angle, $\delta_{Se\text{-}Ni/Co\text{-}Se}$, is distorted from ideal at 110.35(3)º. The refined Rb occupancy from PXRD is 0.92(1).

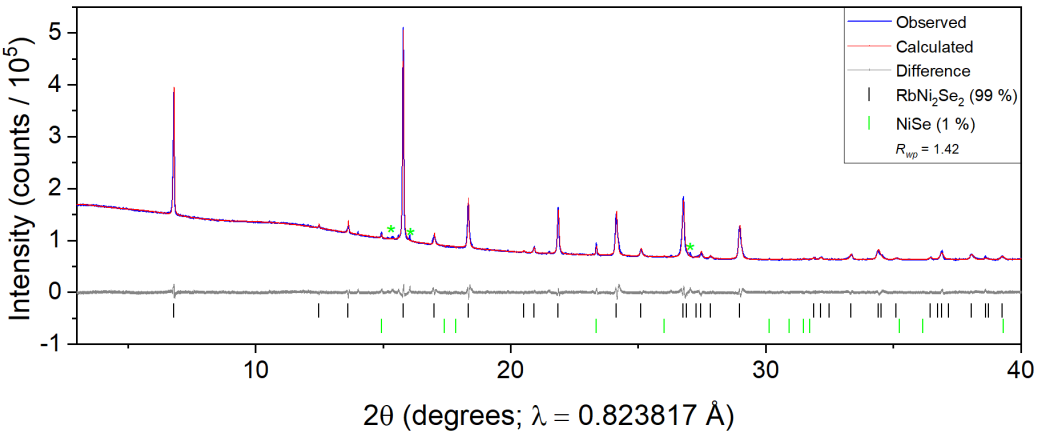


**Figure 3.9** Room-temperature Rietveld refinement of $RbNi_2Se_2$ against Synchrotron PXRD. Green asterisks represent an unknown impurity.

The Rietveld refinement of room temperature Synchrotron PXRD pattern of $RbCoNiSe_2$ (middle member of the series) is shown in Figure 3.10. It is worth noting that the tetrahedral angle $\delta_{Se\text{-}Ni/Co\text{-}Se}$ is distorted from ideal at 108.44(8)º. The refined Rb occupancy from PXRD is 0.75(1), which is more pronounced than in $RbNi_2Se_2$.

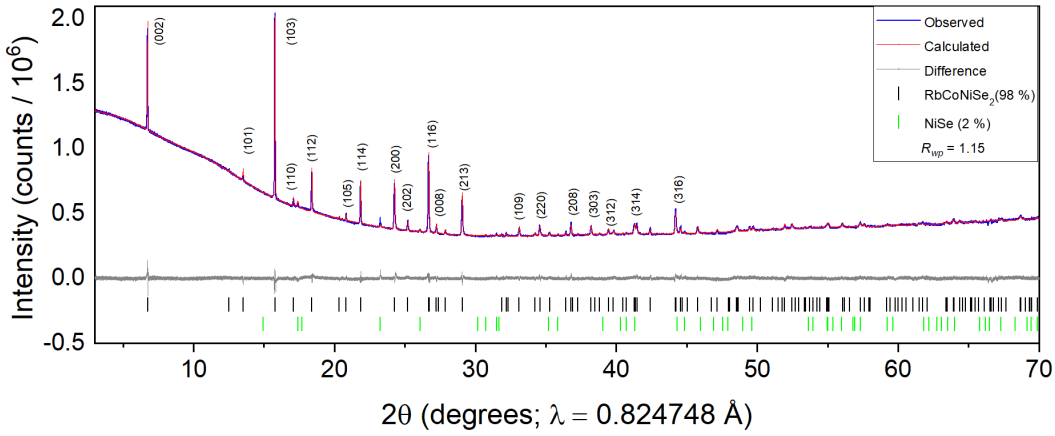


**Figure 3.10** Room-temperature Rietveld refinement of $RbNiCoSe_2$ against Synchrotron PXRD.

The interatomic distances and tetrahedral angles across the $RbCo_{2-x}Ni_xSe_2$ series are shown in Figure 3.11. The metal-metal distance, *T*-*T*, shows a general increase with increasing Ni content. The tetrahedral angle, $\delta_{X\text{-}T\text{-}X}$, and the metal-chalcogen distance, *T*-*X*, show non-linear trends. The trend in the regularity of the tetrahedral angle $\delta_{Se\text{-}Ni/Co\text{-}Se}$ is such that the angle crosses over from being less-than-ideal to more-than-ideal with increasing Ni content and is closest to the ideal value of 109.5º at x = 1.75. The chalcogen-chalcogen distance, *X*-*X*, decreases steadily with increasing Ni content from *x* = 0 to 2, which results from the decrease in *c* lattice parameter across the series, the same as in the case of K-analogue. All unit cell parameters, interatomic distances and angles in $RbCo_{2-x}Ni_xSe_2$ series are shown in Table A.2.1 in Appendix A.2.

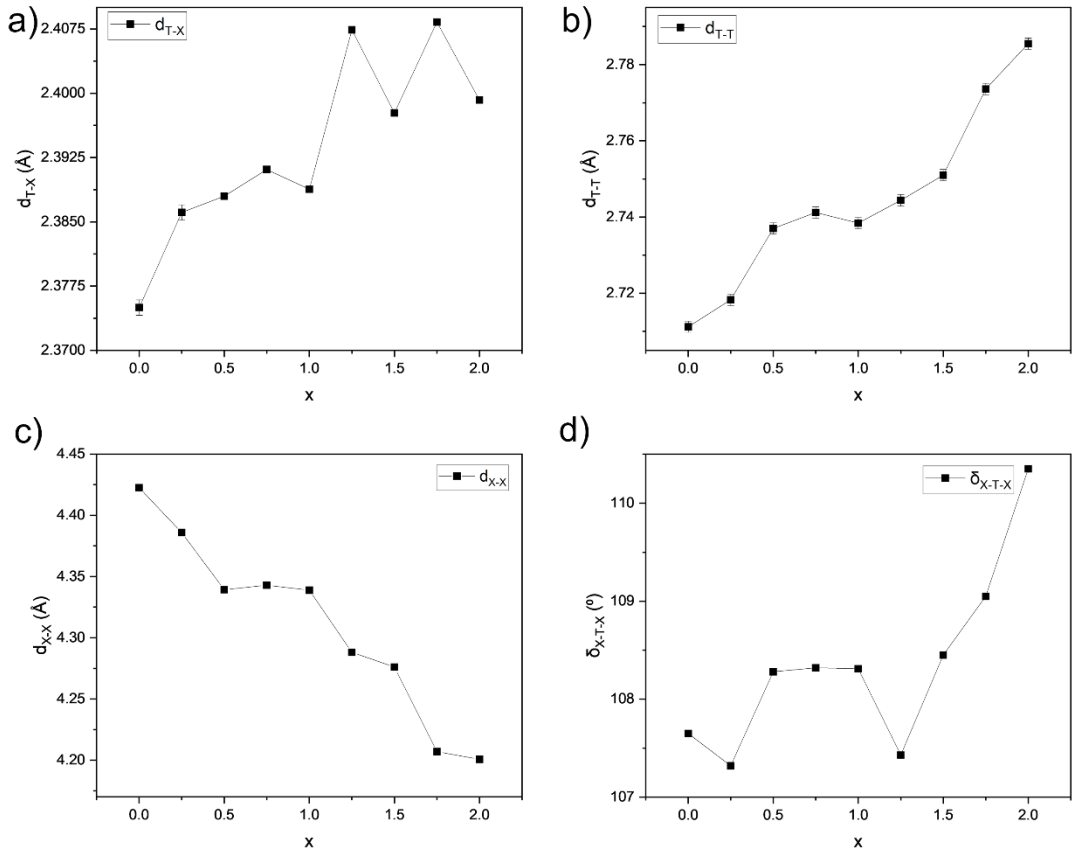


**Figure 3.11** Changes in interatomic distances and angles across the $RbCo_{2-x}Ni_xSe_2$ series; a) Co/Ni-Se distance, b) Co/Ni-Co/Ni distance, c) Se-Se distance, d) tetrahedral angle Se-Co/Ni-Se.

### 3.2.3.4 Variable temperature SXRD of $RbCoNiSe_2$

Similar trends in lattice parameters can be identified for $RbCoNiSe_2$ as for the K-analogue in Section 3.2.3.2. The change in gradient of *a* and *c* lattice parameters occurs at ~170 K, which is close to the $T_N$ observed from magnetometry (162 K - see Section 3.2.4.3). The *c/a* ratio also has a marked change in gradient at ~175 K, where it stops decreasing and remains approximately constant up to room temperature. The unit cell volume expands linearly between 100-300 K.

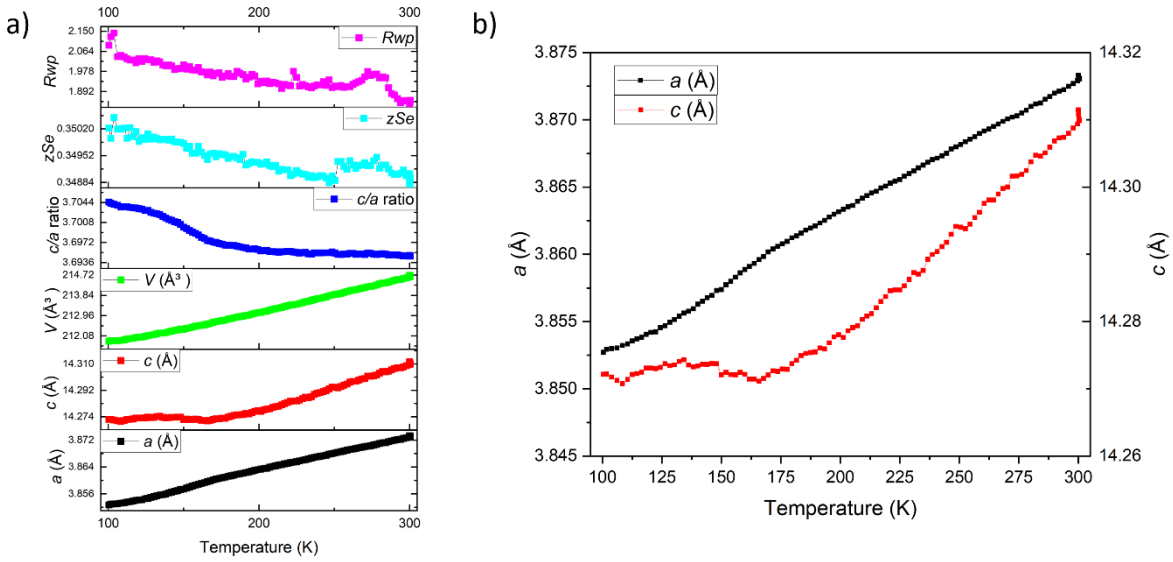


**Figure 3.12** a) Variable temperature SXRD for $RbCoNiSe_2$, b) Changes in *a* and *c* lattice parameters between 100-300K.

### 3.2.3.5 Room temperature SPXRD of $CsCo_{2-x}Ni_xSe_2$

The entire solid solution $CsCo_{2-x}Ni_xSe_2$ with $0.25 \leq x \leq 1.75$ was synthesised with good purity (>90%) according to Synchrotron PXRD at 0.25 intervals, and the region between $1.1 \leq x \leq 1.5$ in 0.05 intervals to probe the structural intricacies of these compositions. End members of the series could not be synthesised using the methods employed for the rest of the series, and other exploratory methods also failed to yield the correct product. Crystalline secondary phases present are small amounts of either $Cs_2Se$ or CoSe (CoSe is present in large amount at $x = 0.25$ only), depending on composition. PXRD patterns of seven members in the $CsCo_{2-x}Ni_xSe_2$ series, namely $0.25 \leq x \leq 1$ and $1.45 \leq x \leq 1.75$, were indexed according to the tetragonal $ThCr_2Si_2$-type structure (Space group: *I*4/*mmm*, no.139) of the parent stoichiometric phases using Rietveld refinement (Figure 3.13). The (002) peak shapes in Figure 3.13a again show some features, indicative of possible phase separation. The compositions in the region $1.1 \leq x \leq 1.4$ were found to exhibit a symmetry lowering to orthorhombic cell (Space group: *Fmmm*, no.69), which is observed by splitting of the 11*l* peaks of the tetragonal *I*4/*mmm* structure (shown in Figure 3.13b and Figure 3.14). The splitting could be accommodated using a monoclinic cell, too, with a space group *I*112/*m* (alternative setting of *C*2/*m*,

no.12), but a larger orthorhombic cell is possible with a higher crystallographic symmetry (two added mirror planes compared to the monoclinic model are present in the *Fmmm* model).

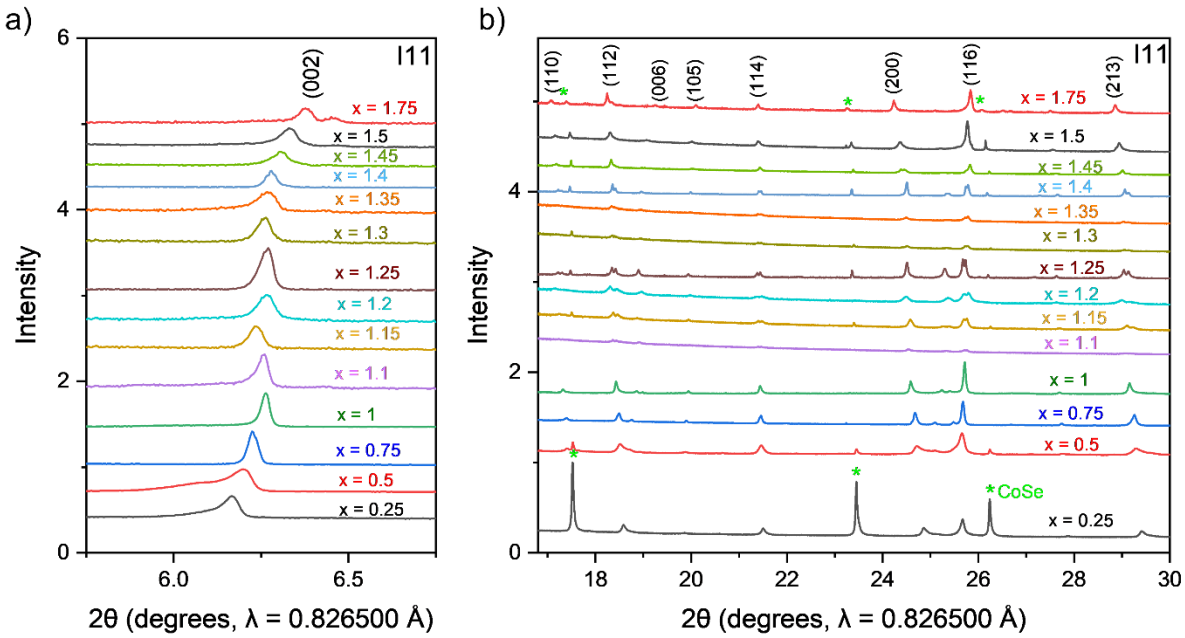


**Figure 3.13** a) (002) peak shifting to higher angles across $CsCo_{2-x}Ni_xSe_2$ with increasing Ni content. b) Synchrotron PXRD patterns of $CsCo_{2-x}Ni_xSe_2$ with $0.25 \leq x \leq 1.75$ between 17-30 2θ degrees, where splitting of reflections is shown in the region $1.1 \leq x \leq 1.4$. Green asterisks denote CoSe impurity (present in large quantities in $x = 0.25$ phase).

The peak splitting in the orthorhombic members of the series is not visible clearly when measuring PXRD patterns on lab diffractometers (Bruker), and Synchrotron PXRD is necessary here. Furthermore, certain members of the series, including as x = 1.1 and x = 1.3, formed in decreased crystallinity (although similar purity) compared to other orthorhombic members of the series, and the distortion could not be observed on lab diffractometers for these two compositions at all. The decreased product crystallinity could have arisen from decreased speed of quenching during synthesis, as quenching in iced water is essential for formation of the product. Figure 3.14 shows the small intensities of $CsCo_{0.9}Ni_{1.1}Se_2$ and $CsCo_{0.7}Ni_{1.3}Se_2$.

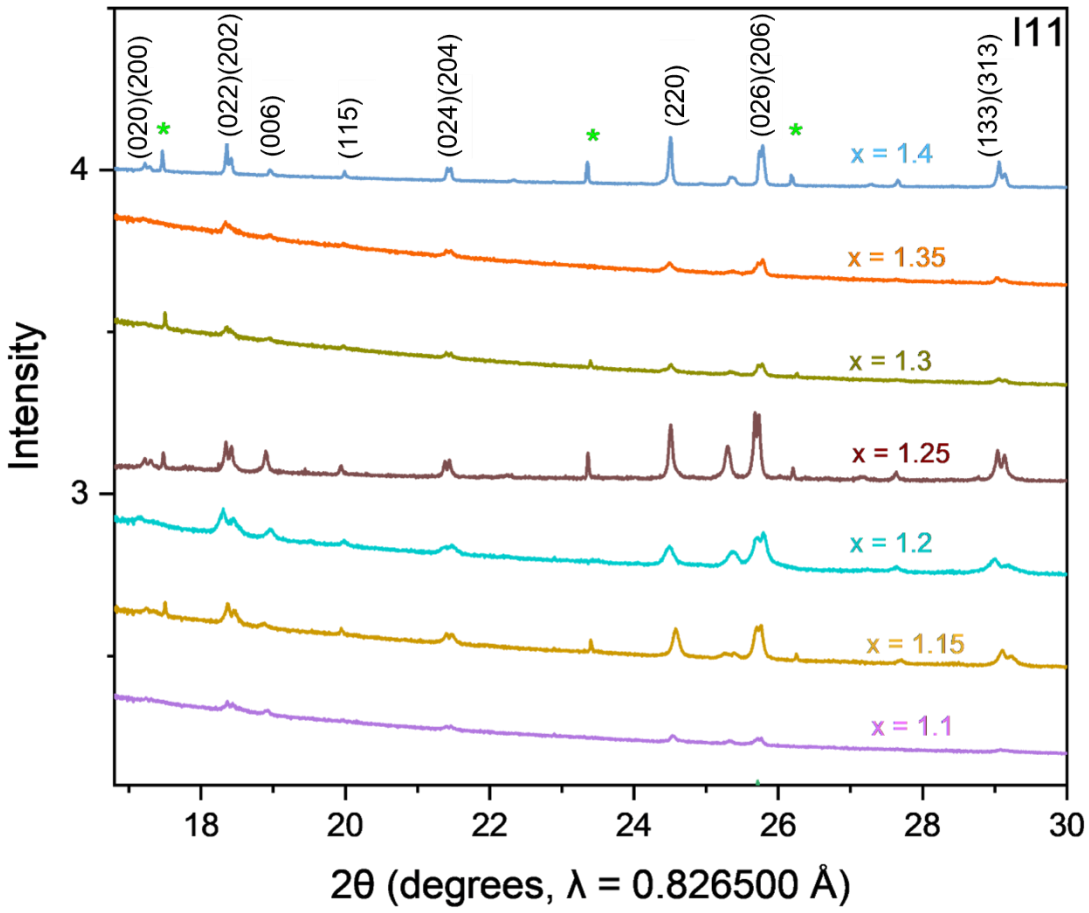


**Figure 3.14** Synchrotron PXRD patterns of $CsCo_{2-x}Ni_xSe_2$ with $1.1 \leq x \leq 1.4$ showing the characteristic peak splitting.

Just like in the case of the K- and Rb-analogues, the main (002) peak of the body-centred cell which shifts to higher angles with increasing Ni content (Figure 3.13a), indicating a contraction of the *c* lattice parameter across the solid solution (by 5.8%). As the basal lattice parameter *a* expands by 3.7%, the overall unit cell volume (*V*) shows a general increase – by 1.42% – with increasing Ni content from $x = 0.25$ to 1.75 in $CsCo_{2-x}Ni_xSe_2$. The variation of the unit cell parameters *a*, *b* ($1.1 \leq x \leq 1.4$), *c*, and unit cell volume, with *x* in $CsCo_{2-x}Ni_xSe_2$ are shown in Figure 3.15.

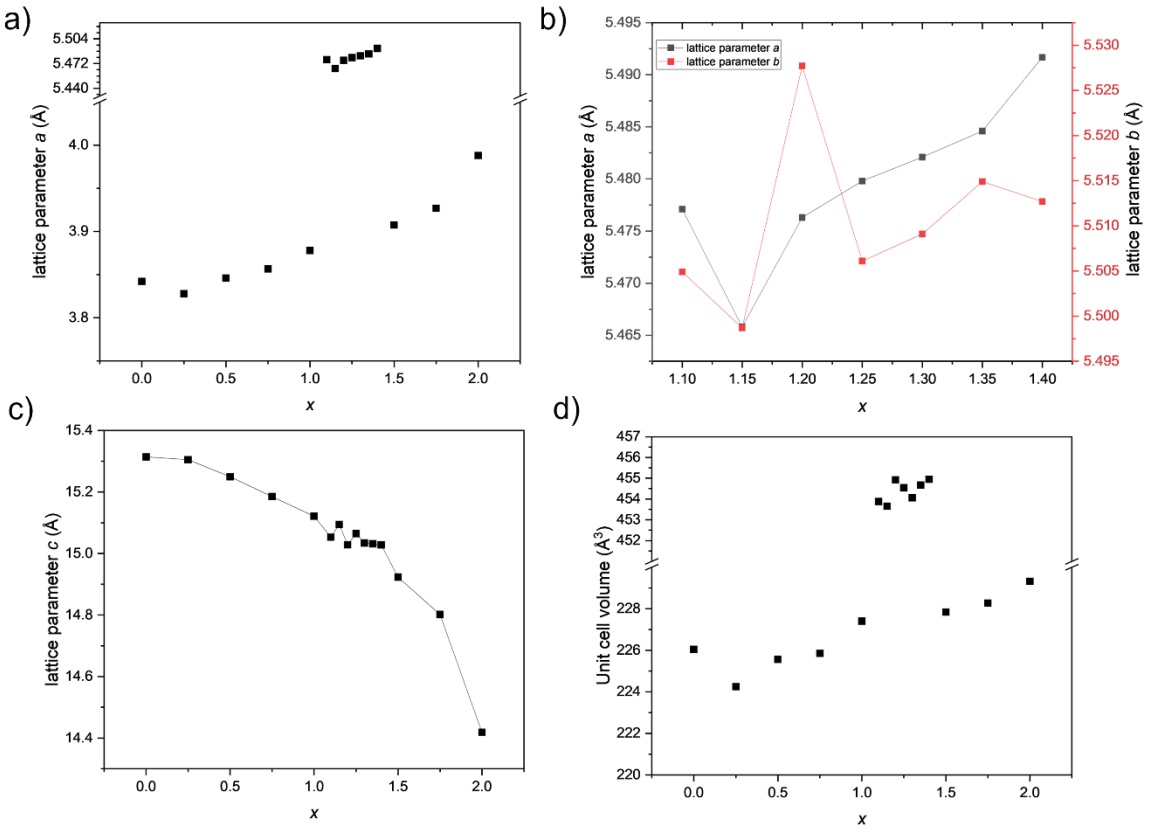


**Figure 3.15** Change in lattice parameters a) *a*, b) *a* and *b* between $1.1 \leq x \leq 1.4$, c) *c*, d) and unit cell volume with *x* in $CsCo_{2-x}Ni_xSe_2$ series obtained from PXRD measurements on the PSD detector at I11 (DLS).

The Rietveld refinement of room temperature Synchrotron PXRD pattern of $CsCoNiSe_2$ ($x = 1$) is shown in Figure 3.16. The tetrahedral angle $\delta_{Se\text{-}Ni/Co\text{-}Se}$ is distorted from ideal at 107.74(3)º. The refined Cs occupancy from PXRD is 0.84(1). Further structural details on this phase can be found in Table A.3.2 in Appendix A.3.

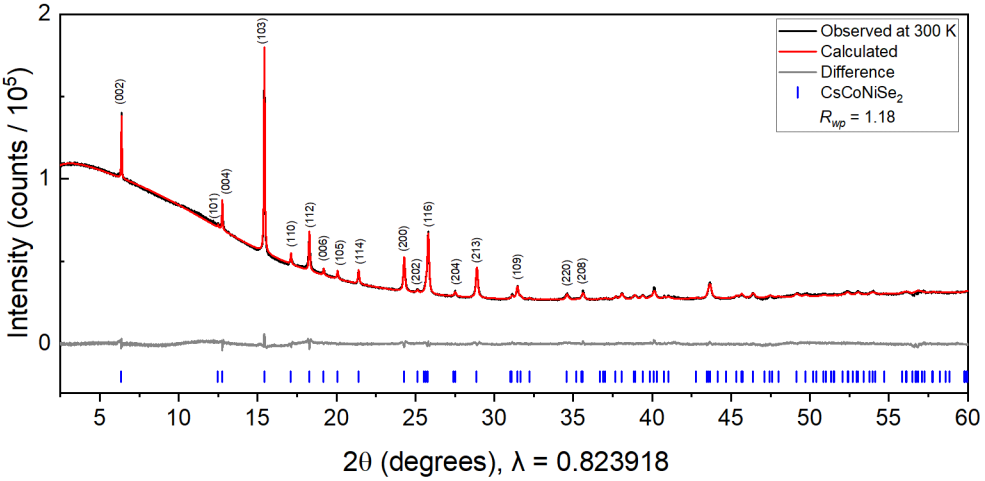


**Figure 3.16** Room-temperature Rietveld refinement of $CsCoNiSe_2$ against Synchrotron PXRD.

The orthorhombic structural model and the Rietveld refinement of room temperature Synchrotron PXRD pattern of $CsCo_{0.75}Ni_{1.25}Se_2$ ($x$ = 1.25) are shown in Figure 3.17a,b and c,d, respectively. Here, a symmetry-lowering to orthorhombic cell is observed by splitting of 11*l* peaks of the tetragonal structure, which become 0 2 *2l* and 2 0 *2l* of different *d*-spacings. As previously discussed, a smaller monoclinic cell the space group setting *I* 1 1 2/*m*, a non-standard setting of the *C*2/*m* space group, with the *c* axis as the unique axis and $\gamma \neq 90^{o}$, can be used and the unit cell shape and volume retained. The *z* coordinates of Co and Ni atoms are no longer on special positions in this monoclinic symmetry, as was the case in the tetragonal symmetry of the rest of the $CsCo_{2-x}Ni_xSe_2$ series. The distortion is very subtle, with *a* and *b* lattice parameters being nearly identical, and $\gamma$ is only slightly smaller than 90º. However, as the higher symmetry orthorhombic model with space group *Fmmm* fits the data just as well, this was the chosen model. Here, a larger cell than the tetragonal and monoclinic cells is used, where $a,b_{ortho} \approx \sqrt{2}a_{tetra}$, and $c_{ortho} \approx c_{tetra}$, and *a* differs from *b* very slightly. The structural parameters of $CsCo_{0.75}Ni_{1.25}Se_2$ are listed in Tables 3.1 and 3.2. The tetrahedral angle, which is bisected by the *c*-axis, $\delta_{Se\text{-}Ni/Co\text{-}Se}$, is distorted from ideal at 110.18(12)º (here, the multiplicity of this angle is 2). There are two other angles valued at 110.18(12)º and 110.56(12)º (both with multiplicity of 2). The refined Cs occupancy from PXRD is 0.852(2).

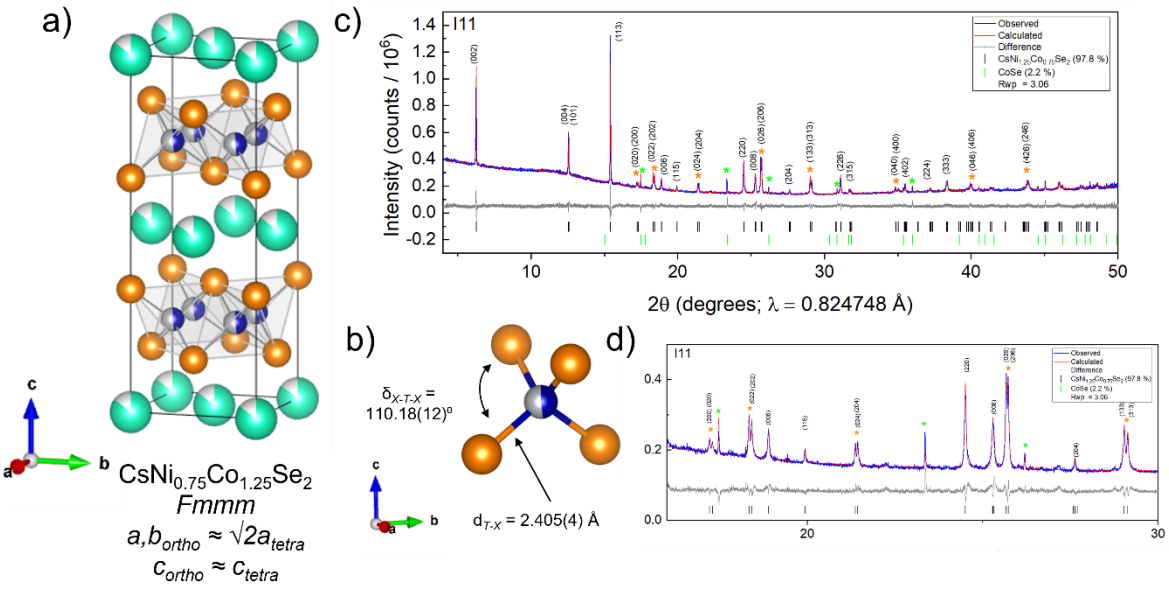


**Figure 3.17** a) The crystal structure of orthorhombic $CsCo_{0.75}Ni_{1.25}Se_2$, b) the distorted Co/$NiSe_4$ tetrahedron, c) Rietveld refinement against Synchrotron PXRD data at 300 K, $R_{wp}$ = 3.06% and $\chi^2$ = 4.43. The reduction of the lattice symmetry and thus the phase transition is indicated by peak splitting (orange asterisks), d) Highlighting the appearance of split peaks.

**Table 3.1** Structure details for orthorhombic $CsCo_{0.75}Ni_{1.25}Se_2$

| **Atom** | **Wyckoff site** | **x** | **y** | **z** | **Occupancy** | **$U_{iso}$** |
|---|---|---|---|---|---|---|
| **Cs** | 4a | 0 | 0 | 0 | 0.852(2) | 0.922(2) |
| **Ni** | 8f | 0.25 | 0.25 | 0.25 | 0.375 | 0.0156(8) |
| **Co** | 8f | 0.25 | 0.25 | 0.25 | 0.625 | 0.0156(8) |
| **Se** | 8i | 0 | 0 | 0.3442 | 1 | 0.4265(1) |

**Table 3.2** Structural parameters for orthorhombic $CsCo_{0.75}Ni_{1.25}Se_2$

| **Space group** | *Fmmm* |
|---|---|
| ***a* (Å)** | 5.4797(1) |
| ***b* (Å)** | 5.5062(1) |
| ***c* (Å)** | 15.0649(2) |
| **V (Å$^3$)** | 454.54(1) |

### 3.2.3.6 Variable temperature SXRD of $CsCo_{2-x}Ni_xSe_2$

#### 3.2.3.6.1 Low-temperature SXRD of tetragonal $CsCoNiSe_2$

The changes in lattice parameters with temperature obtained by PXRD between 100-300 K are slightly different for $CsCoNiSe_2$ as opposed to those observed for K- and Rb-analogous phases shown in Sections 3.2.3.2 and 3.2.3.4: even though lattice parameter *a* shows similar behaviour to $KCoNiSe_2$ and $RbCoNiSe_2$, the *c* lattice parameter firstly decreases between 100-160 K, and then increases sharply up to room temperature (Figure 3.18). Here, the $T_N$ is not coincidental with the temperature at which the lattice parameters show a gradient change ($T_N$ ($CsCoNiSe_2$) = 126 K, see Section 3.2.4.4), but rather the change in gradient occurs at ~170K, which is similar to the K- and Rb-analogous phases. This indicates that a subtle structural change is occurring at a similar temperature for all $ACoNiSe_2$ phases, regardless of the identity of the *A* cation, and could be independent of their magnetic behaviour.

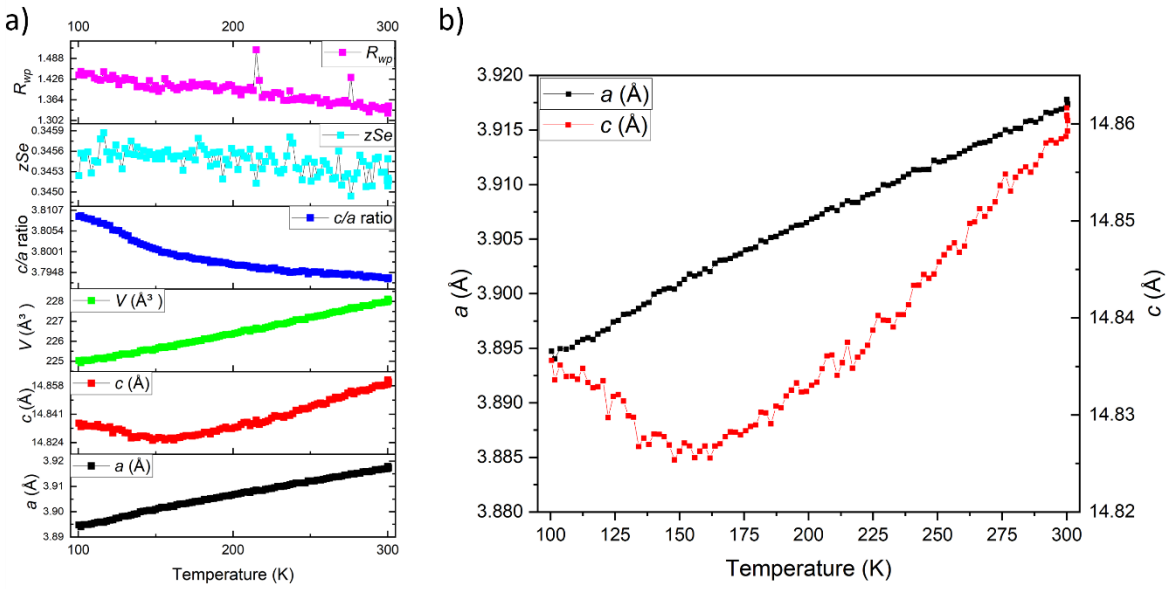


**Figure 3.18** a) Variable temperature SXRD for $CsCoNiSe_2$, b) Changes in *a* and *c* lattice parameters between 100-300K.

#### 3.2.3.6.2 Variable temperature SXRD of orthorhombic $CsCo_{0.8}Ni_{1.2}Se_2$

Variable temperature PXRD patterns were collected on an orthorhombic member of the series with x = 1.2, $CsCo_{0.8}Ni_{1.2}Se_2$. The PXRD patterns were collected on the MAC detector to allow for better observation of the symmetry lowering to orthorhombic cell. The patterns were collected in the

temperature order of 300 K - 100 K - 400 K, and back to 300 K (Figure 3.19). The phase retains its room-temperature orthorhombic cell down to 100 K, and upon heating to 400 K, the structure becomes tetragonal, marked by loss of peak splitting of characteristic reflections (Figure 3.19b). Upon cooling back to room temperature, it can be noted that some features of the PXRD pattern are new compared to the initial pattern collected at 300 K; a low-angle shoulder on the main (002) peak and a high-angle shoulder on the (200) peak can be observed. The orthorhombic-to-tetragonal structural transition therefore has some complication which requires further investigation; some of the possible reasons for these observations could be beam damage to the sample, reaction of sample with ground glass inside the capillary, or a phase separation at elevated temperatures.

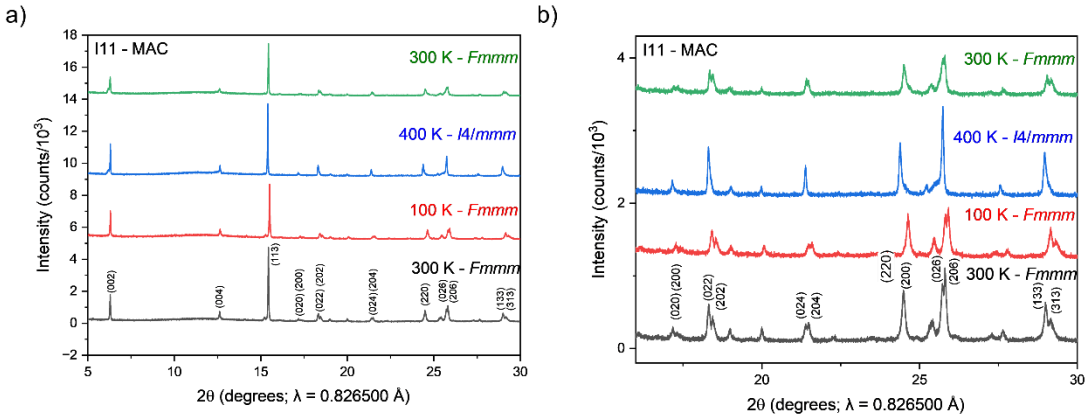


**Figure 3.19** a) Synchrotron PXRD patterns of $CsCo_{0.8}Ni_{1.2}Se_2$ carried out in the order of 300 K (bottom pattern in black), 100 K, 400 K, 300 K, showing the reversibility of the orthorhombic-to-tetragonal transition collected on the MAC detector, b) region between 15-30 degrees 2θ showing the characteristic peak splitting.

$CsCo_{0.8}Ni_{1.2}Se_2$ was also measured as a function of temperature using Synchrotron PXRD from 100 K to 300 K using the cryostream on the I11 beamline (Figure 3.20). The room temperature orthorhombic structure indexed on *Fmmm* cell is observed down to 100 K with no new emerging peaks. The temperature range is marked by a linear increase in unit cell parameters between 100-300 K.

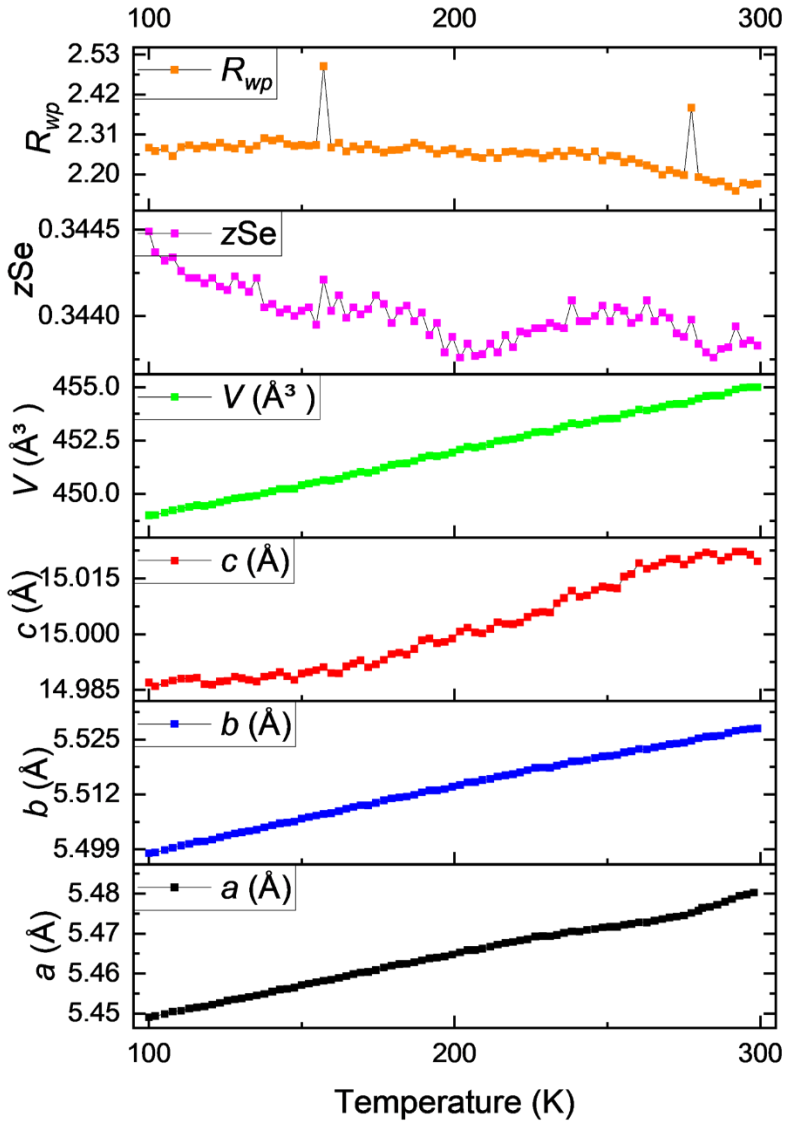


**Figure 3.20** Variable temperature SXRD of $CsCo_{0.8}Ni_{1.2}Se_2$ measured between 100-300 K.

$CsCo_{0.8}Ni_{1.2}Se_2$ was also measured upon heating during two beamtimes; first measurement was carried out between 300-900 K, and analysis of the PXRD patterns in the temperature region between 850-900 K suggested further splitting reflections, namely (022) and (113), shown in the contour plots in Figure 3.21.

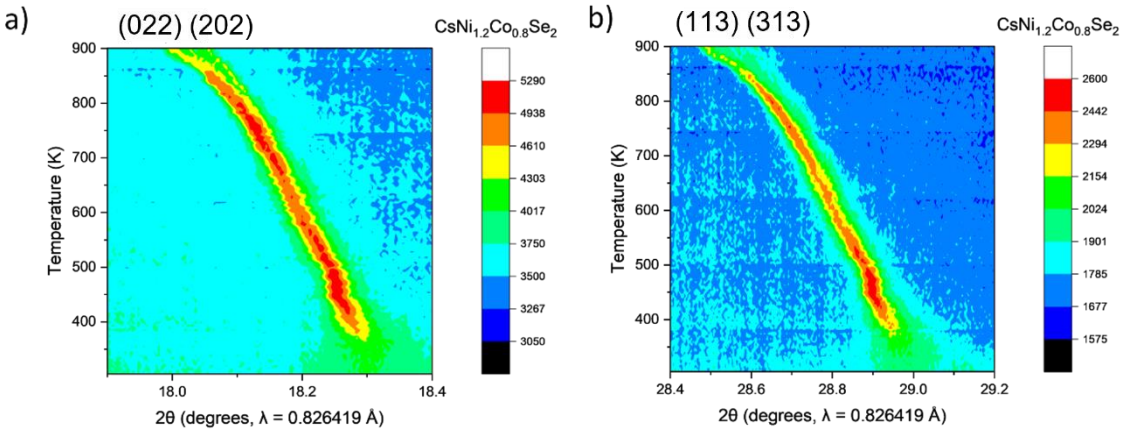


**Figure 3.21**: Contour plot of $CsCo_{0.8}Ni_{1.2}Se_2$ showing the evolution of a) (022) and (202) peaks between 300-900 K, b) (113) and (313) peaks between 300-900 K.

Therefore, a second variable temperature measurement on $CsCo_{0.8}Ni_{1.2}Se_2$ focusing on this region was conducted between 773-1073 K. The contour plots in Figures 3.22-24 show the evolution of the main peaks of the PXRD pattern, namely (002) and (022) (Figure 3.22), (200) and (116) (Figure 3.23), and comparison of (002), (004) and (006) peaks in Figure 3.24. Contour plots of other peaks, namely (110), (103), (114), and (213) can be found in Figures B.1 and B.2 in Appendix B. A number of new features emerge on various peaks, which will be described in this Section, but it is noteworthy that the behaviour could not be fully accounted for and further measurements are needed to understand the behaviour of the phase at elevated temperatures.

Figure 3.22 shows the evolution of (002) and (112) peaks between 300-900 K (a,c), and then 773-1073 K (b,d). In Figure 3.22b, it is visible that a new peak next to (002) emerges between 773-875 K at 6.3 degrees 2θ, and then disappears again. The trajectory of the (002) peak is also somewhat non-linear, as it shifts to higher angles between 300-350 K, where the structure undergoes a orthorhombic-to-tetragonal transition, then shifts to lower angles between 350-800 K, then again shifts to higher angles between 800-900 K before further shifting to lower angles up to 1073 K. These changes are marked by sudden drops in *c* lattice parameter between 300-350 K, and at 800-900 K, which could point to a new structural reorganisation, but further experiments are needed. The (112) peak shows similar non-linear trends between 850-900 K, where at ~885 K it starts shifting to higher

angles, coincidental with the change of shifting of the (002) peak. Figures 3.22c and d show that (112) peak shows some splitting in this temperature range (875-900 K), too.

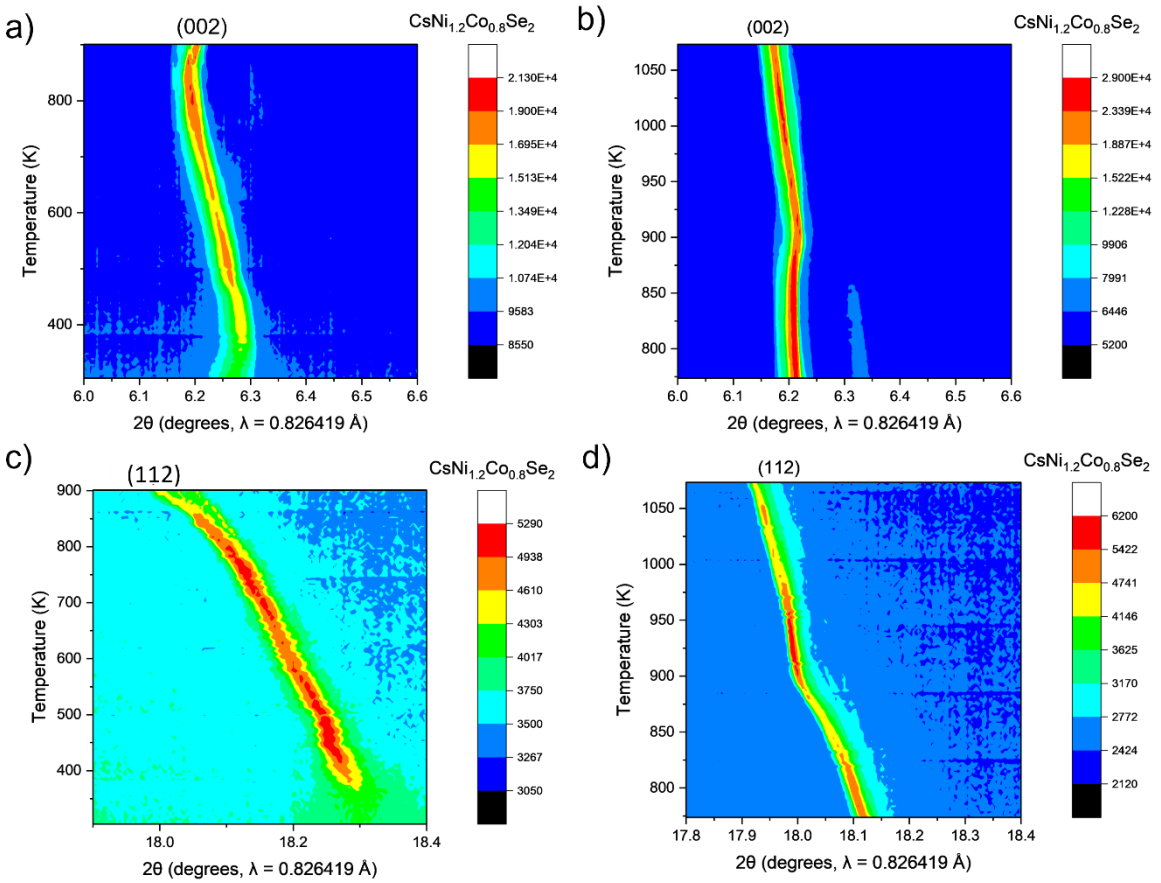


**Figure 3.22** Contour plot of $CsCo_{0.8}Ni_{1.2}Se_2$ showing the evolution of a) (002) peak between 300-900 K, and b) 773-1073 K, c) (112) peak between 300-900 K, and d) 773-1073 K.

Figure 3.23 shows the evolution of (200) and (116) peaks between 300-900 K (a,c), and then 773-1073 K (b,d). The (200) peak shows intriguing features; between 775-875 K it splits into two separate peaks, indicative of a new structural distortion, as (200) peak is not split in the orthorhombic structure of the room-temperature phase. The split peak then coalesces into one at 900 K, before splitting again at 1000-1073 K (Figure 3.23b). The behaviour of (200) peak suggests that a new structural distortion forms in the range between 775-875 K. Peak (116) splits into two peaks at 900 K and remains split up to 1073 K.

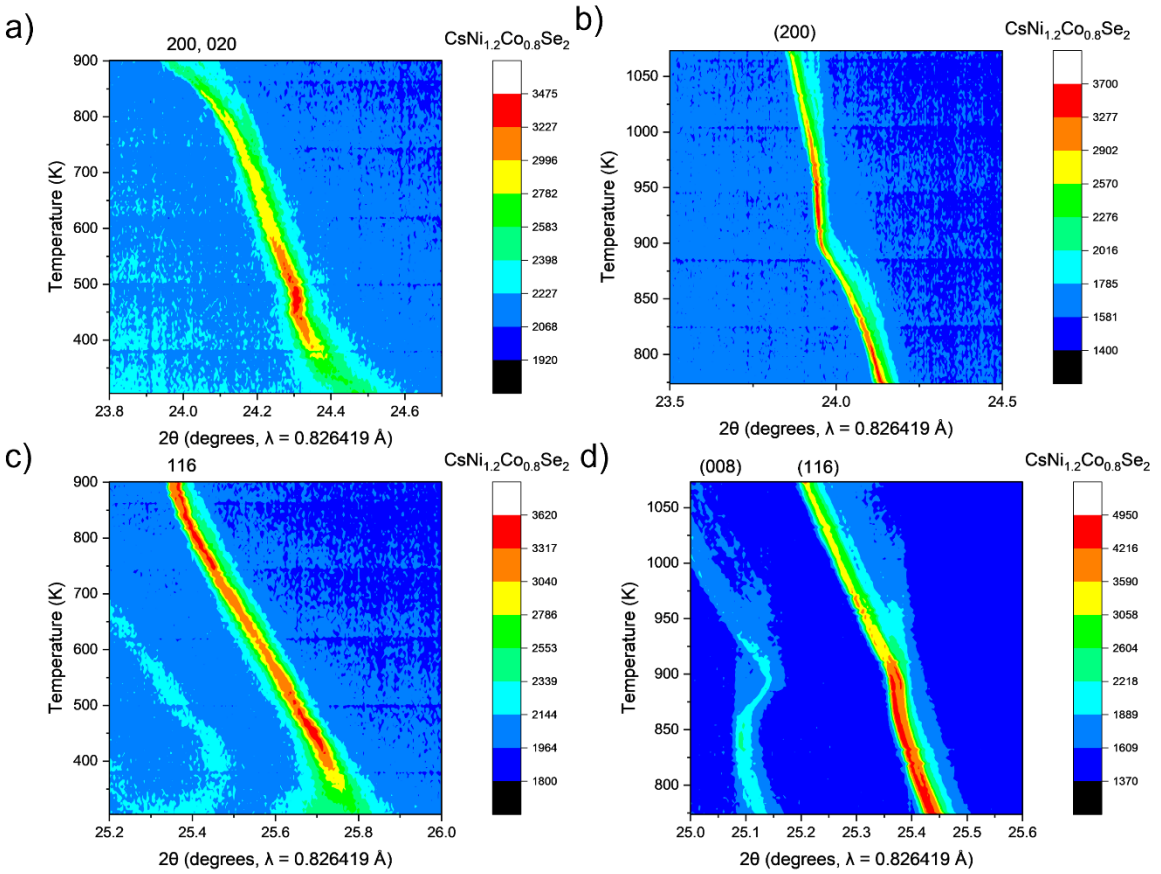


**Figure 3.23** Contour plot of $CsCo_{0.8}Ni_{1.2}Se_2$ showing the evolution of a) (110) peak between 300-900 K, b) (110) peak between 773-1073 K, c) (112) peak between 300-900 K, and d) (112) peak between 773-1073 K.

The 00*l* peaks, namely (002), (004), and (006), all show intriguing features between 773-1073 K; as was previously discussed, an onset of a new peak at slightly higher angle from (002) – at 6.35 degrees 2$\theta$ - emerges between 773-875 K, and then disappears again. A similar feature is shown in Figure 3.24b depicting the contour plot of the (004) peak, where a new peak at a slightly higher angle emerges at 13 degrees 2$\theta$ in the same temperature range and disappears by 875 K. In the case of (006) peak, it is found to split into two above 950 K (Figure 3.24c).

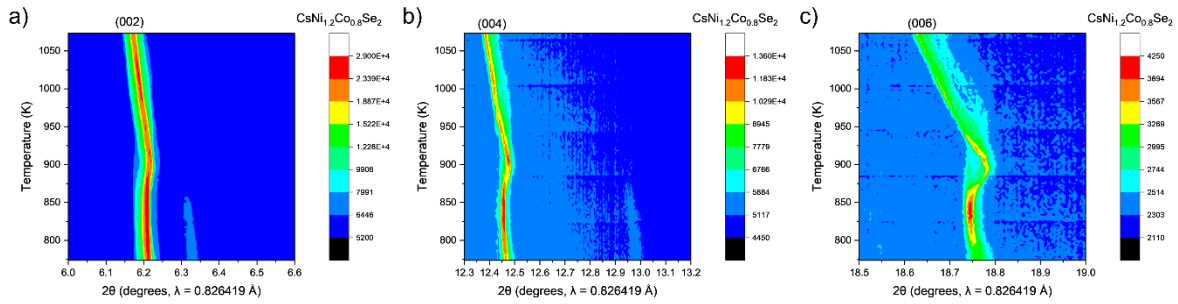


**Figure 3.24** Contour plot of $CsCo_{0.8}Ni_{1.2}Se_2$ showing the evolution of a) (002) peak between 773-1073 K, b) (004) peak between 773-1073 K, and c) (006) peak between 773-1073 K.

The fact that new peaks emerge at elevated temperatures suggests that a possible phase separation occurs, possibly due to varying Cs content and formation of vacancies along the stacking axis. Another possibility is that these peaks are satellite peaks arising from a form of incommensurate modulation, which is consistent with the non-linear behaviour of the 00*l* peaks. As these peaks emerge at high temperatures, it cannot be ruled out that there is a chemical change occurring (although these temperatures are below the synthesis temperature of the sample); a reaction with the glass capillary or a complex structural change are both possibilities and further experiments are needed to determine the origin of new peaks.

As the region around 900 K shows sudden changes in lattice parameters, a PXRD pattern at this temperature was measured on the MAC detector allowing for greater resolution (Figure 3.25). It shows the aforementioned additional peaks that emerge in $CsCo_{0.8}Ni_{1.2}Se_2$ at 773 K, marked by magenta asterisks, which were indexed on a smaller *I*4/*mmm* cell than the main phase. Lattice parameters of the two phases present are shown in Table 3.3. It is noteworthy that these are new peaks, not splitting of existent peaks. However, even though the secondary phase fits some of the new peaks, there are extra peaks that could not be indexed on this cell, namely at 17.3 and 23 degrees 2$\theta$, and other peaks are positioned too close to peaks of the main phase and thus appear as shoulders (peaks just next to 110 and 200 reflections), rendering them difficult to fit. It is therefore not entirely obvious what is happening in this temperature region without conducting further experiments. These would include collecting PXRD patterns on the MAC detector every 100 K between 100-900 K and

then back to 100 K to check for reversibility. Also, low-temperature electron microscopy experiment would be useful to probe whether a new secondary phase emerges at 773 K, and identifying the cell with certainty.

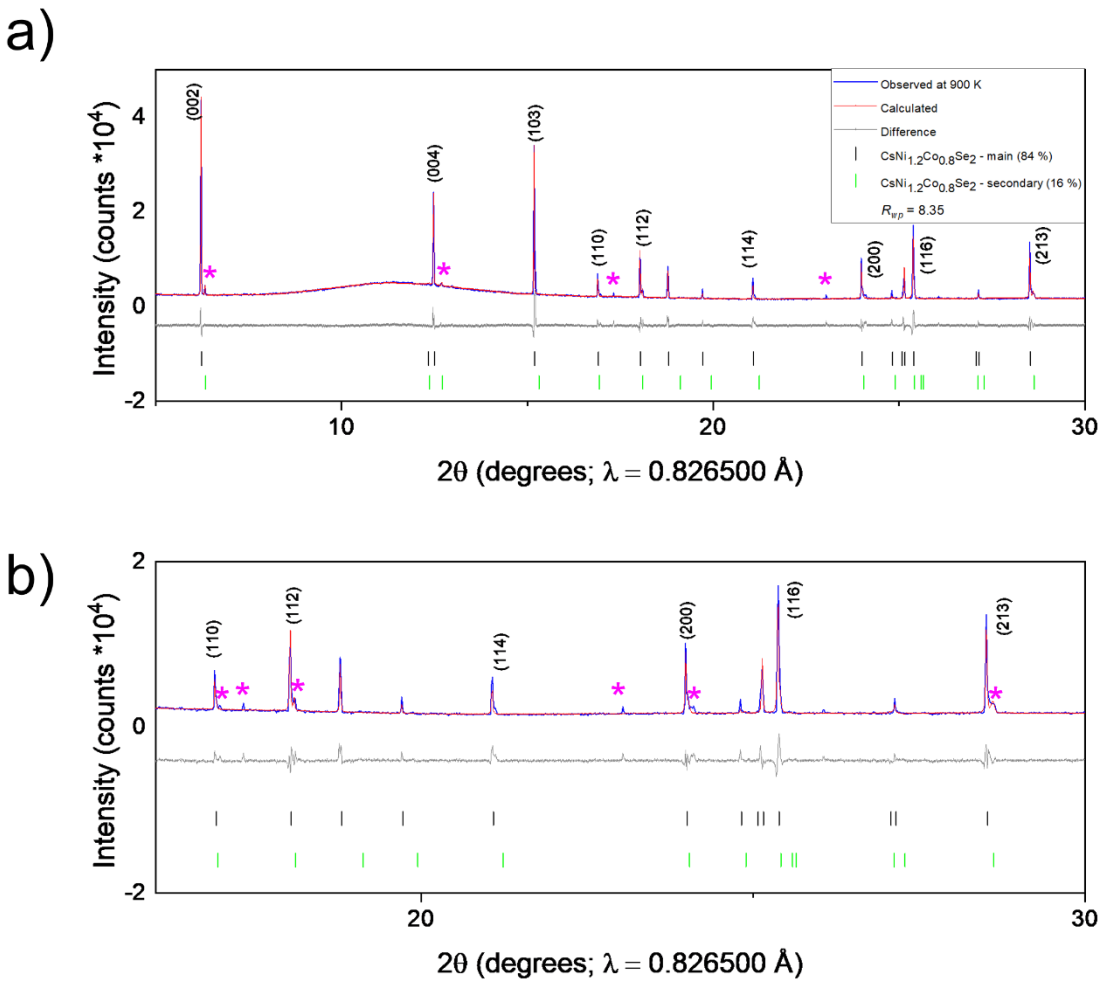


**Figure 3.25** a) Rietveld refinement of Synchrotron PXRD pattern of $CsCo_{0.8}Ni_{1.2}Se_2$ measured with the MAC detector at 900 K, showing the additional peaks of an apparent secondary $CsCo_{2-x}Ni_xSe_2$ phase with magenta asterisks, b) region of the pattern between 15-30 degrees $2\theta$ showing the additional peaks on 110, 112, 200, and 213 reflections and at 17.3, 23 degrees $2\theta$.

**Table 3.3** Lattice parameters of the two $CsCo_{2-x}Ni_xSe_2$ phases at 900 K present in the PXRD pattern shown in Figure 3.25.

| Lattice parameters | Main phase | Secondary phase |
|---|---|---|
| ***a* (Å)** | 3.9742(5) | 3.9679(5) |
| ***c* (Å)** | 15.1801(2) | 14.9263(2) |
| ***V* (Å$^3$)** | 239.752(6) | 235.001(6) |
| ***z*Se** | 0.3415(7) | 0.2914(7) |
| ***occ*Cs** | 0.85(1) | 0.85(1) |

The trends in lattice parameters *a* and *c* and the unit cell volume, *V*, of the main and secondary phase are shown in Figure 3.26. It is noteworthy that the lattice parameters of the two phases show opposite trends; lattice parameter *a* of the main phase increases linearly, while its lattice parameter *c* increases up to 860 K before dropping down again. The opposite is true for the lattice parameters of the secondary phase. Overall, the unit cell volume of the main phase increases linearly while the cell volume of the secondary phase begins dropping at 875 K.

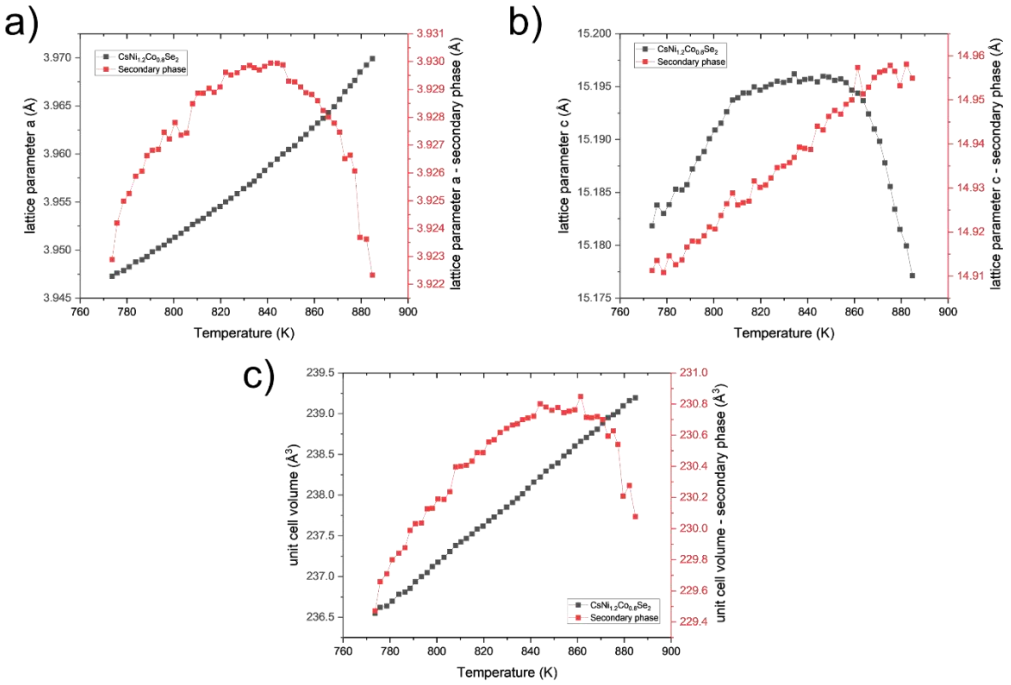


**Figure 3.26**: Variation of lattice parameter *a* (a), *c* (b), and unit cell volume (c) with temperature (773-885 K) in the 2-phase region of the phase diagram of $CsCo_{0.8}Ni_{1.2}Se_2$.

The emergence and subsequent disappearance of the new peak at 6.3 degrees 2$\theta$ between 763-1073 K is shown in Figure 3.27, marked by a magenta asterisk. This peak is indexed as (002) of the secondary phase. Only this peak is shown as other ones belonging to the secondary phase are of too small intensities to be easily visually discerned (they are marked in Figure 3.25 of the MAC scan).

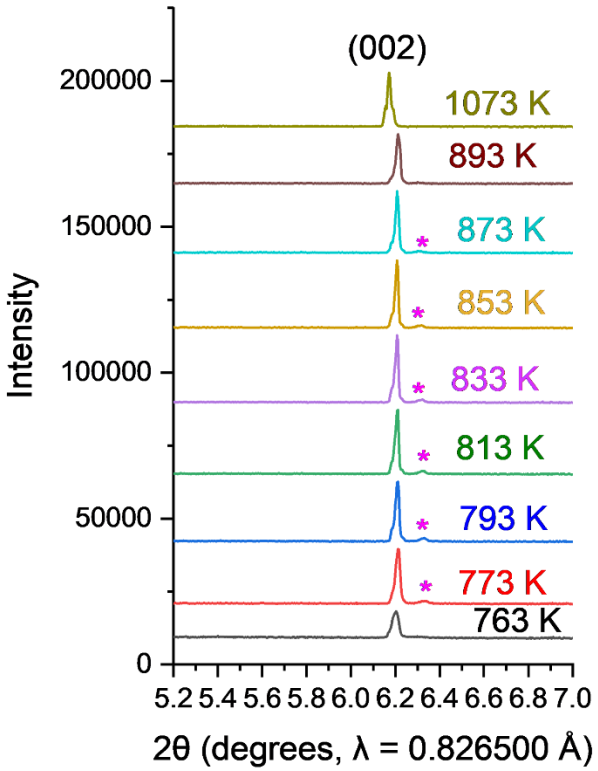


**Figure 3.27** Main (002) peak of $CsCo_{0.8}Ni_{1.2}Se_2$ between 763-1073 K showing the emergence of what is assumed to be a secondary phase with the main (002) peak marked by a magenta asterisk.

Figures 3.28a and b show the variation of *a*, *b*, and *c* lattice parameters of $CsCo_{0.8}Ni_{1.2}Se_2$ between 100-1073 K. There are three regions where the lattice parameters show non-linear features; lattice parameters *a* and *b* plateau between 285-300 K, then between 475-500 K *a* plateaus again, and between 900-950 K *a* increases at a greater gradient. Lattice parameter *c* shows two sudden decreases; first one between 300-375 K, which is where the transition from orthorhombic-to-tetragonal symmetry occurs, and second one at 875-900 K. In the region marked '2-phase region' in orange, the main phase (and the secondary phase, too) is indexed on the same tetragonal *I*4/*mmm* cell as in the blue region.

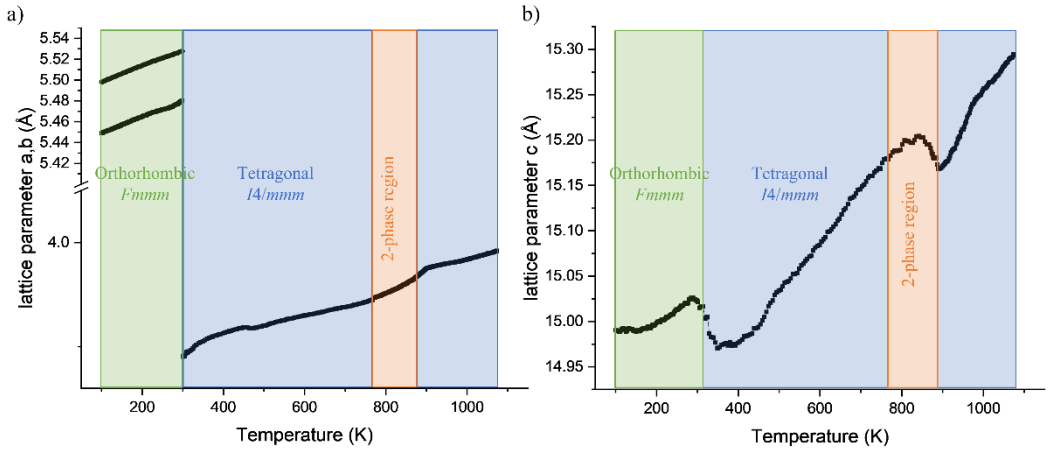


**Figure 3.28** Variation of lattice parameters *a* and *b* (a) and *c* (b) with temperature (100-1073 K) in $CsCo_{0.8}Ni_{1.2}Se_2$.

Figure 3.29 shows the variation of unit cell volume of $CsCo_{0.8}Ni_{1.2}Se_2$ between 100-1073 K. The variation is mostly linear, other than the plateau between 285-300 K.

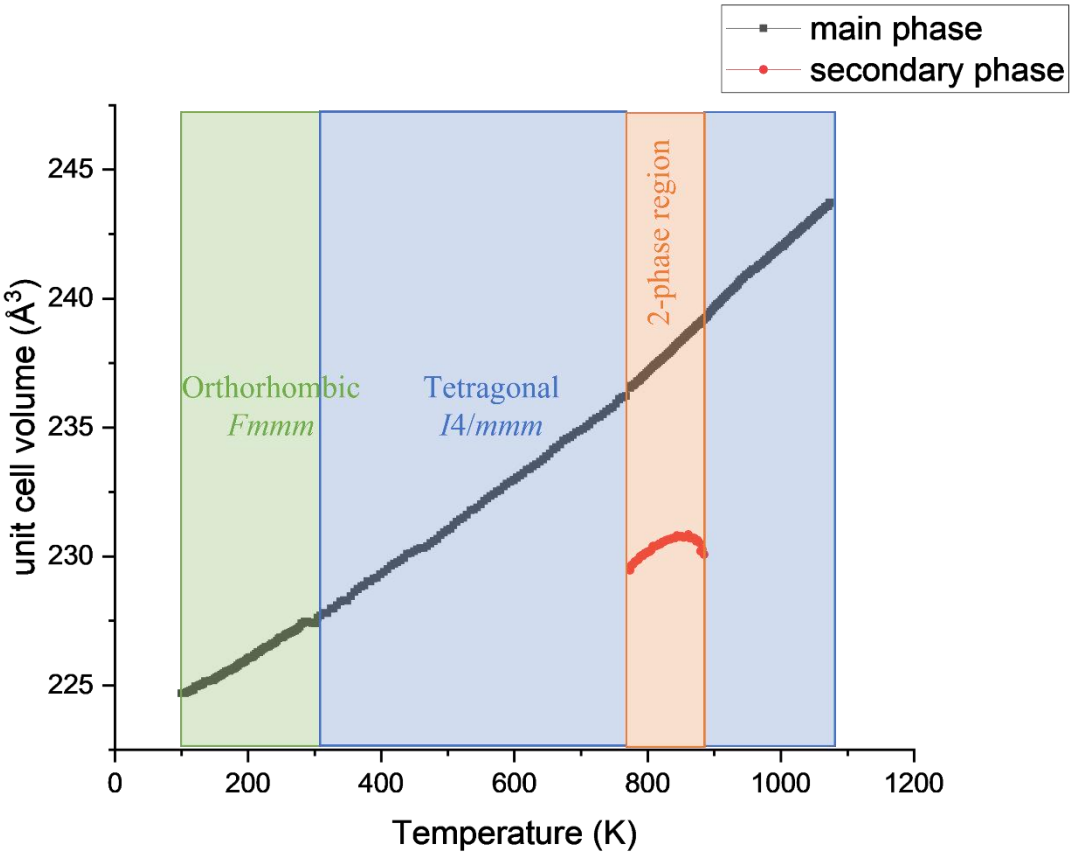


**Figure 3.29** Variation of unit cell volume with temperature (100-1073 K) in $CsCo_{0.8}Ni_{1.2}Se_2$ (black plot) and secondary phase which emerges between 773-885 K.

### *3.2.4 Magnetic structure of $ACo_{2-x}Ni_xSe_2$ (A = K, Rb, Cs)*

#### 3.2.4.1 Magnetometry of $KCo_{2-x}Ni_xSe_2$

As the end members of the solid solutions have differing reported magnetic behaviours ($KCo_2Se_2$ is a ferromagnetic metal,[3] and $KNi_2Se_2$ is a paramagnetic metal with a low temperature superconducting transition[4,9]), mapping out the changes in magnetic behaviour of $KCo_{2-x}Ni_xSe_2$ solid solution was carried out using magnetometry. Figure 3.30 shows the magnetic susceptibility, $\chi$, as a function of temperature for the seven non-stoichiometric samples of the solid solution and the two end members. This Figure shows the susceptibility data as normalised in terms of units, so that each $T_C$ and $T_N$ reach maximum at an arbitrary value of 1 (largest value is set at 1 in each case). This is done as a visual aid, as the change in magnetic susceptibilities (y axis) for ferromagnetic transitions are much larger than for the antiferromagnetic. Figure 3.31 shows the absolute values of magnetic susceptibility, $\chi$, as a function of temperature.

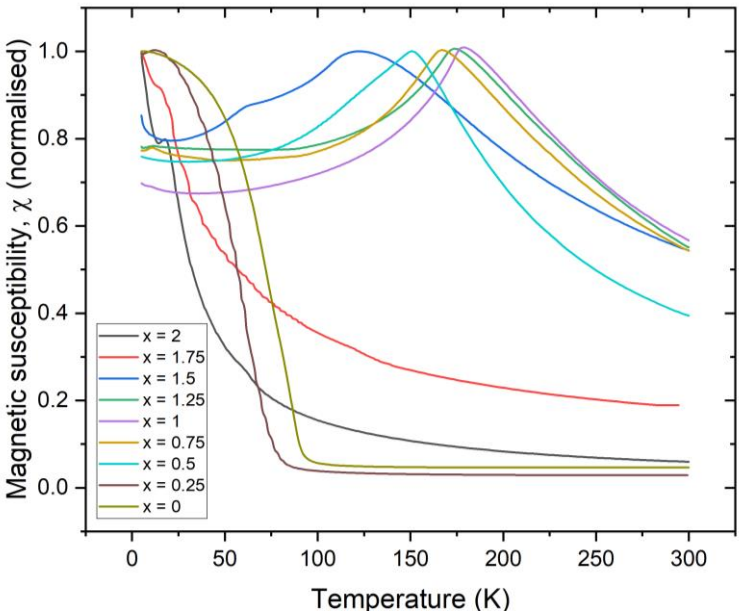


**Figure 3.30** Magnetic susceptibility (ZFC measurements) as a function of temperature for the series $KCo_{2-x}Ni_xSe_2$ ($0 \leq x \leq 2$) on a normalised scale.

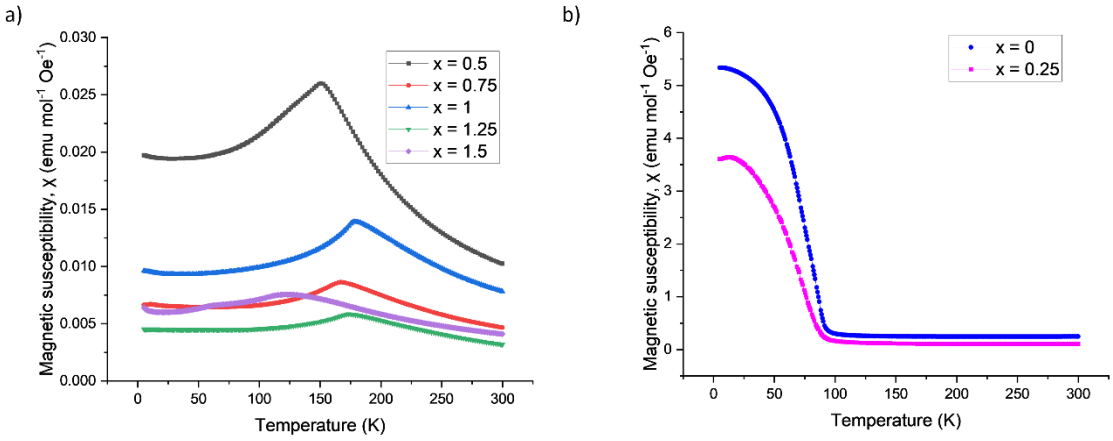


**Figure 3.31**: ZFC curves for a) antiferromagnetic members of $KCo_{2-x}Ni_xSe_2$ series ($0.5 \leq x \leq 1.5$), and b) ferromagnetic members of the series, i.e. $KCo_2Se_2$ (x = 0) and $KCo_{1.75}Ni_{0.25}Se_2$ (x = 0.25) shown in absolute values. Note the different scales.

At high Co contents in the $KCo_{2-x}Ni_xSe_2$ series ($0 \leq x \leq 0.25$), ferromagnetic behaviour is observed with $T_C$ ~ 90 K in the $KCo_2Se_2$ end member, diminishing to about 65 K for $x$ = 0.25. The low temperature magnetisation isotherms for the two ferromagnetic members – $x$ = 0 and 0.25 – are shown in Figure 3.32. Magnetisation saturates in these samples at $H$ ~ 2 T at $\mu_B$/Co = 1.15 and only increases slightly at higher fields.

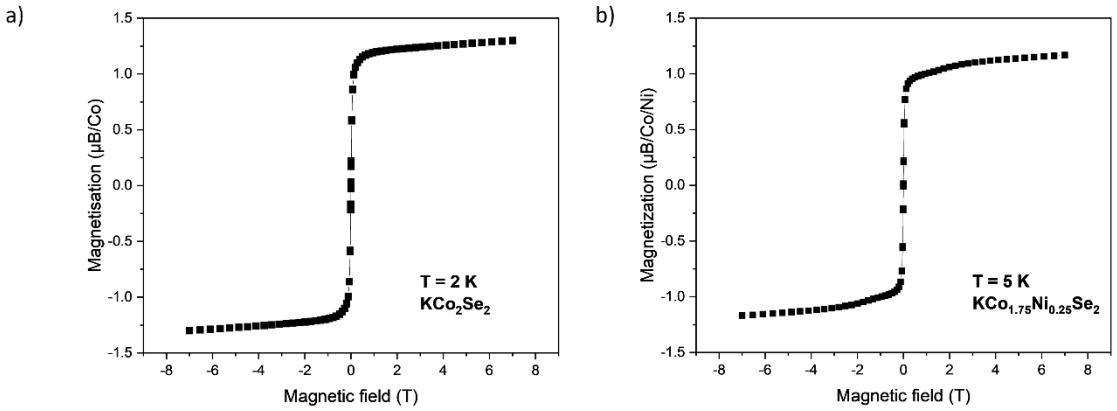


**Figure 3.32** Magnetisation isotherms for a) $KCo_2Se_2$ ($x$ = 0), and b) $KCo_{1.75}Ni_{0.25}Se_2$ ($x$ = 0.25) measured at 2 K and 5 K, respectively.

$KCo_{2-x}Ni_xSe_2$ for $0.5 \leq x \leq 1.5$ show antiferromagnetic behaviour. The Néel temperatures, $T_N$, as judged by the temperature of the susceptibility maximum, initially increase with increasing $x$, reach

a maximum value of 175 K at $x = 1$, and then decrease with increasing $x$. At high Ni contents: $1.5 < x \leq 2$, paramagnetic behaviour is observed down to low temperatures, and for x = 1.5, there is a rather broad transition. Figure 3.33 depicts a magnetic phase diagram for $KCo_{2-x}Ni_xSe_2$ constructed from magnetometry analysis, summarising the four magnetic regions in the solid solution. The superconducting region is not evident in our magnetometry data as the $T_c$ for $KNi_2Se_2$ is as low as 0.7 K, which is below the limits of the instrument used (MPMS-3).

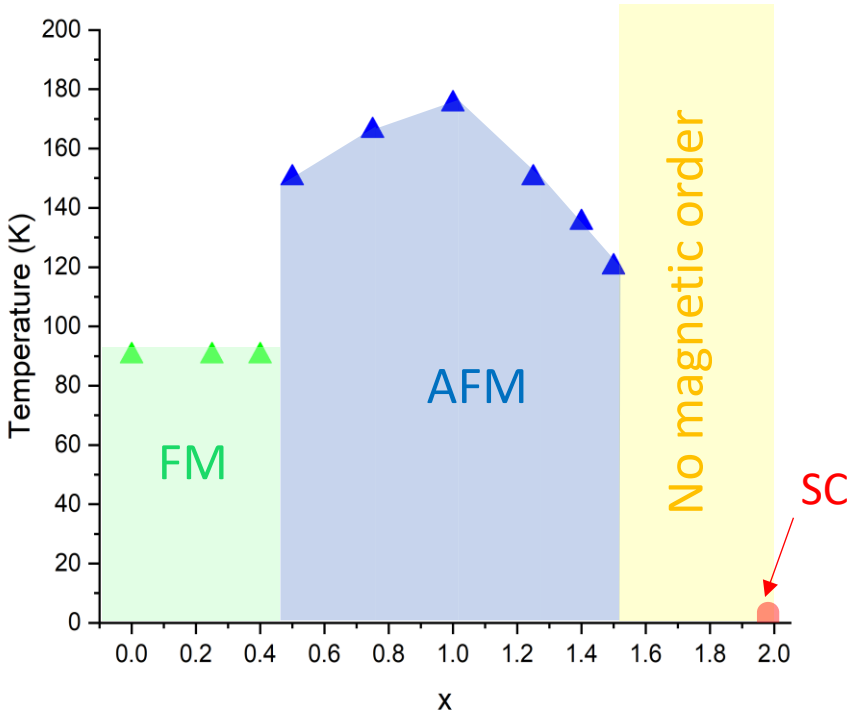


**Figure 3.33** Magnetic phase diagram for $KCo_{2-x}Ni_xSe_2$ ($0 \leq x \leq 2$); showing the ferromagnetic region (green), antiferromagnetic region (blue), paramagnetic region (yellow), and superconducting region (red).

Appendix C.1 shows the Curie-Weiss fits to selected antiferromagnetic members of this series. However, these compounds do not appear obey the Curie-Weiss law, and therefore the results should be interpreted with a level of caution.

### 3.2.4.2 PND of $KCo_{2-x}Ni_xSe_2$ ($x$ = 0.5, 1, 1.5)

Three antiferromagnetic members of the series, $KCo_{0.5}Ni_{1.5}Se_2$, $KCoNiSe_2$, and $KCo_{1.5}Ni_{0.5}Se_2$, were measured at ILL on the D2B beamline using PND to probe long-range magnetic order. Low temperature (3.5 K) PND measurements on $KCoNiSe_2$ (Figure 3.34) and $KCo_{1.5}Ni_{0.5}Se_2$ (Figure 3.35) revealed low angle (001), (003), and (005) Bragg reflections which are systematically absent for the nuclear structure, so must be of magnetic origin.

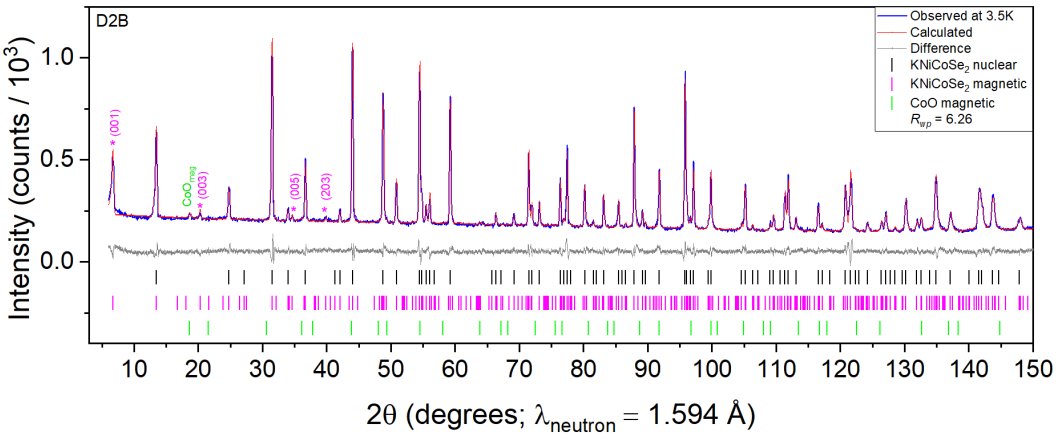


**Figure 3.34** Rietveld refinement of $KCoNiSe_2$ against PND data measured at 3.5 K, $R_{wp}$ = 6.26% and $\chi^2$ = 1.83, with magenta asterisks denoting magnetic Bragg peaks.

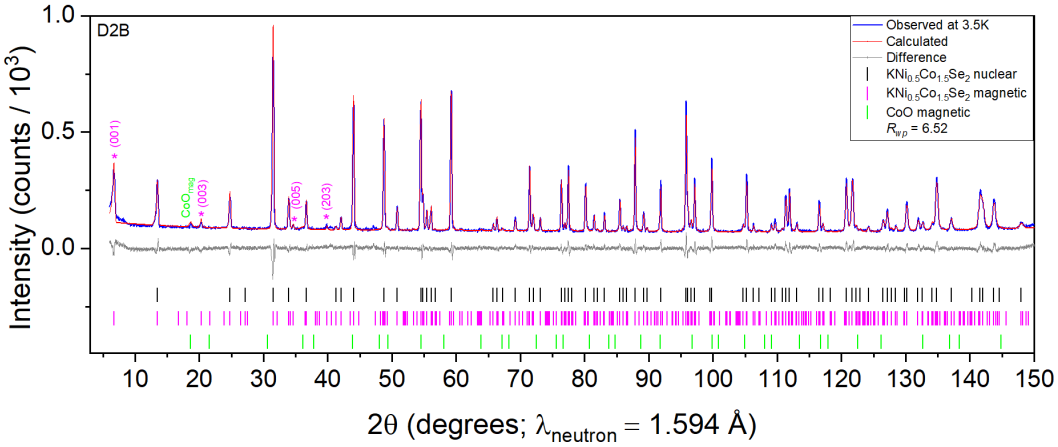


**Figure 3.35** Rietveld refinement of $KCo_{1.5}Ni_{0.5}Se_2$ against PND data measured at 3.5 K, $R_{wp}$ = 6.52% and $\chi^2$ = 2.08, with magenta asterisks denoting magnetic Bragg peaks.

In the Ni-rich phase $KCo_{0.5}Ni_{1.5}Se_2$ these reflections were not evident, and the only extra scattering at low temperature arose from the presence of a magnetic peak for CoO (Figure 3.36). It is noteworthy that in magnetometry measurements, $KCo_{0.5}Ni_{1.5}Se_2$ was shown to exhibit a broader

susceptibility maximum than the other samples showing a peak due to antiferromagnetic order (Figure 3.30).

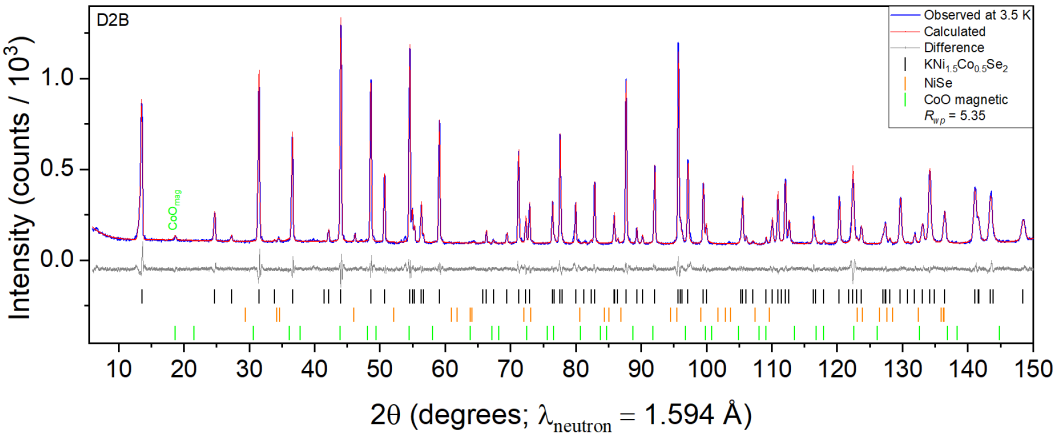


**Figure 3.36** Rietveld refinement of $KCo_{0.5}Ni_{1.5}Se_2$ against PND data measured at 3.5 K, $R_{wp}$ = 5.35% and $\chi^2$ = 2.00.

The magnetic scattering of $KCoNiSe_2$ and $KCo_{1.5}Ni_{0.5}Se_2$ at 3.5 K was indexed using a $\sqrt{2}a \times \sqrt{2}a \times c$ expansion of the nuclear unit cell ((½ ½ 0) propagation k-vector). Initially no symmetry constraints were applied to the magnetic structure, *i.e*. it was initially analysed in *P*1 symmetry, but it was found that a single magnetic mode, mM5−, was found to account for all magnetic peaks of the structure at 2θ = 6.75° (001), 20.07° (003), 34.63° (005), and 39.95° (203) (*hkl* values refer to the expanded cell), which corresponds to ferromagnetic coupling between Co/Ni ions within the $(Co/Ni)_2Se_2$ sheets and an antiferromagnetic interaction between the adjacent $(Co/Ni)_2Se_2$ sheets along the stacking axis. The magnetic-plus-nuclear structure can be described with the orthorhombic space group *Cmcm* (63.468 in the Belov–Neronova–Smirnova (BNS) scheme), as opposed to the tetragonal symmetry (*I*4/*mmm*) of the nuclear-only structure of the $KCo_{2-x}Ni_xSe_2$ series. The magnetic and nuclear model of $KCoNiSe_2$ and $KCo_{1.5}Ni_{0.5}Se_2$ is shown in Figure 3.37. The room-temperature PND patterns for the three studied antiferromagnetic members of the series are shown in Appendix D (Figures D.1-3).

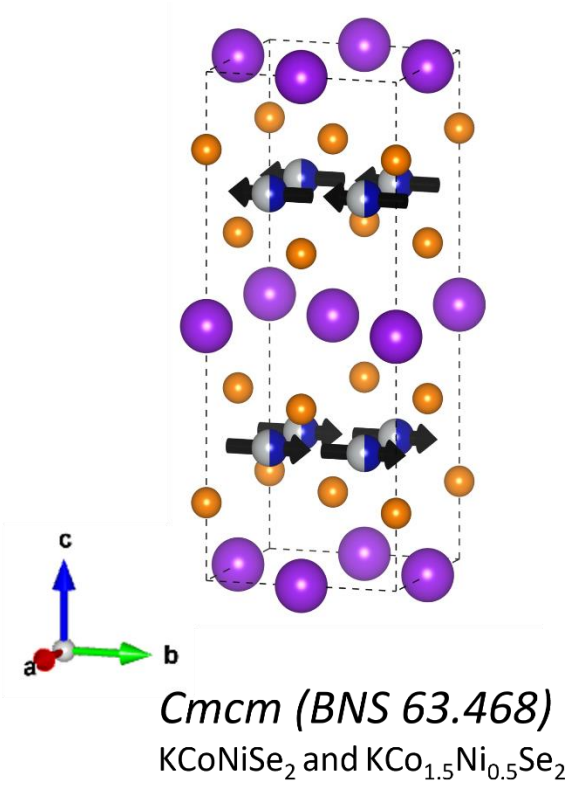


**Figure 3.37** Magnetic plus nuclear structure for $KCoNiSe_2$ and $KCo_{1.5}Ni_{0.5}Se_2$, with ferromagnetic coupling of Co/Ni moments in the ab plane and antiferromagnetic coupling of Co/Ni moments along the stacking axis.

In order to investigate whether a reduction in symmetry of the nuclear structure below the magnetic ordering transition was observable, we measured high-resolution synchrotron PXRD patterns of $KCoNiSe_2$ at 300 K and 100 K and the (200) peak of the *I*4/*mmm* structural cell was fitted with a FWHM (full width at half maximum) of 0.09951(2)° and 0.09202(1)° extracted at 100 K and 300 K, respectively, resulting in a broadening of 0.00749° at low temperatures (Figures 3.38(a,b)). The peak broadening of other peaks, namely 112 (Figures 3.38(c,d)) and 213 (Figures 3.38(e,f)), was calculated to be 0.00558(2)° and 0.0156(1)° at 100 K, respectively. However, the X-ray data are best fit with a tetragonal structural model, and there is no clear evidence for a structural distortion even using a high-resolution diffractometer, although the arrangement of magnetic moments is not tetragonal and needs to be described by the orthorhombic model. It is relatively common for this to be the case whereby subtle distortions cannot be observed within experimental resolution and the magnetostriction is not sufficient enough for peak-splitting to be observed.

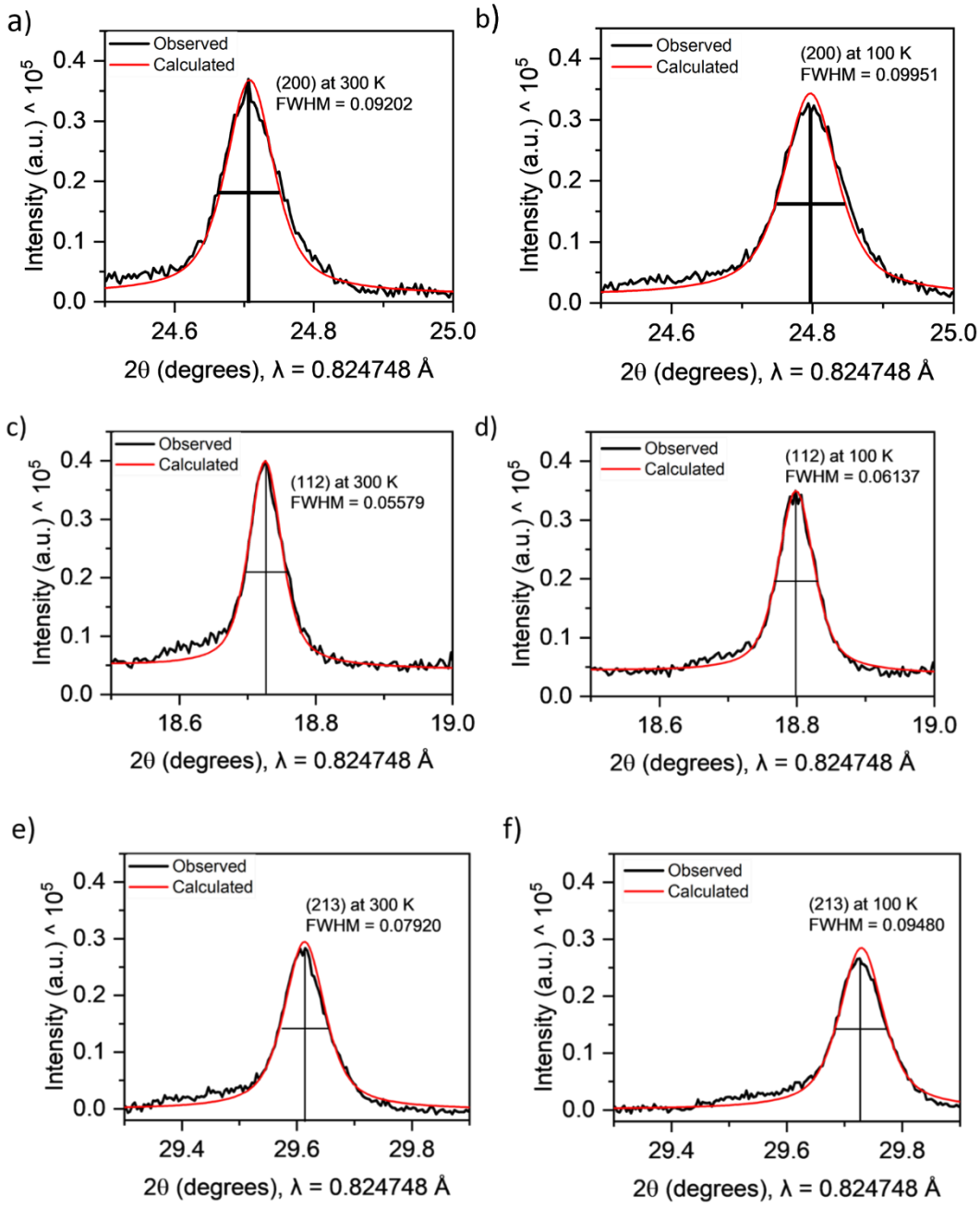


**Figure 3.38** Full width at half maximum (FWHM) calculation of the Gaussian fit of a) 200 peak at 300 K and b) 100 K, c) 112 peak at 300 K and d) 100 K, e) 213 peak at 300 K and f) 100 K. The high-resolution data were collected on instrument I11 at Diamond Light Source.

In the refinements in Figures 3.34-3.36 we refined a nuclear model in *I*4/*mmm* and a separate magnetic model containing just the transition metal moments with symmetry *Cmcm*, but with a metrically tetragonal $\sqrt{2}a \times \sqrt{2}a \times c$ expansion of the nuclear unit cell. Thus, separate tick-marks

show the reflections from the nuclear model and the magnetic model in Figures 3.34 and 3.35. The refined magnetic structure is A-type antiferromagnetic with ferromagnetic coupling of Co/Ni moments within the *ab* plane and the planes coupled antiferromagnetically along the *c* axis (Figure 3.37). The magnetic anisotropy is consistent with the changes of lattice parameters observed at low temperatures described in Section 3.2.3.2; lattice parameter *a* contracts faster below $T_N$, and *c* remains approximately flat below $T_N$ instead of undergoing continued thermal contraction. The likely mechanism for ferromagnetic coupling in the *ab* plane is direct exchange as $d_{T\text{-}T}$ is 2.74 Å, which is comparable to that observed in the elemental metals ($d_{Co\text{-}Co}$ = 2.51 Å in Co metal). The interlayer *T*–*T* distance is too large for any direct interaction. Antiferromagnetic coupling between planes has been proposed to operate via the RKKY mechanism via conduction electrons in this series of metallic compounds,[6,19,20] which is sensitive to the nature of the interlayer electropositive ion, the nature of the band structure, influenced strongly by the electron count, and the interlayer separation. The refined long-range ordered moment of Co/Ni ions in $KCoNiSe_2$ is 1.18 $\mu_B$, while in $KCo_{1.5}Ni_{0.5}Se_2$ it is 1.07 $\mu_B$. The small localised moments are consistent with other electrons being mobile conduction electrons giving rise to metallic behaviour (see resistivity data in Section 3.2.7). As no superstructure peaks were observed from PND data above the magnetic transition, the Ni and Co ions, with very different neutron scattering lengths, must be disordered in the $(Co/Ni)_2Se_2$ layers. PND patterns measured at room temperature of these phases are shown in Figures D.1-3 in Appendix D.

Our magnetometry results confirm ferromagnetic order below 90 K in $KCo_2Se_2$ (Figures 3.31 and 3.32). There were no additional reflections observed for $KCo_2Se_2$ in the PND pattern measured at 3.5 K (Figure 3.39). Inclusion of ferromagnetically arranged moments on the Co ions along *a* axis in a magnetic phase (Figure 3.40) similar to that reported for $RbCo_2Se_2$ from single crystal neutron diffraction suggested a similar small ferromagnetic moment of 0.6(1) $\mu_B$ per Co, although this small moment is at the edge of what could be measured from our data. As Co is replaced by Ni, there is evidently a changeover in the coupling between layers from ferromagnetic to antiferromagnetic, and this is presumably mainly a consequence of the increasing electron count.

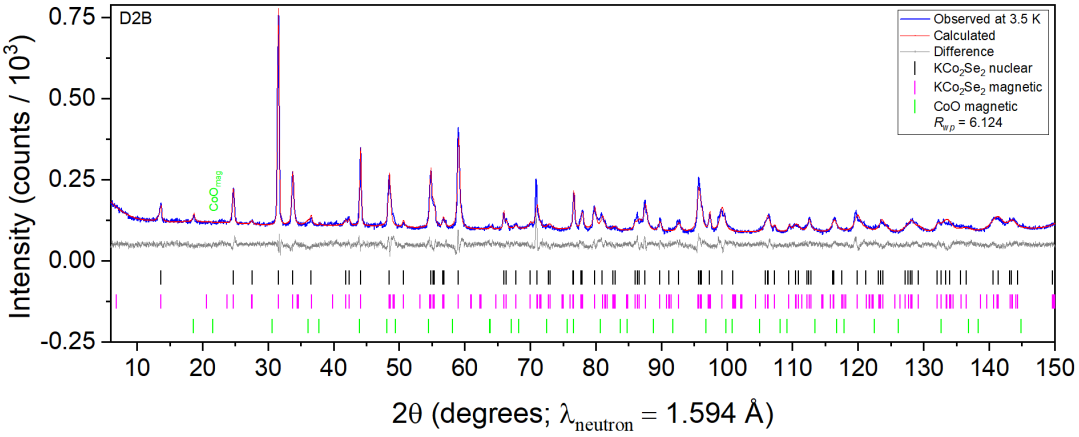


**Figure 3.39** Rietveld refinement of $KCo_2Se_2$ against PND data measured at 3.5 K, $R_{wp}$ = 6.12% and $\chi^2$ = 1.80.

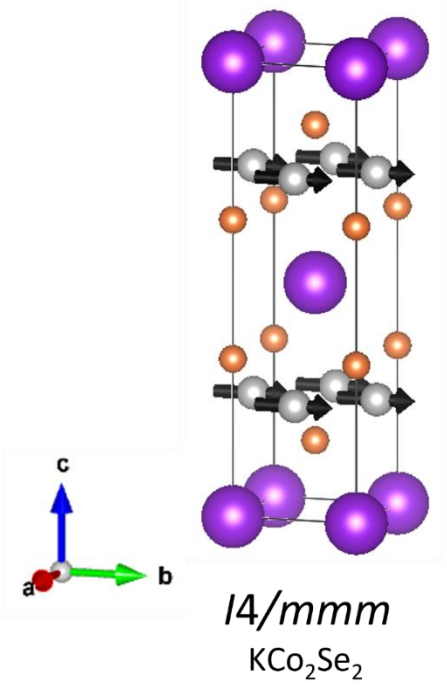


**Figure 3.40** Magnetic structure of $KCo_2Se_2$ (magnetic moments are aligned along the *a* axis).

### 3.2.4.2.1 Variable temperature PND of $KCoNiSe_2$

The magnetic susceptibility data for this compound suggested that the onset of long-range magnetic ordering was at approximately 175 K. To probe this further, low temperature PND was used. The PND patterns at selected temperatures between 3.5 K to 300 K are shown in Figure 3.41. The magnetic Bragg peaks with highest intensity, namely the (001) peak, begins to appear at 150 K,

which is the first dataset collected below the $T_N$ (above $T_N$ there is enough thermal energy in the system to overcome magnetic coupling). Rest of the peaks, namely (003), (005), and (203) peaks, are only visible at 3.5 K due to their low intensities as the magnetic form factor falls off faster than X-ray form factor, and therefore only the low $2\theta$ (or d-spacing) Bragg peaks are visible in a PND pattern.

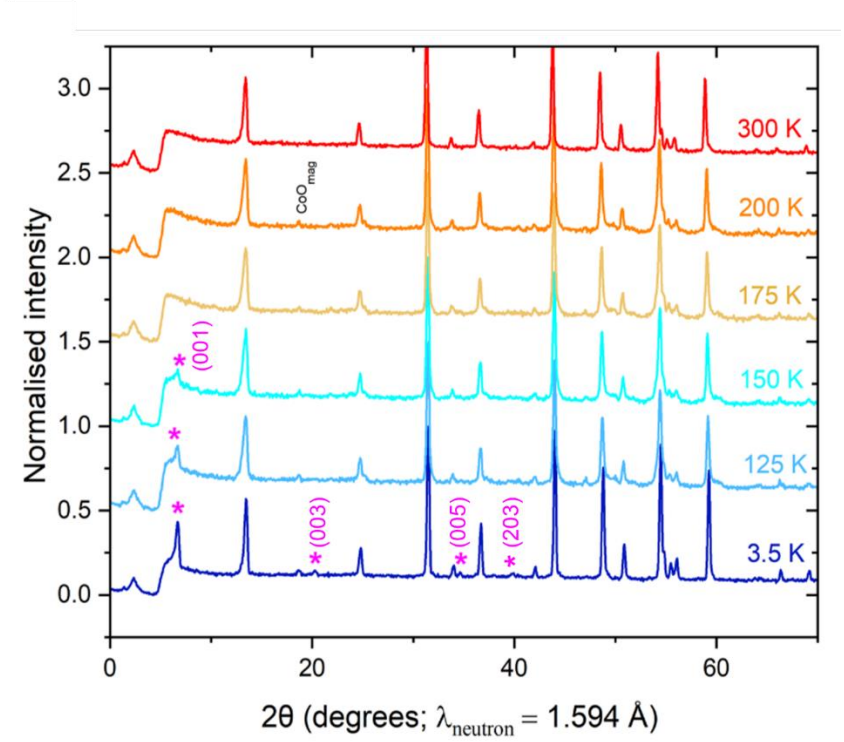


**Figure 3.41** Variable temperature PND of $KCoNiSe_2$ measured between 3.5 K and 300 K showing the appearance of magnetic Bragg peaks (magenta asterisks) below $T_N$.

### 3.2.4.3 Magnetometry of $RbCo_{2-x}Ni_xSe_2$

In the case of the $RbCo_{2-x}Ni_xSe_2$ solid solution, only the Co-end member was previously reported in the literature. $RbCo_2Se_2$ is a ferromagnet below 75 K with an ordered moment of 0.60(4) $\mu_B$ per Co ion aligned along the *a* axis,[7] which was determined from neutron diffraction. On the other hand, the Ni-end member – $RbNi_2Se_2$ – is not a reported phase and its magnetic properties were not previously determined. Again, mapping out the changes in magnetic behaviour of $RbCo_{2-x}Ni_xSe_2$ solid solution was carried out using magnetometry. Figure 3.42 shows the magnetic susceptibility, $\chi$, as a function

of temperature for the seven non-stoichiometric samples of the solid solution on a normalised scale (a) and absolute scale (b).

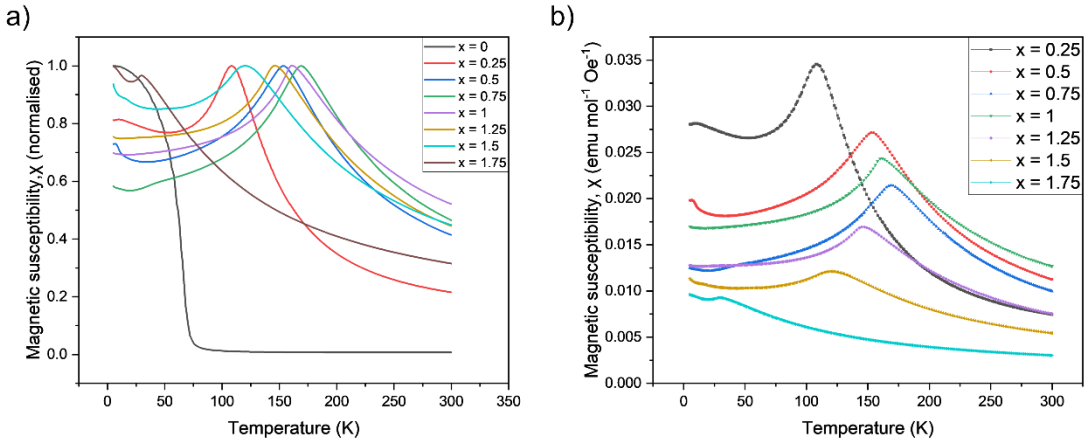


**Figure 3.42 a)** Magnetic susceptibility (ZFC measurements, normalised) as a function of temperature for the series $RbCo_{2-x}Ni_xSe_2$, $0 \leq x \leq 1.75$, b) ZFC measurements with their absolute values.

At high Co contents in the $RbCo_{2-x}Ni_xSe_2$ series ($0 \leq x \leq 0.25$), ferromagnetic behaviour is observed with $T_C$ ~ 75 K in the $RbCo_2Se_2$ end member. The ZFC-FC plot and the low temperature magnetisation isotherm for the ferromagnetic member – $x = 0$ – are shown in Figure 3.43(a,b). The ferromagnetic region only extends between $0 \leq x < 0.25$, as antiferromagnetic coupling of spins becomes dominant at x = 0.25.

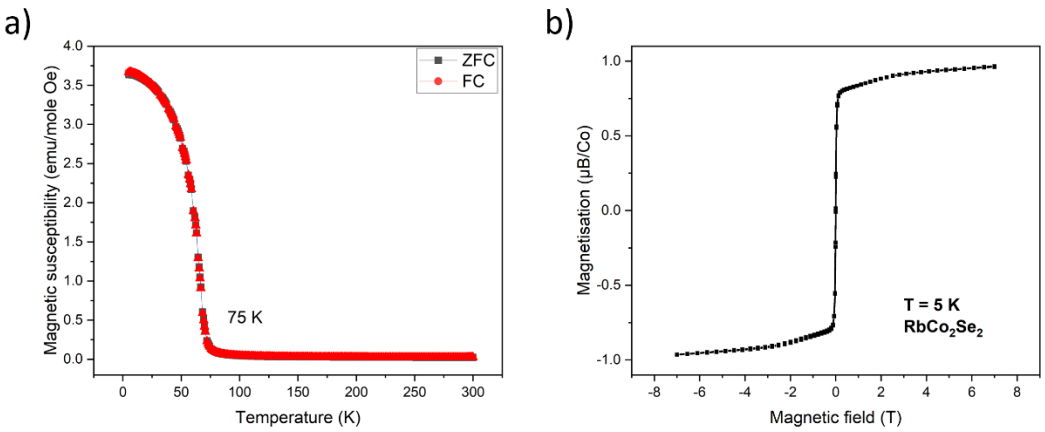


**Figure 3.43** a) ZFC-FC plot of $RbCo_2Se_2$ measured at 1000 Oe, b) Magnetisation isotherm measured at 5 K.

$RbCo_{2-x}Ni_xSe_2$ for $0.25 \leq x \leq 1.75$ show antiferromagnetic behaviour. The Néel temperatures, $T_N$, as judged by the temperature of the susceptibility maximum, initially increase with increasing $x$, reach a maximum value of 162 K at $x = 0.75$, and then decrease with increasing $x$ (Figure 3.42). At high Ni contents: $1.75 < x \leq 2$, no long-range magnetic ordering is observed down to low temperatures (Figure 3.44). $RbNi_2Se_2$ was found not to order magnetically down to 2 K, although related compounds, including $KNi_2Se_2$ show a superconducting transition below 2 K,[4,8] therefore further measurements at lower temperatures may reveal similar behaviour. The ZFC part of the ZFC-FC plot features a broad transition at ~150 K (Figure 3.44a) while the magnetisation isotherm shows no saturation of moments at 7 T (Figure 3.44b). This magnetic behaviour is reminiscent of the x = 1.5 member of the K-analogous solid solution - $KCo_{0.5}Ni_{1.5}Se_2$ – which features a broad transition at ~120 K and PND revealed no long-range order of magnetic moments, despite the broad transition observed in the magnetometry data (Figure 3.30).

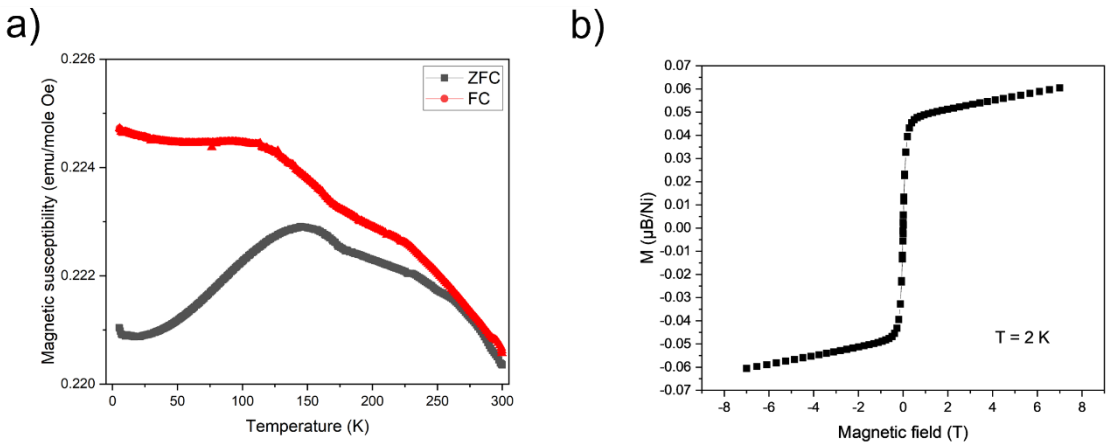


**Figure 3.44** a) ZFC-FC plots of $RbNi_2Se_2$ measured at 1000 Oe, b) Magnetic isotherm for $RbNi_2Se_2$ measured at 2 K.

The sample of $RbNi_2Se_2$ contained trace amounts of ferromagnetic NiSe from PXRD (1%), and this is also obvious from its *M vs H* plot (Figure 3.45a), which has a large initial gradient at low field before levelling off at high field. The presence of ferromagnetic impurity also accounts for the divergence of ZFC and FC curves. A high-field subtraction was performed for $RbNi_2Se_2$ to give an intrinsic magnetic susceptibility by effectively eliminating the contribution from the impurity, and

producing a FC susceptibility which should be a more correct representation of the magnetic susceptibility of the sample. Figure 3.45b shows the subtraction as a flat line, which is typical for a Pauli paramagnetic metal. The value of the magnetic susceptibility (~ 0.0014 emuOe$^{-1}$mol$^{-1}$), which is an order of magnitude lower compared to the antiferromagnetic members of the series.

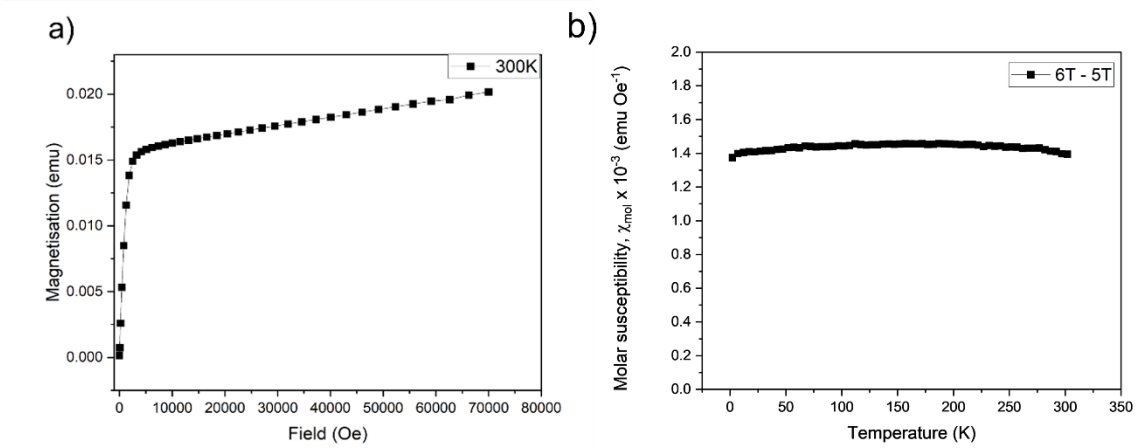


**Figure 3.45** a) Mv H plot for $RbNi_2Se_2$ measured at 300 K. b) Field-cooled magnetic susceptibility of $RbNi_2Se_2$, measured using a 6 – 5 T subtraction.

Figure 3.46 depicts a magnetic phase diagram for $RbCo_{2-x}Ni_xSe_2$ constructed from magnetometry analysis, summarising the four magnetic regions in the solid solution.

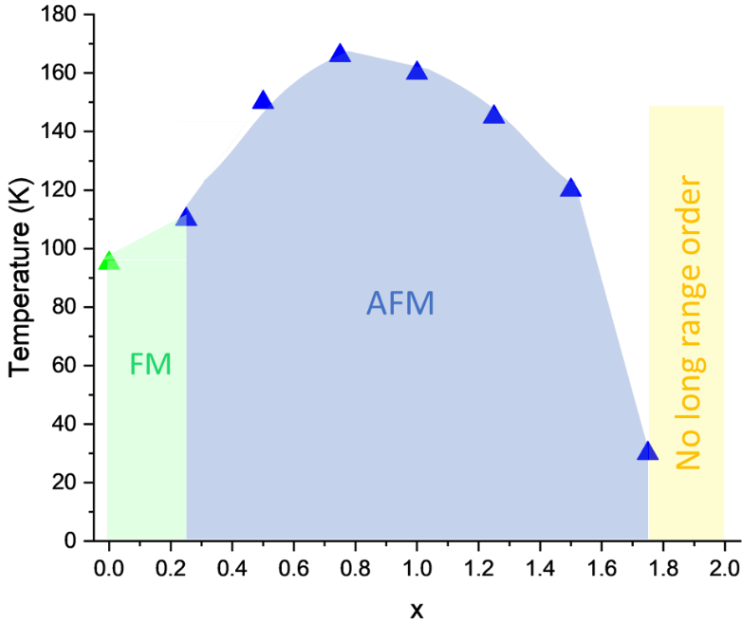


**Figure 3.46** Magnetic phase diagram for $RbCo_{2-x}Ni_xSe_2$ ($0 \leq x \leq 2$); showing the ferromagnetic region (green), antiferromagnetic region (blue), and paramagnetic region (yellow).

Appendix C.2 shows the Curie-Weiss fits to selected antiferromagnetic members of this series. Again, as these compounds do not appear to obey the Curie-Weiss law, the results should be interpreted with a level of caution.

### 3.2.4.4 Magnetometry of $CsCo_{2-x}Ni_xSe_2$

Unlike in the K- and Rb-analogous solid solutions, the Co-end member - $CsCo_2Se_2$ – shows A-type antiferromagnetic order below 66 K from PND, and magnetometry reveals metamagnetism and a transition to a presumably fully ferromagnetic state above 3 T.[3,22] For the *A* = K, Rb, Cs series, these results suggest that for the Co end members, increasing the interlayer separation favours an antiferromagnetic arrangement of adjacent ferromagnetic planes. $CsNi_2Se_2$ is paramagnetic with a low temperature superconducting transition at 2.7 K, similar to the K-analogue.[22] Again, mapping out the changes in magnetic behaviour of $CsCo_{2-x}Ni_xSe_2$ solid solution was carried out using magnetometry. Figure 3.47 shows the normalised magnetic susceptibility, $\chi$, as a function of temperature for the seven non-stoichiometric samples of the solid solution. Figure 3.48 shows the absolute values of magnetic susceptibilities. The end members are not shown, as they were not synthesised in this work.[8,22]

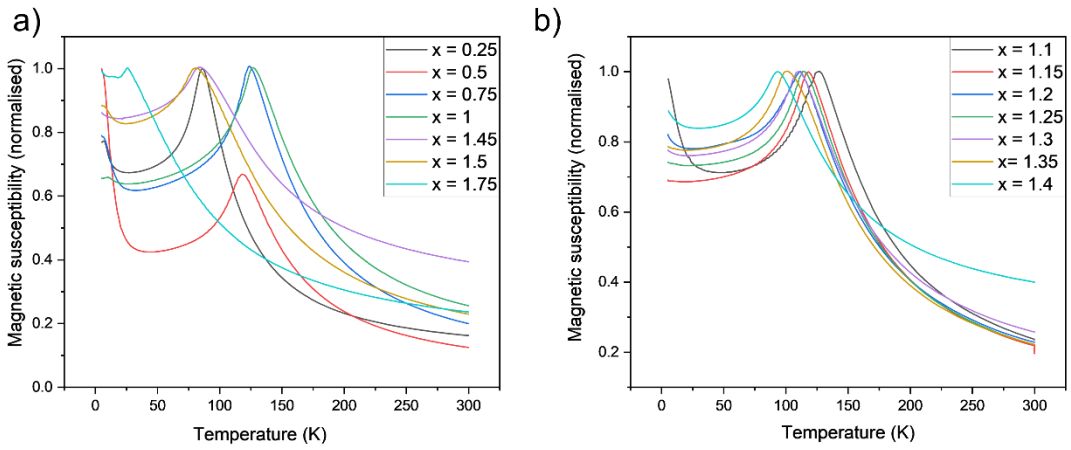


**Figure 3.47 a)** Magnetic susceptibility (normalised ZFC measurements) as a function of temperature for the tetragonal members of $CsCo_{2-x}Ni_xSe_2$ series ($0.25 \leq x \leq 1$, $1.45 \leq x \leq 1.75$), b) Magnetic susceptibility (normalised ZFC measurements) as a function of temperature for the orthorhombic members of $CsCo_{2-x}Ni_xSe_2$ series ($1.1 \leq x \leq 1.4$).

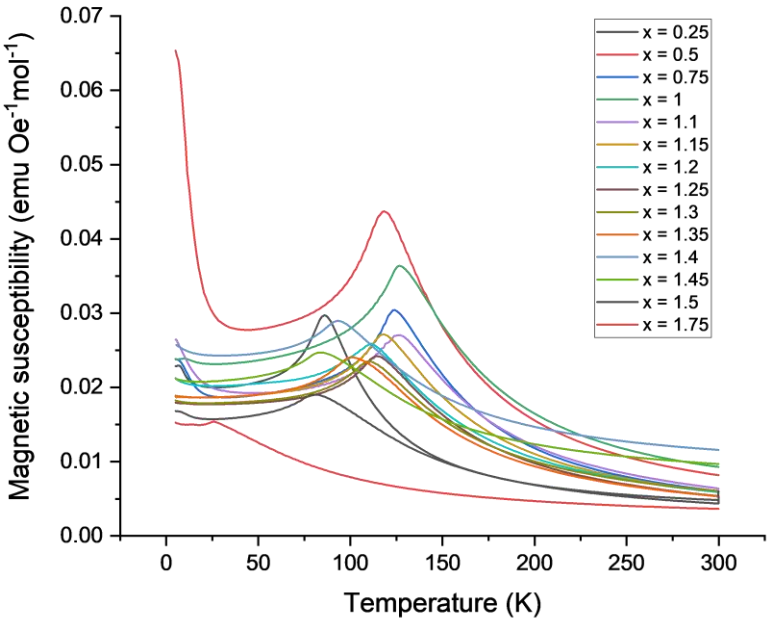


**Figure 3.48** Magnetic susceptibility (ZFC measurements, absolute values) as a function of temperature for all members of $CsCo_{2-x}Ni_xSe_2$ series ($0.25 \leq x \leq 1.75$).

$CsCo_{2-x}Ni_xSe_2$ for $0 \leq x \leq 1.75$ show antiferromagnetic behaviour. The Néel temperatures, $T_N$, as judged by the temperature of the susceptibility maximum, initially increase with increasing $x$, reach a maximum at $x = 1$, and then decrease with increasing $x$. At high Ni contents: $1.75 < x \leq 2$, paramagnetic behaviour is observed down to low temperatures. Figure 3.49 depicts a magnetic phase diagram for $CsCo_{2-x}Ni_xSe_2$ constructed from magnetometry analysis, summarising the four magnetic regions in the solid solution. The magnetometry values for the end members are from literature.[8,22]

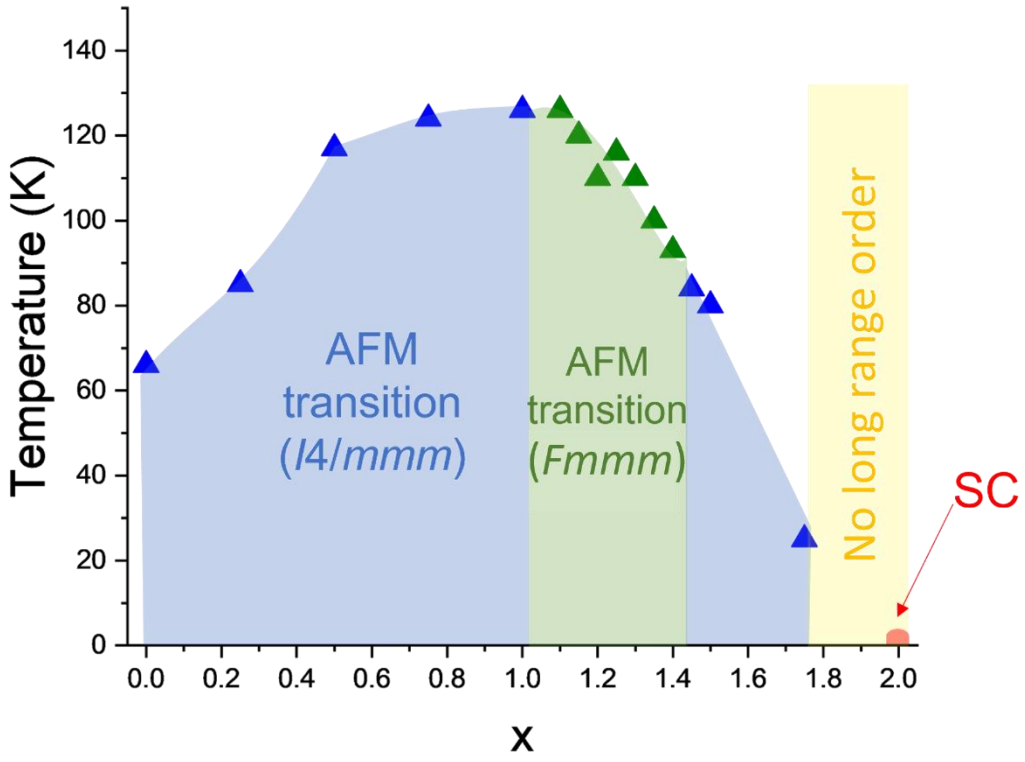


**Figure 3.49** Magnetic phase diagram for $CsCo_{2-x}Ni_xSe_2$ ($0 \leq x \leq 2$); showing the antiferromagnetic region (blue), paramagnetic region (yellow), and superconducting region (red), while the green region shows the antiferromagnetic transition in the magnetometry but the structure is orthorhombic (not tetragonal as the rest of the series).

Appendix C.3 shows the Curie-Weiss fits to selected antiferromagnetic members of this series. Again, as these compounds do not appear obey the Curie-Weiss law, and therefore the results should be interpreted with a level of caution.

### 3.2.4.5 PND of $CsCoNiSe_2$

The magnetic structure of $CsCoNiSe_2$ was probed with PND at 3.5 K (Figure 3.50) and 300 K (Figure D.4 in Appendix D). Like in the analogous compounds discussed above, the magnetic Bragg peaks were accounted for by the A-type antiferromagnetic model in space group *Cmcm*, with a refined long-range ordered moment of 0.80(1) $\mu_B$ per transition metal ion. The magnetic anisotropy (ferromagnetic coupling in-plane and antiferromagnetic coupling out-of-plane) is consistent with the changes of lattice parameters observed at low temperatures described in Section 3.2.3.6; lattice

parameter *a* contracts faster below $T_N$, and *c* remains approximately flat below $T_N$ instead of undergoing continued thermal contraction.

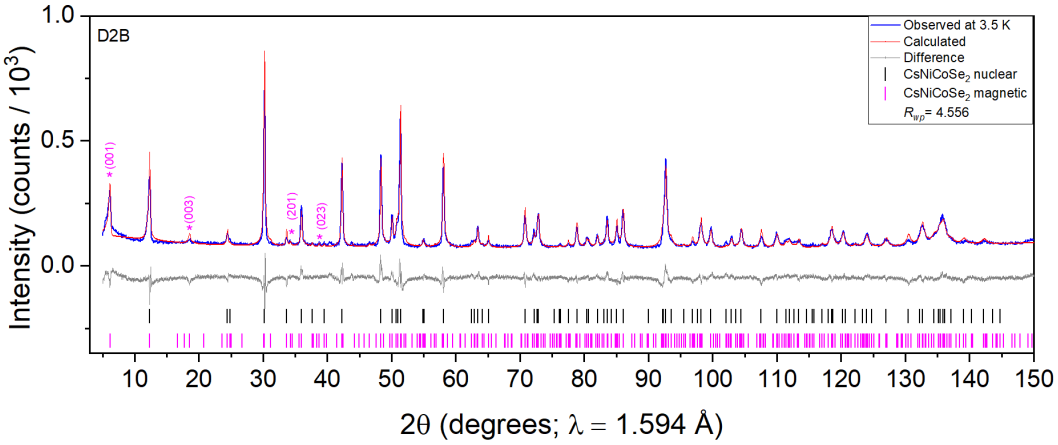


**Figure 3.50** Rietveld refinement of $CsCoNiSe_2$ against PND data measured at 3.5 K, $R_{wp}$ = 4.56% and $\chi^2$ = 1.77.

### *3.2.5 SEM-EDX*

#### 3.2.5.1 SEM-EDX of $KCo_{2-x}Ni_xSe_2$

Elemental analysis by SEM-EDX reveals an even distribution of K, Co, Ni, and Se across a portion of the polycrystalline sample of $KCoNiSe_2$ (Figure 3.51).

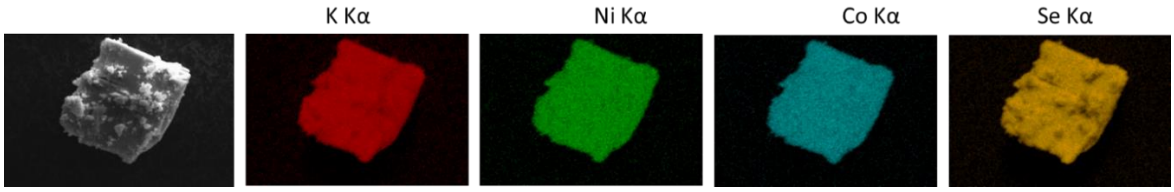


**Figure 3.51** An image of a polycrystalline sample of $KCoNiSe_2$ sample under SEM, showing an even distribution of the constituent elements.

Figure 3.52 shows an SEM image of a second representative of $KCoNiSe_2$, where there are visible K-rich regions that do not contain any other element, including oxygen, and these are of uncertain origin. It is likely from the map data and from specific points that there is some surface oxidation occurring on transfer to the instrument which led to samples being air-exposed for < 2 minutes.

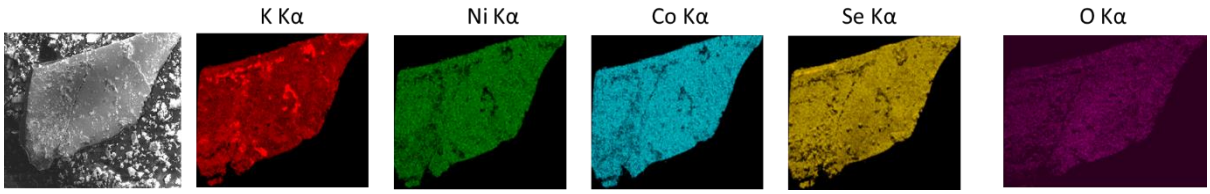


**Figure 3.52** SEM image of $KCoNiSe_2$ single crystal. There are some K-rich regions shown in bright red, which do not contain any other elements, including oxygen

Table 3.3 summarises the data collected from SEM-EDX analysis on compositions $KCo_{2-x}Ni_xSe_2$ and compares them with the refined atomic occupancies from PND analysis. Our SEM-EDX data show a more pronounced deficiency on the K-site compared to PND data. As PND is a bulk technique, and SEM-EDX studies only the surface of the particle, we placed more importance on the data obtained by PND. To further investigate the pronounced K-deficiency in SEM-EDX, we also probed a sample of stoichiometric $K_2Se$ (made in-house on the Schlenk line) to account for systematic over-estimation of Se content by the software and this produced a measured atomic ratio of K:Se of 1.86:1. We corrected the measurements of the ternary phases for this overestimation of the Se content. Ratios obtained prior to scaling from the $K_2Se$ standard can be found in Table E.1 in Appendix E.

**Table 3.3** Nominal and observed compositions from SEM-EDX and PND data on $KCo_{2-x}Ni_xSe_2$.

| **Nominal Composition** | **Observed composition from SEM-EDX** | **Observed composition from PND** |
|---|---|---|
| $KCo_2Se_2$ | $K_{0.88(6)}Co_{2.10(7)}Se_{2.00(1)}$[a] | $K_{1.00(2)}Co_{1.92(3)}Se_{2.00(1)}$[a] |
| $KCo_{1.75}Ni_{0.25}Se_2$ | $K_{0.86(2)}Co_{1.74(7)}$ $Ni_{0.19(2)}Se_{2.00(1)}$ | - |
| $KCo_{1.5}Ni_{0.5}Se_2$ | $K_{0.89(3)}Co_{1.47(8)}Ni_{0.47(3)}Se_{2.00(1)}$ | $K_{0.95(1)}Co_{1.44(1)}Ni_{0.56(1)}Se_{2.00(1)}$ |
| $KCo_{1.25}Ni_{0.75}Se_2$ | $K_{0.89(2)}Co_{1.24(1)}$ $Ni_{0.79(5)}Se_{2.00(1)}$ | - |
| $KCoNiSe_2$ | $K_{0.89(3)}Co_{1.18(6)}Ni_{1.02(6)}Se_{2.00(1)}$ | $K_{0.92(1)}Co_{0.98(1)}Ni_{1.02(1)}Se_{2.00(1)}$ |
| $KCo_{0.75}Ni_{1.25}Se_2$ | $K_{0.98(2)}Co_{0.83(6)}$ $Ni_{1.23(7)}Se_{2.00(1)}$ | - |
| $KCo_{0.5}Ni_{1.5}Se_2$ | $K_{1.00(4)}Co_{0.45(4)}$ $Ni_{1.46(1)}Se_{2.00(2)}$ | $K_{1.00(1)}Co_{0.44(1)}Ni_{1.56(3)}Se_{2.00(1)}$ |
| $KNi_2Se_2$ | $K_{0.90(6)}Ni_{2.01(9)}Se_{2.00(9)}$ | - |

[a]The standard deviations in the EDX measurement come from multiple independent measurements over the sample. The estimated standard deviations from the PND experiments are estimated from the Rietveld software based on data quality and parameter correlations.

These values carry quite large estimated standard deviations on the element content, and suggest slight K-deficiency, but no significant deficiency on the transition metal sites bearing in mind the intrinsic uncertainty of the technique. For $KCoNiSe_2$ there was a slight K-deficiency according to EDX (even after calibrating for the apparent Se excess in the measured data) – observed composition of $K_{0.89(3)}Co_{1.18(6)}Ni_{1.02(6)}Se_{2.00(1)}$ and PND analysis revealed composition $K_{0.92(1)}Co_{0.98(1)}Ni_{1.02(1)}Se_{2.00(1)}$, although the compositions are similar considering the uncertainties. $KCo_2Se_2$ also showed a K-deficient composition in EDX - $K_{0.88(6)}Co_{2.10(7)}Se_{2.00(1)}$, while the composition from PND analysis is slightly Co-deficient ($K_{1.00(2)}Co_{1.92(3)}Se_{2.00(1)}$) (although the uncertainty in the PND is relatively high in this case because of the short scattering length of Co). The SEM-EDX data collected on $KNi_2Se_2$ shows the surface composition is $K_{0.90(6)}Ni_{2.01(9)}Se_{2.00(9)}$, which is in relatively good agreement (within the large uncertainties from our experiment) with the work of Lei *et al.*,[12] who reported the phase as $K_{0.95(1)}Ni_{1.86(2)}Se_{2.00(1)}$. The Co/Ni ratio was determined from PND rather than XRD, as the two metals have very differing scattering lengths. (Co: 2.50 fm; Ni: 10.3 fm). The refined Co/Ni ratios were observed to be in good agreement with nominal compositions in the analysis of both PND and SEM-EDX data.

#### 3.2.5.2 SEM-EDX of $CsCo_{2-x}Ni_xSe_2$

Elemental analysis by SEM-EDX reveals an even distribution of Cs, Co, Ni, and Se across a portion of the polycrystalline sample of $CsCoNiSe_2$ (Figure 3.53). Cs-deficiency is pronounced, between $0.1 \leq y \leq 0.44$ in $Cs_{1-y}Co_{2-x}Ni_xSe_2$, while deficiency on the transition metal site is observed in $CsCo_{1.5}Ni_{0.5}Se_2$. In this sample, Synchrotron PXRD analysis also shows Cs occupancy at low levels of 0.62(5), agreeing well with the SEM-EDX data. There is a good agreement in the occupancies of $CsCoNiSe_2$ between PND and SEM-EDX (Table 3.4). There is, again, a likelihood of an overestimation of Se content, however, without access to an appropriate Cs-Se standard, we could not correct the measurements.

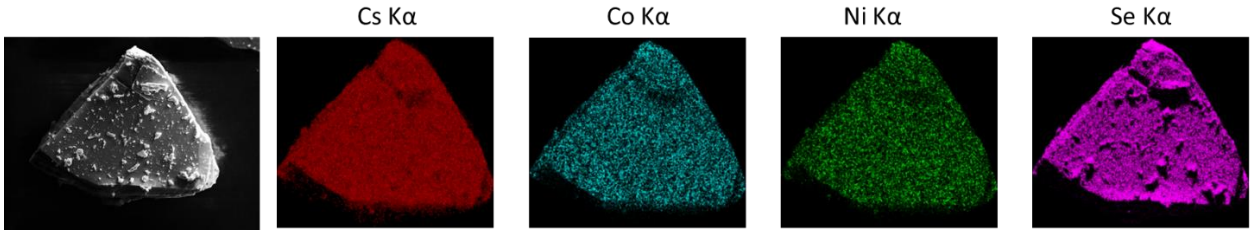


**Figure 3.53** An image of a polycrystalline sample of $CsCoNiSe_2$ sample under SEM, showing an even distribution of Cs, Co, Ni and Se elements.

**Table 3.4** Nominal and observed compositions from SEM-EDX and PND data on selected compositions of $CsCo_{2-x}Ni_xSe_2$ solid solution.

| Nominal Composition | Observed composition from SEM-EDX | Observed composition from PND |
|---|---|---|
| $CsCo_{1.5}Ni_{0.5}Se_2$ | $Cs_{0.56(1)}Co_{1.03(5)}\ Ni_{0.44(2)}Se_{2.00(1)}$ | - |
| $CsCoNiSe_2$ | $Cs_{0.90(4)}Co_{0.95(7)}Ni_{1.04(4)}Se_{2.00(1)}$ | $Cs_{0.81(1)}Co_{0.95(1)}Ni_{1.04(1)}Se_{2.00(1)}$ |
| $CsCo_{0.75}Ni_{1.25}Se_2$ | $Cs_{0.78(3)}Co_{0.73(3)}\ Ni_{1.15(6)}Se_{2.00(1)}$ | - |
| $CsCo_{0.5}Ni_{1.5}Se_2$ | $Cs_{0.82(2)}Co_{0.54(4)}\ Ni_{1.40(7)}Se_{2.00(1)}$ | - |

### *3.2.6 Single crystal XRD of $KCoNiSe_2$ and $KNi_2Se_2$*

Single Crystal X-ray diffraction (SC XRD) was employed to probe the K-deficiency in $KNi_2Se_2$ and $KCoNiSe_2$. The experimental details for $KNi_2Se_2$ can be found in Table 3.5, together with the lattice parameters. Table 3.6 contains the refined atomic coordinates, occupancies, and thermal displacement parameters obtained from the SC XRD experiment. The SC XRD data collected on $KNi_2Se_2$ is in good agreement with the SEM-EDX data on the same sample; the composition from SC XRD is ~10% deficient on the K site with a refined composition of $K_{0.90(3)}Ni_{1.948(14)}Se_{2.00(9)}$. This result and the structural parameters agree relatively well (within 3 × the estimated standard deviations on the refined parameters) with the work of Lei *et al.*,[12] who reported the phase as $K_{0.95(1)}Ni_{1.86(2)}Se_{2.00(1)}$, and their lattice parameter *a* was reported to be 3.8707(5) Å and *c* as 13.591(4) Å, while the unit cell volume was 203.62(7) $Å^3$.

**Table 3.5** Experimental details of Single crystal X-ray diffraction experiment on $KNi_2Se_2$

| | |
|---|---|
| Crystal data | |
| Chemical formula | $K_{0.90(3)}Ni_{1.948(14)}Se_{2.00(9)}$ |
| $M_r$ | 310.3 |
| Crystal system, space group | Tetragonal, *I*4/*mmm* |
| Temperature (K) | 150 |
| *a*, *c* (Å) | 3.8709 (13), 13.583 (5) |
| *V* (Å$^3$) | 203.53 (12) |
| *Z* | 2 |
| Radiation type | Mo *K*α |
| Crystal size (mm) | 0.05 × 0.04 × 0.01 |
| Diffractometer | (Rigaku) Oxford Diffraction SuperNova A |
| $T_{min}$, $T_{max}$ | 0.31, 1 |
| No. of measured, independent and observed [$I > 3\sigma(I)$] reflections | 1504, 121, 103 |
| $R_{int}$ | 0.123 |
| Refinement | |
| $R[F^2 > 2\sigma(F^2)]$, $wR(F^2)$, $S$ | 0.058, 0.146, 4.44 |
| No. of reflections | 121 |
| No. of parameters | 9 |
| $\Delta\rho_{max}$, $\Delta\rho_{min}$ (e Å$^{-3}$) | 1.59, −1.23 |

**Table 3.6** Structural details for Single crystal X-ray diffraction experiment on $KNi_2Se_2$

| Atom | Wyckoff site | x | y | z | Occupancy | $U_{eq}/U_{iso}$(Å$^2$) |
|---|---|---|---|---|---|---|
| K1 | 2a | 0 | 0 | 0 | 0.90(3) | 0.022(2) |
| Ni1 | 4d | 0 | 0.5 | 0.25 | 0.947(7) | 0.0185(8) |
| Se1 | 4e | 0 | 0 | 0.35402(18) | 1 | 0.0166(7) |

Anisotropic displacement factor harmonic parameters

| Atom | $U_{11}$ (Å$^2$) | $U_{22}$(Å$^2$) | $U_{33}$(Å$^2$) | $U_{12}$(Å$^2$) | $U_{13}$(Å$^2$) | $U_{23}$(Å$^2$) |
|---|---|---|---|---|---|---|
| K1 | 0.024 (3) | 0.024 (3) | 0.019 (5) | 0 | 0 | 0 |
| Ni1 | 0.0135(11) | 0.0135 (11) | 0.0285 (19) | 0 | 0 | 0 |
| Se1 | 0.0114 (9) | 0.0114 (9) | 0.0270 (15) | 0 | 0 | 0 |

Note: off-diagonal terms are 0 by symmetry

Attempted single crystal X-ray analysis of a candidate single crystal of $KCoNiSe_2$ as a representative of the $KCo_{2-x}Ni_xSe_2$ series showed severely elongated spots (Figure 3.54), suggesting high mosaicity, possibly due to compositional inhomogeneity or stacking faults.[23, 24] So this technique was not pursued for further samples.

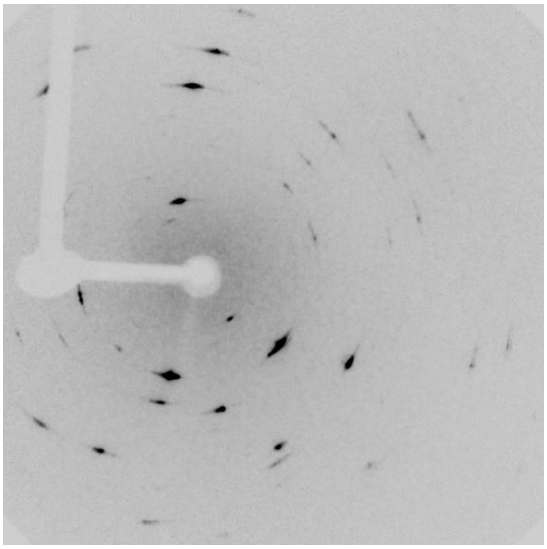

**Figure 3.54** Sample single crystal diffraction frame (CCD image) of $KCoNiSe_2$ at 150 K showing elongated spots.

### *3.2.7 Resistivity of $KCoNiSe_2$*

The resistivity ($\rho$) measurement on a representative sample of $KCoNiSe_2$ was performed on a small piece of a sintered pellet connected to four copper wires using silver paint and mounted on a custom-made probe. The resistivity of $KCoNiSe_2$ increases linearly with increasing temperature, corresponding to metallic behaviour in the temperature range 30-300 K, with $\rho$ of the order of $10^{-2}$ Ωcm at room temperature (Figure 3.55). Further quantitative comparisons of the resistivity of the

series would require larger single crystal samples to eliminate grain boundary effects. The measurement noise is presumably the reason for the slight wiggling of the data.

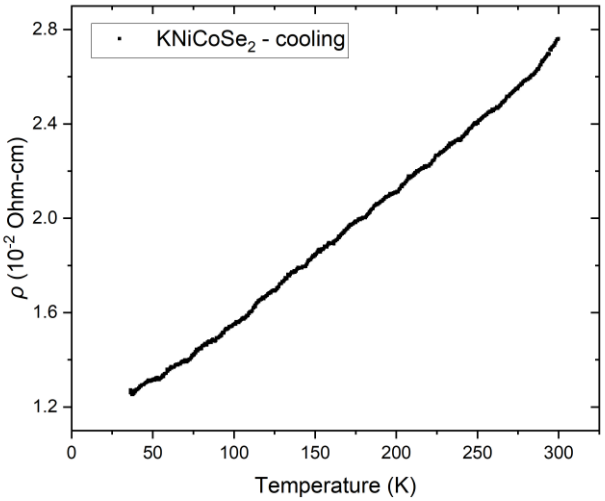


**Figure 3.55** The resistivity as a function of temperature for $KNiCoSe_2$ measured on cooling.

### 3.2.8 First principles calculations of $KCo_2Se_2$ and $KNi_2Se_2$

Bannikov *et al*. studied the two end members of $KCo_{2-x}Ni_xSe_2$ solid solution studied here - $KCo_2Se_2$ and $KNi_2Se_2$ - from first principles calculations.[25,26] Their studies revealed the details of the electronic structures and Fermi surfaces, as well as densities of states (DoS) for the examined phases. Their calculations shows that there is no gap at the Fermi level ($E_F$), confirming the metallicity of the compounds. The inter-atomic bonding in $KT_2Se_2$, and by extension the bonding in $KCo_{2-x}Ni_xSe_2$ solid solution, can be rationalised; the bonding here is of mixed ionic-covalent-metallic character. The metallic-like bonding is due to the interaction of the near-Fermi Ni states inside $Ni_2Se_2$ blocks. Covalent bonding dominates in the $T_2Se_2$ sheets, confirmed by the atomic -resolved DoSs. As to ionic bonding, Bader's model was used for estimating the actual atomic charges, resulting in $K^{0.801+}$ $Ni^{0.466+}{}_2Se^{0.866-}{}_2$, which differs substantially from the formal ionic charges owing to covalence in $Ni_2Se_2$ blocks. ionic bonding dominates between the K atomic sheets and $Co_2Se_2$ sheets.

In $KCo_2Se_2$, the $E_F$ is dominated by flat bands, and only some dispersive bands can be identified. The flat bands are present in $KNi_2Se_2$, but here, a greater number of high-dispersive bands can be

seen at $E_F$. These differences in electronic structures, and the change in electron count, are the likely the causes for the differing magnetic behaviour of the two phases, described in Section 3.2.4.

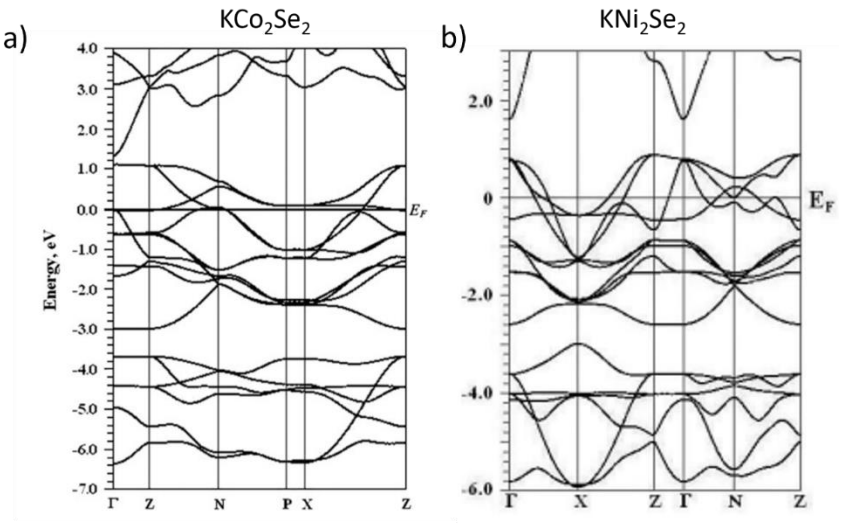


**Figure 3.56** Electronic band structures of a) $KCo_2Se_2$ and b) $KNi_2Se_2$. (Figures taken from References 25 and 26.)

## 3.3 Synthesis and characterisation of $KCo_{2-x}Ni_xS_2$, and $ACoNiS_2$ ($A$ = Rb, Cs)

### *3.3.1 Synthesis of $KCo_{2-x}Ni_xS_2$, and $RbCoNiS_2$ and $CsCoNiS_2$*

#### 3.3.1.1 Synthesis of $KCo_{2-x}Ni_xS_2$

The same synthesis method was employed for members of the $KCo_{2-x}Ni_xS_2$ series ($0 \leq x \leq 2$) prepared with 0.25 increments in $x$ as in the case of $KCo_{2-x}Ni_xSe_2$ described in Section 3.2.1.1. Precursor $K_2S$ was prepared in-house similar to $K_2Se$ (see Section 3.2.1.4).

#### 3.3.1.2 Synthesis of $RbCoNiS_2$ and $CsCoNiS_2$

$RbCoNiS_2$ and $CsCoNiS_2$ were synthesised as single crystals using a self-flux method described previously in Section 3.2.1.2. Powder precursors NiS and CoS were synthesised at 900°C/12hrs in a silica tube in the form of pressed pellets. The SXRD patterns and structural details are shown in Appendix F.

### *3.3.2 Crystal structure determination of $ACo_{2-x}Ni_xS_2$ ($A$ = K, Rb, Cs)*

#### 3.3.2.1 Room temperature SPXRD of $KCo_{2-x}Ni_xS_2$

PXRD patterns of all 7 measured samples in the $KCo_{2-x}Ni_xS_2$ series (Figure 3.57a), were indexed according to the tetragonal $ThCr_2Si_2$-type structure (Space group: $I4/mmm$, no.139) of the parent stoichiometric phases using Rietveld refinement, indicating the formation of a solid solution across

the whole $0 \leq x \leq 2$ range. The members of the sulfide solid solution were more difficult to synthesise with high purity than the selenide analogues. In particular, $Co_9S_8$ and $K_2Ni_3S_4$ were found as competing transition-metal-containing impurities (marked by green and blue asterisks, respectively, in Figure 3.57a).

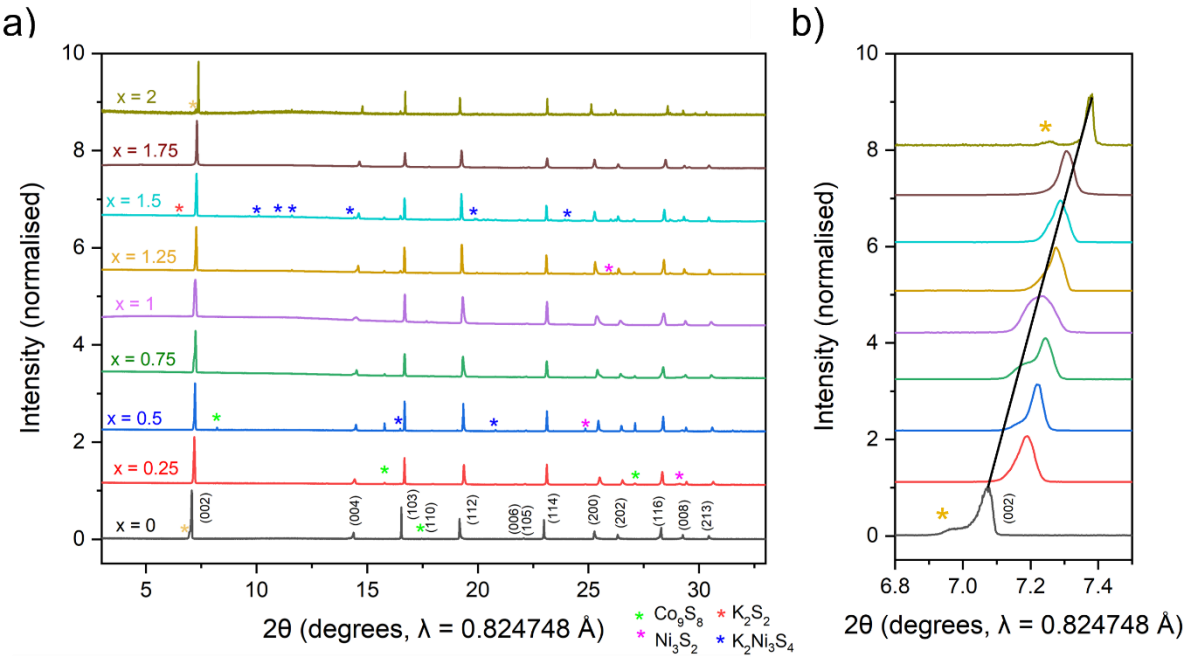


**Figure 3.57** a) Synchrotron PXRD patterns of $KCo_{2-x}Ni_xS_2$ with $0 \leq x \leq 2$. Impurities are marked by asterisks: $Co_9S_8$ in green, $K_2S_2$ in red, $Ni_3S_2$ purple, and $K_2Ni_3S_4$ blue. Yellow asterisks denote an unknown impurity. b) (002) peak shifting to higher angles across $KCo_{2-x}Ni_xS_2$ with increasing Ni content.

Figure 3.57b shows the main (002) peak of the body-centred cell which shifts to higher angles with increasing Ni content, indicating a contraction of the *c* lattice parameter across the solid solution (by 2.7%). The basal lattice parameter *a* expands by 1.9%, resulting in the overall unit cell volume (*V*) showing a general increase – by 1.25% – with increasing Ni content from $x = 0$ to 2 in $KCo_{2-x}Ni_xS_2$. The variations of the unit cell parameters *a* and *c*, unit cell volume, and the *c*/*a* ratio with *x* in $KCo_{2-x}Ni_xSe_2$ are shown in Figure 3.58 and follow similar trends to those of the selenide analogues. Again, some of the peak shapes in Figure 3.57b are unusual, and it is possible that the phases separate between the end member and the non-stoichiometric member. For $x = 0.75$, there is a visible shoulder to the main (002) peak, which is a likely case of phase separation. Unlike the selenides, the sulfide

phases do not increase in purity with annealing, but rather the impurities become more prominent, namely $Co_9S_8$.

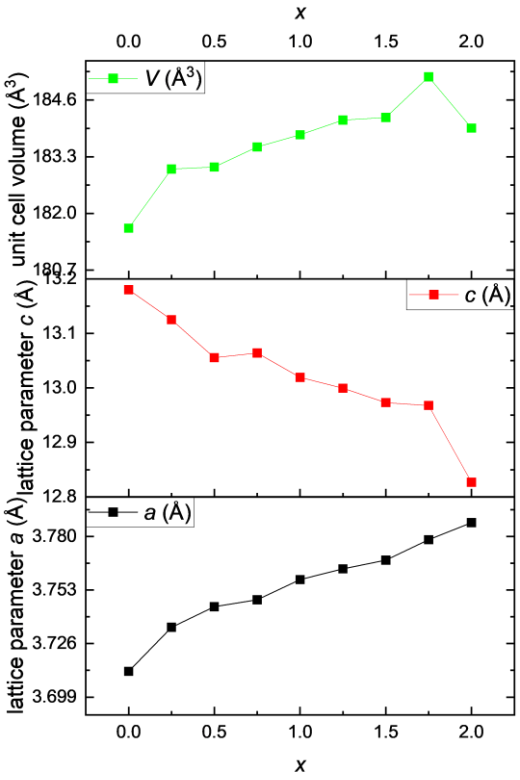


**Figure 3.58** Changes in lattice parameters *a* and *c* and unit cell volume with *x* for $KCo_{2-x}Ni_xS_2$. (DLS).

The Rietveld refinement of room temperature Synchrotron PXRD pattern of $KCoNiS_2$ ($x$ = 1) is shown in Figure 3.59. It is worth noting that the tetrahedral angle, $\delta_{Se\text{-}Ni/Co\text{-}Se}$, is distorted from ideal at 111.15(3)º.

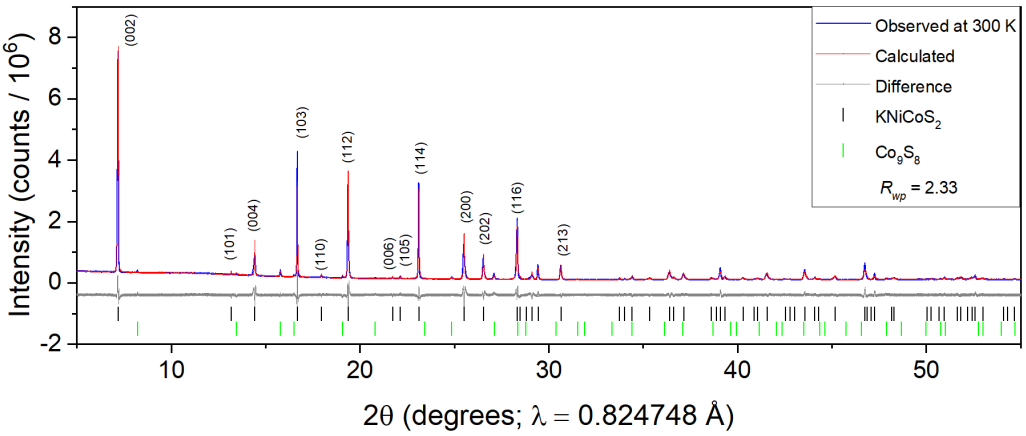


**Figure 3.59** Room-temperature Rietveld refinement of $KCoNiS_2$ against Synchrotron PXRD.

The interatomic distances and tetrahedral angles across the series are shown in Figure 3.60. The tetrahedral angle, $\delta_{X\text{-}T\text{-}X}$, the metal-chalcogen distance, *T*-*X*, and the metal-metal distance, *T*-*T*, show a general increase with increasing Ni content. The chalcogen-chalcogen distance, *X*-*X*, decreases steadily with increasing Ni content from $x = 0$ to 2, which presumably drives the decrease in the *c* lattice parameter across the series. The increase in ionic radii from Co to Ni is demonstrated in an increase in the basal lattice parameter *a*, the overall unit cell volume, T-T distance, and $\delta_{X\text{-}T\text{-}X}$. All unit cell parameters, interatomic distances and angles in $KCo_{2-x}Ni_xS_2$ series are shown in Table A.4.1 in the Appendix A.4.

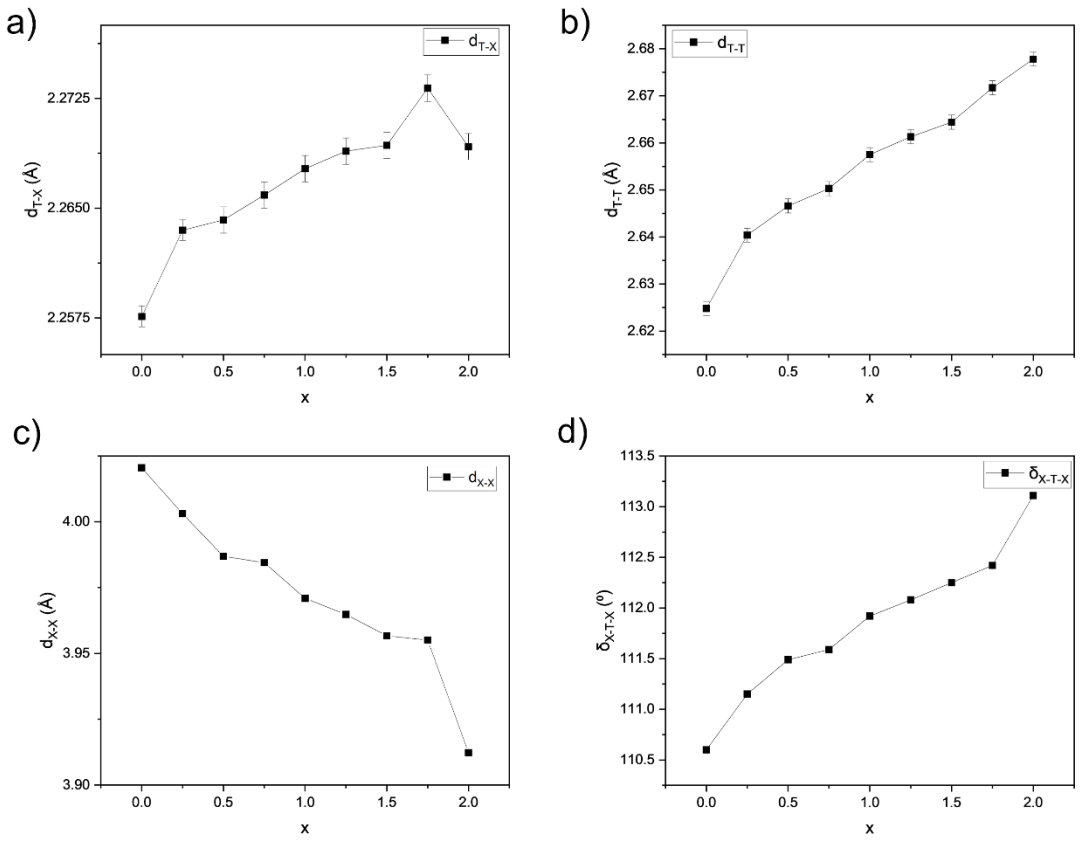


**Figure 3.60** Changes in interatomic distances and angles across the $KCo_{2-x}Ni_xS_2$ series; a) Co/Ni-S distance, b) Co/Ni-Co/Ni distance, c) S-S distance, d) tetrahedral angle S-Co/Ni-S.

#### 3.3.2.1.1 Variable temperature SPXRD of $KCoNiS_2$

Variable temperature PXRD data were collected on $KCoNiS_2$ between 100-300 K using the cryostream at the Diamond Light Source (Figure 3.61). Individual Rietveld refinements were observed visually and no peak splitting or extra superstructure peaks were visible down to 100 K. The trends in lattice parameters upon cooling are consistent with those observed for selenide analogues described in Sections 3.2.3.2 and 3.2.3.6. The change in gradient of *a* lattice parameter occurs at ~160 K; between 100-170 K the *a* parameter expands at a higher rate than between 170-300 K. The *c* lattice parameter initially decreases between 100-150 K, then remains constant up to ~200 K, and between 200-300 K a sharp increase can be observed. The *c/a* ratio decreases between 100-175 K, and then remains approximately constant up to room temperature. Unit cell volume expands linearly between 100-300 K. The reason for this behaviour is related to the long-range

magnetic properties of the phase and will be discussed in Section 3.3.3.2.

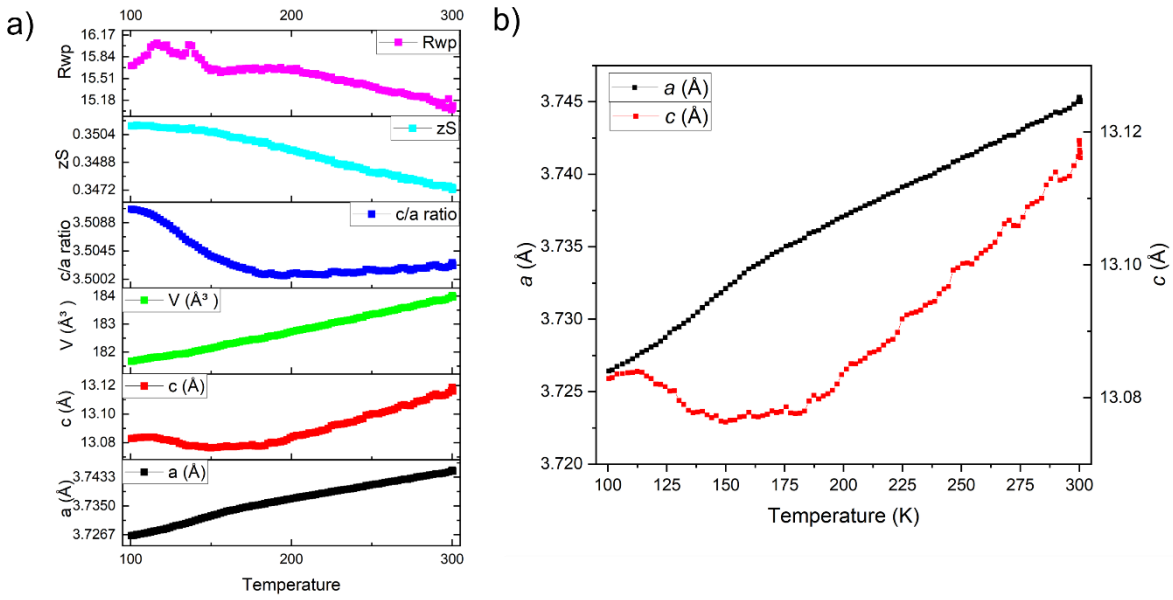


**Figure 3.61** a) Variable temperature SXRD for $KCoNiS_2$, b) Changes in *a* and *c* lattice parameters between 100-300 K.

The synthesis of Rb- and Cs-analogues of the sulfide series were attempted, however due to time constraints only the middle members were synthesised and their magnetic properties characterised. These can be found in Appendix H.

### *3.3.3 Magnetic structure of $ACo_{2-x}Ni_xS_2$ (A = K, Rb, Cs)*

#### 3.3.3.1 Magnetometry of $KCo_{2-x}Ni_xS_2$

As the end members of the solid solutions have differing magnetic behaviours ($KCo_2S_2$ is a ferromagnetic metal,[21] and $KNi_2S_2$ is a paramagnetic metal with a low temperature superconducting transition),[9] mapping out the changes in magnetic behaviour of $KCo_{2-x}Ni_xS_2$ solid solution was carried out using magnetometry. Figure 3.62 shows the magnetic susceptibility, $\chi$, as a function of temperature for the seven non-stoichiometric samples of the solid solution and the two end members on a normalised scale.

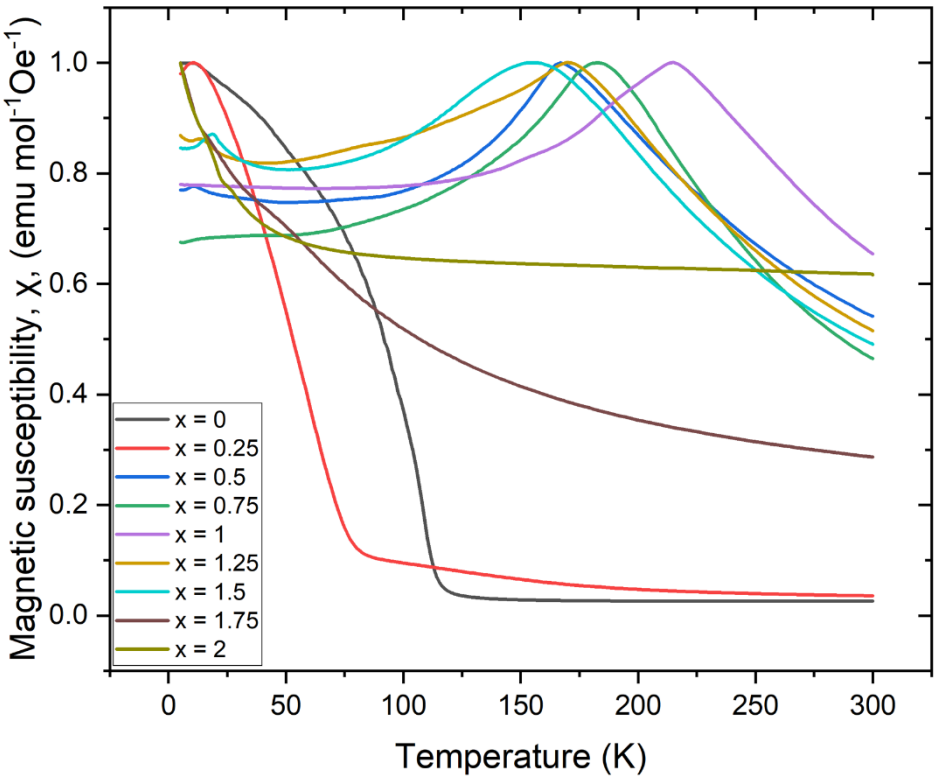


**Figure 3.62** Magnetic susceptibility (ZFC measurements) as a function of temperature for the series $KCo_{2-x}Ni_xS_2$ ($0 \leq x \leq 2$).

At high Co contents in the $KCo_{2-x}Ni_xS_2$ series ($0 \leq x \leq 0.25$), ferromagnetic behaviour is observed with $T_C$ ~ 120 K in the $KCo_2S_2$ end member, diminishing to about 80 K for $x$ = 0.25. The low temperature magnetisation isotherms for the two ferromagnetic members – $x$ = 0 and 0.25 – are shown in Figure 3.63. For x = 0, the magnetisation isotherm saturates at $H$ ~ 2 K at $\mu_B$/Co = 1.15, which is similar to the value obtained for the selenide analogue (Figure 3.63a). On the other hand, the $x$ = 0.25 member shows a hysteresis loop between ± 3T and there is no saturation even at high fields (Figure 3.63b).

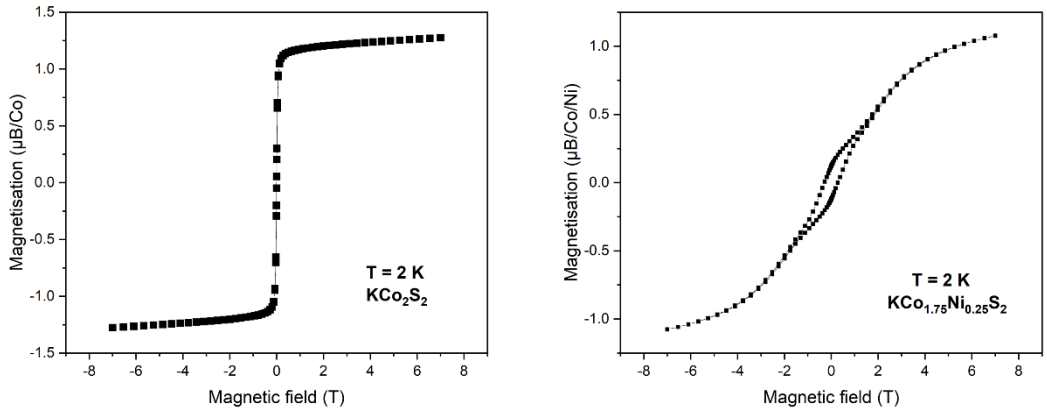


**Figure 3.63** Magnetisation isotherms for a) $KCo_2S_2$ ($x = 0$), and b) $KCo_{1.75}Ni_{0.25}S_2$ ($x = 0.25$) measured at 2K and 5K, respectively.

$KCo_{2-x}Ni_xS_2$ for $0.5 \leq x \leq 1.5$ show antiferromagnetic behaviour. The Néel temperatures, $T_N$, as judged by the temperature of the susceptibility maximum, initially increase with increasing $x$, reach a maximum value of 220 K at $x = 1$, and then decrease with increasing $x$. At high Ni contents: $1.5 < x \leq 2$, paramagnetic behaviour is observed down to low temperatures with evidence of a magnetic transition of uncertain origin around 10 K. Figure 3.64 depicts a magnetic phase diagram for $KCo_{2-x}Ni_xS_2$ constructed from magnetometry analysis, summarising the four magnetic regions in the solid solution. The superconducting region is not evident in our magnetometry data as the $T_c$ for $KNi_2S_2$ is as low as 0.46 K,[9] which is below the limits of the instrument used (MPMS-3).

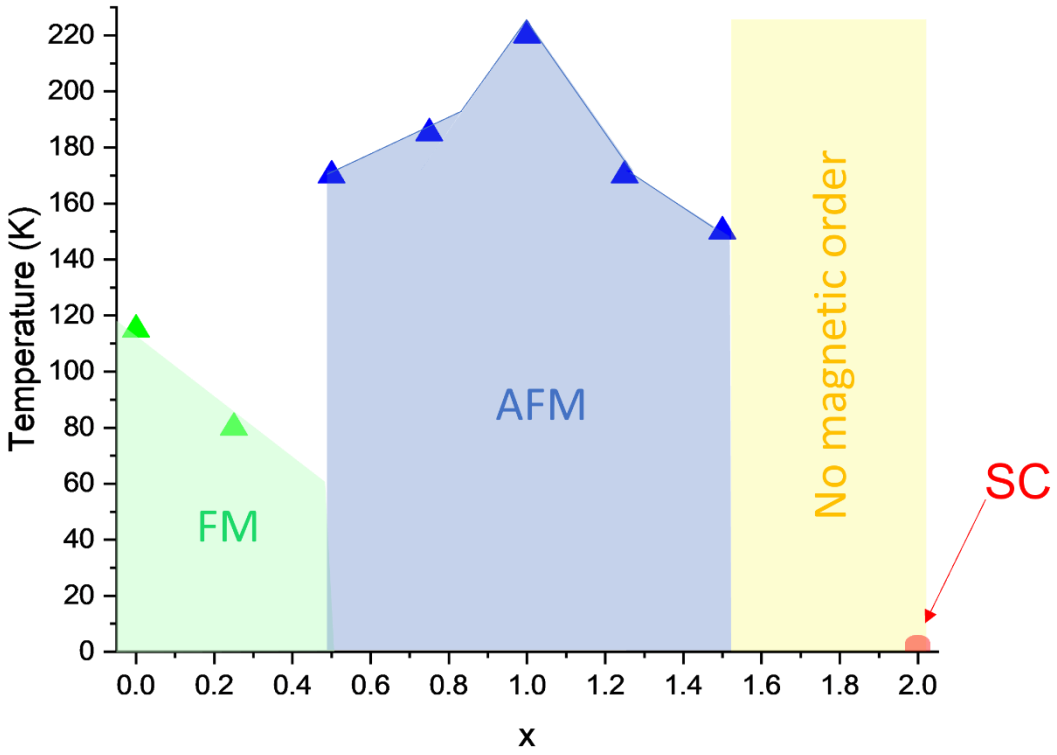


**Figure 3.64** Magnetic phase diagram for $KCo_{2-x}Ni_xS_2$ ($0 \leq x \leq 2$); showing the ferromagnetic region (green), antiferromagnetic region (blue), paramagnetic region (yellow), and superconducting region (red).

Appendix C.4 shows the Curie-Weiss fits to $KCoNiS_2$. However, the phase does not appear obey the Curie-Weiss law, and therefore the results should be interpreted with a level of caution.

### 3.3.3.2 PND of $KCo_{2-x}Ni_xS_2$ ($x$ = 0.5, 1, 1.5)

Three antiferromagnetic members of the series, $KCo_{0.5}Ni_{1.5}S_2$, $KCoNiS_2$, and $KCo_{1.5}Ni_{0.5}S_2$, were measured using PND on the WISH beamline at ISIS. Low temperature (1.5 K) PND measurements reveal (003), (005), (203), (025) and (207) Bragg reflections (marked by magenta asterisks), which have zero intensity in the body-centred tetragonal nuclear structure (so must be of magnetic origin), in $KCoNiS_2$ (Figure 3.65) and $KCo_{1.5}Ni_{0.5}S_2$ (Figure 3.66). These figures show Rietveld refinements

against the 5/6 bank of the WISH diffractometer, while the rest of the banks can be found in the Appendix G in Figures G.5-8 for $KCoNiS_2$ and Figures G.1-4 for $KCo_{1.5}Ni_{0.5}S_2$.

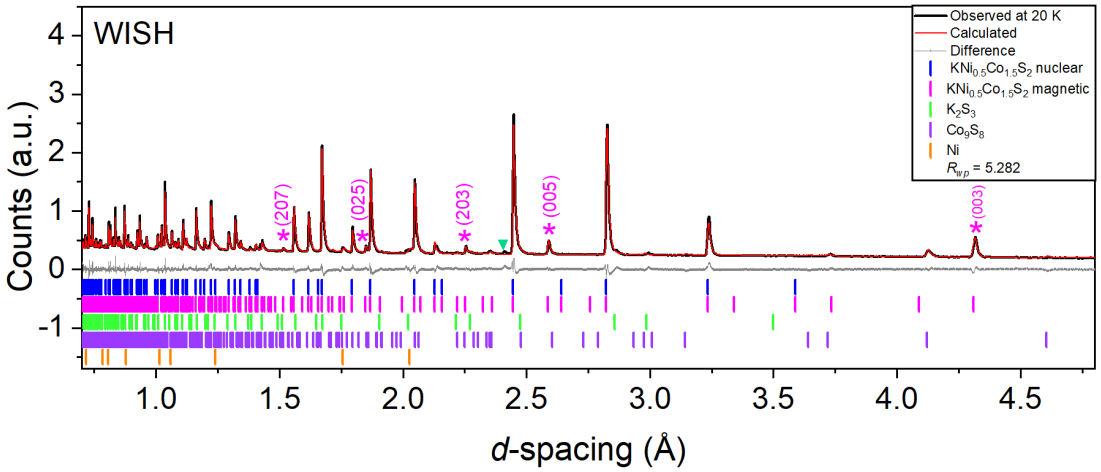


**Figure 3.65** Rietveld refinement at 20 K of $KCo_{1.5}Ni_{0.5}S_2$ against bank 5/6 of the WISH diffractometer at ISIS. $R_{wp}$ = 5.28%.

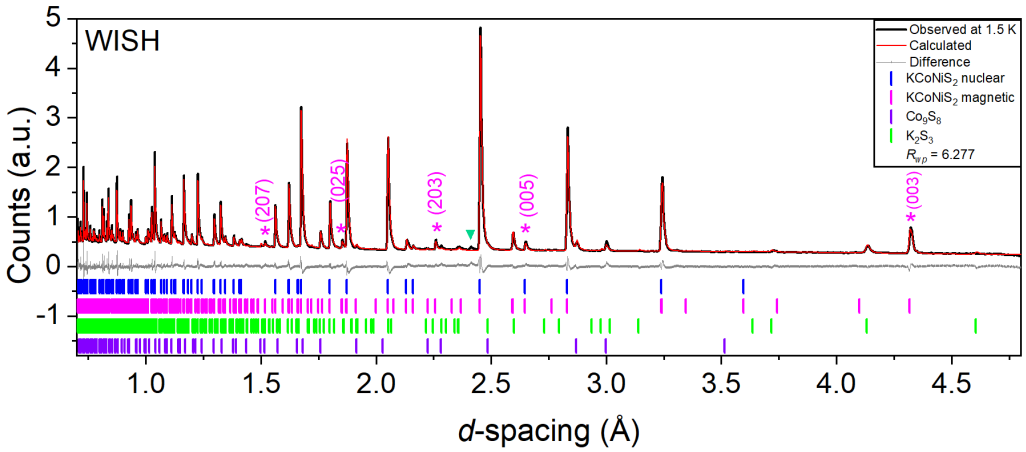


**Figure 3.66** Rietveld refinement at 1.5 K of $KCoNiS_2$ against bank 5/6 of the WISH diffractometer at ISIS. $R_{wp}$ = 6.28%.

In $KCo_{0.5}Ni_{1.5}S_2$ these reflections were not evident (Figure 3.67) suggesting that the rather broader susceptibility maximum in this compound (Section 3.3.3.1, Figure 3.61, $x$ = 1.5) is not associated with the long-range magnetic ordering which can be probed by diffraction.

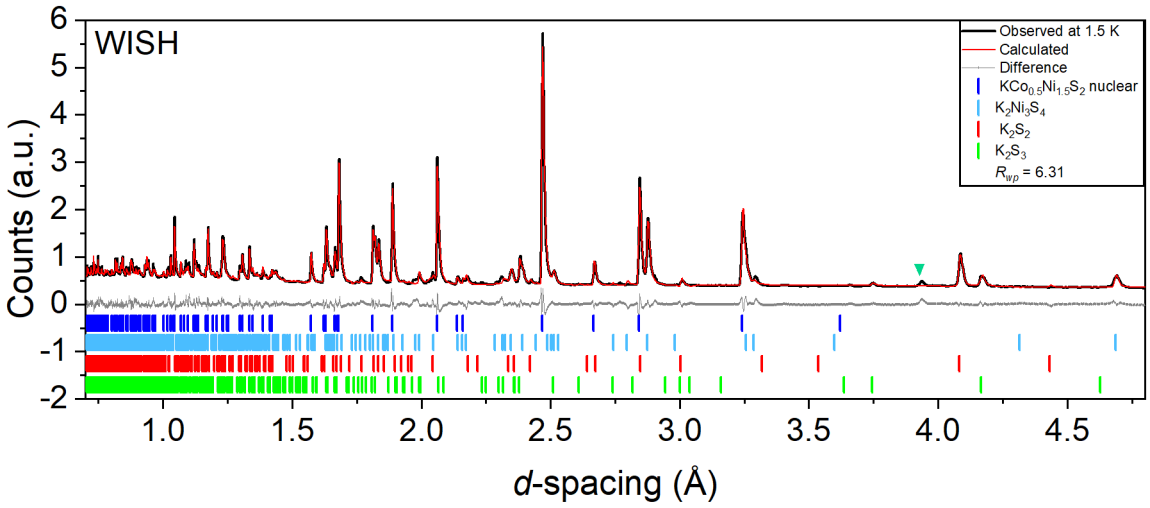


**Figure 3.67** Rietveld refinement at 1.5 K of $KCo_{0.5}Ni_{1.5}S_2$ against bank 5/6 of the WISH diffractometer at ISIS. $R_{wp}$ = 6.31%. Green triangle marks an unknown impurity.

The magnetic scattering of $KCoNiS_2$ and $KCo_{1.5}Ni_{0.5}S_2$ at 1.5 K was indexed using a $\sqrt{2}a \times \sqrt{2}a \times c$ expansion of the nuclear unit cell ((½ ½ 0) propagation vector) on an orthorhombic *Cmcm* unit cell, similar to the case of the selenide analogues. Magnetic peaks of the structure are located at *d*-spacing = 4.3188 Å (003), 2.5912 Å (005), 2.2553 Å (203), 1.8509 Å (025), and 1.5164 Å (207) (*hkl* values refer to the expanded cell), which corresponds to ferromagnetic coupling between Co/Ni ions within the $(Co/Ni)_2Se_2$ sheets and an antiferromagnetic interaction between the adjacent $(Co/Ni)_2Se_2$ sheets along the stacking axis, also known as A-type antiferromagnetic ordering (Figure 3.68), as described above for the selenide analogues (Section 3.2.4.2). The non-linear changes in lattice parameters at low temperatures described in Section 3.3.2.1.1 are consistent with the observation of this type of magnetic anisotropy (intralayer ferromagnetic coupling and interlayer antiferromagnetic coupling), again, just like in the case of all selenide analogues reported in this thesis. The long-range ordered moments of Co/Ni ions of 1.22(2) $\mu_B$ in $KCoNiS_2$ and 1.06(2) $\mu_B$ in $KCo_{1.5}Ni_{0.5}S_2$. Room temperature PND patterns of the three sulfide members presented are shown in Figures G.9-11 in Appendix G.

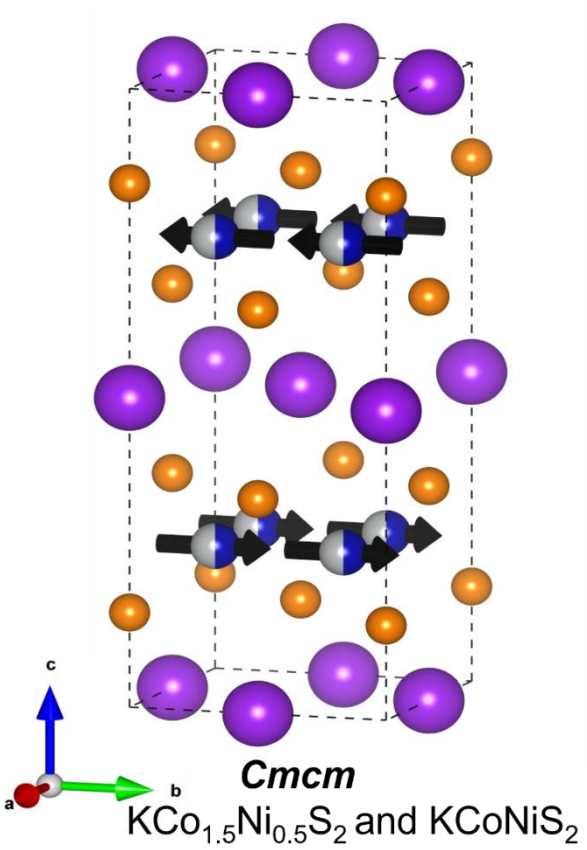


**Figure 3.68** Magnetic plus nuclear structure of $KCo_{1.5}Ni_{0.5}S_2$ and $KCoNiS_2$, with ferromagnetic coupling of Co/Ni moments in the ab plane and antiferromagnetic coupling of Co/Ni moments along the stacking axis.

#### 3.3.3.2.1 VT PND of $KCo_{1.5}Ni_{0.5}S_2$

The magnetic susceptibility data for this compound suggested that the onset of long-range magnetic ordering was at approximately 180 K (Figure 3.61, $x = 0.5$). To probe this further, low temperature PND was used. The PND patterns at selected temperatures between 20 K to 250 K are shown in Figure 3.69. Magnetic Bragg peaks with highest intensity, namely (003) and (005) peaks, begin to appear at 180 K, close to the Néel temperature of the phase, while the rest appear at lower temperatures due to their low intensities.

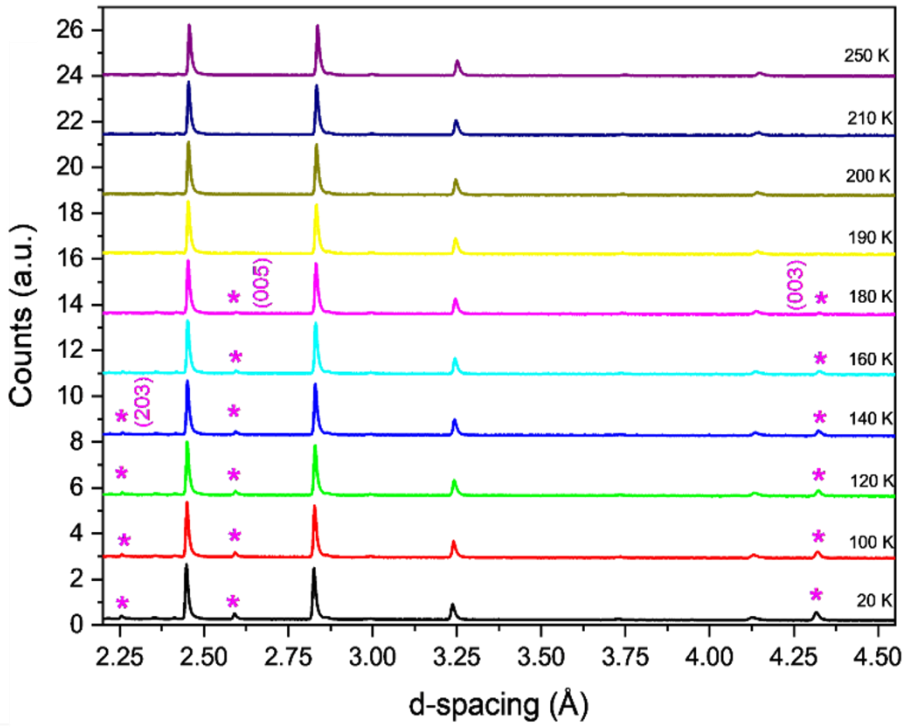


**Figure 3.69** Variable temperature PND of $KCoNiS_2$ measured between 20 K and 250 K showing the appearance of magnetic Bragg peaks (magenta asterisks) below $T_N$.

### *3.3.4 SEM-EDX of $KCo_{2-x}Ni_xS_2$*

Elemental analysis by SEM-EDX reveals an even distribution of K, Co, Ni, and S across a portion of the polycrystalline sample of $KCoNiS_2$ (Figure 3.70).

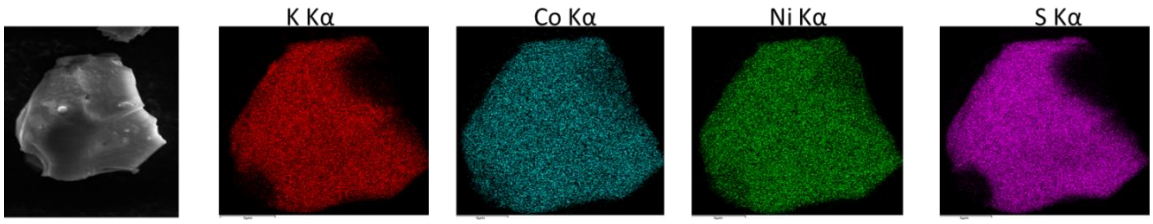


**Figure 3.70** An image of a polycrystalline sample of $KCoNiS_2$ sample under SEM, showing an even distribution of the constituent elements.

Table 3.7 summarises the data collected from SEM-EDX analysis on compositions $KCo_{2-x}Ni_xS_2$ and compares them with the refined atomic occupancies from PND analysis. These value of atomic ratios from SEM-EDX carry quite large estimated standard deviations on the element content. Our SEM-EDX data show only a slight deficiency on K-site compared to the selenide analogues, where the

alkali metal deficiency was much more pronounced. The values of K-content from SEM-EDX also agree well with PND data, where refined occupancies of K-site were between $0.98 \leq x \leq 1$. A small deficiency on the transition metal sites is shown in SEM-EDX, varying between $0.94 \leq x \leq 1$. The refined Co/Ni ratios from PND were observed to be in good agreement with nominal compositions in the analysis of both PND and SEM-EDX data.

**Table 3.7** Nominal and observed compositions from SEM-EDX and PND data on $KCo_{2-x}Ni_xS_2$.

| Nominal Composition | Observed composition from SEM-EDX | Observed composition from PND |
|---|---|---|
| $KCo_{1.5}Ni_{0.5}S_2$ | $K_{0.93(3)}Co_{1.35(5)}Ni_{0.55(6)}S_{2.00(1)}$ | $K_{1.00(1)}Co_{1.34(1)}Ni_{0.66(1)}S_{2.00(1)}$ |
| $KCo_{1.25}Ni_{0.75}S_2$ | $K_{0.98(2)}Co_{1.20(3)}Ni_{0.72(4)}S_{2.00(1)}$ | - |
| $KCoNiS_2$ | - | $K_{1.00(1)}Co_{1.00(1)}Ni_{1.00(1)}S_{2.00(1)}$ |
| $KCo_{0.75}Ni_{1.25}S_2$ | $K_{1.07(3)}Co_{0.78(5)}Ni_{1.22(4)}S_{2.00(1)}$ | - |
| $KCo_{0.5}Ni_{1.5}S_2$ | $K_{0.97(3)}Co_{0.49(4)}Ni_{1.39(3)}S_{2.00(1)}$ | $K_{1.00(1)}Co_{0.54(1)}Ni_{1.46(1)}S_{2.00(1)}$ |

## 3.4 Conclusions

Four new solid solutions of the $ThCr_2Si_2$-type structure were synthesised, and their magnetic properties were analysed. $KCo_{2-x}Ni_xSe_2$, $RbCo_{2-x}Ni_xSe_2$, $CsCo_{2-x}Ni_xSe_2$, and $KCo_{2-x}Ni_xS_2$ solid solutions were synthesised with $0 \leq x \leq 2$, and synchrotron PXRD reveals linear trends in lattice parameters, which are summarised in Table 3.8 and Figures 3.71 below.

**Table 3.8** Changes in lattice parameters *a*, *c*, and unit cell volume, *V*, across the four synthesised solid solutions.

| | **Δ*a* (%)** | **Δ*c* (%)** | **Δ*V* (%)** |
|---|---|---|---|
| **$KCo_{2-x}Ni_xSe_2$** | 1.6 | −2.6 | 0.72 |
| **$RbCo_{2-x}Ni_xSe_2$** | 2.7 | −3.9 | 1.36 |
| **$CsCo_{2-x}Ni_xSe_2$** | 3.7 | −5.8 | 1.42 |
| **$KCo_{2-x}Ni_xS_2$** | 1.9 | −2.7 | 1.25 |

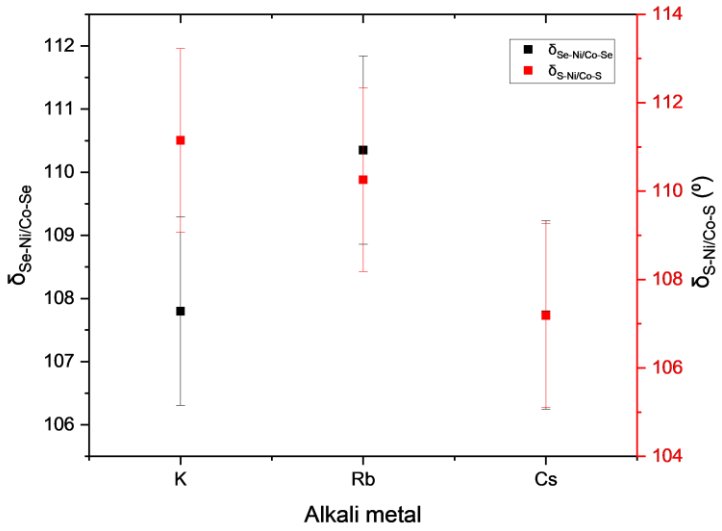


**Figure 3.71** Change in the tetrahedral angle of the middle members of $A\mathrm{Co}_{2-x}\mathrm{Ni}_x Ch_2$ (*A* = K, Rb, Cs; *Ch* = S, Se) as a function of alkali metal (*x* axis) and chalcogen atom (selenides shown in black, sulfides in red).

The trends in lattice parameters of the selenides reveal that the larger the unit cell, the greater the changes in lattice parameters.

In $\mathrm{CsCo}_{2-x}\mathrm{Ni}_x\mathrm{Se}_2$, a structural distortion from tetragonal-to-ortorhombic occurs between $1.1 \leq x \leq 1.4$, and the unit cell can be indexed in the *I*112/*m* space group, which is an alternative setting of *C*2/*m*. The distortion is very subtle, as *a* and *b* lattice parameters are nearly identical, and angle gamma is very slightly distorted from 90º. Preliminary variable temperature PXRD measurements reveal intriguing features in the behaviour or lattice parameters at elevated temperatures, and there is a temperature region between 750-900 K where new phase or structural distortion emerges marked by appearance of new peaks. As this could not be resolved in this thesis, further measurements are needed to conclude the origin of these features. An important measurement will be neutron powder diffraction of the orthorhombic members of the series which show antiferromagnetic transition from magnetometry, but long-range order may not be present in this value of *x* ($1.1 \leq x \leq 1.4$), as these compositions showed lack of long-range magnetic order in the K-analogues.

Magnetometry measurements of these systems show drastic changes in magnetism: addition of Ni causes change from long-range ferromagnetic to antiferromagnetic ordering, while further Ni substitution gives rise eventually to Ni-rich compositions that do not exhibit magnetic long-range order. The antiferromagnetic region extends between $0.5 \leq x \leq 1.5$ for $KCo_{2-x}Ni_xS_2$ and $KCo_{2-x}Ni_xSe_2$, while in $RbCo_{2-x}Ni_xSe_2$ it is between $0.25 \leq x \leq 1.75$. This is, however, not the case in $CsCo_{2-x}Ni_xSe_2$, where the Co-rich region is antiferromagnetic. Our results suggests that within the *A* = alkali metal series, increasing the interlayer separation favours antiferromagnetic arrangement of adjacent ferromagnetic planes. Neutron powder diffraction revealed A-type antiferromagnetism in $KCoNiSe_2$, $KCo_{1.5}Ni_{0.5}Se_2$ (and their sulfide analogues) and $CsCoNiSe_2$: ferromagnetic coupling within $(Co/Ni)_2Se_2$ layers and antiferromagnetic coupling between layers. The refined long-range ordered moment per transition metal ion varied between 0.8-1.22 $\mu_B$ among the studied phases. The small localised moments are consistent with other electrons being mobile conduction electrons giving rise to metallic behaviour (from resistivity data). The likely mechanism for ferromagnetic coupling in the *ab* plane is direct exchange as $d_{T\text{-}T}$ is ~ 2.7 Å, which is comparable to that observed in the elemental metals ($d_{Co\text{-}Co}$ = 2.51 Å in Co metal). The interlayer *T*–*T* distance is too large for any direct interaction. Antiferromagnetic coupling between planes has been proposed to operate via the RKKY mechanism via conduction electrons in this series of metallic compounds. The PND results show that there is no long-range chemical order of the Ni and Co species within the chalcogenide layers, and the chemical disorder within these layers does not suppress long-range magnetic order. Our results suggest that the reasons for drastic changes in magnetism across the series are due to the addition of an extra electron per Ni to the 3d band of the system.

Two sulfide solid solutions - $RbCo_{2-x}Ni_xS_2$ and $CsCo_{2-x}Ni_xS_2$ – were identified as an area of potential future work. As $CsCoNiS_2$ remains ferromagnetic like its $CsCo_2S_2$ end member,[3] it is intriguing at what substitution level (value of *x*) antiferromagnetic coupling becomes dominant, like in the selenide analogue. In $RbCoNiS_2$, antiferromagnetism is observed from magnetometry, and while $RbNi_2S_2$ was not synthesised in this work and is not a reported phase, it could be valuable to determine the range of *x* at which the solid solution can be synthesised.

## References

[1] Shatruk, M. (2018) $ThCr_2Si_2$ Structure Type: The 'Perovskite' of Intermetallics. *J. Solid State Chem.*, *272*, 198–209. https://doi.org/10.1016/j.jssc.2019.02.012.

[2] Rotter, M.; Tegel, M.; Johrendt, D. (2008) Superconductivity at 38 K in the Iron Arsenide $(Ba_{1-x}K_x)Fe_2As_2$. *Phys. Rev. Lett.*, *101*, 107006. https://doi.org/10.1103/PhysRevLett.101.107006.

[3] Jinhu, Y., Chen, B., Wang, H., Mao, Q., Imai, M., Yoshimura, K., Fang, M. (2013) Magnetic Properties in Layered $ACo_2Se_2$ (A = K, Rb, Cs) with the $ThCr_2Si_2$-Type Structure. *Phys. Rev. B*, *88*, 064406. https://doi.org/10.1103/PhysRevB.88.064406.

[4] Neilson, J. R.; Llobet, A.; Stier, A.; Wu, L.; Wen, J.; Tao, J.; Zhu, Y.; Tesanovic, Z.; Armitage, N.; McQueen, T. M. (2012) Mixed-Valence-Driven Heavy-Fermion Behavior and Superconductivity in $KNi_2Se_2$. *Phys. Rev. B*, *86*, 054512. https://doi.org/10.1103/PhysRevB.86.054512.

[5] Zhongnan, G.; Zhang, H.; Wang, D.; Han, B.; Jin, S.; Yuan, W. (2016) Ferromagnetic Interlayer Interaction in $KCo_2Se_{2-x}S_x$ ($0 \leq x \leq 2$) and its Chemical Origin. *Dalton Trans.*, *45*, 8248–8252. https://doi.org/10.1039/c6dt00731g.

[6] Ronneteg, S.; Berger, R.; Levitin, R. Z.; Popova, E. A.; Scherbov, R. M.; Vasiliev, A. N. (2004) Longitudinal Spin Fluctuations in Thermal and Magnetic Properties of $TlCo_2Se_{2-x}S_x$. *J. Magn. Magn. Mater.*, *281*, 388–93. https://doi.org/10.1016/j.jmmm.2004.05.002.

[7] Jianwei, H.; Wang, Z.; Pang, H.; Wu, H.; Cao, H.; Mo, S. K.; Rustagi, A.; Kemper, A. F.; Wang, M.; Yi, M.; Birgeneau, R. J. (2021) Flat-Band-Induced Itinerant Ferromagnetism in $RbCo_2Se_2$. *Phys. Rev. B*, *103*, 165105. https://doi.org/10.1103/PhysRevB.103.165105.

[8] Juanjuan, L.; Sheng, J.; Luo, W.; Wang, J.; Bao, W.; Yang, J.; Fang, M.; Danilkin, S. A. (2018) A Single-Crystal Neutron Diffraction Study on Magnetic Structure of $CsCo_2Se_2$. *Chinese Phys. B*, *27*, 117401. https://doi.org/10.1088/1674-1056/27/11/117401

[9] Neilson, J. R.; McQueen, T. M.; Llobet, A.; Wen, J.; Suchomel, M. R. (2011) Charge Density Wave Fluctuations, Heavy Electrons, and Superconductivity in $KNi_2S_2$. *Phys. Rev. B*, *87*, 045124. https://doi.org/10.1103/PhysRevB.87.045124.

[10] Bacsa, J.; Ganin, A. Y.; Takabayashi, Y.; Christensen, K. E.; Prassides, K.; Rosseinsky, M. J.; Claridge, J. B. (2011) Cation vacancy order in the $K_{0.8+x}Fe_{1.6-y}Se_2$ system: Five-fold cell expansion accommodates 20% tetrahedral vacancies *Chem. Sci.*, *2*, 1054-1058. https://doi.org/10.1039/C1SC00070E.

[11] Lei, H.; Petrovic, C. (2011) Anisotropy in transport and magnetic properties of $K_{0.64}Fe_{1.44}Se_2$. *Phys. Rev. B*, *83*, 184504. https://doi.org/10.1103/physrevb.83.184504.

[12] Lei, H.; Abeykoon, M.; Wang, K.; Bozin, E.S.; Ryu, H.; Graf, D.; Warren, J.B.; Petrovic, C. (2014) Physical Properties of $K_xNi_{2-y}Se_2$ Single Crystals. *J. Phys. Condens. Mat.*, *26*, 015701. https://doi.org/10.1088/0953-8984/26/1/015701.

[13] Ying, T.-P.; Wang, G.; Jin, S.-F.; Shen, S.-J.; Zhang, H.; Zhou, T.-T.; Lai, X.-F.; Wang, W.-Y.; Chen, X.-L. (2013) Exploring FeSe-based superconductors by liquid ammonia method. *Chinese Phys. B*, *22*, 087412. https://doi.org/10.1088/1674-1056/22/8/087412

[14] Hofmann, W. K.; Jeitschko W. (1984) Structural Investigations of Ternary Lanthanoid and Uranium Nickel Phosphides. *J. Solid State Chem.*, *51*, 152–158. https://doi.org/10.1016/0022-4596(84)90328-1.

[15] Jeitschko, W.; Hofmann, W.K.; Terbüchte, L.J. (1988) Lanthanoid and Uranium Nickel Arsenides with $CaBe_2Ge_2$- and $ThCr_2Si_2$-Type Structures. *Journal of the Less-Common Metals*, *137*, 133–142. https://doi.org/10.1016/0022-5088(88)90081-1.

[16] Gvozdetskyi, V.; Hlukhyy, V.; Gladyshevskii, R.; Fässler, T. F. (2016) Crystal Structure and Magnetic Properties of $SrNi_{2-x}Sb_2$. *Z. Anorg. Allg. Chem.*, *641*, 1859–1862. https://doi.org/10.1002/zaac.201500518.

[17] Bobev, S.; Xia, S.Q.; Bauer, E.D.; Ronning, F.; Thompson, J.D.; Sarrao, J.D. Nickel Deficiency in $RENi_{2-x}P_2$ (RE = La, Ce, Pr). (2014) Combined Crystallographic and Physical Property Studies. *J. Solid State Chem.*, *182*, 1473–1480. https://doi.org/10.1016/j.jssc.2009.03.014.

[18] Thompson, C.M.; Tan, X.; Kovnir, K.; Garlea, V.O.; Gippius, A.A.; Yaroslavtsev, A.A.; Menushenkov, A.P.; Chernikov, R.V.; Büttgen, N.; Krätschmer, W.; Zubavichus, Y.V.; Shatruk, M. (2014) Synthesis, Structures, and Magnetic Properties of Rare-Earth Cobalt Arsenides, $RCo_2As_2$ (R = La, Ce, Pr, Nd). *Chem. Mater.*, *26*, 3825-3837. https://doi.org/10.1021/cm501522v.

[19] Newmark, A. R.; Huan, G.; Greenblatt, M.; Croft, M. (2014) Magnetic Ordering in $TlCo_{2-x}Ni_xSe_2$ with the $ThCr_2Si_2$ Structure. *Solid State Commun.*, *71*, 1025–1032. https://doi.org/10.1016/0038-1098(89)90584-X.

[20] Broddefalk, A.; Nordblad, P.; Berger, R. (2000) Structural and Magnetic Properties of $TlCo_{2-x}Cu_xSe_2$, $0 \leq x \leq 1$. *Physica B*, *288*, 1317–1318. https://doi.org/10.1016/S0921-4526(99)02591-0.

[21] Zhou, X.; Wilfong, B.; Vivanco, H. K.; Paglione, J.; Brown, C. M.; Rodriguez, E. E. (2016) Metastable Layered Cobalt Chalcogenides from Topochemical Deintercalation. *J. Am. Chem. Soc.*, *138*, 16432–16442. https://doi.org/10.1021/jacs.6b10229.

[22] Chen H.; Yang, J.; Cao, C.; Li, L.; Su, Q.; Chen, B.; Wang, H.; Mao, Q.; Xu, B.; Du, J.; Fang M. (2016) Superconductivity in a new layered nickel selenide $CsNi_2Se_2$. *Supercond. Sci. Technol.*, *29*, 045008. https://doi.org/10.1088/0953-2048/29/4/045008.

[23] Chavez-Angel, E.; Reuter, N.; Komar, P.; Heinz, S.; Kolb, U.; Kleebe, H. J.; Jakob, G. (2019) Subamorphous Thermal Conductivity of Crystalline Half-Heusler Superlattices. *Nanoscale and Microscale Thermophysical Engineering*. *23*, 1–9. https://doi.org/10.1080/15567265.2018.1505987.

[24] Hallensleben, P.; Scholz, F.; Thome, P.; Schaar, H.; Steinbach, I.; Eggeler, G.; Frenzel, J. (2019) On crystal mosaicity in single crystal Ni-based superalloys. *Crystals*, *9*(3), 149. https://doi.org/10.3390/cryst9030149.

[25] Bannikov, V.; Ivanovskii, A. (2013). Trends in structural, electronic properties, Fermi surface topology, and inter-atomic bonding in the series of ternary layered dichalcogenides $KNi_2S_2$, $KNi_2Se_2$, and $KNi_2Te_2$ from first principles calculations. *Physica B: Condensed Matter*, *418*, 76–80. https://doi.org/10.1016/j.physb.2013.02.035.

[26] Bannikov, V.; Shein, I.; Ivanovskii, A. (2011). Structural, electronic, magnetic and elastic properties of tetragonal layered diselenide $KCo_2Se_2$ from first principles calculations. *Physica B: Condensed Matter*, *407*(2), 271–275. https://doi.org/10.1016/j.physb.2011.10.046.

# Chapter 4. Investigation of non-stoichiometry in Fe-based superconductors with the '1144' structure type

## 4.1 Introduction

### *4.1.1 The 1144 structure type*

Since their discovery in 2008 by Kamihara *et al*., Iron-based superconductors (IBSCs) have garnered considerable interest due to their rich structural variety, high critical temperatures ($T_c$), which mark the onset temperature of the superconducting regime, and high critical current densities ($J_c$).[1] Their characteristic layered structures contain Fe*Pn* or Fe*Ch* tetrahedra (*Pn* = pnictogen atom, *Ch* = chalcogen), which is where superconductivity is believed to operate.[1] The first IBSC reported was LaOFeAs (Figure 4.1), which undergoes a transition to a superconducting state upon substitution with $F^-$ ions on the oxygen site, which increases the electron count. The $T_c$ of this phase was reported at 26 K, and it was soon increased to 43 K by substitution of Sm for La.[2] Compounds with just FeSe layers are superconducting and are classed as '11' IBSCs, to describe the stoichiometry of the constituent elements, shown in Figure 4.1.[3] When an electropositive atom is inserted between the superconducting FeSe sheets, a new structural family is observed – 122 IBSCs, examples of which include $BaFe_2As_2$, where superconductivity emerges upon aliovalent substitution with K in $(Ba_{1-x}K_x)Fe_2As_2$.[4,5,6] These adopt the versatile $ThCr_2Si_2$-type structure (Space group n. 139, *I*4/*mmm*) and members of this family have in general higher $T_c$ than those observed for 11-type members.[7,8] In 2016, Iyo *et al*. reported a new structure type of IBSCs: the 1144 phases have a general formula *Ae*A$Fe_4As_4$ (Space group n.123, *P*4/*mmm*), also written as *Ae*A1144, where *Ae* is an alkaline earth metal (Ca, Sr, Ba), and *A* is an alkali metal (K, Rb, Cs).[9] *Ae*A1144 phase is obtained when *Ae* ions occupy spacer layers between $Fe_2As_2$ layers alternately with *A* ions. This structure type is closely related to the 122- type: *Ae*A1144 can be regarded as a hybrid phase between *Ae*122 and *A*122. *Ae*

and *A* do not occupy crystallographically equivalent sites because of the large differences between their ionic radii, giving rise to symmetry reduction from body-centred tetragonal to primitive tetragonal due to ordering of *Ae* and *A* layers.

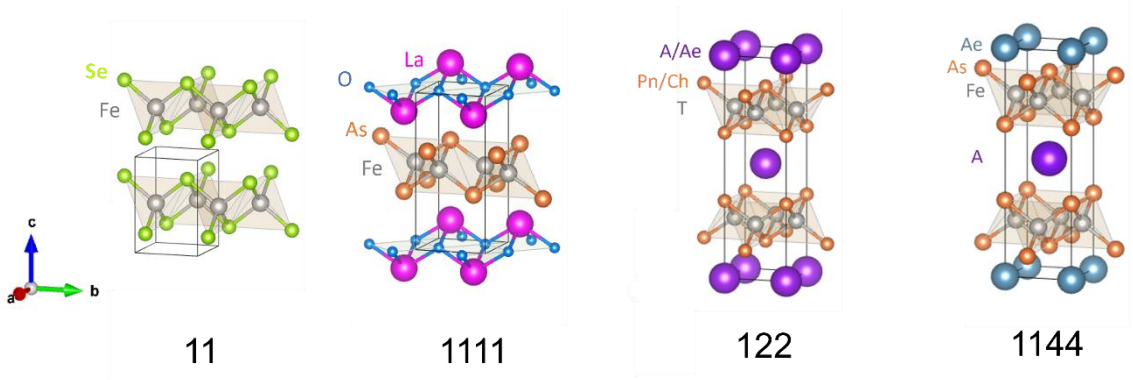


**Figure 4.1** Comparison of 11, 111, 122, and 1144 structure types of IBSCs.

Figure 4.2 (centre) shows the primitive tetragonal structure of *AeA*$Fe_4As_4$ in detail as an intergrowth of two 122 phases; the alternating *Ae* and *A* planes break the body centring, resulting in the loss of *n*-glide planes at $z$ = ¼ and ¾ (red dashed lines).[10] This change brings about two inequivalent As sites (depicted in yellow and orange), which in turn give rise to a distorted FeAs tetrahedron; $\alpha_1$ and $\alpha_2$ tetrahedral angles can be observed.

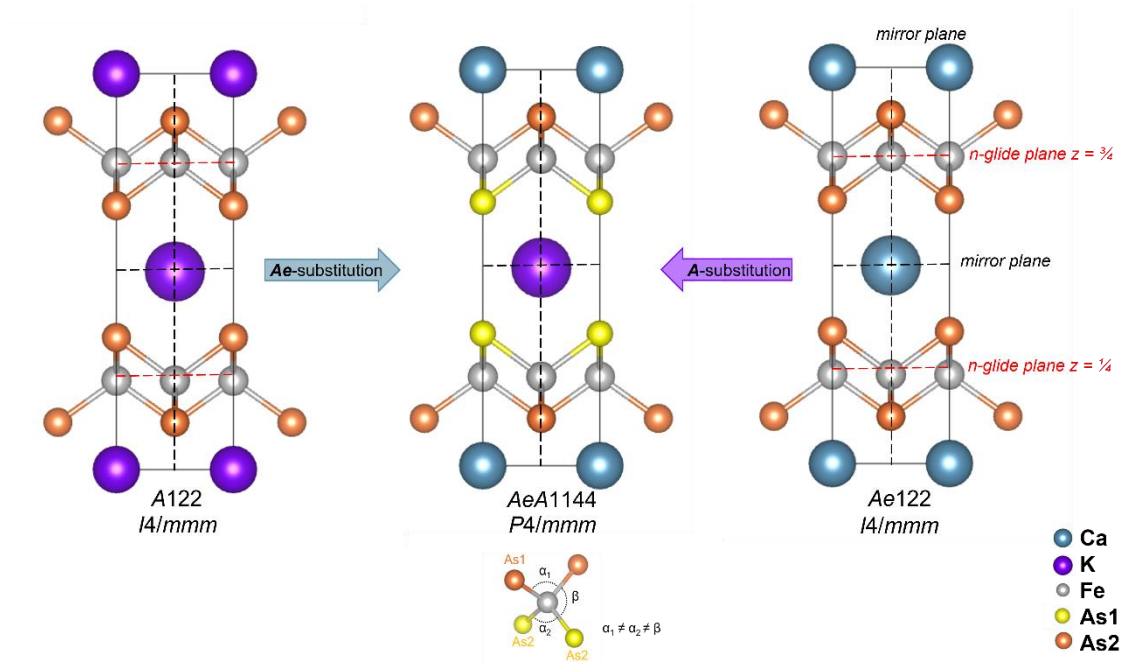


**Figure 4.2** Structure of *AeA*$Fe_4As_4$ (middle) and the distorted FeAs tetrahedron observed in *AeA*1144 phases, shown as an intergrowth of the two constituent 122 phases, *A*122 and *Ae*122.

With a divalent $Ae^{2+}$ and a monovalent $A^+$, the Fe valence is fixed at +2.25 (middle value between +2.0 for *Ae*122 and +2.5 for *A*122), which is found to be ideal for observation of superconductivity in terms of electron count.[9] Tuning the electron count in superconducting materials is of high importance as electron correlations have a strong influence on superconducting properties and heavily depend on the filling of the Fe 3d orbitals.[11] The $d_{xy}$ orbital plays a prominent role as its occupancy and the strength of its correlations impact the SC properties (according to Angle-resolved photoemission spectroscopy[11] and DFT calculations[12]); this $d_{xy}$ orbital is crucial in the formation of the Fermi surface. In the case of $CaKFe_4As_4$, the electron count is ideal with no chemical disorder, as opposed to superconducting 122 systems, such as $(Ba_{1-x}K_x)Fe_2As_2$, where Ba and K are disordered on the *A* site.

In the original paper, Iyo *et al.* found that the 1144 phases do not form solid solutions like 122 phases: the large contrast between the ionic radii of the $Ae^{2+}$ and $A^+$ ions does not allow them to occupy the same atomic positions and as a consequence, the *Ae/A* ratio is fixed at 1:1 (away from this ratio there is phase separation).[9] The large difference in ionic radii was found to be crucial for formation of 1144

phases as the constituent ions do not mix with each other in one layer. Iyo *et al.* quantified the large difference in radii to be equal or larger than 0.35 Å ($\Delta r^{Ae-A} > 0.35$ Å) for 1144 phase formation, as opposed to cases when the $\Delta r^{Ae-A}$ is too small, a mixed cation 122 phase is formed.[9] In addition, a small difference of no more than 0.07 Å between the *a* lattice parameters of the constituent 122 phases is required ($\Delta a = | a_{Ae122} - a_{A122} | < 0.07$ Å) to avoid phase separation. These laws for 1144 phase formation are summarised graphically in Figure 4.3 (from Ref.9). The red square depicts the region of formation for 1144 phases in terms of the limiting parameters Δa and $\Delta r^{Ae-A}$.[9]

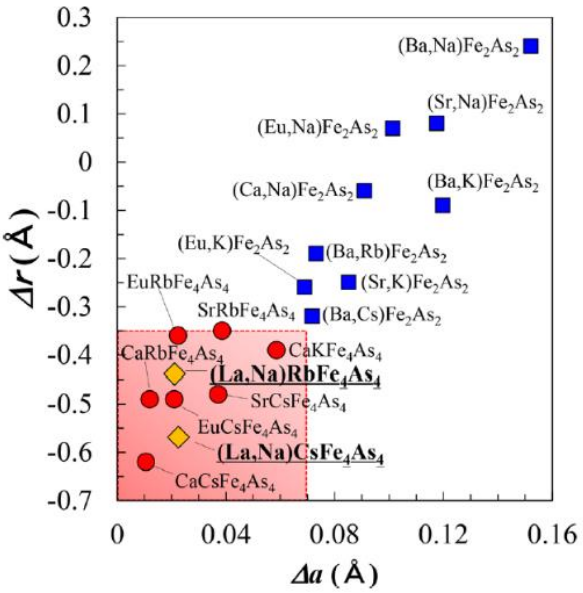


**Figure 4.3** Diagram of *Ae*A1144 phase formation according to the limiting parameters Δa and $\Delta r^{Ae-A}$ (the difference in radii of *Ae* and *A*). Diagram adapted from Reference [9].

### *4.1.2 Non-stoichiometry in 1144 compounds*

Iyo *et al.* describe a certain robustness of $T_c$ against compositional deviations arising from the fact that *Ae*A1144 phases are line phases (*i.e.* no disorder is allowed to be introduced into the structure), which means that $T_c$ does not change despite small changes in stoichiometry of starting elements. This gives an advantage of a well-defined superconducting transition. In order to probe non-stoichiometry in $CaKFe_4As_4$, Iyo *et al.* attempted to introduce excess Ca in $CaKFe_4As_4$. Their substitution level was large - nominal composition of their target phase being $Ca_{1.5}K_{0.5}Fe_4As_4$ - and the resulting product was a mixture of $0.5CaKFe_4As_4$ and $CaFe_2As_2$. The $T_c$ of this product remained unchanged compared to that of the stoichiometric sample.[9] Four years later, the same group of

chemists reported on introduction of defects in $CaKFe_4As_4$, with the intended goal to enhance its critical current density ($J_c$). The $J_c$ parameter describes the maximum current density a superconductor can carry without resistance and is determined by the material's ability to trap vortices (quantized units of magnetic flux). Vortex trapping or also called 'vortex-pinning' occurs when defects or impurities act as pinning sites and disrupt the movement of the vortices through a magnetic lattice. This results in a structure where superconductivity is locally disrupted, and the vortices have smaller energy (are pinned).[13,14] In the case of $CaKFe_4As_4$, the improvement of $J_c$ was successful by introduction of nanoscale intergrowths of $CaFe_2As_2$ coherently grown in the CaK1144 matrix by targeting a non-stoichiometric product with following starting reactants ratios : Ca:K:FeAs weighed as 1:1.1:10.[13] The intergrowth was realised with dimensions of ~5.5 nm along *c* axis which corresponds to ~ 5 unit cells, revealed by Scanning transmission electron microscopy (STEM).[13] This is graphically shown in Figure 4.4 which was made according to the STEM image shown in Reference 13. This finding showed that the 1144 structure allowed for violated alternation of Ca and K layers, while the local FeAs-layer structure was maintained.[13] No intergrowths of $KFe_2As_2$ or FeAs were observed by high resolution STEM in the sample, whose exact composition was not revealed. Furthermore, no trace of separate $CaFe_2As_2$ (Ca122) and $KFe_2As_2$ (K122) phases was observed within the resolution of lab X-ray diffractometer.

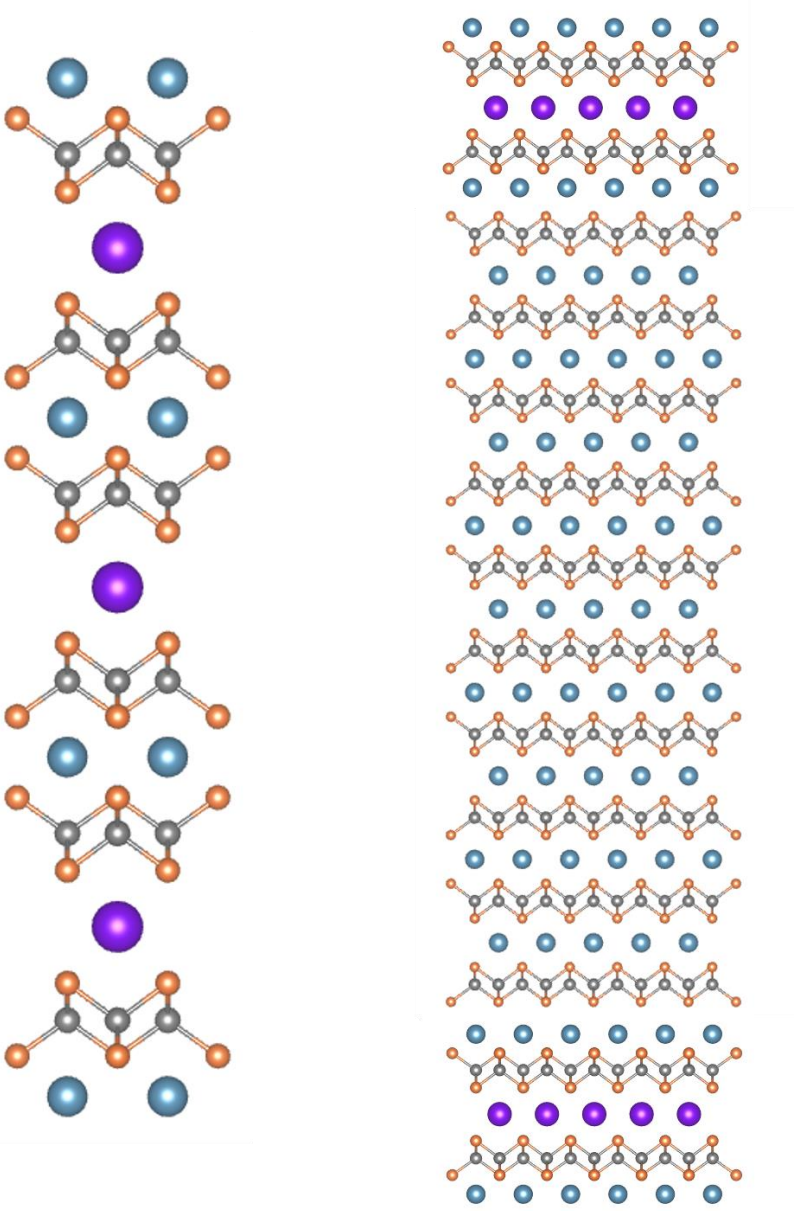

**Figure 4.4** Left: Strictly alternating layered structure of $CaKFe_4As_4$ (z = 3). Right: A schematic representation of Ca122 intergrowth (defect region) in CaK1144 matrix viewed along [100] axis.

There are, however, reports of successful doping in *AeA*1144; Xiyang *et al.* report on pressure dependence of the magnetic and superconducting transitions in $CaK(Fe_{1-x}Ni_x)_4As_4$ and $CaK(Fe_{1-x}Co_x)_4As_4$.[15] Here, the substitution is on the transition metal sites and the levels are very small and upper limit was stated as x = 0.049(1) for both compounds, which is about 5% substitution level. Reports of substitution on the As site include a decrease in $T_c$ upon incorporation of phosphorus in $RbEuFe_4As_4$ single crystal; here the upper substitution limit is again fairly low: x = 0.12(3) in

$RbEuFe_4(As_{1-x}P_x)_4$.[16] Recently, Duchenko *et al.* reported mechanochemical synthesis of Ba- and Na-doped $CaKFe_4As_4$.[17] Here, 20% Ba-substitutions and 40% Na-substitutions are achieved in two solid solutions, namely $Ca_{0.8}Ba_{0.2}KFe_4As_4$ and $CaK_{0.6}Na_{0.4}Fe_4As_4$. The authors confirmed the presence of the target 1144 phase by identification of the (001) reflection in the Synchrotron PXRD substituted phases, as this is a characteristic reflection of 1144 compounds, representative of the ordered stacking of planes occupied by alternating *Ae* and *A* ions, which is absent in the body centred cubic cell of 122 phases. According to Equation 4.1, the structure factor is equal to zero when ($h + k + l$) = odd in a body-centred cell, shown in Figure 4.5 with the atomic coordinates of constituent atoms.

$$F_{hkl} = \sum_{j=1}^{n} f_j \left(\cos 2\pi\left(hx_j + ky_j + lz_j\right) \mathrm{q} + i \sin 2\,\pi\left(hx_j + ky_j + lz_j\right)\right) q \qquad \text{(Equation 4.1)}$$

$$F = \sum_i^n f_i \, e^{2\pi i \,(hx_i + ky_i + lz_i)} \qquad \text{(4.1 continued)}$$

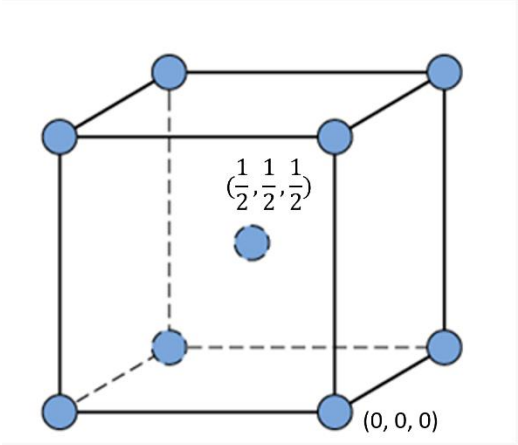


**Figure 4.5** Body-centred cell (cubic shown in this case).

$$i = 1 \quad x_i = 0 \quad y_i = 0 \quad z_i = 0$$

$$i = 2 \quad x_i = {}^1\!/_2 \quad y_i = {}^1\!/_2 \quad z_i = {}^1\!/_2$$

$$F = f\,(e^{2\pi i\,(0+0+0)} + e^{2\pi i\left(\frac{1}{2}h + \frac{1}{2}k + \frac{1}{2}l\right)}) \qquad \text{Equation 4.2}$$

$$F = f\,(e^{0} + e^{\pi i\,(h+k+l)}) \qquad \text{4.2 continued}$$

$$F = f\,(1 + e^{\pi i\,(h+k+l)}) \qquad \text{4.2 continued}$$

Where F = 0 $$e^{2\pi i(h+k+l)} = -1 \qquad \text{4.2 continued}$$

From Euler's equation, $e^{n\pi i} = (-1)^n$ , where $n$ is odd, $e^{n\pi i} = -1$, giving rise to destructive interference (F = 0). From Equations 4.1 and 4.2 we can conclude that any plane with $h+k+l$ odd will give destructive interference, and will represent a systematic absence in the diffraction pattern. This is the reason why in 122 phases the (001) reflection is absent, while in 1144 phases (primitive *P*4/*mmm* cell) this reflection is allowed.

Most literature reports on doped *AeA*1144 phases are theoretical and computational studies probing superconducting regimes,[10,18] where the studies rely on one crystal sample and our literature search revealed only a handful of chemical studies probing testing the line-phase nature of AeA1144 compounds using diffraction techniques.[15,16,17] The investigations presented in this thesis probe the non-stoichiometry in $CaKFe_4As_4$ by varying the *Ae:A* ratios, and by introducing phosphorus on As site in $CaKFe_4As_4$. In this way, we investigate the possibility of introduction of disorder in the robust 1144 structure using high resolution X-ray diffraction and magnetometry.

## 4.2 Synthesis and characterisation of $Ca_{1+x}K_{1-x}Fe_4As_4$

### *4.2.1 Synthesis of $Ca_{1+x}K_{1-x}Fe_4As_4$*

The synthesis of $Ca_{1+x}K_{1-x}Fe_4As_4$ with $0 \leq x \leq 0.25$ was carried out in the same way as was reported for the stoichiometric $CaKFe_4As_4$.[19] Polycrystalline $Ca_{1+x}K_{1-x}Fe_4As_4$ was prepared by a solid-state reaction of stoichiometric amounts of precursors CaAs, KAs, and $Fe_2As$ (synthesis of precursors detailed in Section 4.2.1.1 below). The precursors were combined in a mortar and ground for ~5 minutes to allow for good contact of powder grains. The powder was then pelletised and the pellet was placed in a tantalum (Ta) tube which was weld-sealed under Ar gas. The sealed Ta tube was then placed in a silica tube and vacuum-sealed. Three heating cycles were employed to obtain highly crystalline product; at each cycle, the tube was placed in a preheated oven and quenched in ice water at the end of the cycle. The first heating was at 950ºC/6hrs, the second was again at 950ºC/6hrs, and

the third was at 950ºC/2hrs. Between each heating cycle, the pellet was ground and pelletised under a uniaxial pressure of 3MPa.

#### *4.2.1.1 Precursor preparation*

High purity starting reagents including Ca chunks (Sigma Aldrich, 99.99%), Fe powder (Alfa Aesar, 99.99%), K (Alfa Aesar, 99.95%) and As (Alfa Aesar, 99.99%) pieces were used. Firstly, precursors CaAs and KAs were prepared by placing stoichiometric amounts of Ca or K and As in a Ta tube, which was then weld sealed in an Ar atmosphere. Such a sealed Ta tube was then sealed in an evacuated silica tube. The sealed tube was heated to 860 °C / 30h for CaAs and to 650 °C / 12h for KAs (both heating rates were $1^{o}min^{-1}$ and cooling rates were natural oven cooling by turning the oven off). A similar method was used to prepare $Fe_2As$ by heating Fe and As powders at 700 °C / 12h.

### 4.2.2 Room temperature *PXRD*

As opposed to Iyo *et al.*'s work,[9] we attempted low substitution levels in $CaKFe_4As_4$: solid solution $Ca_{1+x}K_{1-x}Fe_4As_4$ with $0 \leq x \leq 0.25$. The samples synthesised in this series contained impurities at varying quantities, namely $KFe_2As_2$, $CaFe_2As_2$, $Ca_4As_3$, and $K_5As_4$. The PXRD pattern of the composition synthesised at highest purity is shown in Figure 4.6. Curiously, the purest sample obtained was for x = 0.15, not for the stoichiometric sample.

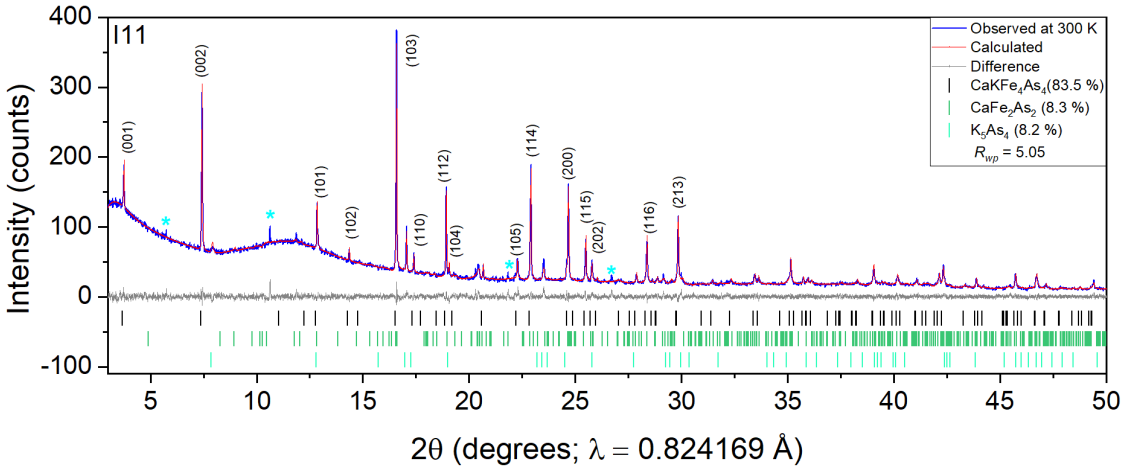


**Figure 4.6** Synchrotron PXRD pattern of non-stoichiometric $CaKFe_4As_4$ measured using the MAC detector at I11 (Diamond): nominal composition is $Ca_{1.15}K_{0.85}Fe_4As_4$. High resolution PXRD revealed two secondary phases - $K_5As_4$ and $CaFe_2As_2$ - present in the annealed sample.

Figure 4.7 shows Synchrotron PXRD patterns of the series collected at λ = 0.8242 Å, which could all be indexed according to the tetragonal *P*4/*mmm* space group of the parent stoichiometric compound using Rietveld refinement. The intensity is normalised for easy visual comparison between the individual members.

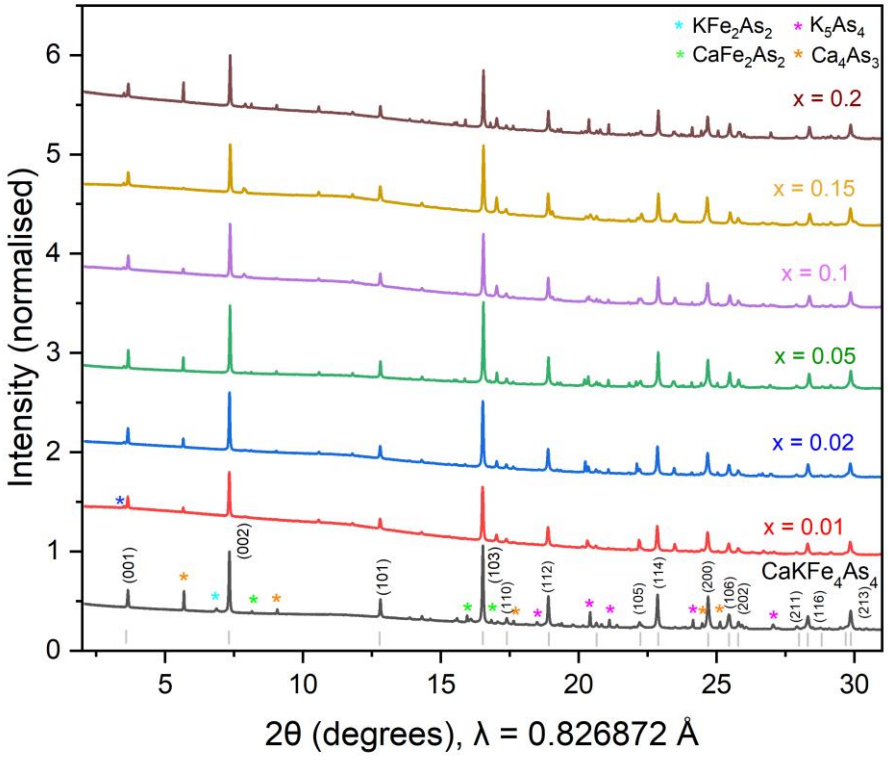


**Figure 4.7** Synchrotron PXRD patterns of non-stoichiometric $Ca_{1+x}K_{1-x}Fe_4As_4$ $_4$, $0 \leq x \leq 0.25$. Blue asterisk represents an unknown impurity.

Figure 4.8 shows enlarged images of two main low-angle peaks: (001) and (002) reflections. Both show a slight shift to higher angles, with the characteristic (001) peak of 1144 phases moving from 3.65 2$\theta$ degrees for x = 0 to 3.67 2$\theta$ degrees for x = 0.25, and the main (002) peak moving from 7.33 2$\theta$ degrees for x = 0 to 7.36 2$\theta$ degrees for x = 0.25 upon doping with small amounts of Ca. A much more pronounced shift to higher angles was expected, especially at high substitution levels, as the difference in ionic radii of $Ca^{2+}$ and $K^{+}$ is large. The presence of the characteristic (001) reflection of *P*4/*mmm* symmetry, representative of the ordered arrangement of *Ae:A* ions along the stacking axis,

highlights that the target phase does not disappear with increasing substitution levels. This reflection is absent in 122 phases which show a higher average symmetry (*I*4/*mmm*) due to *A* and *Ae* ions randomly occupying the same crystallographic site. The small shifts in these reflections to higher angles signal slight unit cell contraction upon substitution with smaller Ca ions, hinting at a small degree of solid solution formation ($r_{Ca}$ = 1.12 Å, $r_K$ = 1.56 Å). The PXRD data present in Figure 4.8 were collected on the Mythen detector of I11 beamline at Diamond, which can cause some slight shifting in peak position. This can sometimes be mitigated by measuring on the MAC detector, which was not done in this case. Therefore, the very slight shift to higher angles of (002) peak in $Ca_{1+x}K_{1-x}Fe_4As_4$ patterns could be caused by the instrument.

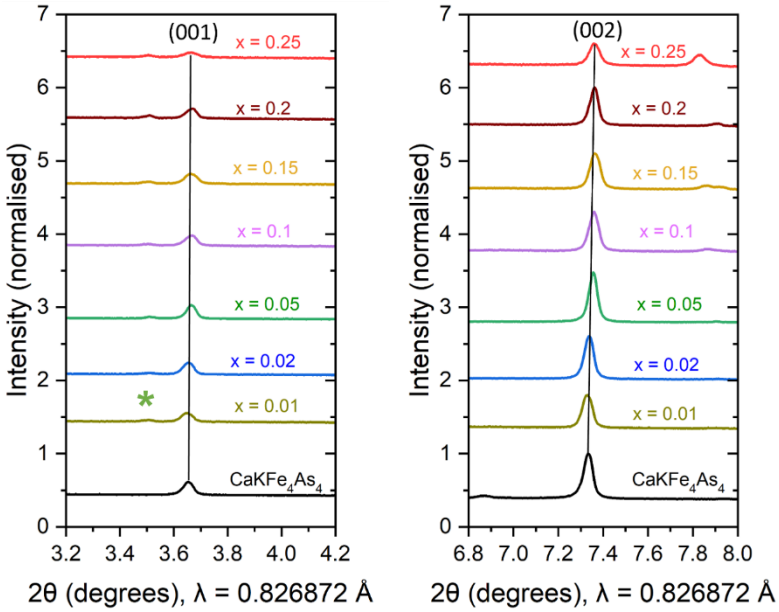


**Figure 4.8** Left: An enlarged image of the (001) peak. Right: Image of the (002) peak, which reveals slight gradual shift to higher angles with increasing *x* (Ca content). The green asterisk marks an unidentified impurity.

The mole fractions of impurity Ca122 and K122 phases were calculated from Synchrotron PXRD and the variation of the amounts of these impurities across the series is shown in Figure 4.9. The mole fraction of Ca122 increases with increasing Ca nominal content (except for the x = 0.15 member, which was synthesised to the highest purity). This seems to suggest that instead of incorporation of Ca into the structure of $CaKFe_4As_4$, the excess calcium forms the Ca122 phase,

which is thermodynamically very stable compared to CaK1144. This may happen as intergrowth on small scales, but would require precise microscopy techniques to confirm the hypothesis. Also, the high molar percentages of Ca122 and K122 show that the system might not be at equilibrium. The 1144 phases are reported to be difficult to synthesise in pure form, and this study agrees with those reports.

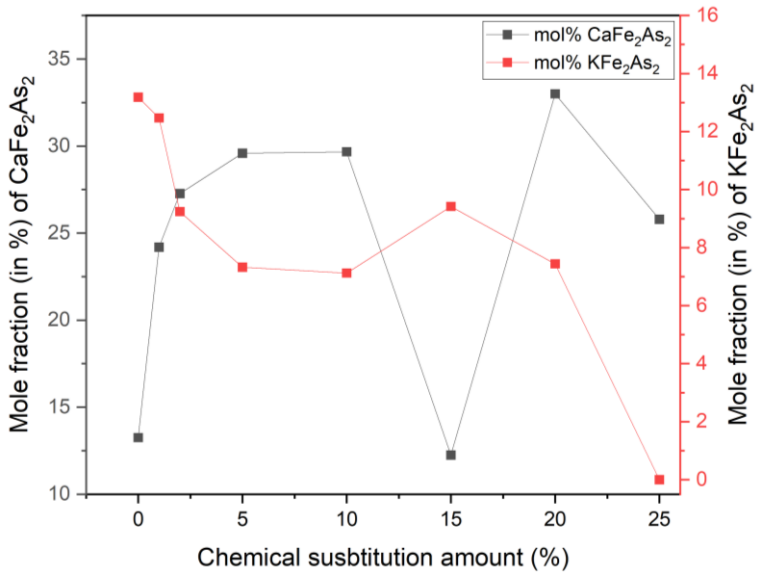


**Figure 4.9** Variation of mole fractions of $CaFe_2As_2$ and $KFe_2As_2$ impurities with *x* in $Ca_{1+x}K_{1-x}Fe_4As_4$ series.

Figure 4.10 shows the variation of lattice parameters *a* and *c* with *x*; *a* parameter (black plot) is found to increase very slightly by 0.0045 Å (by 0.11%), and *c* parameter (red plot) shrinks by 0.07 Å (0.54%) between $0 < x < 0.25$. The large error bars here suggest that there is no real change in lattice parameters between $0 \leq x \leq 0.25$. If a solid solution with Ca and K disordered on the *Ae* and *A* sublattices were to form, we would expect a larger change in lattice parameters; the incorporation of smaller Ca in place of larger K at 25% substitution is comparable (in terms of ionic radii size difference) to Na-substituted $BaFe_2As_2$,[20] when we take into account the ionic radii of 8-coordinated $Ca^{2+}$ (1.12 Å), $K^+$ (1.51 Å), $Na^+$ (1.18 Å), and $Ba^{2+}$ (1.42 Å). In Na-substituted $BaFe_2As_2$, the ionic mismatch is 0.24 Å, while in the ionic mismatch in $CaKFe_4As_4$ is 0.39 Å. In Na-substituted $BaFe_2As_2$, 30% Na substitution causes a 1.3% decrease in *a* parameter and 0.3% increase in *c* parameter.[20,21]

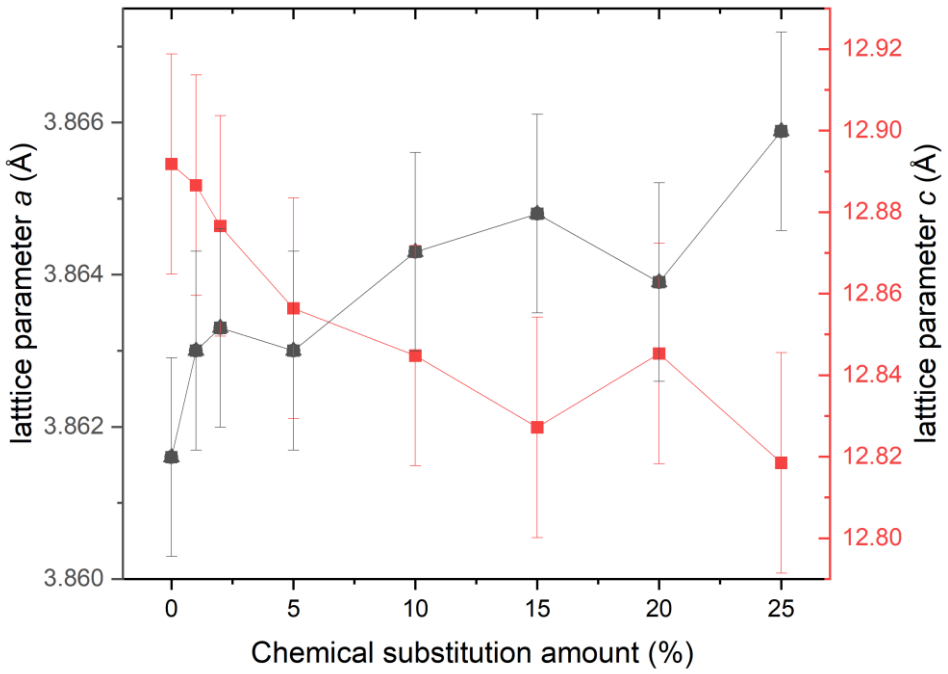


**Figure 4.10** Variation in *a* and *c* lattice parameters with x for $Ca_{1+x}K_{1-x}Fe_4As_4$ with $0 \leq x \leq 0.25$.

Figure 4.11 shows the variation of unit cell volume (*V*) with *x*; a very slight decrease in volume is observed (by 0.33%) between $0 < x < 0.25$, however, the large error bars signal that there no real change across the solid solution. In the case of Na-substituted $BaFe_2As_2$, 30% substitution leads to 2.22% decrease in unit cell volume.[20,21]

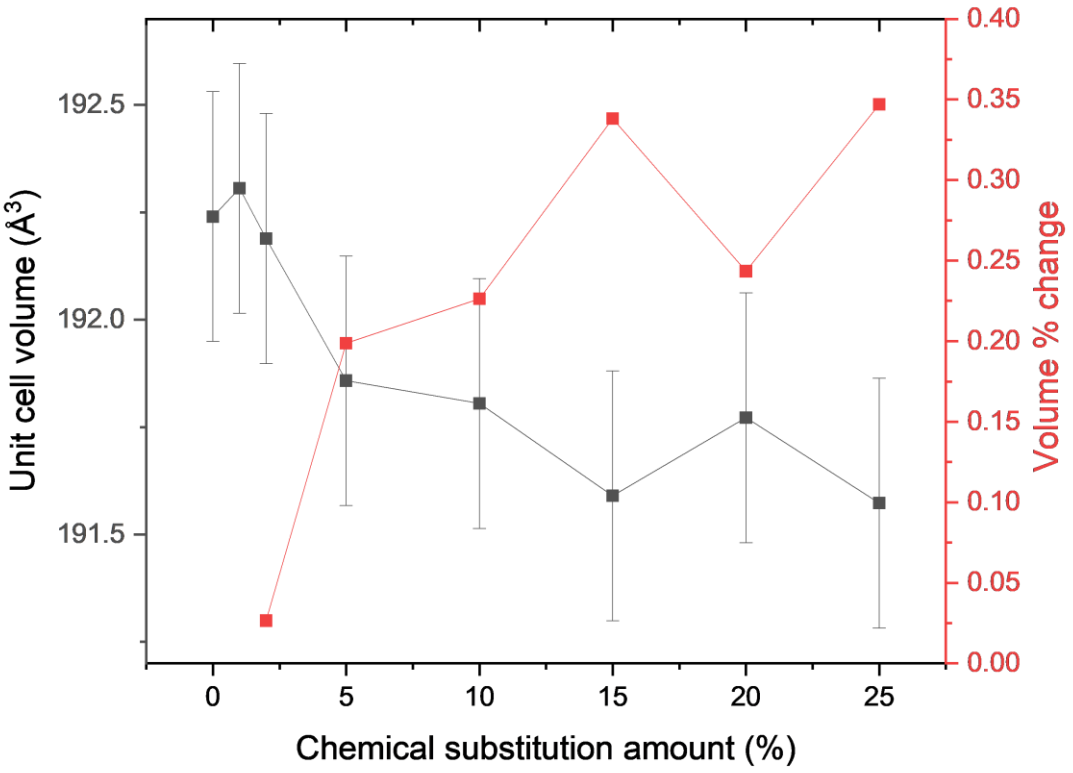


**Figure 4.11** Variation of unit cell volume with *x* for $Ca_{1+x}K_{1-x}Fe_4As_4$ with $0 \leq x \leq 0.25$, also shown as a percentage change (red plot).

Bond lengths and tetrahedral angle ($\delta_{As\text{-}Fe\text{-}As}$) from Synchrotron PXRD data are shown in Figure 4.12. These do not follow any trend with compositional changes, which is not surprising since there are only small changes observed in lattice parameter trends.

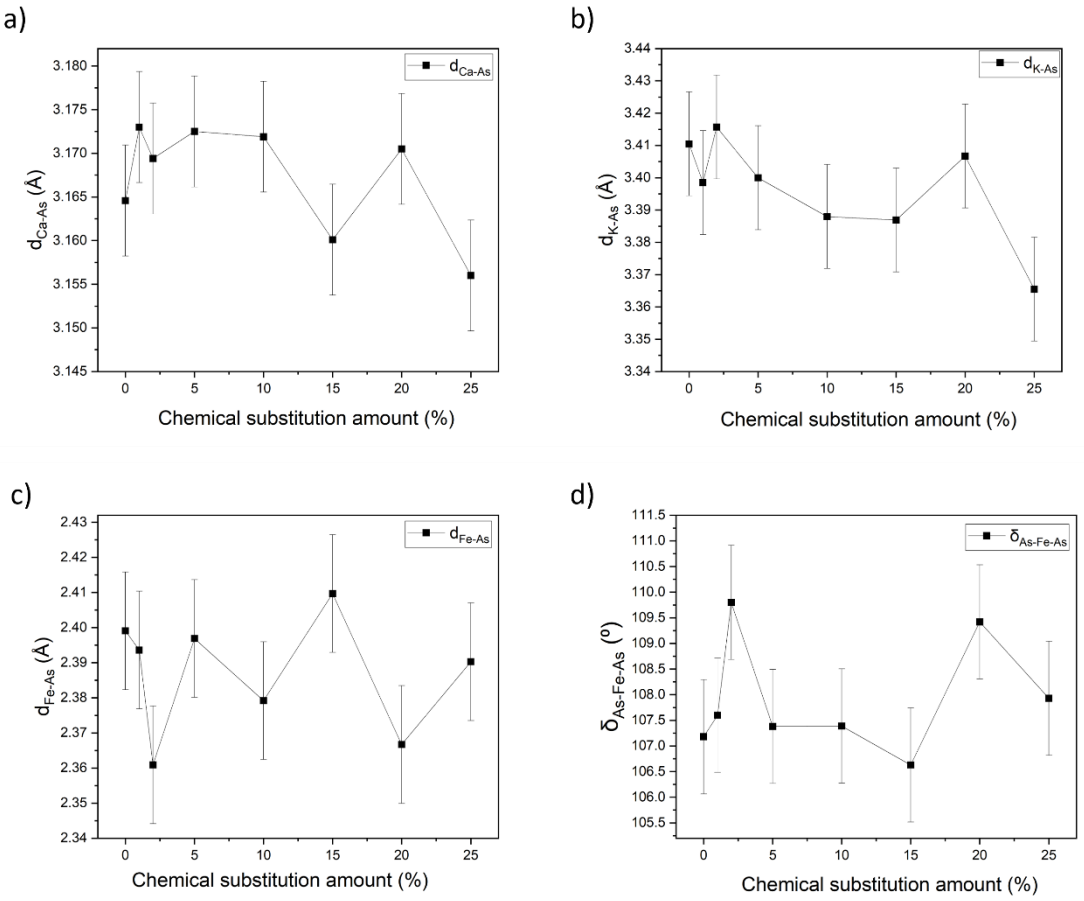


**Figure 4.12** Variation in bond lengths and tetrahedral angle across the $Ca_{1+x}K_{1-x}Fe_4As_4$ series with $0 \leq x \leq 0.25$.

A structural parameter of Fe-based superconductors that was reported to have a significant effect on the superconducting properties is the anion (pnictogen/chalcogen) height ($h_{anion}$).[22,23] It is defined as the shortest distance between the plane of Fe atoms and the neighbouring plane of anions, in the case of $CaKFe_4As_4$ that is As anions (Figure 4.13).[22] It is calculated as the difference in the *z* coordinates of Fe and As atoms multiplied by the *c* lattice parameter:

$$h_{anion} = \Delta z_{Fe-As} \times c_{latt} \qquad \text{Equation. 4.3}$$

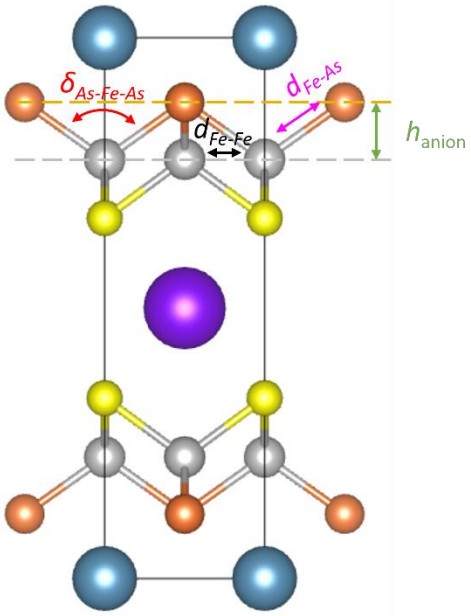


**Figure 4.13** The anion height, $h_{anion}$, of IBSCs, and its relationship to structural parameters, including the Fe-As distance ($d_{Fe\text{-}As}$), Fe-Fe distance within the plane ($d_{Fe\text{-}Fe}$), and tetrahedral angle, $d_{As\text{-}Fe\text{-}As}$.

Kuroki *et al.* proposed that the $h_{anion}$ is a structural parameter that strongly affects $T_c$, which is enhanced by increasing $h_{anion}$.[22] The correlation between $h$ and $T_c$ is comparable to that between $T_c$ and the tetrahedral angle, $\delta_{As\text{-}Fe\text{-}As}$.[23] But it is worth being critical about the parameter as it strongly depends on other structural parameters of IBSCs: the Fe-As distance ($d_{Fe\text{-}As}$), Fe-Fe distance within the plane ($d_{Fe\text{-}Fe}$), and the tetrahedral angle, $\delta_{As\text{-}Fe\text{-}As}$, shown in Figure 4.13. In $CaKFe_4As_4$, the ordering of the cations cannot be easily quantified from X-ray diffraction techniques, as $Ca^{2+}$ and $K^+$ ions are isoelectronic, *i.e.* have the same number of electrons. Therefore, the symmetry breaking caused by disorder of the cations would be most obvious in the As positions, which can be quantified by measuring $h_{anion}$. As the 1144 structure (*P*4/*mmm* symmetry) has two inequivalent As sites, As1 and As2, there are two $h_{anion}$ distances. These are summarised in Table 4.1 for the synthesised compositions in $Ca_{1+x}K_{1-x}Fe_4As_4$ series with $0 \leq x \leq 0.25$ and shown in Figure 4.14. There is no clear trend in the change in anion heights and the large error bars suggest that other than for samples x = 0.15 and 0.25, there is no real change.

**Table 4.1** The anion height ($h_{anion}$) values for $Ca_{1+x}K_{1-x}Fe_4As_4$ series with $0 \leq x \leq 0.25$.

| ***x*** | ***h1*$_{anion}$ (Å)** | ***h2*$_{anion}$ (Å)** |
|---|---|---|
| 0 | 1.418(1) | 1.375(1) |
| 0.01 | 1.412(1) | 1.408(1) |
| 0.02 | 1.378(1) | 1.414(1) |
| 0.05 | 1.376(1) | 1.392(1) |
| 0.1 | 1.410(1) | 1.393(1) |
| 0.15 | 1.463(1) | 1.369(1) |
| 0.2 | 1.367(1) | 1.411(1) |
| 0.25 | 1.406(1) | 1.463(1) |
| ***Average*** | **1.404(1)** | **1.403(1)** |

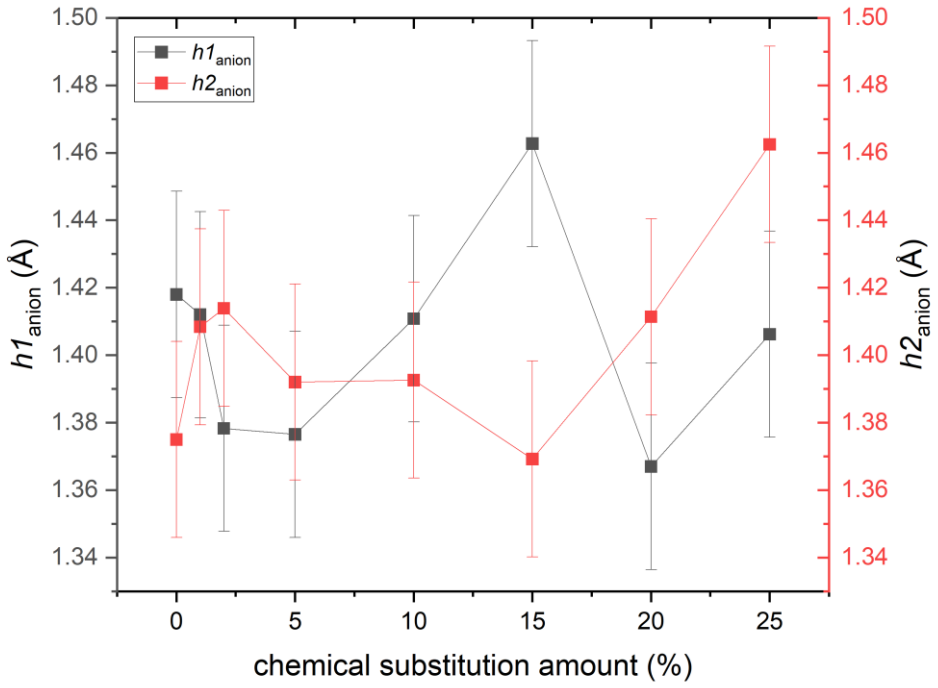


**Figure 4.14** Variations in anion height (*h1* and *h2*) across the $Ca_{1+x}K_{1-x}Fe_4As_4$ series with $0 \leq x \leq 0.25$.

### 4.2.3 Variable temperature SXRD

Structural details of the stoichiometric $CaKFe_4As_4$ were investigated as function of temperature between 100-300 K with high resolution PXRD, shown in Figure 4.15. The unit cell volume and lattice parameters *a* and *c* show a linear increase between 100 – 300 K. The *z* atomic coordinates of the two As sites were refined and remained very close to the room temperature values. There is no evidence for any structural phase transition in this range.

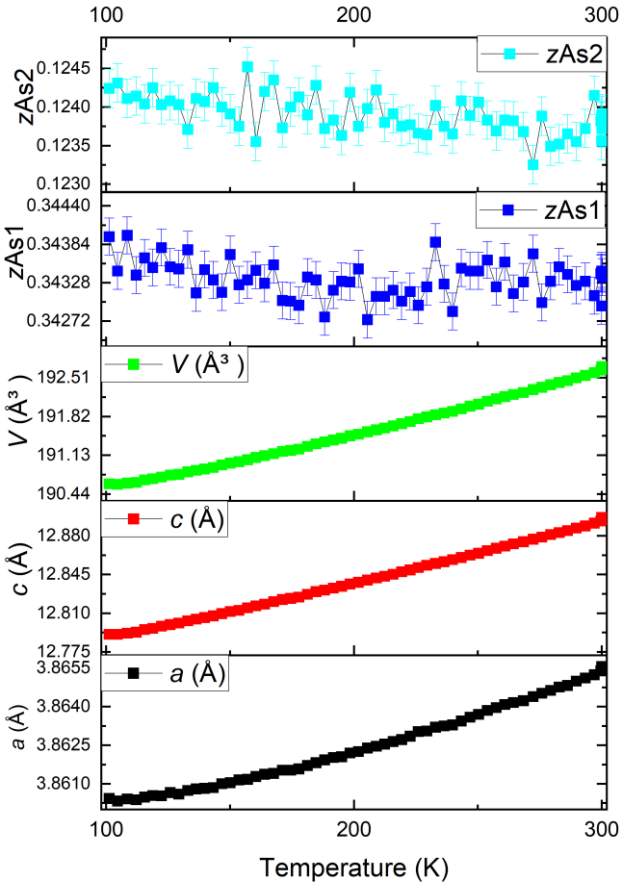


**Figure 4.15** Variable temperature (100-300 K) Synchrotron PXRD data of stoichiometric $CaKFe_4As_4$.

As the $T_c$ of $CaKFe_4As_4$ lies below the temperature range of the cryostat at I11, the structural parameters at $T_c$ were investigated using the Empyrean PheniX instrument with a molybdenum source. The structural parameters are constant in this small temperature range and do not show any variation with temperature (Figure 4.16) through the superconducting transition at 34 K. The PXRD pattern obtained at 15 K is shown in Figure 4.17.

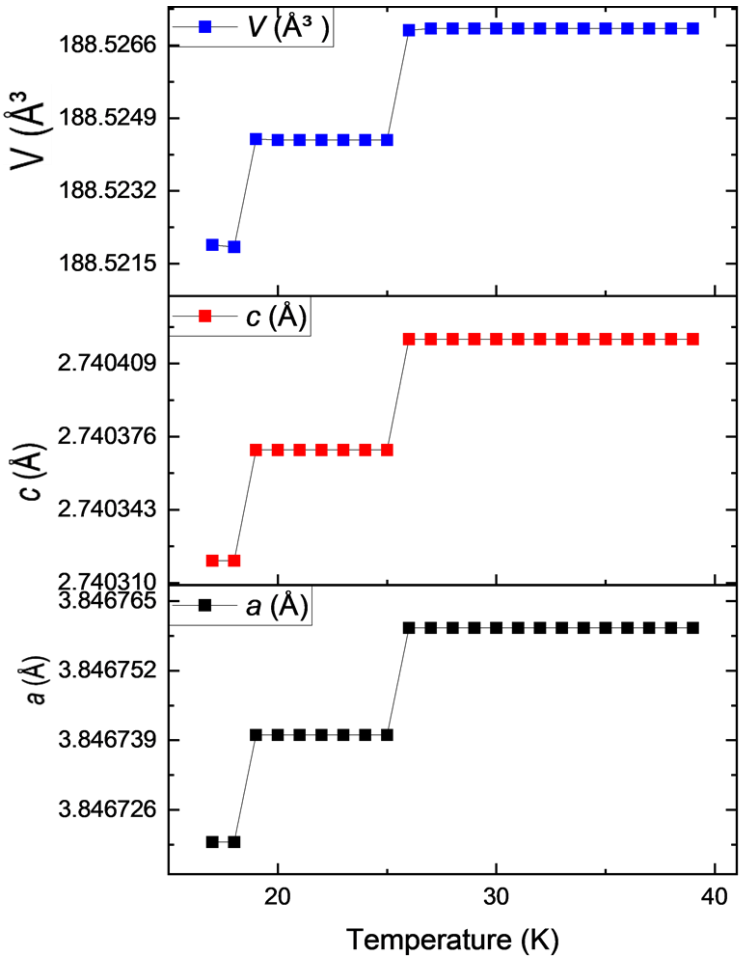


**Figure 4.16** Variable temperature (15-40 K) PXRD data of stoichiometric $CaKFe_4As_4$.

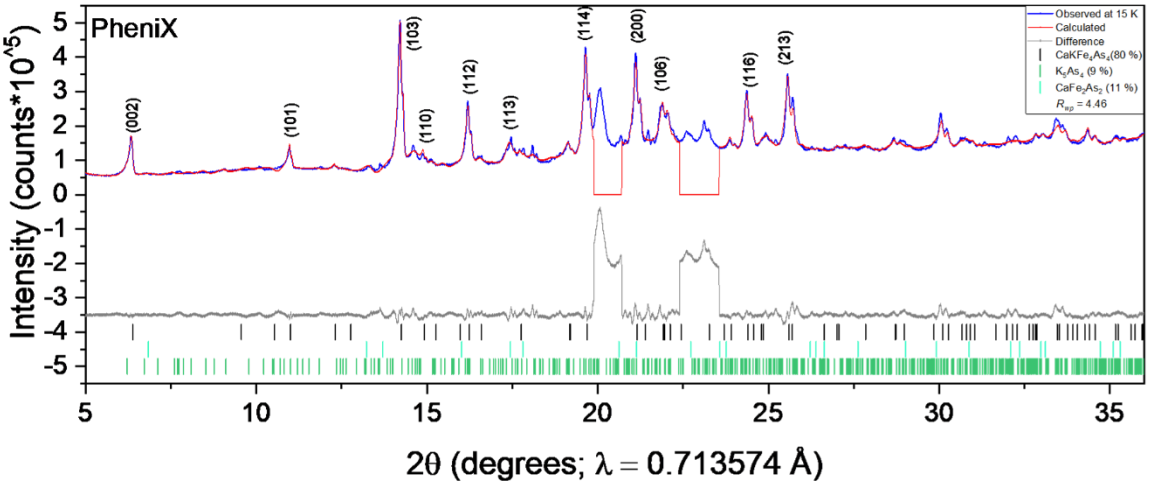


**Figure 4.17** Low-temperature (15 K) PXRD pattern of stoichiometric $CaKFe_4As_4$ measured on Empyrean PheniX instrument. Peaks at 20-20.8º and 22.42-23.55º $2\theta$ belong to the sample holder.

### *4.2.4 Magnetometry of $Ca_{1+x}K_{1-x}Fe_4As_4$*

The $T_c$ values for the members of the $Ca_{1+x}K_{1-x}Fe_4As_4$ series were measured by magnetometry on the MPMS-3 instrument at a small applied field of 20Oe, between temperatures 20 – 50 K. A small applied field is important when studying $T_c$, as the critical fields $H_{c1}$ (the "lower critical field", above which magnetic flux begins to penetrate the superconductor) and $H_{c2}$ (the "upper critical field", where magnetic flux fully penetrates the sample, destroying superconductivity) must not be exceeded. The lower critical field was estimated by a measurement of *M vs H* at 2 K (Figure 4.18). The data in Figure 4.17 show that a field of 20 Oe is not strong enough to penetrate the superconductor, where $H_{c1}$ ~ 1000 Oe. On the other hand, $H_{c2}$, the upper critical field, is extremely high and greatly exceeds 1 T, as reported by Bristow *et al.*[24]

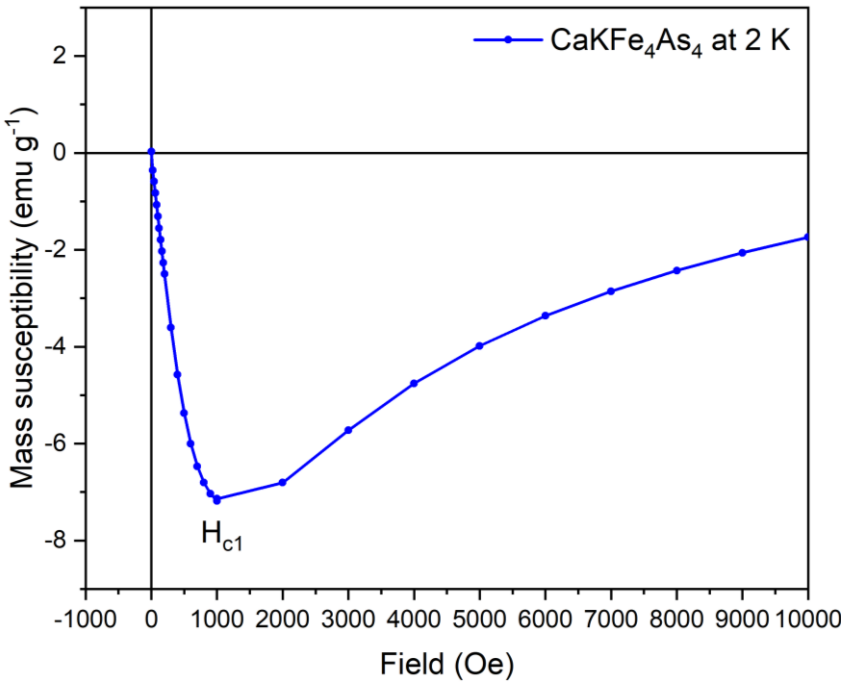


**Figure 4.18** Magnetisation isotherm at 2 K for stoichiometric $CaKFe_4As_4$. Measuring field used in scans of *M vs T* throughout this work was 20 Oe, which is well below $H_{c1}$ for this sample.

The synthesised non-stoichiometric samples were measured using magnetometry to probe any differences in their $T_c$ upon doping. It is worth noting that the doped samples have varying impurity content. The doped samples show slight variation in $T_c$ from the parent phase. Figure 4.19 shows the temperature dependence of the magnetic susceptibility all synthesised samples. At $T_c$ > 34, all

samples exhibit weak temperature-independent paramagnetism, as expected for the normal metallic state (Pauli paramagnetism). In the region $T_c$ < 34 K, the differences between samples become apparent. Although all samples undergo a transition to a strongly diamagnetic state, there are two ways in which the samples differ from each other. Firstly, the $T_c$, calculated from magnetic susceptibility, vary between 30 – 34 K. There is no trend in the variation of $T_c$ with $x$, and two samples (x = 0.05 and 0.15) have $T_c$ of 34 K, similar to the stoichiometric sample (x = 0). These results suggest that there could be small compositional or microstructural differences between the stoichiometric and the non-stoichiometric samples, which are too small to resolve by diffraction measurements, likely similar to that depicted in Figure 4.4, where a block richer in Ca is observed at nanoscale. Secondly, the transitions to a diamagnetic state are sharper for some samples than others. The stoichiometric sample (x = 0) has superconducting volume fraction (*SVF*) = 100%, that of an ideal superconductor, while the sample with highest amount of Ca-doping (x = 0.25) reaches only 40% (Figure 4.19). This result may suggest that at high doping levels, the Ca122 impurity begins to supress superconductivity in $CaKFe_4As_4$ due to intergrowing and causing defects in the superconducting 1144 structure, as the fraction of Ca122 impurity is high at this doping level (from PXRD). This finding comes in contrast to what Iyo *et al*. observed from magnetometry measurements on their 'non-stoichiometric' samples with nominal composition $Ca_{1.5}K_{0.5}Fe_4As_4$, which showed identical behaviour to the stoichiometric sample. Our findings show that small variations in composition in $CaKFe_4As_4$ have an effect on its superconducting properties, whether it might be due to small compositional differences of the main 1144 phase, or due to Ca122 impurity intergrowths at very small scales.

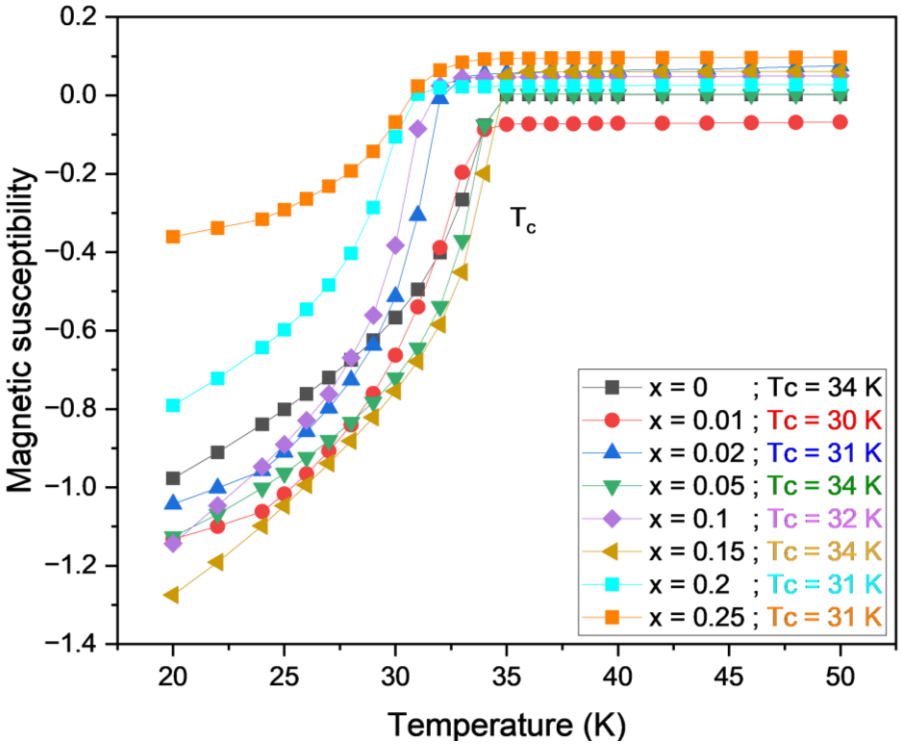


**Figure 4.19** *M vs T* plot measured at zero field at the transition temperature ($T_c$ = 34 K) for $CaKFe_4As_4$ and Ca-doped samples showing the Meissner effect in all samples.

Figure 4.20 shows the relationship between $T_c$ and the anion height, $h_{anion}$. Neither the anion height nor the $T_c$ show any clear trend across the series, but other than for x = 0.05 (5% substitution) sample, the trends are similar between the two parameters.

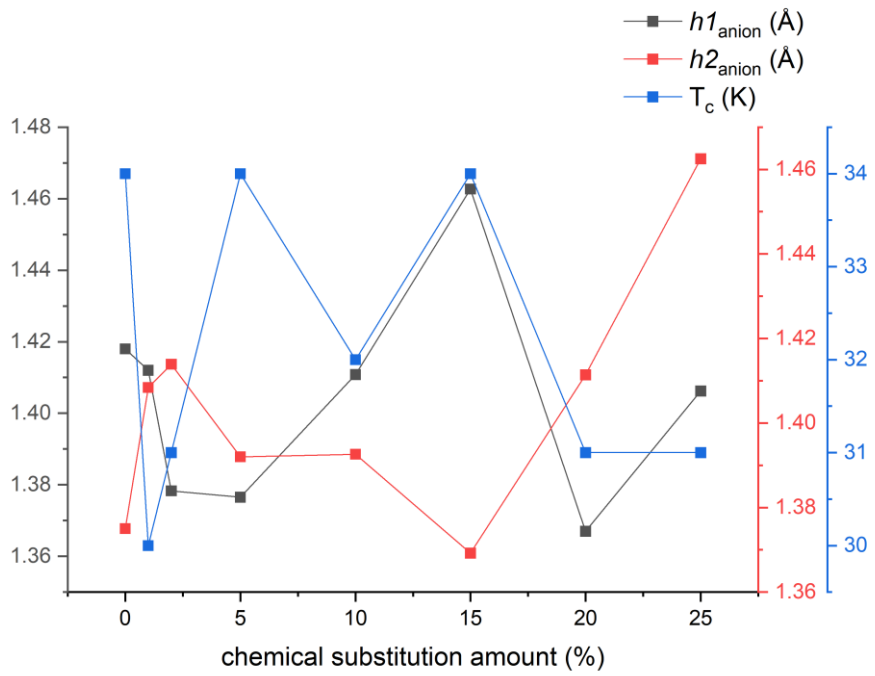


**Figure 4.20** Plot of the relationship between $T_c$ and $h_{anion}$ in the $Ca_{1+x}K_{1-x}Fe_4As_4$ series with $0 \leq x \leq 0.25$.

Figure 4.21 shows the comparison of ZFC-FC plots of stoichiometric $CaKFe_4As_4$ and sample doped with 25% Ca shows the difference in $T_c$ and *SVF* between the two.

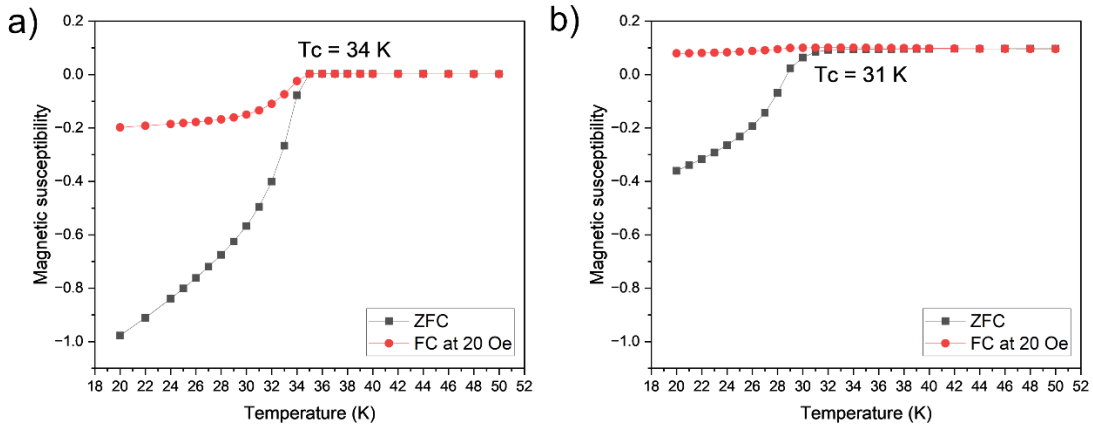


**Figure 4.21** Plot of *magnetic susceptibility vs temperature* measured at zero field (red plots) and a small field of 20 Oe (black plots) for a) stoichiometric $CaKFe_4As_4$ and b) 25% Ca-doped $CaKFe_4As_4$.

## 4.3 Synthesis and characterisation of $CaKFe_4As_{4-x}P_x$

### *4.3.1 Synthesis of $CaKFe_4As_{4-x}P_x$*

The synthesis of $CaKFe_4As_{4-x}P_x$. followed Reference [19], just like in the case of $Ca_{1+x}K_{1-x}Fe_4As_4$ (described in Section 4.2.1), and additional FeP precursor powder was added to the mixture along with Fe in stoichiometric amounts. The FeP precursor was made similarly to $Fe_2As$ by heating stoichiometric amounts of Fe (Alfa Aesar, 99.99%) and P powders (Alfa Aesar, 99.99%) in a Ta tube to 700ºC/12hrs.

### *4.3.2 Room temperature PXRD*

Following reports of P-substitution on the As site in $BaFe_2As_{2-x}P_x$,[25,26] we decided to probe the phase space of $CaKFe_4As_{4-x}P_x$. Substituting with a smaller phosphorus ion on the arsenic site can result in an effect similar to exerting pressure on the phase (a so-called "chemical pressure").[24] The five non-stoichiometric samples synthesised included an extra impurity – $Fe_2P$ – in addition to the same impurities observed in the stoichiometric sample, namely $KFe_2As_2$, $CaFe_2As_2$, $Ca_4As_3$, and $K_5As_4$ resulting in highly impure phases. The Synchrotron PXRD patterns measured at $\lambda = 0.826872$ Å are shown in Figure 4.22a, and Figure 4.22b shows the main (002) peak, which is no longer present at x =1.2, where the main phase is $Fe_2P$ (peaks marked by green asterisks), instead of the target 1144 phase. A shift to higher angles was expected as increasing amounts of smaller phosphorus ion are incorporated to the phase, but this is not observed, as the main (002) peak shifts from 7.33 $2\theta$ degrees for x = 0 to 7.37 $2\theta$ degrees for x = 0.8. A much more pronounced shift was expected, especially since the substitution level is not small, and the shift is in the range observed for previously studied solid solution $Ca_{1+x}K_{1-x}Fe_4As_4$ where upper substitution level was 20%.

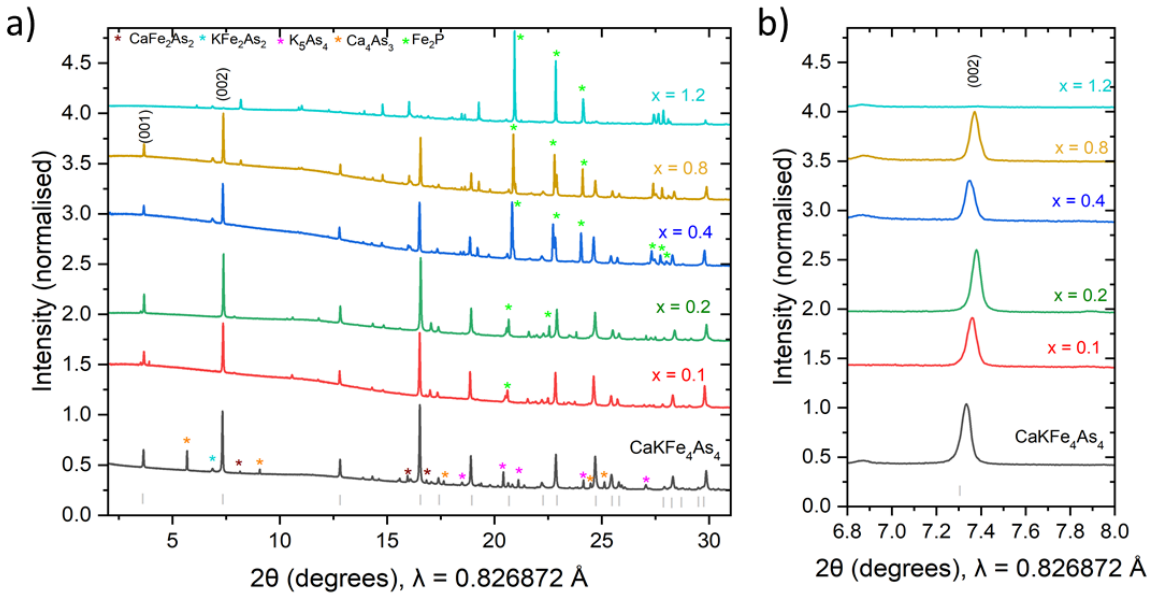


**Figure 4.22** a) Synchrotron PXRD patterns for $CaKFe_4As_{4-x}P_x$, $0 < x \leq 1.2$. b) An enlarged image of the (002) peak, showing the disappearance of the peak by x = 1.2.

Figure 4.23 shows the variation of unit cell parameters in $CaKFe_4As_{4-x}P_x$ upon attempted incorporation of increasing amount of P. As the main 1144 phase disappears by x = 1.2, the data for this phase isn't shown. The lattice parameters and the unit cell volume do not show a linear trend with increasing *x*. The lattice parameter *a* increases in the region $0 < x \leq 0.4$, and at x = 0.8 it decreases. Lattice parameter *c* and the unit cell volume drop off from the values observed for the stoichiometric sample. In the case of $BaFe_2(As_{1-x}P_x)_2$, the lattice parameters *a* and *c*, and the unit cell volume decrease linearly with increasing *x*.[25] The change in *c* lattice parameter ($\Delta c_{lat}$) between x = 0.115 and x = 0.790 is 0.39 Å in $BaFe_2(As_{1-x}P_x)_2$, and the change in the overall unit cell volume is 14.35 Å$^3$, while $\Delta c_{lat}$ in $CaKFe_4As_{4-x}P_x$ is 0.05 Å (Figure 4.22a) and the $\Delta V$ = 0.5 Å$^3$(Figure 4.23b).

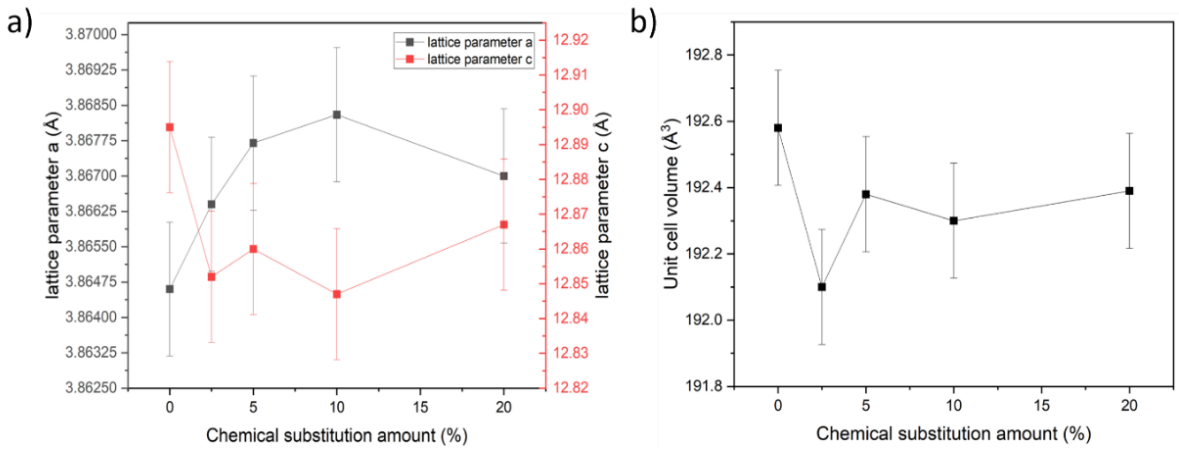


**Figure 4.23** a) Variation of lattice parameters *a* and *c* with *x* in $CaKFe_4As_{4-x}P_x$, $0 < x \leq 0.8$. b) Variation of *V* with *x* in $CaKFe_4As_{4-x}P_x$, $0 < x \leq 0.8$.

At x = 1.2, the PXRD pattern does not show any evidence of presence of target 1144 phase, as both signature peaks (001) and (002) disappear (Figure 4.21). This sample is dominated by $Fe_2P$ impurity. Figure 4.24 shows the increase of wt% of $Fe_2P$ with *x* in $CaKFe_4As_{4-x}P_x$.

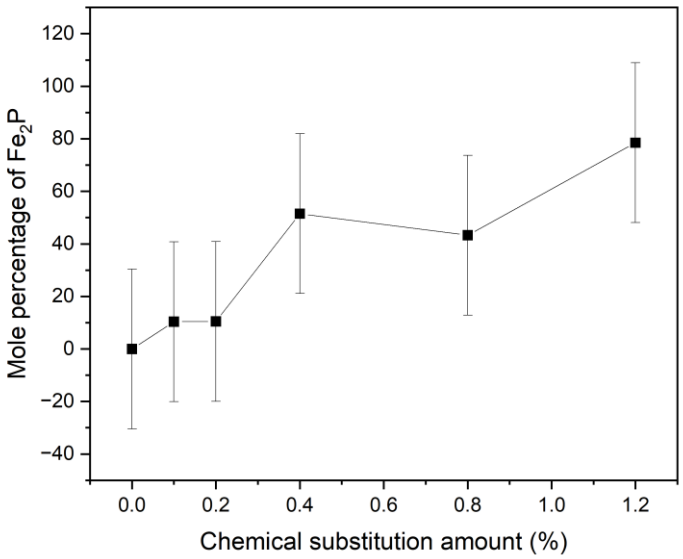


**Figure 4.24** Variation of wt% of $Fe_2P$ with *x*. At *x* = 1.2, the impurity dominates the sample.

### *4.3.3 Magnetometry of $CaKFe_4As_{4-x}P_x$*

Magnetisation *vs* temperature *(M vs T)* measurements were conducted at 20Oe to probe the superconducting regimes of the P-substituted samples in $CaKFe_4As_{4-x}P_x$. The *M vs T* plots at zero-field for $0 < x \leq 0.8$ are shown in Figure 4.25. Similar to Ca-substituted samples, the different samples show slightly different $T_c$ and *SVF*. For x = 0.1 and 0.2, $T_c$ is unchanged, but the *SVF* differs from the stoichiometric sample. Samples x = 0.4 and 0.8 have $T_c$ at 31 and 32 K, respectively, while their *SVF* again differs from that of the stoichiometric sample. This result suggests that there may be small compositional changes between the substituted samples which have an effect of the superconducting features of the $CaKFe_4As_4$ phase, but the changes are too small to be resolved by diffraction techniques.

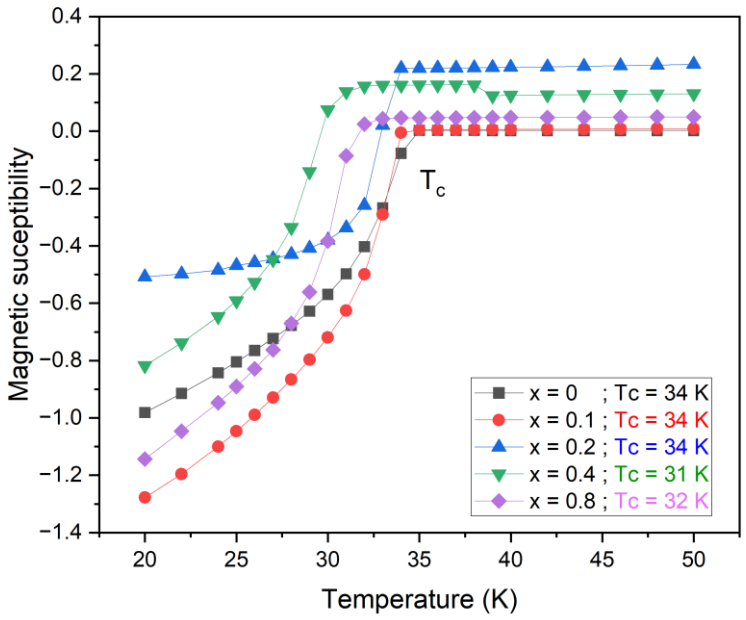


**Figure 4.25** *χ vs T* plot measured at zero field at the transition temperature ($T_c$ = 34 K) for $0 < x \leq 0.8$ in $CaKFe_4As_{4-x}P_x$.

As mentioned, the sample x = 1.2 is dominated by $Fe_2P$ impurity and shows no evidence of a 1144 phase from PXRD. However, its magnetic susceptibility *vs* temperature plot shows a characteristic superconducting feature of 1144 phases at 34 K (Figure 4.26a), even though it is observed at positive

susceptibility values. This suggests that a part of the sample may still contain 1144 phase even, at very small amounts, as it cannot be observed by PXRD. The ZFC-FC plot shows divergence of the individual zero-field-cooled and field-cooled curves, which signals the presence of a ferromagnetic component, likely $Fe_2P$ or elemental Fe, which can be observed in the non-linearity of the *M v H* plot in Figure 4.26b. As the ferromagnetic impurity doesn't saturate, we could not estimate the amount of the impurity contributing to the ferromagnetic signal.

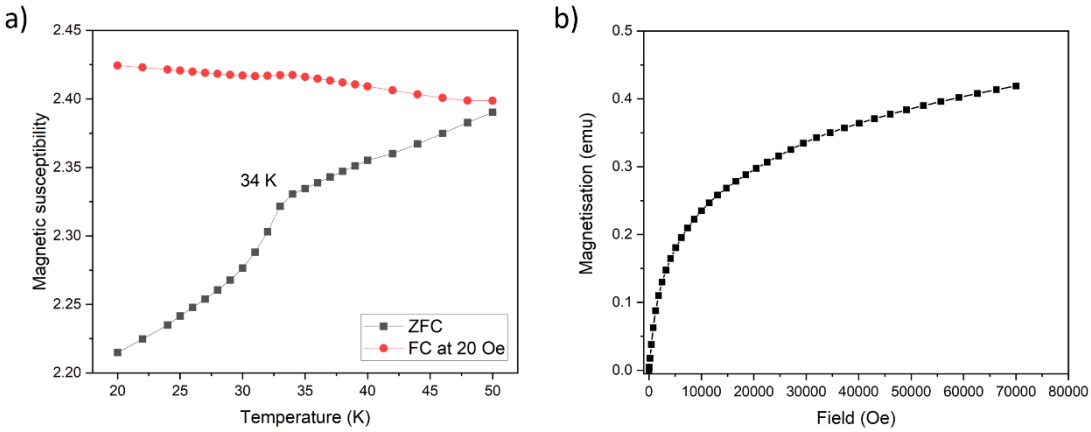


**Figure 4.26** a) ZFC-FC magnetic susceptibility curve measured at 20 Oe on the $x$ = 1.2 sample, b) *M v H* plot of $x$ = 1.2 sample.

## 4.4 Conclusions

This investigation probes the non-stoichiometry in $CaKFe_4As_4$, an iron-based superconductor. Disorder was introduced by chemical substitution on *Ae/A* sites by varying the *Ae : A* ratios, and doping with phosphorus on arsenic site. As the structural details do not change in any linear manner (or one that could be described by a trend in the series) with increasing substitution levels, we conclude that instead of incorporation of excess Ca into $CaKFe_4As_4$, Ca may be intergrown at a very small scale into the 1144 as $CaFe_2As_2$. These are phases are difficult to prepare in a phase pure form, which is well-described in previous literature reports on 1144 phases.[27,28] Furthermore, the control of chemical doping during the synthesis process produced inhomogeneities in the target compounds and number of impurities.[27,28] The small compositional changes have subtle effects on the structure and the superconducting properties of the stoichiometric $CaKFe_4As_4$. The structure doesn't change

and lattice parameters do not seem to change in any linear manner with small compositional changes, and the superconducting features show very little fluctuations with composition, suggesting that $CaKFe_4As_4$ is effectively a line phase; the $T_c$ and the *SVF* of substituted samples slightly differ from the stoichiometric $CaKFe_4As_4$ with observed $T_c$ varying between 30 – 34 K in $Ca_{1+x}K_{1-x}Fe_4As_4$, and 31 – 34 K in $CaKFe_4As_{4-x}P_x$. This finding of slightly supressed $T_c$ could be due to intergrowths of $CaFe_2As_2$ coherently grown in the CaK1144 matrix present in the non-stoichiometric samples in $Ca_{1+x}K_{1-x}Fe_4As_4$ and $CaKFe_4As_{4-x}P_x$ solid solutions.

## References

[1] Kamihara, Y., Watanabe, T., Hirano, M., & Hosono, H. (2008). Iron-based layered superconductor La[$O_{1-x}F_x$]FeAs (x = 0.05-0.12) with $T_c$ = 26 K. *Journal of the American Chemical Society*, *130*(11), 3296–3297. https://doi.org/10.1021/ja800073m

[2] Chen, X.H. *et al.* (2008) 'Superconductivity at 43 K in $SmFeAsO_{1-x}F_x$', *Nature*, 453(7196), pp. 761–762. https://doi:10.1038/nature07045.

[3] Kotegawa, H., Masaki, S., Awai, Y., Tou, H., Mizuguchi, Y., & Takano, Y. (2008). Evidence for unconventional superconductivity in arsenic-free iron-based superconductor FeSe: A77Se-NMR study. *Journal of the Physical Society of Japan*, *77*(11). https://doi.org/10.1143/JPSJ.77.113703

[4] Rotter, M., Tegel, M., & Johrendt, D. (2008). Superconductivity at 38 K in the iron arsenide ($Ba_{1-x}K_x$)$Fe_2As_2$. *Physical Review Letters*, *101*(10). https://doi.org/10.1103/PhysRevLett.101.107006

[5] Mittal, R., Mishra, S. K., Chaplot, S. L., Ovsyannikov, S. v., Greenberg, E., Trots, D. M., Dubrovinsky, L., Su, Y., Brueckel, T., Matsuishi, S., Hosono, H., & Garbarino, G. (2011). Ambient- and low-temperature synchrotron x-ray diffraction study of $BaFe_2As_2$ and $CaFe_2As_2$ at high pressures up to 56 GPa. *Physical Review B - Condensed Matter and Materials Physics*, *83*(5). https://doi.org/10.1103/PhysRevB.83.054503.

[6] Ni, N., Bud'ko, S. L., Kreyssig, A., Nandi, S., Rustan, G. E., Goldman, A. I., Gupta, S., Corbett, J. D., Kracher, A., & Canfield, P. C. (2008). Anisotropic thermodynamic and transport properties of single-crystalline $Ba_{1-x}K_xFe_2As_2$. (x = 0 and 0.45). *Physical Review B - Condensed Matter and Materials Physics*, *78*(1). https://doi.org/10.1103/PhysRevB.78.014507.

[7] Cortes-Gil, R., & Clarke, S. J. (2011). Structure, magnetism, and superconductivity of the layered iron arsenides $Sr_{1-x}Na_xFe_2As_2$. *Chemistry of Materials*, *23*(4), 1009–1016. https://doi.org/10.1021/cm1028244

[8] Torchetti, D. A., Fu, M., Christensen, D. C., Nelson, K. J., Imai, T., Lei, H. C., & Petrovic, C. (2011). Se77 NMR investigation of the $K_xFe_{2-y}Se_2$ high-$T_c$ superconductor ($T_c$ = 33 K). *Physical Review B - Condensed Matter and Materials Physics*, *83*(10). https://doi.org/10.1103/PhysRevB.83.104508.

[9] Iyo, A., Kawashima, K., Kinjo, T., Nishio, T., Ishida, S., Fujihisa, H., Gotoh, Y., Kihou, K., Eisaki, H., & Yoshida, Y. (2016). New-Structure-Type Fe-Based Superconductors: $CaAFe_4As_4$ (A = K, Rb, Cs) and $SrAFe_4As_4$ (A = Rb, Cs). *Journal of the American Chemical Society*, *138*(10), 3410–3415. https://doi.org/10.1021/jacs.5b12571

[10] Meier, W. R., Ding, Q. P., Kreyssig, A., Bud'Ko, S. L., Sapkota, A., Kothapalli, K., Borisov, V., Valentí, R., Batista, C. D., Orth, P. P., Fernandes, R. M., Goldman, A. I., Furukawa, Y., Böhmer, A. E., & Canfield, P. C. (2018). Hedgehog spin-vortex crystal stabilized in a hole-doped iron-based superconductor. *Npj Quantum Materials*, *3*(1). https://doi.org/10.1038/s41535-017-0076-x.

[11] Muriel, W. A., Novoa, T., Cárdenas, C., & Contreras-García, J. (2024). Introducing electron correlation in solid-state calculations for superconducting states. *Faraday Discussions*. https://doi.org/10.1039/d4fd00073k.

[12] Li, H., Zhou, X., Parham, S., Reber, T. J., Berger, H., Arnold, G. B., & Dessau, D. S. (2018). Coherent organization of electronic correlations as a mechanism to enhance and stabilize high-$T_c$ cuprate superconductivity. *Nature Communications*, *9*(1). https://doi.org/10.1038/s41467-017-02422-2.

[13] Ishida, S., Iyo, A., Ogino, H. *et al*. Unique defect structure and advantageous vortex pinning properties in superconducting $CaKFe_4As_4$. *npj Quantum Mater.* **4**, 27 (2019). https://doi.org/10.1038/s41535-019-0165-0

[14] Blatter, G., Feigel'Man, M. V., Geshkenbein, V. B., Larkin, A. I., Vinokur, V. M. Vortices in high-temperature superconductors. *Rev. Mod. Phys.* **66**, 1125–1388 (1994).

[15] Xiang, L., Meier, W. R., Xu, M., Kaluarachchi, U. S., Bud'Ko, S. L., & Canfield, P. C. (2018). Pressure-temperature phase diagrams of $CaK(Fe_{1-x}Ni_x)_4As_4$ superconductors. *Physical Review B*, *97*(17), 1–8. https://doi.org/10.1103/PhysRevB.97.174517.

[16] Usman, M., Zhou, X., Malliakas, C. D., Welp, U., Kwok, W. K., Chung, D. Y., & Kanatzidis, M. G. (2023). Probing Phosphorus Solubility and Its Effect on Critical Temperature ($T_c$) in the Helical Superconducting Magnet $RbEuFe_4As_{4-x}P_x$. *Chemistry of Materials*, *35*(20), 8494–8501. https://doi.org/10.1021/acs.chemmater.3c01310.

[17] Duchenko, A., Masi, A., Augieri, A., Barba, L., Campi, G., Celentano, G., Gigli, L., Plaisier, J. R., Pompeo, N., Rizzo, F., & Varsano, F. (2024). Relation Between Composition and Crystalline Structure in Substituted $CaKFe_4As_4$. *IEEE Transactions on Applied Superconductivity*, *34*(3). https://doi.org/10.1109/TASC.2023.3336613.

[18] Song, B. Q., Nguyen, M. C., Wang, C. Z., Canfield, P. C., & Ho, K. M. (2018). Is it possible to stabilize the 1144-phase pnictides with tri-valence cations? *Physical Review Materials*, *2*(10). https://doi.org/10.1103/PhysRevMaterials.2.104802.

[19] Singh, S. J., Cassidy, S. J., Bristow, M., Blundell, S. J., Clarke, S. J., & Coldea, A. I. (2019). Optimization of superconducting properties of the stoichiometric $CaKFe_4As_4$. *Superconductor Science and Technology*, *33*(2). https://doi.org/10.1088/1361-6668/ab58be.

[20] Avci, S., Allred, J. M., Chmaissem, O., Chung, D. Y., Rosenkranz, S., Schlueter, J. A., Claus, H., Daoud-Aladine, A., Khalyavin, D. D., Manuel, P., Llobet, A., Suchomel, M. R., Kanatzidis, M. G., & Osborn, R. (2013). Structural, magnetic, and superconducting properties of Ba 1-xNaxFe2As2. *Physical Review B - Condensed Matter and Materials Physics*, *88*(9). https://doi.org/10.1103/PhysRevB.88.094510.

[21] Rotter, M., Hieke, C., & Johrendt, D. (2010). Different response of the crystal structure to isoelectronic doping in BaFe2(As1-xPx)2 and (Ba 1-x Srx) Fe2 As2. *Physical Review B - Condensed Matter and Materials Physics*, *82*(1). https://doi.org/10.1103/PhysRevB.82.014513.

[22] Kuroki, K., Usui, H., Onari, S., Arita, R., & Aoki, H. (2009). Pnictogen height as a possible switch between high- $T_c$ nodeless and low- $T_c$ nodal pairings in the iron-based superconductors. *Physical Review B - Condensed Matter and Materials Physics*, *79*(22). https://doi.org/10.1103/PhysRevB.79.224511.

[23] Hosono, H., Yamamoto, A., Hiramatsu, H., & Ma, Y. (2018). Recent advances in iron-based superconductors toward applications. *Materials Today*, 21 (3), 278–302. https://doi.org/10.1016/j.mattod.2017.09.006.

[24] Bristow, M., Knafo, W., Reiss, P., Meier, W., Canfield, P. C., Blundell, S. J., & Coldea, A. I. (2020). Competing pairing interactions responsible for the large upper critical field in a

stoichiometric iron-based superconductor $CaKFe_4As_4$. *Physical Review B*, *101*(13). https://doi.org/10.1103/PhysRevB.101.134502.

[25] Allred, J. M., Taddei, K. M., Bugaris, D. E., Avci, S., Chung, D. Y., Claus, H., dela Cruz, C., Kanatzidis, M. G., Rosenkranz, S., Osborn, R., & Chmaissem, O. (2014). Coincident structural and magnetic order in $BaFe_2(As_{1-x}P_x)_2$ revealed by high-resolution neutron diffraction. *Physical Review B - Condensed Matter and Materials Physics*, *90*(10). https://doi.org/10.1103/PhysRevB.90.104513.

[26] Kobayashi, T., Miyasaka, S., Tajima, S., Nakano, T., Nozue, Y., Chikumoto, N., Nakao, H., Kumai, R., & Murakami, Y. (2013). Change of electronic state and crystal structure by postannealing in superconducting $SrFe_2(As_{0.65}P_{0.35})_2$. *Physical Review B - Condensed Matter and Materials Physics*, *87*(17). https://doi.org/10.1103/PhysRevB.87.174520.

[27] Singh, S. J., & Sturza, M. I. (2022). Bulk and single crystal growth progress of iron-based superconductors (Fbs): 1111 and 1144. *Crystals*, 12(1). https://doi.org/10.3390/cryst12010020.

[28] Manasa, M., Azam, M., Zajarniuk, T., Diduszko, R., Cetner, T., Morawski, A., Wisniewski, A., & Singh, S. J. (2024). Enhancement of Superconducting Properties of Polycrystalline CaKFe4As4 by High-Pressure Growth. *IEEE Transactions on Applied Superconductivity*, *34*(3), 1–5. https://doi.org/10.1109/TASC.2023.3345821.

# Chapter 5. Pressure-induced structural phase transitions in $SrRbFe_4As_4$

## 5.1 Introduction

Iron-Based Superconductors (IBSCs) with the 1144 structure type and general formula *Ae*A$Fe_4As_4$ (*Ae* = alkaline earth metal, *A* = alkali metal) were discovered by Iyo *et al*. in 2016 as one of the latest structure types of this class of compounds.[1] They possess high $T_c$ and $H_{c2}$ and are therefore candidates for technological applications in superconducting wires. Due to the strict ordering of *Ae* and *A* ions along the stacking axis, which was a theme explored in Chapter 4 of this thesis, the structure crystallises in a primitive tetragonal symmetry (*P*4/*mmm* space group), as the symmetry is lowered from the body-centred *I*4/*mmm* structure of the closely related 122 structure type of IBSCs. 122-type phases (with general formula $AT_2X_2$, where *A* = electropositive ion, *T* = transition metal, *X* = main group anion) are known to undergo a unit cell collapse, which is marked by a drastic decrease in the *c/a* ratio of lattice parameters of the tetragonal cell, driven by formation of *X*-*X* bonds especially *Pn*-*Pn*/*Ch*-*Ch* bonds (*Pn* = pnictogen atom, such as As; *Ch* = chalcogen atom, Se), shown in Figure 5.1.[2,3,4] The so-called uncollapsed tetragonal (ucT) structure (space group *I*4/*mmm*), is often characterized as the $BaZn_2P_2$ structure type, where *c/a* ratio > 3, and no *X*-*X* (*Pn*-*Pn*/*Ch*-*Ch*) bonding is present. The so-called collapsed tetragonal (cT) phase is normally described as the $ThCr_2Si_2$-type structure, where the *c*/*a* ratio ~ 2.5 and there is *X*-*X* bonding (Si-Si bonding in $ThCr_2Si_2$). The main structural difference between the two is that the uncollapsed phases have a long separation between the [$T_2X_2$] layers, while the collapsed phases exhibit short separation, typically corresponding to a nearly single-bond *X*–*X* interlayer distance. In terms of the space group symmetry and Wyckoff sites both types are isostructural, so transitions between the two forms must be first order.[2,3]

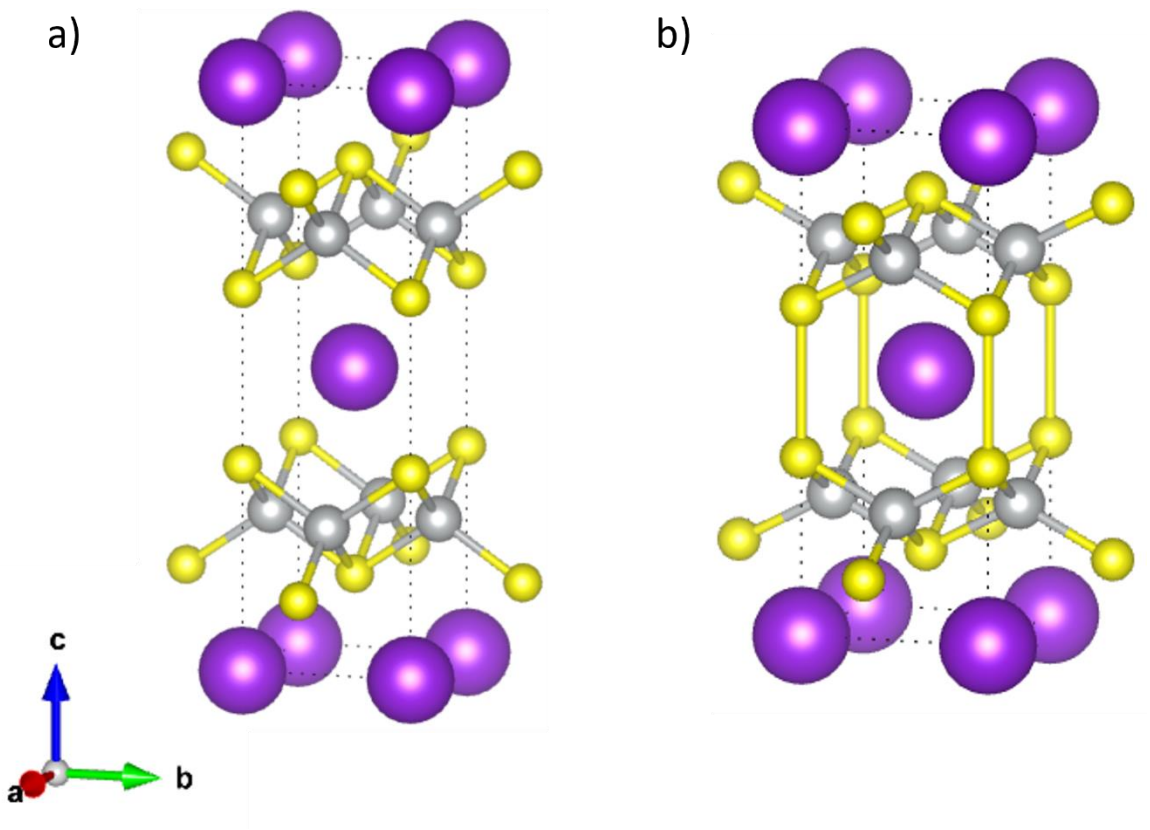


**Figure 5.1** a) Uncollapsed tetragonal 122-type structure (ucT, $BaZn_2P_2$ structure type), b) collapsed structure (cT, $ThCr_2Si_2$ structure type).

Structural phase transitions are very common for this type of compounds, both temperature- and pressure-induced. For example, Huhnt *et al*. recognized a large difference in the interlayer P–P distance between $SrRh_2P_2$ (3.284 Å) and $SrPd_2P_2$ (2.217 Å).[2] Consequently, they applied pressure to $SrRh_2P_2$ and observed a collapse of this structure along the tetragonal *c* axis at 6 GPa at room temperature. The structural phase transition was associated with a 14.6% decrease in the *c* axis and 4.1% increase in the *a* axis, resulting in an overall 7.5% decrease in the unit cell volume. The expansion of the structure in the *ab* plane as it collapses along the *c* axis is a common observation in the case of structural phase transitions in the $BaZn_2P_2$/$ThCr_2Si_2$ structure type. The interlayer P–P distance in the collapsed $ThCr_2Si_2$-typephase was estimated as 2.227 Å, which corresponds to the normal length of a single P–P bond. Similar behaviour under pressure was observed for $CaFe_2As_2$,[3] $BaFe_2As_2$,[4] $SrNi_2P_2$,[5] $TlFe_{1.6}Se_2$,[6] and $LaM_2P_2$ (M = Fe, Co).[7]

The aforementioned 1144 structure type of IBSCs, namely $CaKFe_4As_4$ and $CaRbFe_4As_4$, have

superstructures of the structure shown in Figure 5.1 in which there is strict ordering of the $Ca^{2+}$ and alkali metal ions.[8,9] These have the optimal electron count for high-temperature superconductivity and the perfect ordering of the electropositive metals means that there is no chemical disorder on any sublattice. Under pressure they undergo a two-stage collapse of the unit cell at pressures of up to about 20 GPa (Figure 5.2). In $CaKFe_4As_4$, there is collapse of the Ca layer with As-As bonding at 4 GPa and this is concomitant with suppression of superconductivity; superconductivity is being suppressed upon increasing pressure between 0-4 GPa, demonstrated on decreasing $T_c$, and completely disappears at 4 GPa.[7] It is believed that it is the collapse itself that leads to the suppression of superconductivity.[8,9] There is further collapse of the thicker K-containing layer at correspondingly higher pressures > 12GPa, confirming a second structural transition. In $CaRbFe_4As_4$, the initial half-collapsed tetragonal phase is observed for 6 < P < 22 GPa, with suppression of superconductivity, and full collapse occurs near P = 22 GPa.[9]

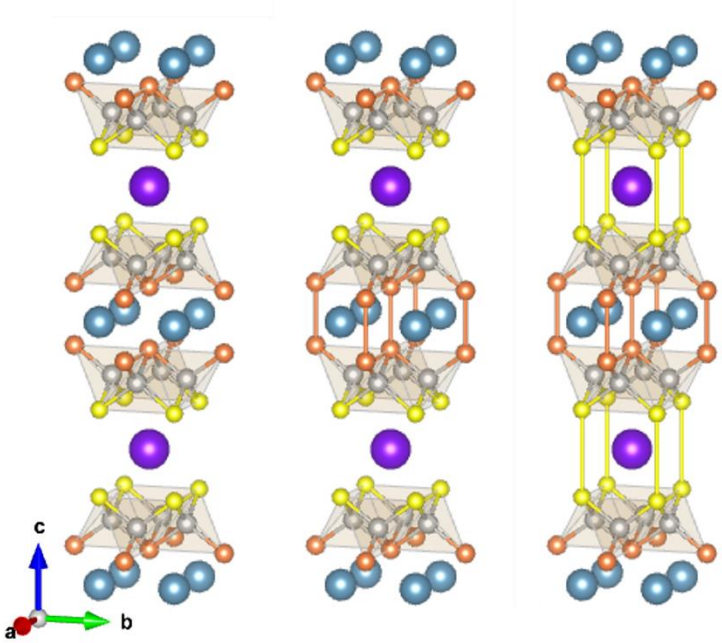


**Figure 5.2** Structure of $CaKFe_4As_4$ showing the strict ordering of cations along the stacking axis: Ca ions (blue) alternate with K ions (purple) as they occupy different crystallographic sites and therefore cannot mix in the same layer. The sequence shows the two-stage collapse of the structure; left: Uncollapsed structure at ambient pressure, centre: half-collapsed structure at 4 GPa with As-As bonds forming across Ca layer, right: fully collapsed structure at 12 GPa with As-As bonds forming across K-layer.

$SrRbFe_4As_4$ is a related compound with relatively high $T_c$ of 33 K,[1] and our investigations probe the sequence of collapse with much larger ions present to investigate qualitative and quantitative differences with the Ca-containing phases. High pressure PXRD experiment at the BL10XU beamline of SPring-8 Synchrotron in Japan was performed to study the effect of pressure on $SrRbFe_4As_4$. The aim of this work is to characterize structural changes under pressure to add a further dimension to the research on these complex compounds and correlate these changes with investigations of the effect of pressure on their physical properties.

## 5.2 Synthesis and characterisation of $SrRbFe_4As_4$

### *5.2.1 Synthesis of $SrRbFe_4As_4$*

Synthesis of $SrRbFe_4As_4$ was performed in the same way as $CaKFe_4As_4$ described in Chapter 4.2.1 according to Reference [10]. The only difference were the starting materials, in this case SrAs and RbAs. These precursors were prepared in the same way as CaAs and KAs, respectively, as described in Chapter 4.2.1.1, from high purity starting reagents including Sr pieces (Sigma Aldrich, 99.99%), Fe powder (Alfa Aesar, 99.99%), Rb ingot (Alfa Aesar, 99.75%) and As (Alfa Aesar, 99.99%) pieces.

### *5.2.2 BL10XU High pressure PXRD experiment*

The high-pressure Diamond Anvil cell (DAC) was loaded with daphne oil as the pressure transmitting medium at the University of Nagoya by Dr Satoshi Nakano and Dr Yuki Shibazaki. Daphne oil was used as it does not react with the sample and gives reasonably hydrostatic conditions up to 5 GPa. The better option of using He gas as the pressure transmitting medium was not available and requires specialised high-gas-pressure loading capability. The DAC was mounted in Experimental hutch 2 at the BL10XU beamline of the SPring-8 synchrotron for ambient temperature measurements under pressures ranging from ambient to 26 GPa measured by Raman spectroscopy on a ruby chip co-loaded with the sample. Once the DAC was positioned in the centre of the beam, a helium gas membrane was attached to the DAC, which allows for remote control of the pressure inside the DAC, and compresses the DAC upon application of pressure. As the gas pressure is inequivalent to the pressure inside the DAC, measuring the inside pressure is done by the Raman spectroscopy measurements on the ruby chip. At each pressure step, the sample (radius 2 μm) needs to be re-aligned with beam, as the X-ray beam (radius 10 μm) has to hit only the sample, not oil or

ruby chip, and its position changes slightly upon pressure increase. The position of the sample can be adjusted with a precision of 0.01 μm. 41 keV X-rays (~0.41 Å) were used to measure the diffraction pattern of the well-ground powder samples. The diffraction patterns were measured in steps of 1-2 GPa on the application of pressure and two patterns were collected on release.

### *5.2.3 Room temperature PXRD*

As described previously in Chapter 4.2.2, members of the *AeA*$Fe_4As_4$ structural family are challenging to prepare in high purity. Figure 5.3 shows room temperature Rietveld refinement of $SrRbFe_4As_4$ against Synchrotron PXRD patterns collected at $\lambda = 0.824169$ Å, which could be indexed according to the tetragonal *P*4/*mmm* space group. The target 1144 phase was challenging to prepare in a pure form and secondary phases are present, including $SrFe_2As_2$ and $Fe_2As$ and an unknown impurity is marked by a cyan asterisk.

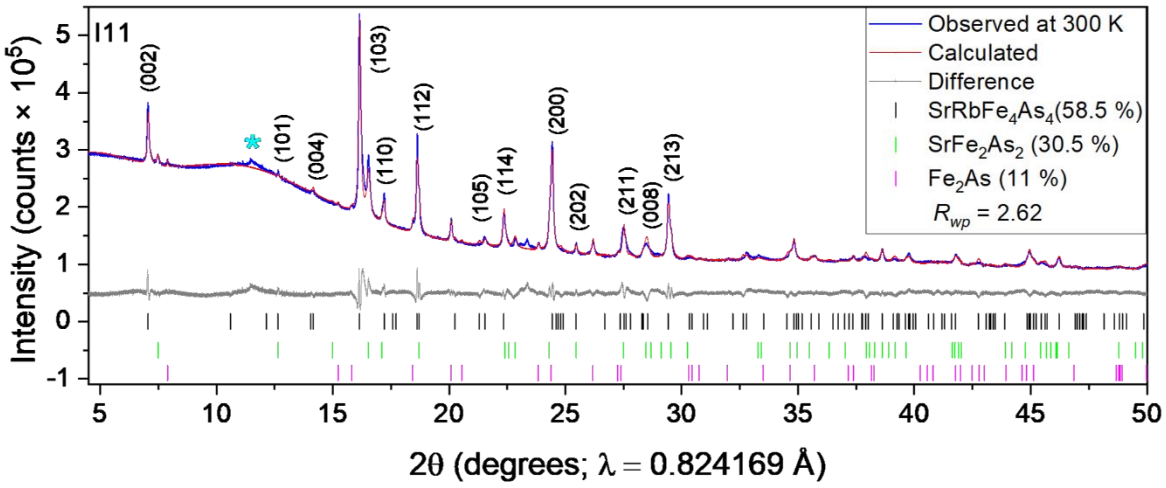


**Figure 5.3** Room-temperature Rietveld refinement of $SrRbFe_4As_4$ against Synchrotron PXRD (I11 beamline at Diamond). Cyan asterisk marks an unknown impurity.

Figure 5.4 shows the Rietveld refinement of $SrRbFe_4As_4$ against Synchrotron PXRD patterns collected at $\lambda = 0.41328$ Å in the DAC prior to applying pressure, which could also be indexed according to tetragonal *P*4/*mmm* space group.

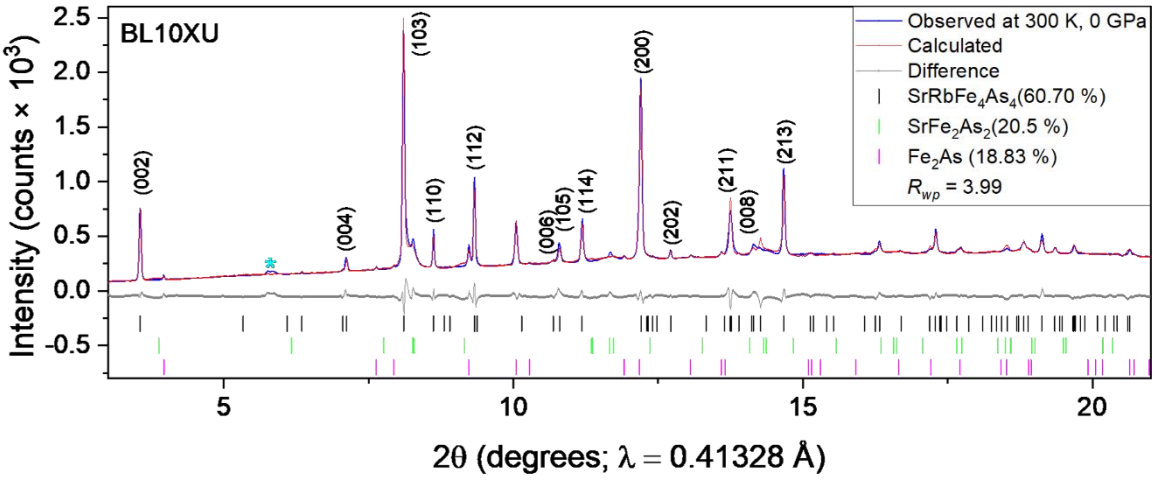


**Figure 5.4** Room-temperature Rietveld refinement of $SrRbFe_4As_4$ against Synchrotron PXRD (BL10XU beamline at Spring-8) under no applied pressure.

### *5.2.2 Variable temperature SXRD*

Structural details of the stoichiometric $SrRbFe_4As_4$ were investigated as function of temperature between 100-300 K with high resolution PXRD, shown in Figure 5.5. The unit cell volume and lattice parameters *a* and *c* show a linear increase between 100 – 300 K. The *z* atomic coordinates of two As sites were refined and remained very close to the room temperature values. There is no evidence for any structural phase transition in this range.

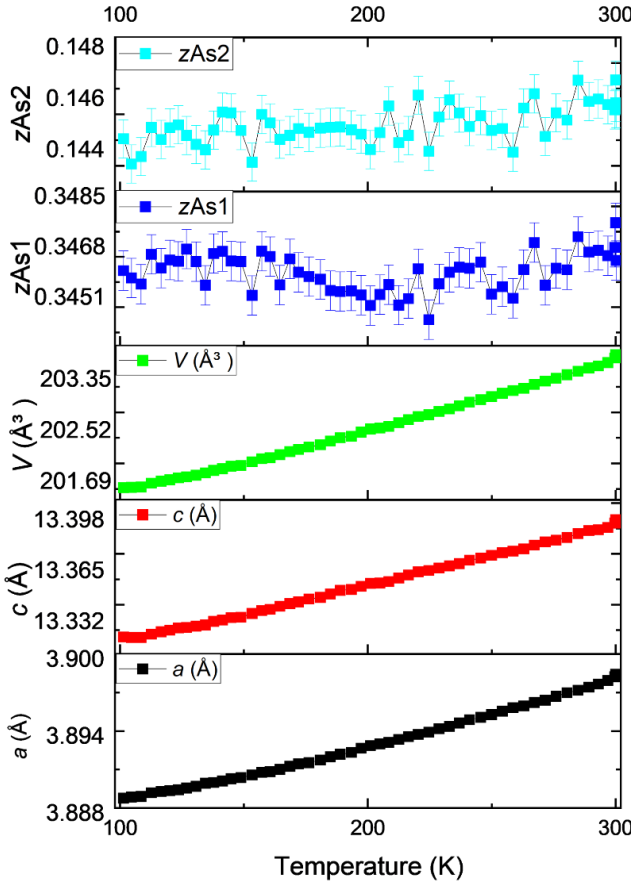


**Figure 5.5** Variable temperature SXRD for $SrRbFe_4As_4$ between 100-300 K (I11 beamline at Diamond Light Source).

### *5.2.3 Magnetometry*

The $T_c$ of synthesised $SrRbFe_4As_4$ was probed via ZFC-FC magnetometry measurement at 20 Oe. Figure 5.6 shows that at 33 K the sample undergoes a transition to superconducting regime and that the superconductivity originates from the bulk, as the *SVF* is high (~80%). These magnetometry data agree well with Iyo *et al.*'s work on the phase.[1]

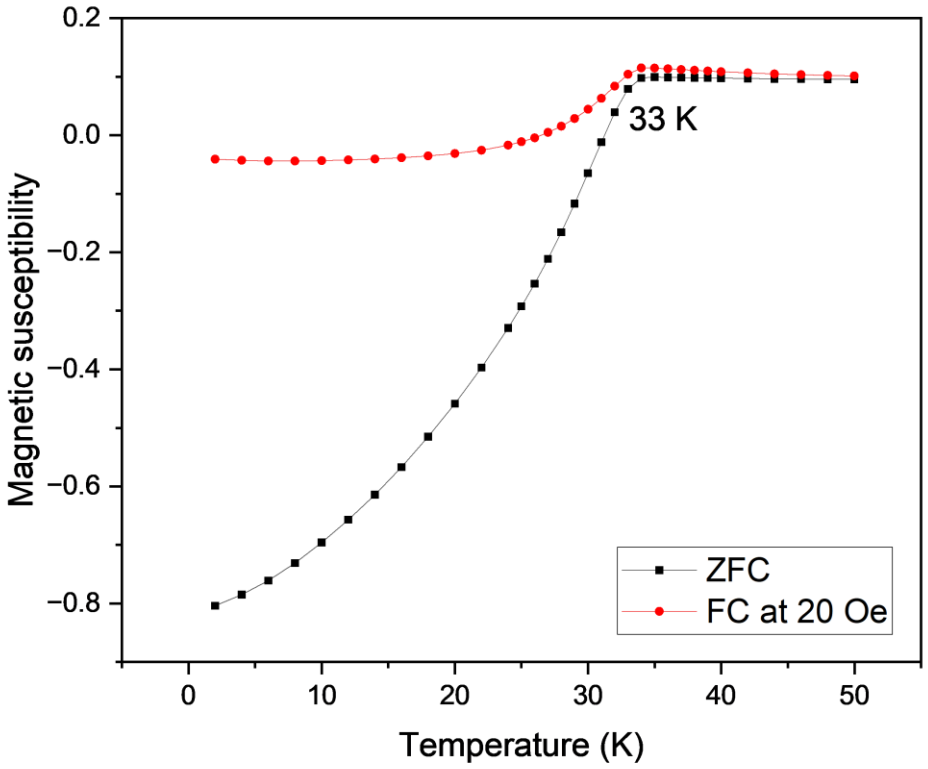


**Figure 5.6** ZFC-FC curves at 20 Oe between 2-50 K for $SrRbFe_4As_4$.

### *5.2.4 High-pressure PXRD*

The high-pressure PXRD experiment at BL10XU beamline of the SPring-8 synchrotron was carried out at ambient temperatures and pressures between 0-26 GPa in 2GPa steps between 0-16GPa and then in 0.5GPa steps between 16.5-20 GPa, and then again in 2 GPa steps between 20-26 GPa due to the increased difficulty of achieving accurate target pressure inside the DAC through a gas (He) membrane. Figure 5.7 shows the PXRD diffraction patterns of $SrRbFe_4As_4$ measured between 0-16 GPa. A gradual shift to higher angles is observed as the lattice contracts with increasing pressure. In addition, diffraction peaks broaden noticeably which is an effect exacerbated by using a liquid pressure medium inside the DAC. No structural changes were observed in this pressure range which would resemble a collapse of the lattice driven by As-As bond formation across the Sr- or Rb-containing layers.

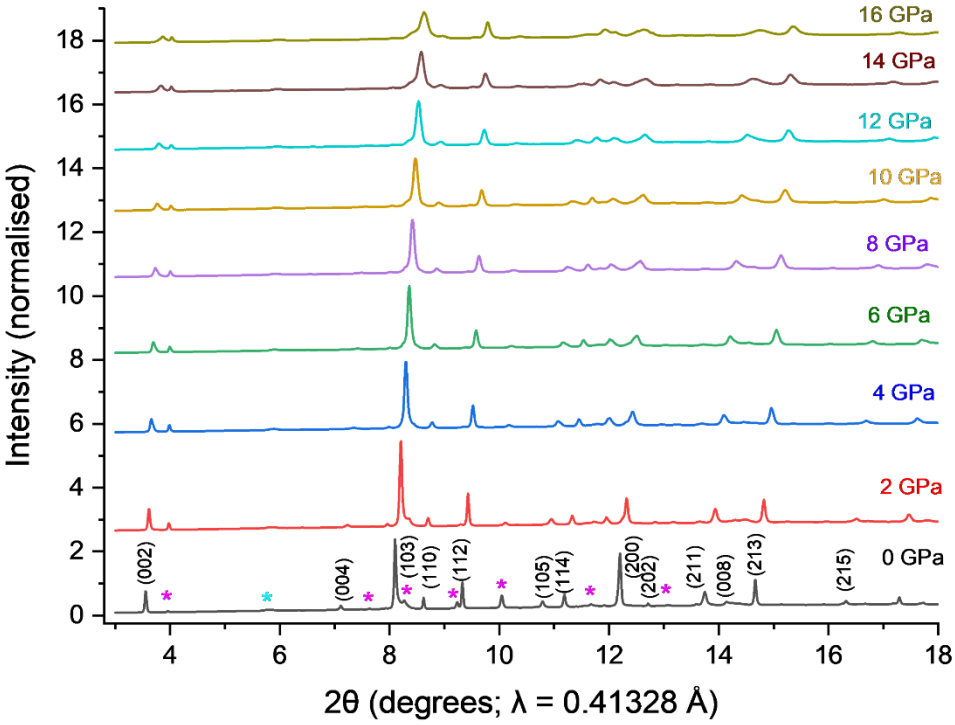


**Figure 5.7** Synchrotron PXRD patterns of $SrRbFe_4As_4$ upon application of pressure between 0-16 GPa. Magenta asterisks mark $Fe_2As$ and $SrFe_2As_2$ impurities, and cyan asterisk marks an unknown impurity.

Figure 5.8 shows the main (002) peak broaden considerably and shift from 3.55º to 3.875º 2$\theta$ between 0-16 GPa.

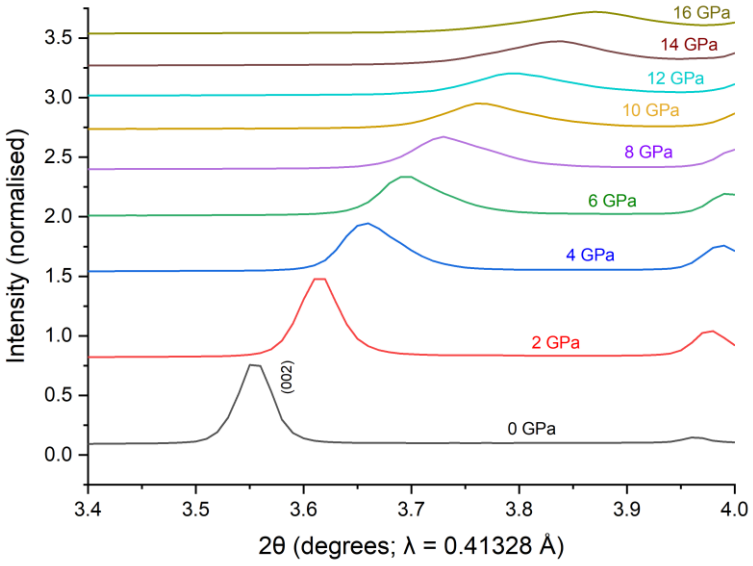


**Figure 5.8** Main (002) peak shifting to higher angles with increasing pressure between 0-16 GPa.

The variation of lattice parameters *a* and *c* extracted from Rietveld refinements between 0-16 GPa is shown in Figure 5.9. Both parameters contract at similar rates, with no indication of a sudden collapse of the lattice; between 0-6 GPa the lattice parameters contract fast and then contraction slows down between 6-16 GPa.

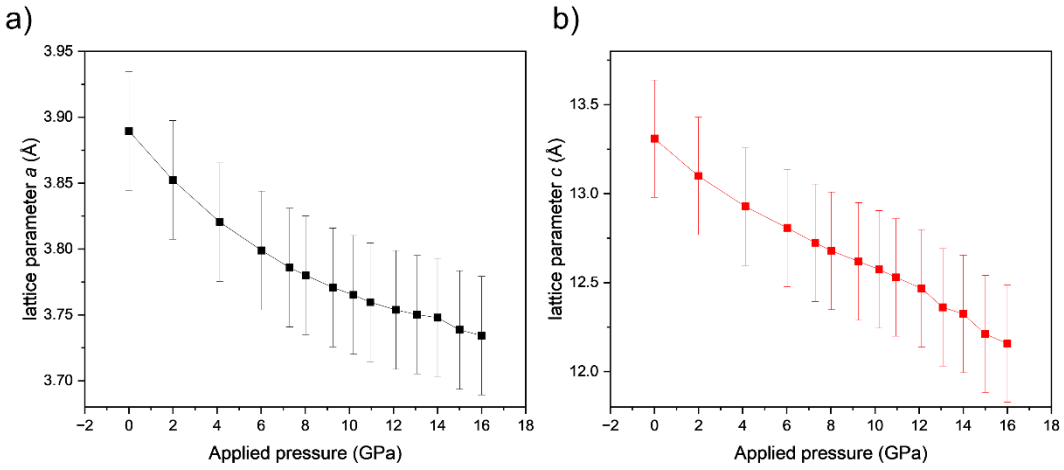


**Figure 5.9** Variation of lattice parameters *a* (left) and *c* (right) of $SrRbFe_4As_4$ with applied pressure of 0-16 GPa from BL10XU Synchrotron PXRD data.

Figure 5.10 shows the variation of unit cell volume between 0-16 GPa. Again, no sudden change in volume is observed, with the lattice shrinking at a fast rate (~5 Å/2GPa step) between 0-6 GPa and afterwards the lattice contraction slows down to ~1 Å/2GPa step.

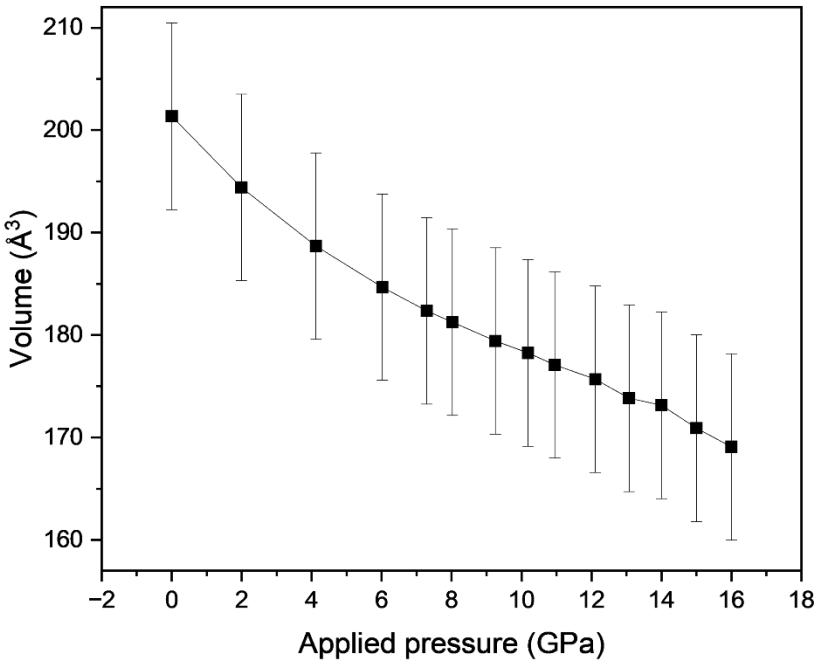


**Figure 5.10** Variation of unit cell volume of $SrRbFe_4As_4$ with applied pressure of 0-16 GPa from BL10XU Synchrotron PXRD data.

As the variation of the volume, *V*, as a function of pressure, *P*, was found to be uniform up to 16 GPa, the dependence could be fitted to a third-order Birch−Murnaghan equation of state[11] (Equation 5.1, Figure 5.11). Using the EosFit7-GUI software[12], the following parameters were obtained from the data, focusing on the low-pressure region from which $K_{0'}$ is heavily dependent on: $V_0$ = 200.541 Å$^3$, the bulk modulus $K_0 = -V_0(\partial P/\partial V)$ = 61.10 GPa, and its first pressure derivative $K_{0'}$ = 5.52.

$$P = \frac{3K_0}{2}\left[\left(\frac{V_0}{V}\right)^{\frac{7}{3}} - \left(\frac{V_0}{V}\right)^{\frac{5}{3}}\right]\left\{1 - \frac{3}{4}(4 - K_0')\left[\left(\frac{V_0}{V}\right)^{\frac{2}{3}} - 1\right]\right\} \quad \text{Equation 5.1}$$

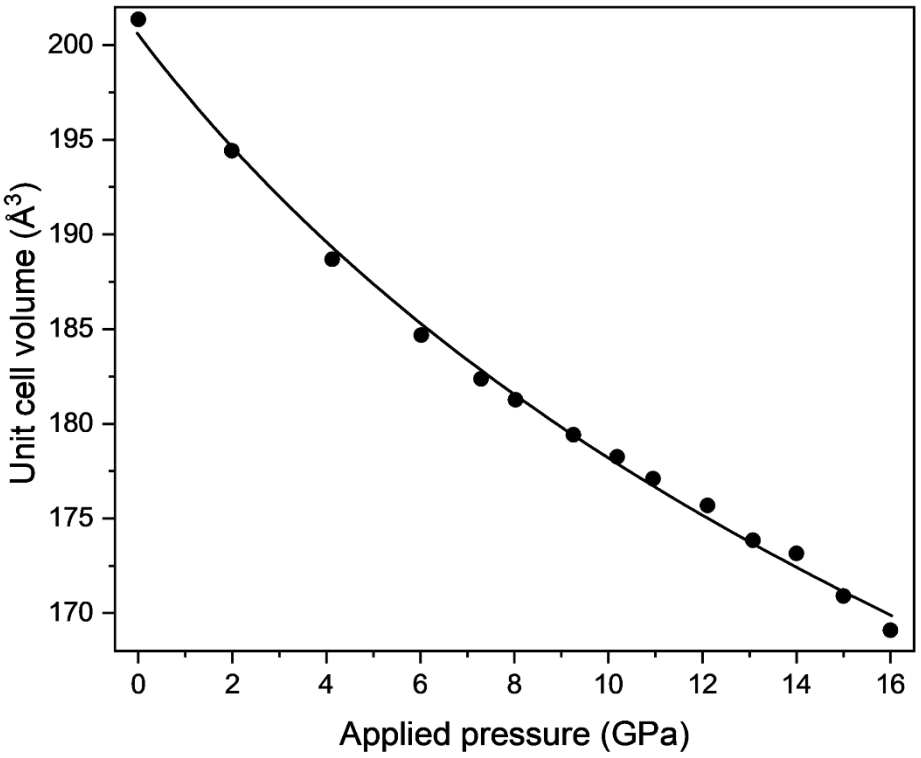


**Figure 5.11** Variation of the unit cell volume of $SrRbFe_4As_4$ with pressure collected between 0-16 GPa. The solid line is the fit to the data using a third-order Birch-Murnaghan Equation of State (Equation 5.1).

Similar treatment of the lattice parameters *a* and *c* can also be analysed by treating them as a volume component (Figure 5.12), that is, $a^3$ and $c^3$, which resulted in two directional compressibilities. Values extracted from this treatment for lattice parameter *c* agree reasonably well with the unit cell volume (the *c*- axis has a bulk modulus $K_0(c)$ of 56.19 GPa with a $K_0'(c) = 1.55$, Figure 5.12b), while lattice parameter *a* deviated from this behaviour and a third-order Birch-Murnaghan equation of state fitting resulted in anomalous $K_0$ and $K_0'$ values. However, an improved fit was achieved to fourth-order Birch-Murnaghan equation of state (Equation 5.2, Figure 5.12a), which yielded a bulk modulus of $K_0(a)$ of 64.39 GPa, $K_0'(a)$ of 0.0546, and $K_0''(a)$ of 4.7242 $GPa^{-1}$. The fourth-order Birch-Murnaghan equation provides a more accurate description of material behaviour under high pressure

compared to the lower-order equations, especially at extreme compressions, by including higher-order terms in the strain expansion, namely the second derivative $K_0''$ term.[13,14]

$$P = \frac{3K_0}{2}\left[\left(\frac{V_0}{V}\right)^{\frac{7}{3}} - \left(\frac{V_0}{V}\right)^{\frac{5}{3}}\right]\left\{1 - \frac{3}{4}(4 - K_0')\left[\left(\frac{V_0}{V}\right)^{\frac{2}{3}} - 1\right] + \frac{3}{8}(K_0'(K_0' - 7) + \left(\frac{143}{9}\right) + \left(\frac{8}{3}\right)K_0''\ K_0\left[\left(\frac{V_0}{V}\right)^{\frac{2}{3}} - 1\right]^2\right\} \quad \text{Equation 5.2}$$

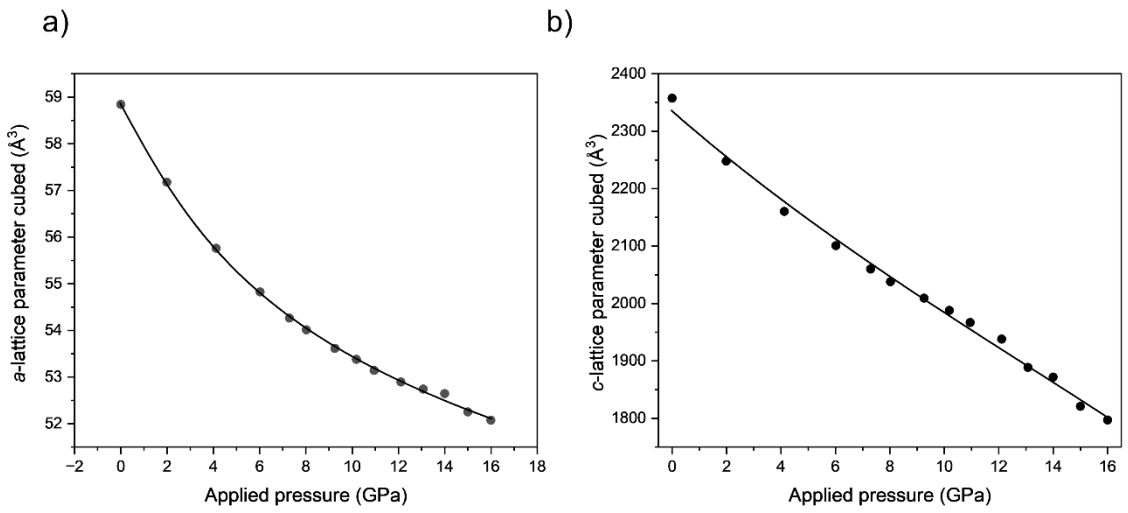


**Figure 5.12** a) Variation of lattice parameters *a* of $SrRbFe_4As_4$ with pressure collected between 0-16 GPa. The solid line is the fit to the data using a fourth-order Birch-Murnaghan Equation of State (Equation 5.2). b) Variation of lattice parameters *c* of $SrRbFe_4As_4$ with pressure collected between 0-16 GPa. The solid line is the fit to the data using a third-order Birch-Murnaghan Equation of State (Equation 5.1).

Figure 5.13 shows the PXRD patterns collected between 16.5-20 GPa in 0.5GPa steps. These PXRD patterns were very difficult to analyse using Rietveld refinement due to considerable peak broadening and therefore no lattice parameters were extracted for this pressure range. At 19 GPa, a number of new peaks emerge, which are marked by orange asterisks, resembling a structural transition (Figure 5.14). Despite attempting to fit a number of structural transitions (lattice collapse, shifting of $[Fe_2As_2]$ layers in different directions etc.), our investigations could not come to conclusions as to the origin of the newly emerged peaks.

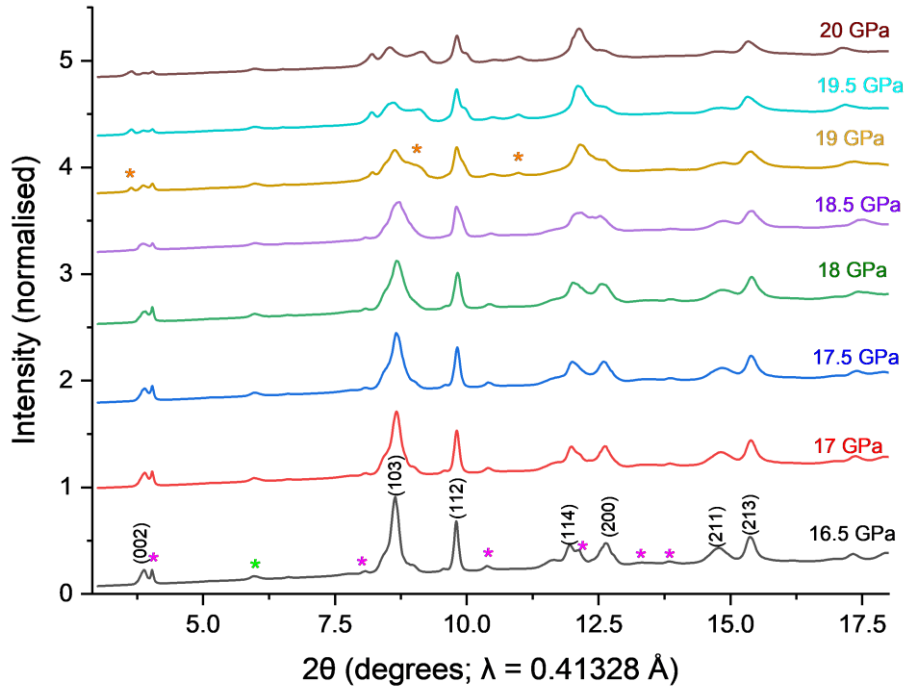


**Figure 5.13** Synchrotron PXRD patterns of $SrRbFe_4As_4$ upon application of pressure between 16.5-20 GPa. Magenta asterisks mark $Fe_2As$ and $SrFe_2As_2$ impurities, cyan asterisk marks an unknown impurity, and orange asterisks mark newly emerged peaks at 19 GPa.

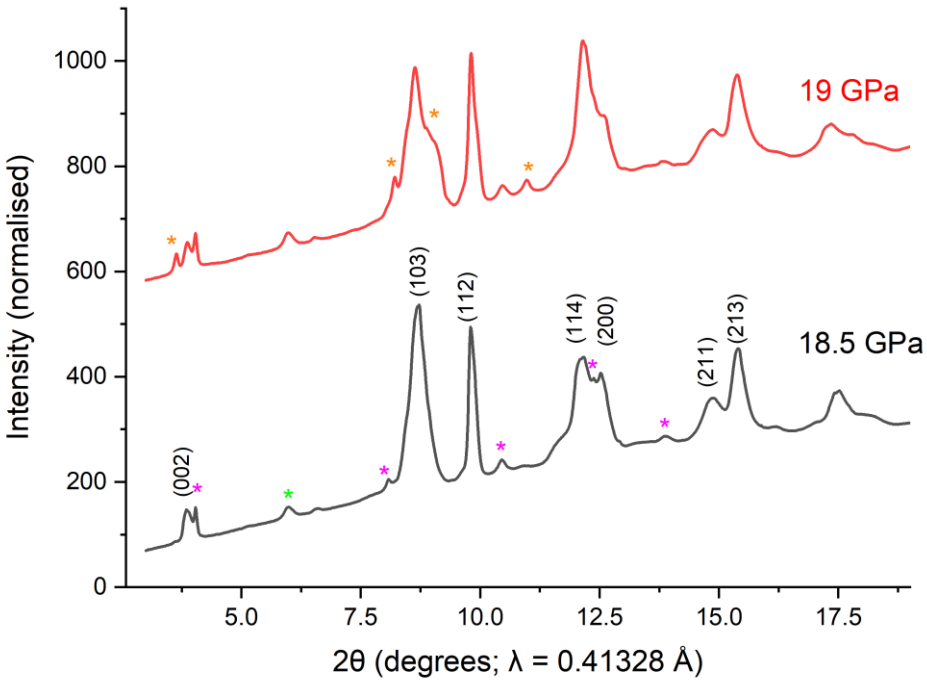


**Figure 5.14** Comparison of Synchrotron PXRD patterns of $SrRbFe_4As_4$ at structural transition between 18.5-19 GPa. Orange asterisks mark newly emerged peaks.

In the pressure range above 20 GPa, the pressure measurements by Raman spectroscopy on a ruby chip became increasingly unstable, and the rest of the experiment was carried out in 2 GPa pressure steps. Figure 5.15 shows the PXRD patterns collected in this pressure range, and they are marked by considerable broadening of peaks.

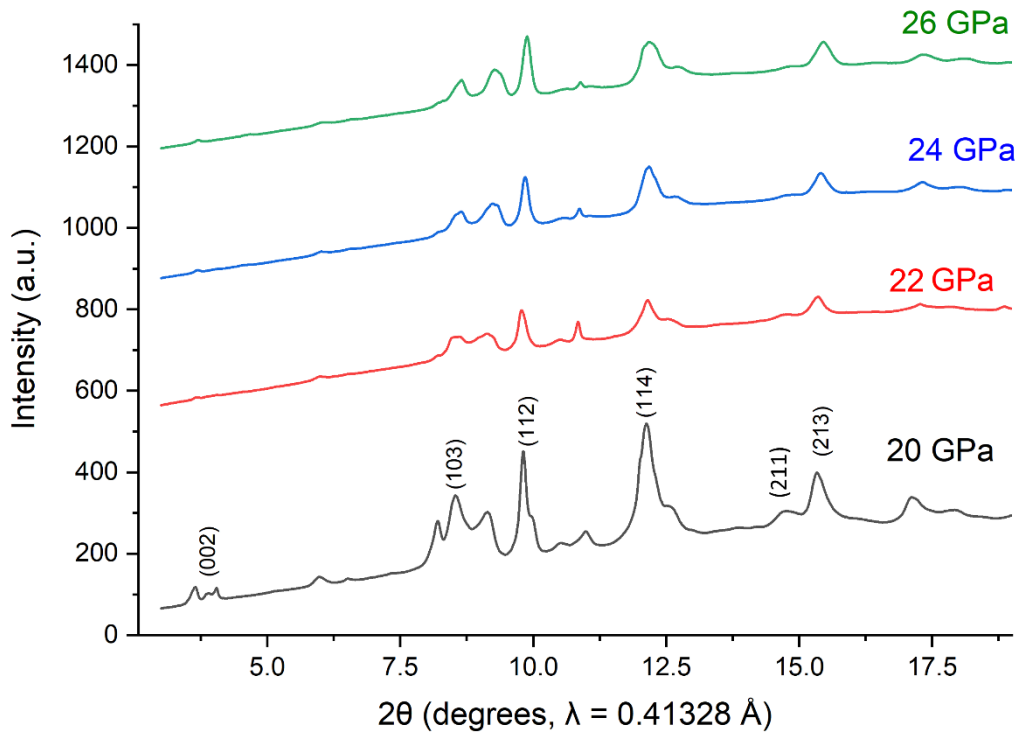


**Figure 5.15** Synchrotron PXRD patterns of $SrRbFe_4As_4$ measured between 20-26 GPa.

Figure 5.16 shows the PXRD patterns obtained upon pressure release at 15 GPa and 10 GPa. The PXRD pattern at complete pressure release at ambient pressure was not recorded. The two patterns collected on pressure release look very similar to the final PXRD pattern collected at 26 GPa, with the only new peak emerging at 3º 2$\theta$. This suggests that the change in the high-pressure region may be irreversible.

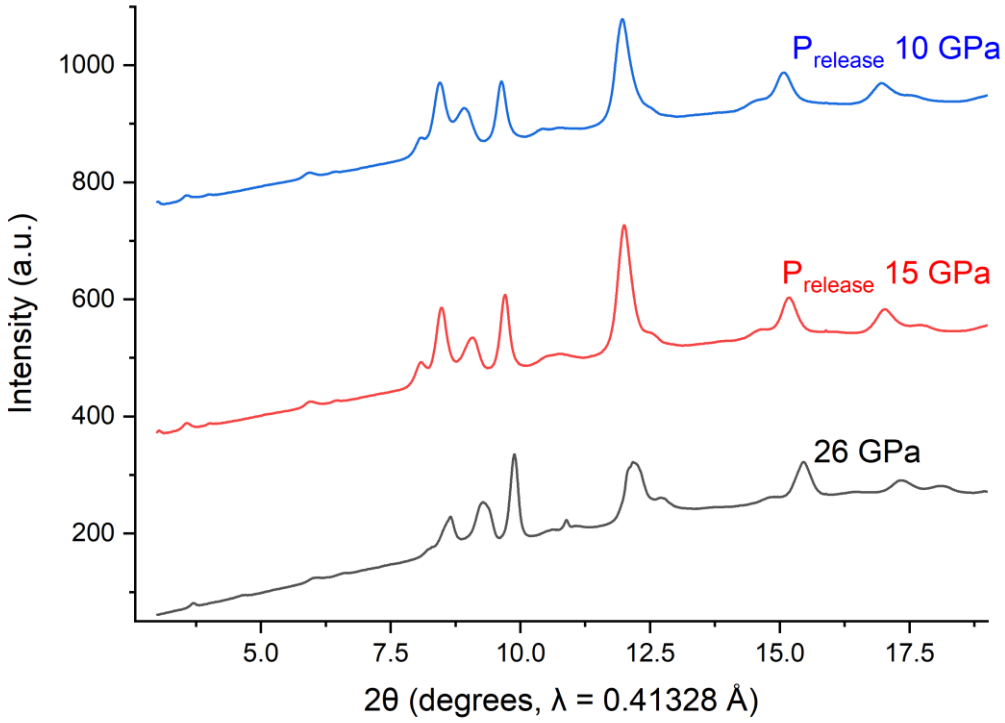


**Figure 5.16** Synchrotron PXRD patterns of $SrRbFe_4As_4$ measured upon pressure release. PXRD pattern at complete pressure release at ambient pressure was not recorded.

The structural data available from Rietveld refinements of PXRD patterns between 0-16 GPa suggests that $SrRbFe_4As_4$ requires much larger pressure for observation of the lattice collapse driven by As-As bond formation observed for $CaKFe_4As_4$ and $CaRbFe_4As_4$. The As-As distance in $SrRbFe_4As_4$ at 18 GPa is 3.34 Å, while distance of As-As planes in $CaRbFe_4As_4$ at first collapse at 6 GPa is 2.99 Å.[9] Figure 5.17 shows the variation in As-As distance across the thinner Sr layer in $SrRbFe_4As_4$ between 0-18 GPa.

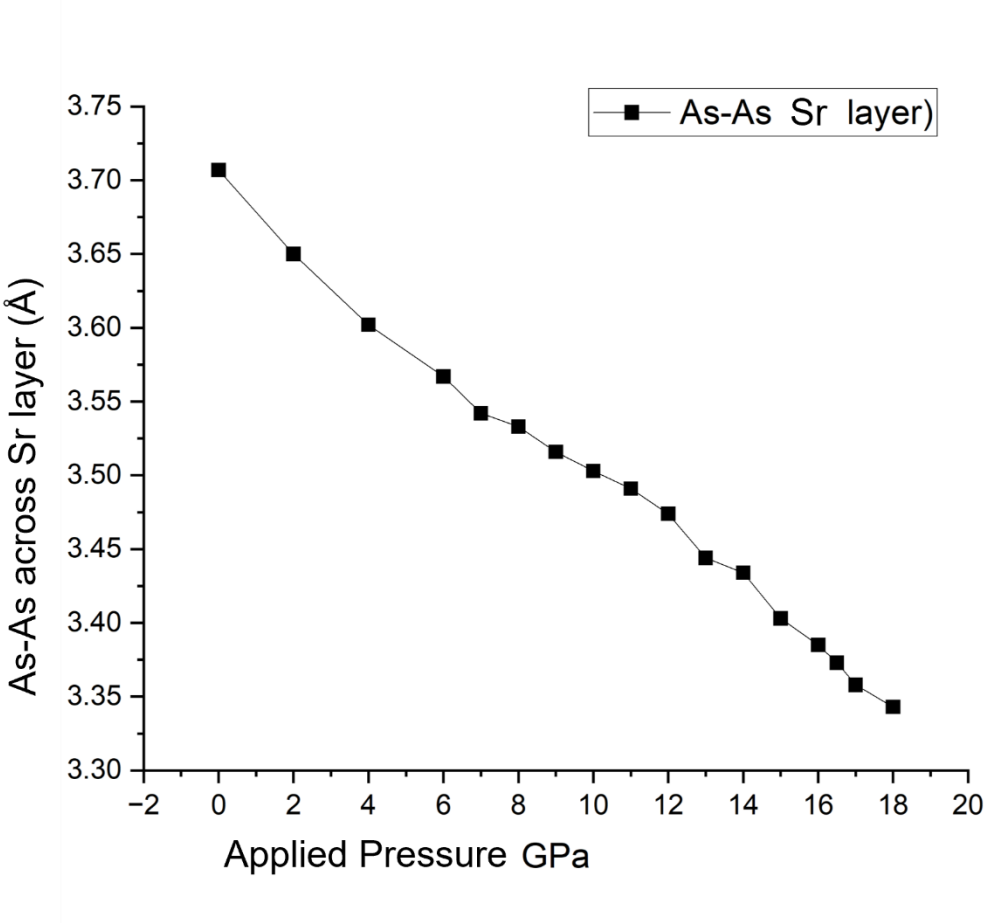


**Figure 5.17** Variation of As-As distance across the Sr layer in $SrRbFe_4As_4$ with applied pressure of 0-16 GPa from BL10XU Synchrotron PXRD data.

## 5.3 Conclusion

The high-pressure PXRD experiment on $SrRbFe_4As_4$ at BL10XU beamline of SPring-8 synchrotron did not reveal any structural phase transition in the region of 0-26 GPa that would resemble the unit cell collapse reported for $CaAFe_4As_4$ ($A$ = K, Rb) driven by formation of As-As bonds. This is likely due to the larger unit cell dimensions of $SrRbFe_4As_4$ compared to the Ca-analogues, and much higher pressure (> 30 GPa) is probably necessary for an observation of unit cell collapse in this phase. The data up to 16 GPa could be fitted to a third-order Birch-Murnaghan Equation of State. The calculated bulk moduli of unit cell volume agree well with similar literature reports on pressure studies of 1144 phases; Jackson *et al*. performed similar measurements on $AEuFe_4As_4$ ($A$ = Rb, Cs) and found for $CsEuFe_4As_4$, $K_0 = -V_0(\partial P/\partial V)$ = 46.3(2)GPa and $K_{0'}$ = 5.59(6), while for $RbEuFe_4As_4$, $K_0 = -V_0(\partial P/\partial V)$ = 50.7(7)GPa and $K_{0'}$ = 4.1(3).[15] Their $a$ and $c$ lattice parameter were, however, not fitted

to an equation of state as they showed a non-linear behaviour due to an observed half-collapse of lattice. Our data show smooth variation of *c* lattice parameter which yielded reasonable $K_0$ and $K_{0'}$ values when fitted to a third-order Birch-Murnaghan equation of state, however lattice parameter *a* was found to obey the fourth-order Birch-Murnaghan equation of state. As the data quality of this experiment was hindered by the considerable peak broadening, it was not possible to determine the exact structural reorganisation that occurs under pressure in $SrRbFe_4As_4$. For future work, it is advised to use helium gas as pressure medium instead of daphne oil to avoid this issue.

## References

[1] Iyo, A., Kawashima, K., Kinjo, T., Nishio, T., Ishida, S., Fujihisa, H., Gotoh, Y., Kihou, K., Eisaki, H., & Yoshida, Y. (2016). New-Structure-Type Fe-Based Superconductors: $CaAFe_4As_4$ (A = K, Rb, Cs) and $SrAFe_4As_4$ (A = Rb, Cs). *Journal of the American Chemical Society*, *138*(10), 3410–3415. https://doi.org/10.1021/jacs.5b12571.

[2] Huhnt C. *et al.* (1997), 'First-order phase transitions in the ThCr2Si2-type phosphides ARh2P2 (A = Sr, Eu)', *Physica B: Condensed Matter*, 240, 1–2, 26-37. doi:10.1016/S0921-4526(97)00431-6.

[3] Ni N. *et al.* (2008), 'First order structural phase transition in CaFe2As2', *Physical Review B*, 78, 014523. https://doi.org/10.1103/PhysRevB.78.014523.

[4] Rotter, M. *et al.* (2008) 'Spin-density-wave anomaly at 140 K in the ternary iron arsenide BaFe2As2', *Physical Review B*, 78(2), 020503. doi:10.1103/physrevb.78.020503.

[5] Ronning, F. et al. (2009) 'Superconductivity and the effects of pressure and structure in single crystalline SrNi2P2', *Physical Review B*, 79(1), 134507. doi:0.1103/PhysRevB.79.134507

[6] Naumov, A. et al. (2017) 'Pressure-induced magnetic collapse and metallization of TlFe1.6Se2' *Physical Review B*, *96*(1), 064109. doi:10.1103/PhysRevB.96.064109

[7] Huhnt, C. *et al.* (1998) 'First- and second-order phase transitions in ternary europium phosphides with ThCr2Si2-type structure', *Physica B: Condensed Matter*, 252(1–2), 44–54. doi:10.1016/s0921-4526(97)00904-6.

[8] Kaluarachchi, U.S. *et al.* (2017) 'Pressure-induced half-collapsed-tetragonal phase in CaKFe4As4', *Physical Review B*, *96*(14), 140501. doi:10.1103/physrevb.96.140501.

[9] Stillwell, R.L. *et al.* (2019) 'Observation of two collapsed phases in CaRbFe4As4', *Physical Review B*, *100*(4), 045152. doi:10.1103/physrevb.100.045152.

[10] Singh, S.J. et al. (2019) 'Optimization of superconducting properties of the stoichiometric CaKFe4As4', *Superconductor Science and Technology*, 33(2), 025003. doi:10.1088/1361-6668/ab58be.

[11] Birch, F. Finite Elastic Strain of Cubic Crystals. (1947). *Phys. Rev. 71* (11), 809–824. https://doi.org/10.1103/physrev.71.809.

[12] Gonzalez-Platas, J.; Alvaro, M.; Nestola, F.; Angel, R. EosFit7-GUI: A New Graphical User Interface for Equation of State Calculations, Analyses and Teaching. (2016). *J. Appl. Crystallogr. 49* (4), 1377–1382. https://doi.org/10.1107/s1600576716008050.

[13] Clough, L.A., Funnell, N.P., Ridley, C.J., Daisenberger, D., Hriljac, J.A., Lozinšek, M., Angel, R.J. and Parsons, S. (2025). An extended thermal pressure equation of state for sodium fluoride. *Journal of Applied Crystallography*, 58(1), 227–232. https://doi.org/10.1107/s1600576725000330.

[14] Ahmad, J. F., & Alkammash, I. Y. (2012). Theoretical study of some thermodynamical properties for solid under high pressure using finite-strain EOS. *Journal of the Association of Arab Universities for Basic and Applied Sciences*, *12*(1), 17–22. https://doi.org/10.1016/j.jaubas.2012.04.002

[15] Jackson, D. E., Vangennep, D., Bi, W., Zhang, D., Materne, P., Liu, Y., Cao, G. H., Weir, S. T., Vohra, Y. K., & Hamlin, J. J. (2018). Superconducting and magnetic phase diagram of RbEuFe4As4 and CsEuFe4As4 at high pressure. *Physical Review B*, *98*(1), 014518. https://doi.org/10.1103/PhysRevB.98.014518

# Chapter 6. Effect of Ni vacancies on superconductivity in $LaNi_xBi_2$

## 6.1 Introduction

Similar to high-*Tc* cuprates, superconductivity emerges in IBSCs in part thanks to their quasi-two-dimensional electronic structures, where electronic coupling along the stacking (*c*) axis is reduced.[1] Mizoguchi *et al*. described a route for the design of new superconductors which lies in the alternative stacking of a metallic square net and a blocking layer, which is either insulating or conductive, highlighting the importance of a layered crystal structure in new materials.[1] Of the known IBSCs, significant attention has been paid towards *ZrCuSiAs*-type compounds since the discovery of superconductivity in F-doped LaFeAsO with a $T_c$ of 26 K.[2] Here, layers of tetrahedral $La_2O_2$ alternate with tetrahedral $Fe_2As_2$, shown in Figure 6.1a. In contrast to the *ZrCuSiAs*-type structure of LaFeAsO, the 112-type is an intriguing structural variant of the IBSC family displaying high $T_c$; La-doped $CaFeAs_2$ has a $T_c$ of 34 K,[2] while co-doping with Sb increases the $T_c$ to 47 K.[3] Here, As forms zigzag chains along the *ab* plane, and an interesting structural detail is that As exists in two valence states (and hence in two different crystallographic positions, coordination environments, and geometries) in $Ca_{1-x}La_xFeAs_2$ (Figure 6.1b); As(1) forms $FeAs_4$ tetrahedra and its formal charge is −3, while As(2) forms zig-zag chains and its formal charge is −1 (i.e. these zig-zag chains are comparable to chains in elemental chalcogens, which are isoelectronic). Upon Sb-doping, it was found that Sb selectively occupies the As(2) positions. As $Ca_{1-x}La_xFeAs_2$ crystallises in the monoclinic $P2_1$ space group (n.4), its structure differs from rest of the known 112 phases, which have the *HfCuSi*$_2$-type structure and crystallise in the tetragonal *P*4/*nmm* space group (n.129) (Figure 6.1c). The difference between the two 112 structural variants (*i.e.* $P2_1$ and *P*4/*nmm* space groups) is that instead of As zigzag chains, the $Pn(2)^{-1}$ ions form a metallic square net (band calculations show linearly dispersed bands crossing the Fermi level, $E_F$).[4] The two structure types are compared with the *ZrCuSiAs*-type in Figure 6.1.

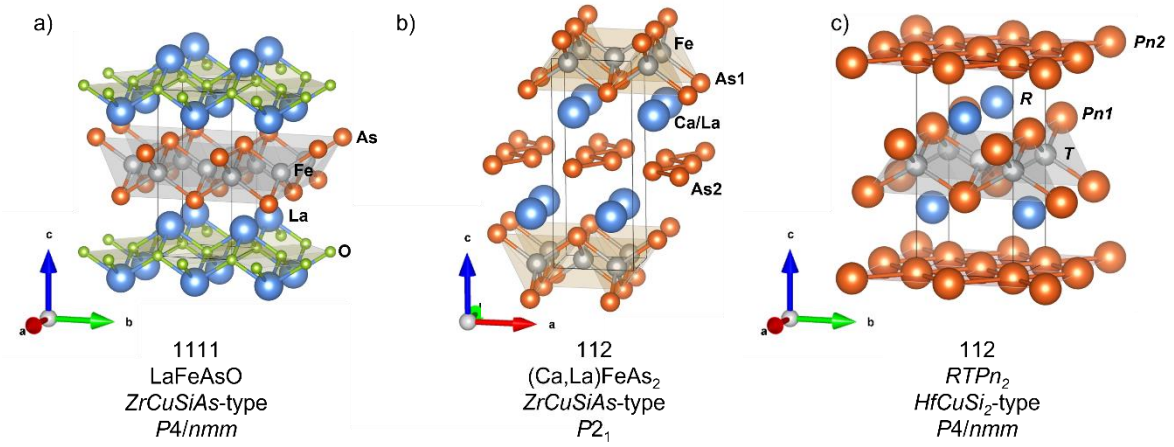


**Figure 6.1** Comparison of crystal structures of the a) 1111-type LaFeAsO, b) 112-type $Ca_{1-x}La_xFeAs_2$, and c) 112-type $RTPn_2$ (*R* = rare earth metal, *T* = transition metal, *Pn* = pnictogen).

112 intermetallic phases with the *HfCuSi*$_2$-type structure can accommodate a variety of transition metal and pnictide ions in its tetrahedral layer. Low-temperature superconductivity ($T_c \leq 5$K) which coexists with antiferromagnetic order was observed in *T*-deficient 112-compounds including $LaPd_xBi_2$, $LaPd_xSb_2$, and $CeNi_xBi_2$.[5,6] The $RNi_xBi_2$ intermetallic series, with *R* = La-Nd, Sm, Gd-Dy, have a chemical formula which can be written as $R^{3+}(Ni_x)^{1+}Bi(1)^{3-}Bi(2)^{1-}$, as Bi is present in two valence states; the Bi-array here forms the metallic square net, where the Bi 6p-band is not fully occupied because $Bi^{-1}$ has electronic configuration of $(6s)^2$ $(6p)^4$.[5] The two-dimensional electronic structure of the Bi(2) square net overlaps with the $Ni_xBi(1)$ conductive layer near the Fermi level ($E_F$).[5] Superconductivity in $CeNi_xBi_2$ is believed to originate from Ni deficiency as there is no evidence of bulk superconductivity in the parent compound, $CeNiBi_2$.[5,6,7] It is generally agreed upon that superconductivity in $CeNi_xBi_2$ pertains to the bulk, with high superconducting volume fraction (*SVF*) of 96%.[5,6,7] However, Mizoguchi *et al.* report the high *SVF* of $CeNi_xBi_2$ in contrast to other analogues of the series, namely *R* = La (1% SVF), Nd (14% SVF), and Y (17% SVF), with $T_c$ ranging between 4.0-4.2 K.[5] If this discrepancy arose from the fact that in the Ce-analogue, one less electron participates in bonding (*i.e.* $Ce^{4+}$ $4f^0$ vs $Ce^{3+}$ $4f^1$), this would then have an effect on the structural parameters, and $Ce^{4+}Ni_xBi_2$ would be smaller than the rest of the $RNi_xBi_2$ series, which is, however, not the case. Also, if $Ce^{4+}$ was to be stabilised in the presence of bismuthide anions, these would get rather easily oxidised, so the presence of $Ce^{4+}$ seems reasonably unlikely. The unit cell volume

decreases linearly in the series *R* = La-Nd, Sm, Gd-Dy, according to work by Lin *et al.* on single crystalline $R\mathrm{Ni_xBi_2}$.[8] Lin *et al.'s* detailed study on single crystals of the series show that Ni-Bi contamination of the main phase leads to observation of superconducting behaviour in the series: superconducting features in magnetometry and transport measurements were sample-dependant and irreproducible, hence the authors concluded that they originate from Ni-Bi impurities (NiBi and $\mathrm{NiBi_3}$) with identical $T_c$ of 4 K.[8,9,10] The single crystalline $\mathrm{LaNi_{0.84}Bi_{2.04}}$ (composition confirmed from SEM-EDX) showed low residual resistivity ratio (*RRR*) and incomplete and irreproducible transitions in resistivity data and had a low *SVF* of 3%. Lin *et al.*'s finding of extrinsic superconductivity in $R\mathrm{Ni_xBi_2}$ was shared by Rosa *et al.*, who investigated the role of Ni vacancies on the physical properties of $\mathrm{CeNi_xBi_2}$ and $\mathrm{LaNi_xBi_2}$ single crystals. They concluded that even though superconductivity is not observed in the parent (stoichiometric) compounds, and Ni deficiency is necessary for the observation of superconductivity due to the need to stabilize the electronic structure, the superconducting transitions lack bulk signature.[7] However, they fail to comment whether the origin of superconductivity is in secondary phases. Hence, it is clear that there is a division/gap in literature regarding the superconductivity in $R\mathrm{Ni_xBi_2}$ and whether it arises from bulk (intrinsic) or secondary phase origins (extrinsic). A major problem in assessing the origin of superconductivity in $R\mathrm{Ni_xBi_2}$ is the difficulty of obtaining pure phases; even a small amount of residual Bi will lead to an observation of the signature 4 K superconducting transition of elemental Bi in magnetometry, as SQUID magnetometers are highly sensitive to superconducting impurities. Yakita *et al.* report that phase pure $(\mathrm{Ca},R)\mathrm{FeAs_2}$ ($P2_1$ 112 structure type) were obtained from high pressure synthesis method,[11] which was also reported to produce phase pure 1111 phases in the past.[12] Our investigation assesses whether high pressure synthesis can aid in obtaining highly pure *HfCuSi*$_2$-type compounds, namely $\mathrm{LaNi_xBi_2}$, and the effect of Ni vacancies on superconductivity in $\mathrm{LaNi_xBi_2}$.

## 6.2 Synthesis and characterisation of $\mathrm{LaNi_xBi_2}$

### *6.2.1 Synthesis at ambient pressure*

Polycrystalline $\mathrm{LaNi_xBi_2}$ samples with x = 0.65, 0.7, 0.75, and 0.8 were synthesised via a traditional ceramic route reported in Reference [5]. These values of *x* were selected as literature reports suggest an ideal region of formation of high purity $\mathrm{LaNi_xBi_2}$ lies between 0.7-0.8.[7,10] Stoichiometric amounts

of La ingot (Alfa Aesar, 99.99%, filed to powder form from the ingot for easy manipulation), Ni powder (Alfa Aesar, 99.99%), and Bi powder (Alfa Aesar, 99.99%) were combined in a mortar and ground for ~5 minutes to allow good contact of powder grains. The powder was pelletised under uniaxial pressure of 3MPa, and the resulting pellet was placed at the bottom of a silica tube, which was vacuum-sealed. The tube was then heated slowly at 1°C/min to 500°C where it was held for 10 hours before allowing the oven to cool at its natural rate by switching it off. The pellet was then ground, pelletised, and reheated to 750°C for 20 hours, with the same heating and cooling rates. Multiple additional heat treatments (2-3) were performed at 800°C for 10 hours, at which point a crystalline product was obtained.

### *6.2.2 Synthesis at high pressure*

Polycrystalline $LaNi_xBi_2$ with x = 0.7, 0.75, 0.8, 0.85, and 1, were synthesised via high pressure synthesis reported in Reference [8] at University of Kyoto. Stoichiometric amounts of La ingot (Alfa Aesar, 99.99%, filed to powder form from the ingot for easy manipulation), Ni powder (Alfa Aesar, 99.99%), and Bi powder (Alfa Aesar, 99.99%) were combined in a mortar and ground for ~5 minutes to allow good contact of powder grains. The powder was then pelletised into a pellet with diameter of 4mm in order to fit into the high-pressure cell employed in the synthesis. To assemble the cell, the pellet composed of the starting materials was loaded into a boron nitride crucible, which was enclosed in a graphite tube heater inside a pyrophyllite cell. Both ends of the cell were capped with boron nitride caps, Mo sheets, and pyrophyllite rings (from above and below). The pressure applied by the cubic anvil press was set to 2 GPa. The sample was heated to 1000°C at a rate of 50°C/min, held for 60 minutes, and cooled to room temperature with a simultaneous pressure release over 40 minutes. A visual representation of the assembly of the high-pressure cell is shown in Figure 6.2. More details on the cubic anvil press are described in Chapter 2.1.2.

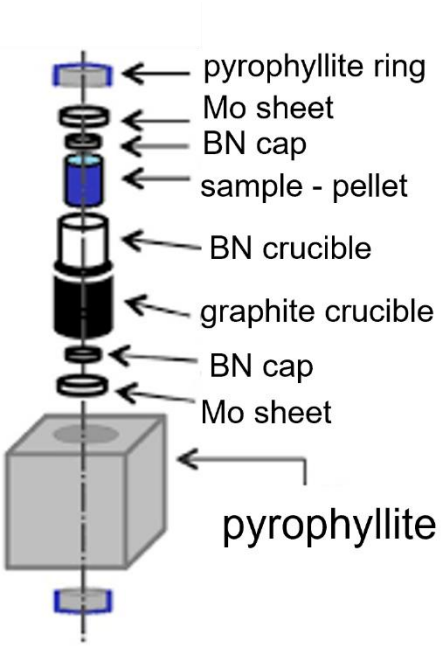


**Figure 6.2** Assembly of a pyrophyllite-type high-pressure cell.

### *6.2.3 Room temperature SXRD*

#### 6.2.3.1 SXRD of ambient pressure $LaNi_xBi_2$

The ambient pressure (*i.e.* high temperature ceramic method) route was employed to obtain $LaNi_xBi_2$ with $x$ = 0.65, 0.7, 0.75, and 0.8. Literature reports on $RNi_xBi_2$ concluded that Ni-deficiency is necessary for formation of the pure phase and avoidance of Ni-Bi impurities. Mizoguchi *et al.* noted that $LaNi_xBi_2$ sample with x = 0.65 resulted in a pure product, but no PXRD patterns were provided in the study. Our investigations found that $LaNi_xBi_2$ sample with x = 0.7 was formed at highest crystallinity and purity and this $x$ value seems to be the ideal composition for obtaining a pure product via ambient pressure route (throughout this chapter, we will refer to this sample as Low-Pressure-$LaNi_{0.7}Bi_2$, when comparing with $LaNi_xBi_2$ obtained via high-pressure synthesis). Its purity reached 86.5 mol% after reheating at 800°C/10hrs, however the high mole percentage of $NiBi_3$ impurity (13.5%) did not decrease upon annealing. Figure 6.3 compares the PXRD patterns for the series of $LaNi_xBi_2$ with x = 0.65, 0.7, 0.75, and 0.8, which could all be indexed according to tetragonal *P*4/*nmm* space group of the parent stoichiometric compound using Rietveld refinement. It is noticeable that

other than sample x = 0.7, all other samples contain large amounts of Ni-Bi impurities, marked by green and cyan asterisks.

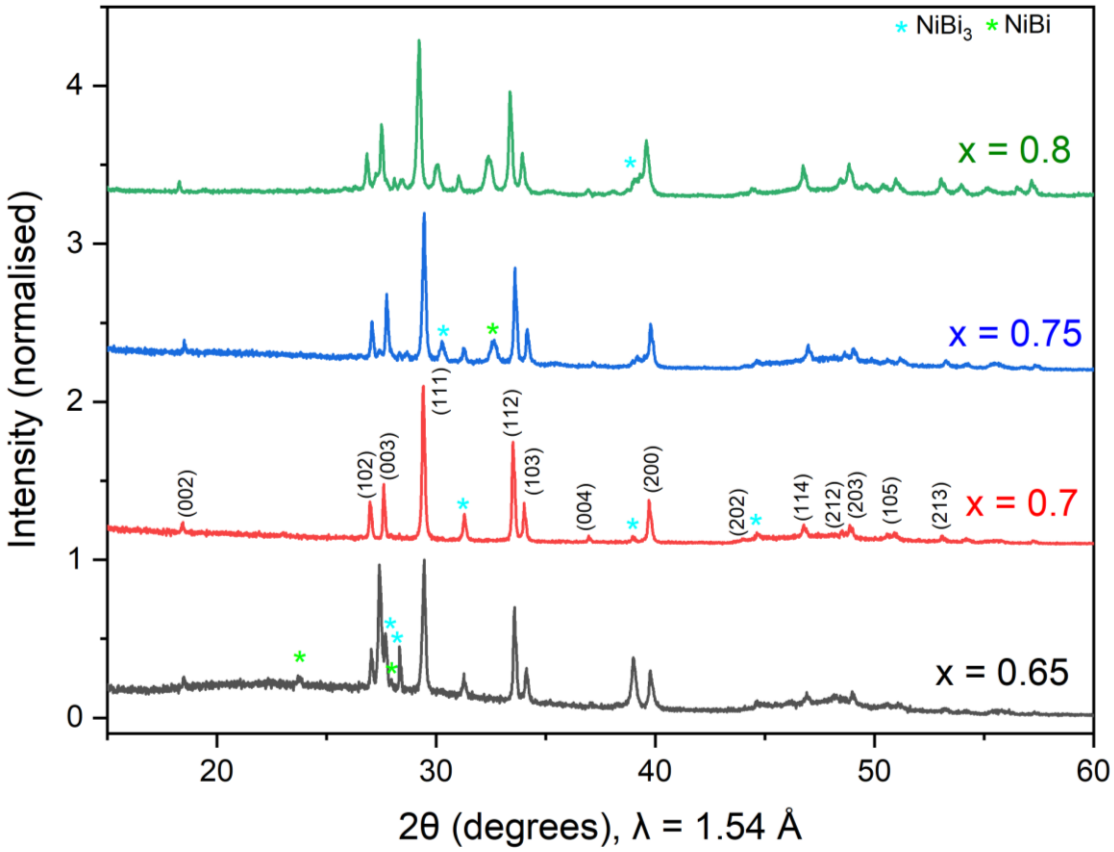


**Figure 6.3** Laboratory PXRD patterns of LP-$LaNi_xBi_2$ with x = 0.65, 0.7, 0.75, and 0.8. Green and cyan asterisks represent NiBi and $NiBi_3$ impurities, respectively.

The lattice parameters of these low-pressure phases change very slightly with *x*, as shown in Figure 6.4. $LaNi_xBi_2$ with x = 0.7, which formed at highest purity and crystallinity, is shown to display largest lattice parameters. There is no clear trend in the variation of lattice parameters with *x*.

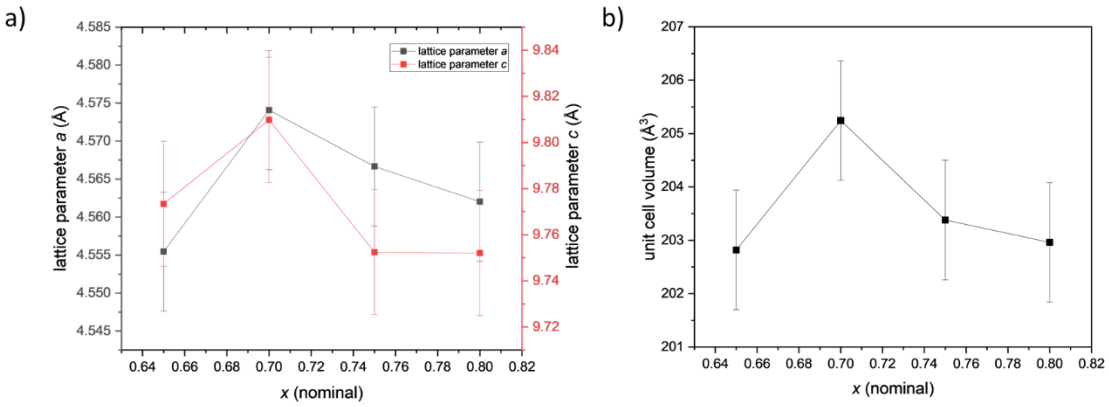


**Figure 6.4** Variation of lattice parameters a) *a* (black plot) and *c* (red plot), and b) unit cell volume with *x* in LP-$LaNi_xBi_2$.

The high resolution PXRD pattern of low-pressure $LaNi_{0.7}Bi_2$ synthesised at highest purity is shown in Figure 6.5. The refined Ni occupancy is 0.66(1) from PXRD. The intriguing point of the analysis is the high percentage of $NiBi_3$ present in the pattern, considering that no La-containing impurity has been identified.

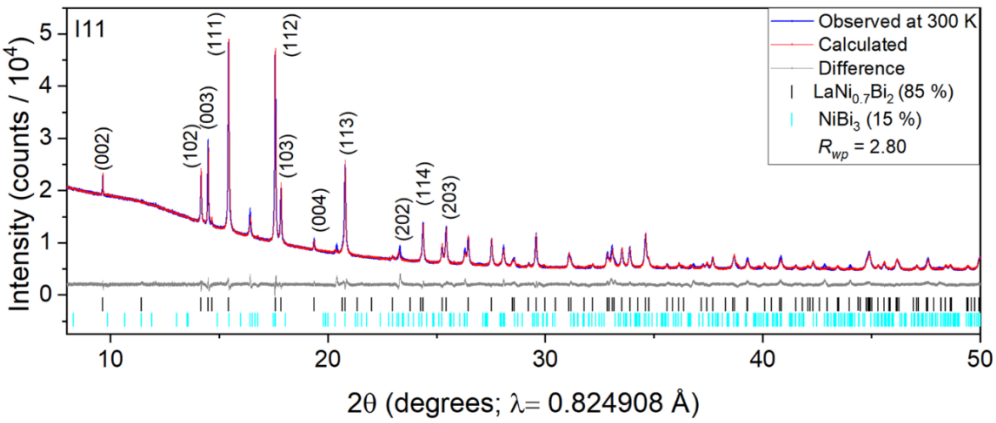


**Figure 6.5** Room-temperature Rietveld refinement of LP-$LaNi_{0.7}Bi_2$ against Synchrotron PXRD. The refined *occ*Ni is 0.66(1) which is very close to the nominal value.

Figure 6.6 shows the crystal structure of low-pressure $LaNi_{0.7}Bi_2$ obtained from Rietveld refinement. Due to Bi occupying two distinct sites, there are two distances between La-Bi: La-Bi(2)$^{-1}$ is 3.486(3)

Å, and La-Bi(1)$^{-3}$ is 3.367(10) Å, which is slightly shorter due to the lower valence state of Bi, and La forms tighter bonds with the more negative Bi(1) ion. The two tetrahedral angles are both greatly distorted from ideal; at 104.56(4)° and 119.82(8)°.

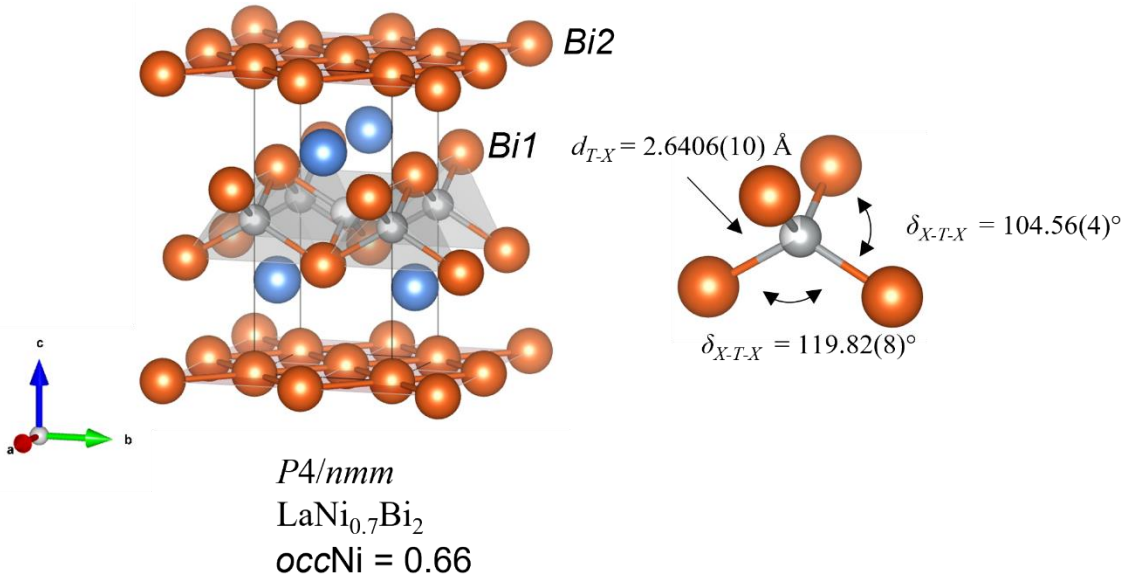


**Figure 6.6** Crystal structure of LP-$LaNi_{0.7}Bi_2$.

### 6.2.3.2 SXRD of high pressure $LaNi_xBi_2$

As the ambient pressure synthesis route did not yield pure $LaNi_xBi_2$, a high-pressure route was employed to obtain $LaNi_xBi_2$ with $x$ = 0.7, 0.75, 0.8, 0.85, and 1 (throughout this chapter we will refer to these compounds as HP-$LaNi_xBi_2$). Even though this synthesis route was not realised for $RNi_xBi_2$ phases before, it was successfully employed in the case of (Ca,La)$FeAs_2$.[9] The PXRD patterns of the series are shown in Figure 6.7 and all samples were found to crystallise in the *P*4/*nmm* space group.

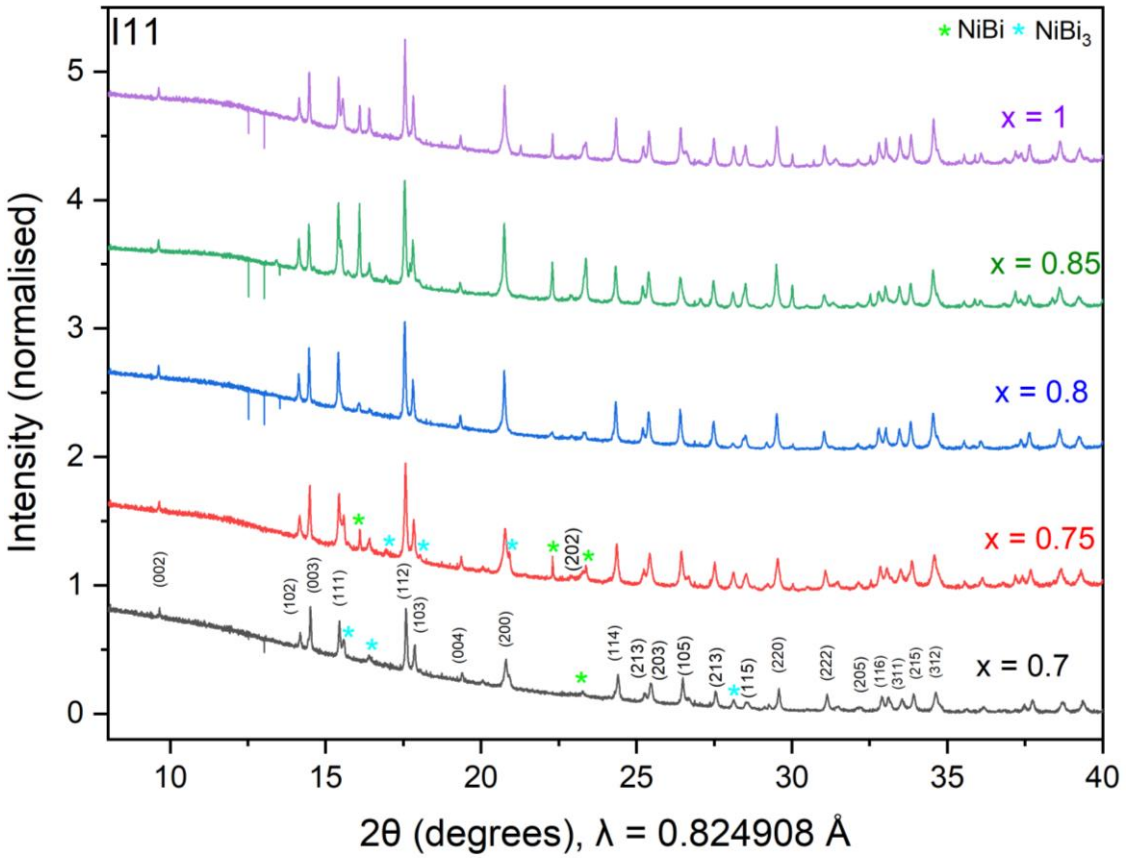


**Figure 6.7** Synchrotron PXRD patterns of HP $LaNi_xBi_2$ with $0.7 \leq x \leq 1$. Green and cyan asterisks represent NiBi and $NiBi_3$ impurities, respectively. Negative peaks between 12.5-13.5º are instrumental artefacts.

HP-$LaNi_xBi_2$ phases contain varying amounts of NiBi and $NiBi_3$ impurities. Figure 6.8 summarises the weight percentage of the two impurities; it is clear that x = 0.8 is the ideal composition for obtaining a pure product via high-pressure route, with only 1% NiBi formed as secondary phase, while on both sides of this *x* value the product forms with substantial Ni-Bi secondary phases.

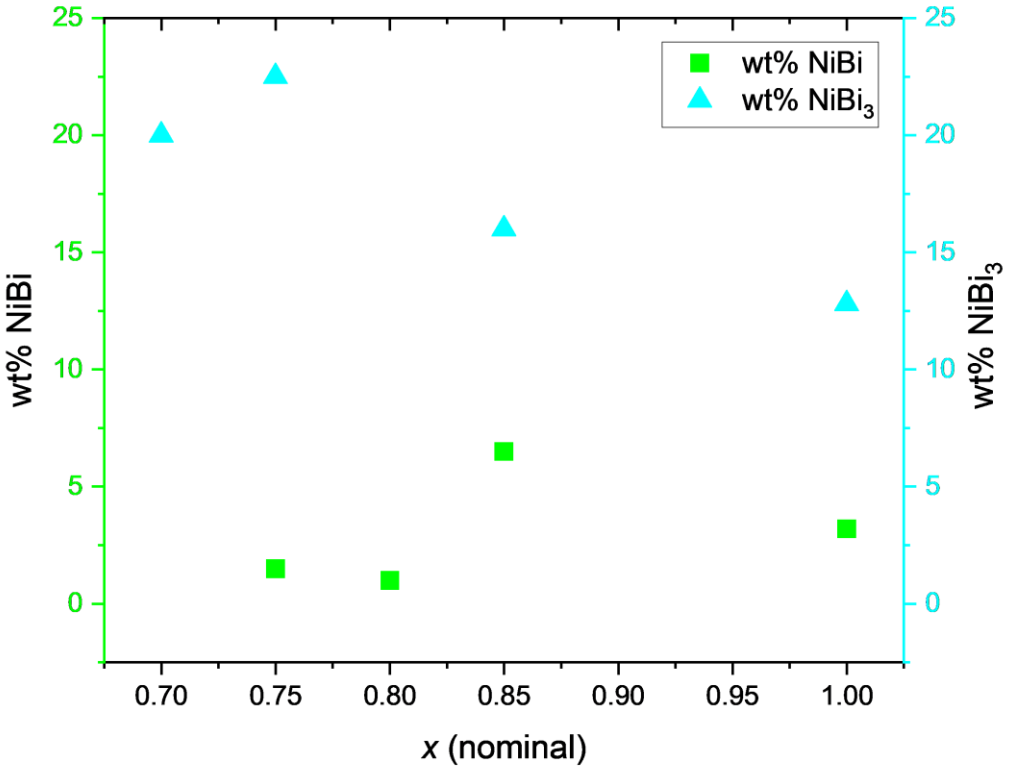


**Figure 6.8** Variation of NiBi and $NiBi_3$ impurities in HP-$LaNi_xBi_2$ with $0.7 \leq x \leq 1$.

Figure 6.9 shows the Rietveld refinement of HP-$LaNi_{0.7}Bi_2$. The refined Ni occupancy from PXRD is 0.75(1) which is very close to the nominal value. $NiBi_3$ formed at 20% as a secondary phase.

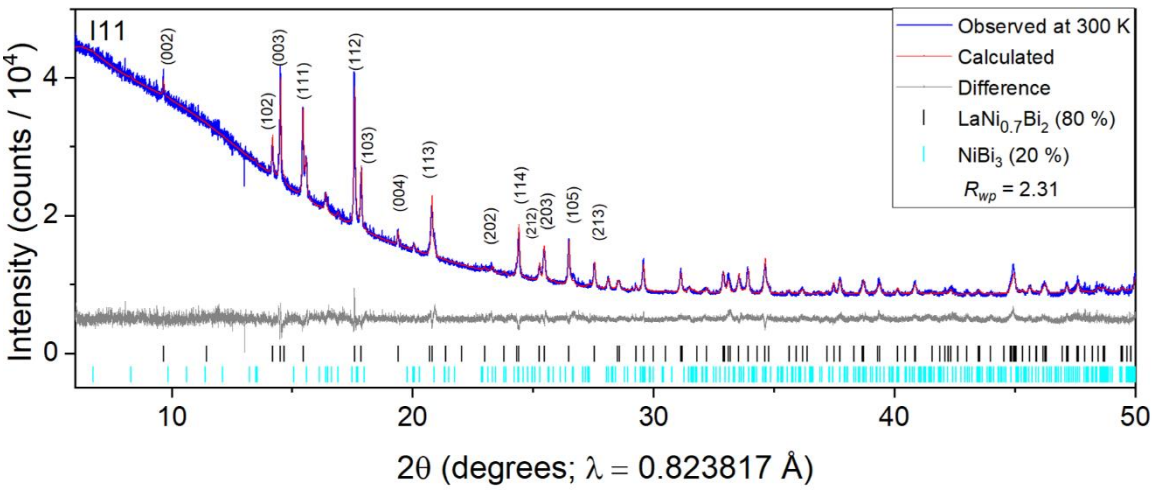


**Figure 6.9** Room-temperature Rietveld refinement of $LaNi_{0.7}Bi_2$ against Synchrotron PXRD. The negative intensity peak at ~13º is an instrumental artefact.

Figure 6.10 shows the Rietveld refinement of HP-$LaNi_{0.75}Bi_2$. The refined Ni occupancy from PXRD is 0.85(1). $NiBi_3$ and NiBi formed at 22.5% and 1.5%, respectively, as secondary phases.

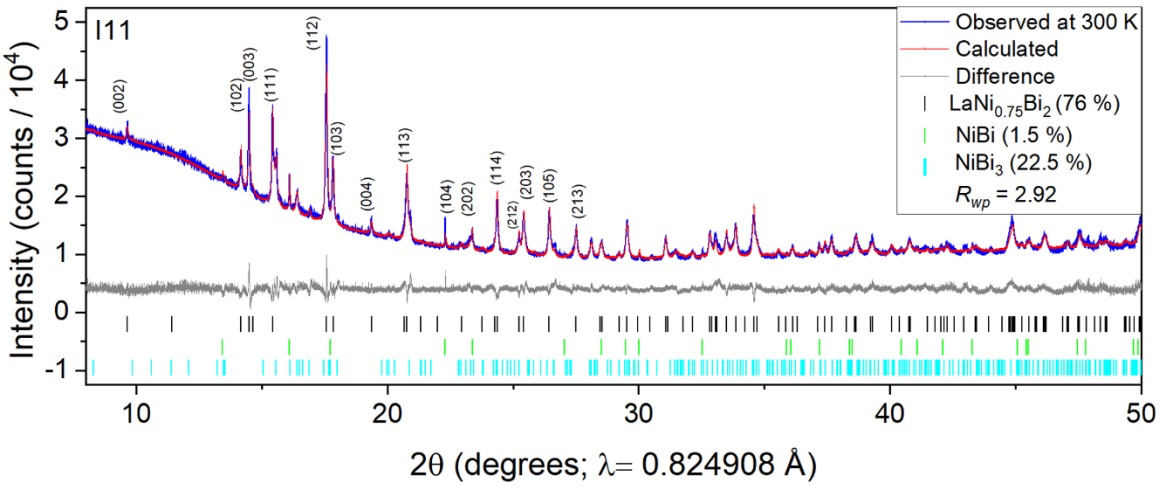


**Figure 6.10** Room-temperature Rietveld refinement of $LaNi_{0.75}Bi_2$ against Synchrotron PXRD.

Figure 6.11 shows the Rietveld refinement of HP-$LaNi_{0.8}Bi_2$. The refined Ni occupancy from PXRD is 0.87(1) which is very close to the nominal value. NiBi formed at 1% as a secondary phase.

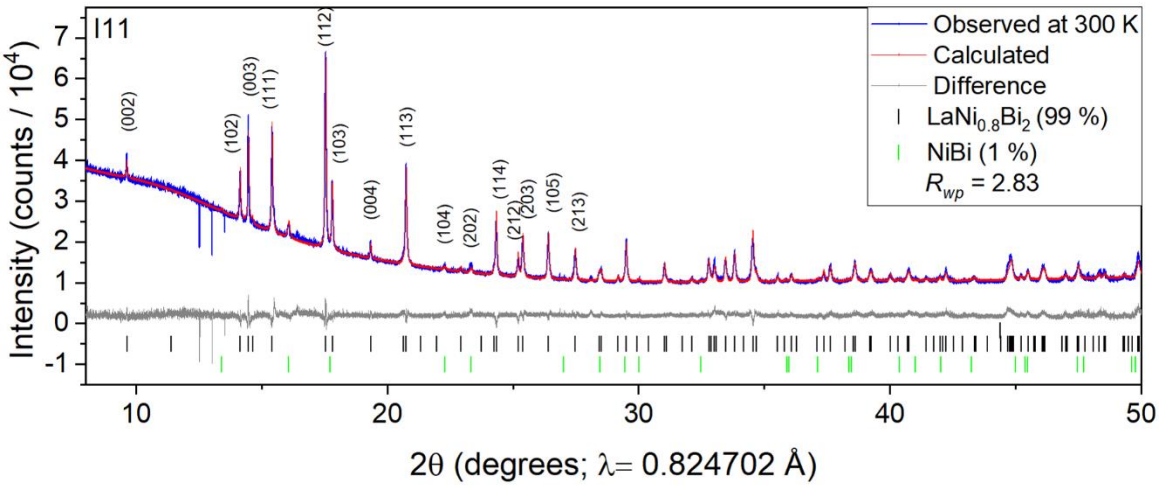


**Figure 6.11** Room-temperature Rietveld refinement of $LaNi_{0.8}Bi_2$ against Synchrotron PXRD. The three negative intensity peaks at ~12.5-13.5º are an instrumental artefact.

Figure 6.12 shows the Rietveld refinement of HP-$LaNi_{0.85}Bi_2$. The refined Ni occupancy from PXRD is 0.92(1). $NiBi_3$ and NiBi formed at 16% and 6.5%, respectively, as secondary phases.

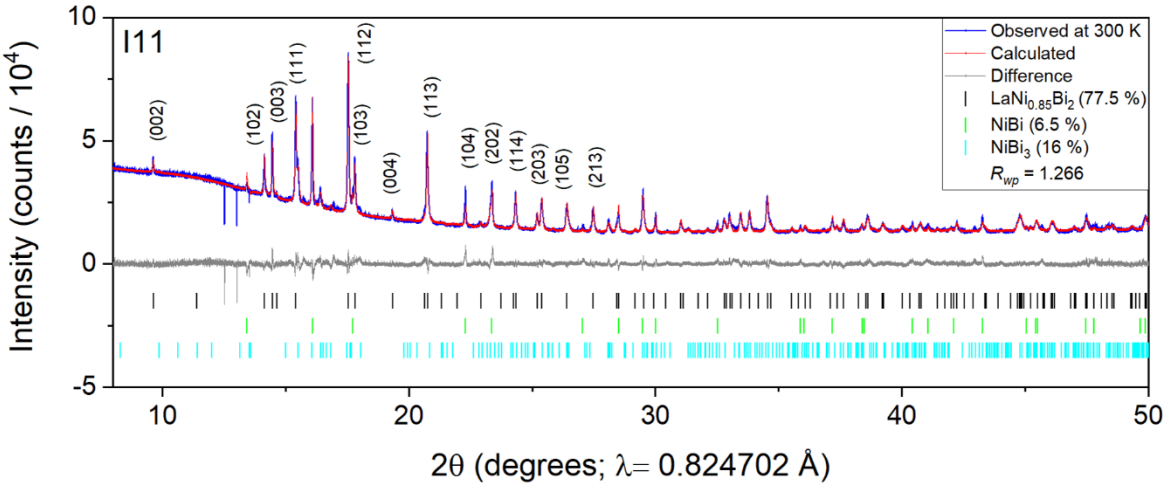


**Figure 6.12** Room-temperature Rietveld refinement of $LaNi_{0.85}Bi_2$ against Synchrotron PXRD. The three negative intensity peaks at ~12.5-13.5º are an instrumental artefact.

Figure 6.13 shows the Rietveld refinement of HP-$LaNiBi_2$. The refined Ni occupancy from PXRD is 0.94(1) which is very close to the nominal value. $NiBi_3$ and NiBi formed at 12.8% and 3.2%, respectively, as secondary phases.

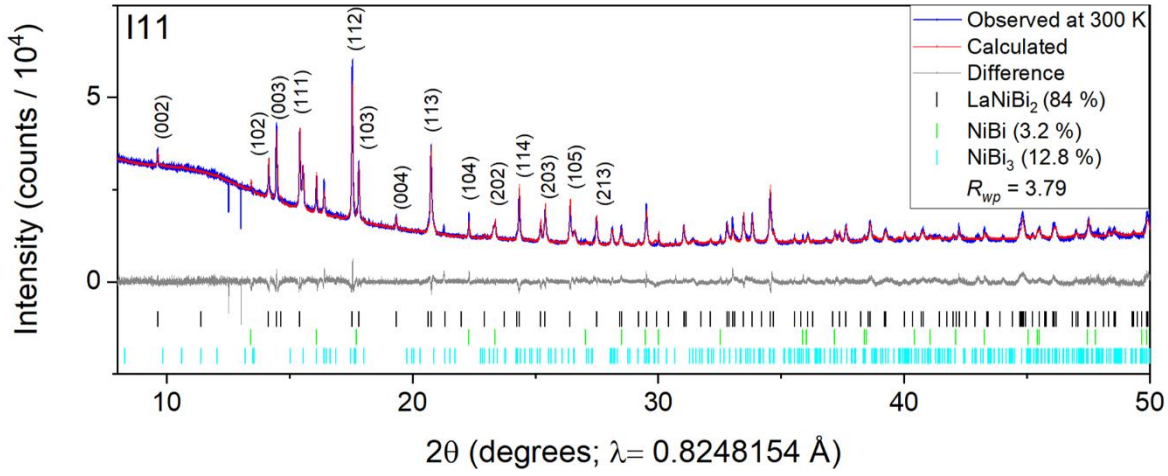


**Figure 6.13** Room-temperature Rietveld refinement of $LaNiBi_2$ against Synchrotron PXRD. The three negative intensity peaks at ~12.5-13º are an instrumental artefact.

Figure 6.14 shows the crystal structure of HP-$LaNi_{0.8}Bi_2$ obtained from Rietveld refinement, which is the composition synthesised at highest purity (99%) from the high-pressure series. The two distances between La-Bi are: La-Bi(2)$^{-1}$ = 3.464(3) Å (versus 3.486(3) Å in LP-$LaNi_{0.7}Bi_2$) , and La-Bi(1)$^{-3}$ = 3.3765(11) Å (versus 3.367(10) Å in LP-$LaNi_{0.7}Bi_2$). The two tetrahedral angles are both

greatly distorted from ideal; at 104.68(4)° and 119.54(8)° (versus 104.56(4)° and 119.82(8)° in LP-$LaNi_{0.7}Bi_2$).

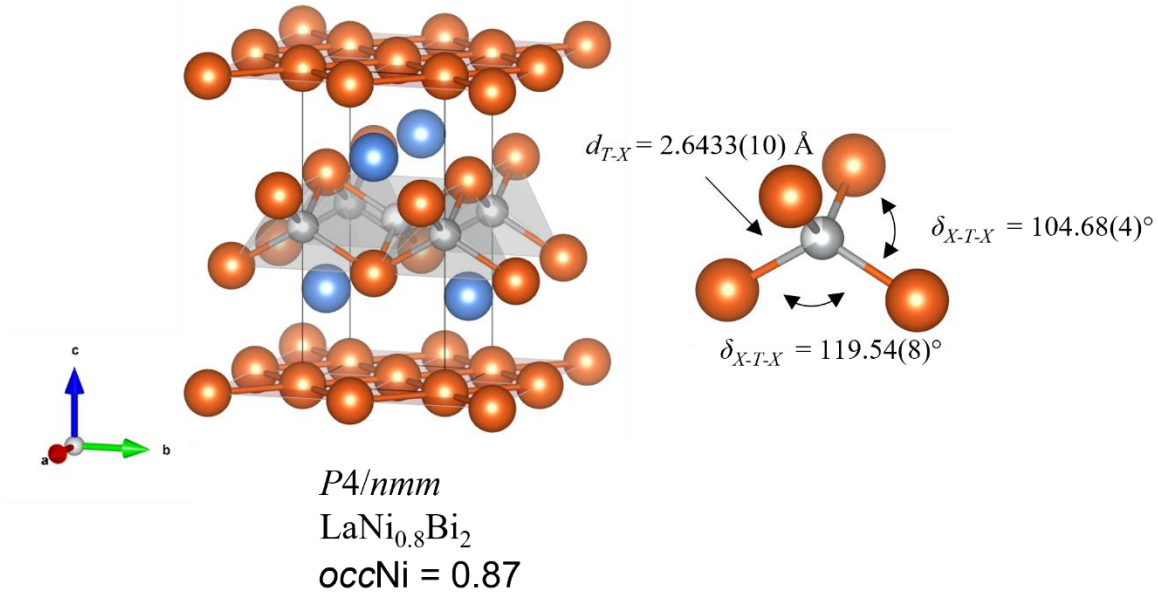


**Figure 6.14** Crystal structure of HP-$LaNi_{0.8}Bi_2$ with structural details obtained from Synchrotron PXRD (purest sample obtained via high-pressure synthesis).

Figure 6.15 shows the variation of lattice parameters *a* and *c* with *x* for HP-$LaNi_xBi_2$ with $0.7 \leq x \leq 1$ and LP-$LaNi_xBi_2$. It is clear that for LP-$LaNi_xBi_2$ phases, there is no trend in either of the lattice parameters, which both peak at x = 0.7. On the other hand, for HP-$LaNi_xBi_2$ phases, the figures show that both lattice parameters show the same trend of increasing between $0.7 \leq x \leq 0.8$ and then remaining approximately constant between $0.8 \leq x \leq 1$. The large error bars here suggest that the phase width to this compound is small.

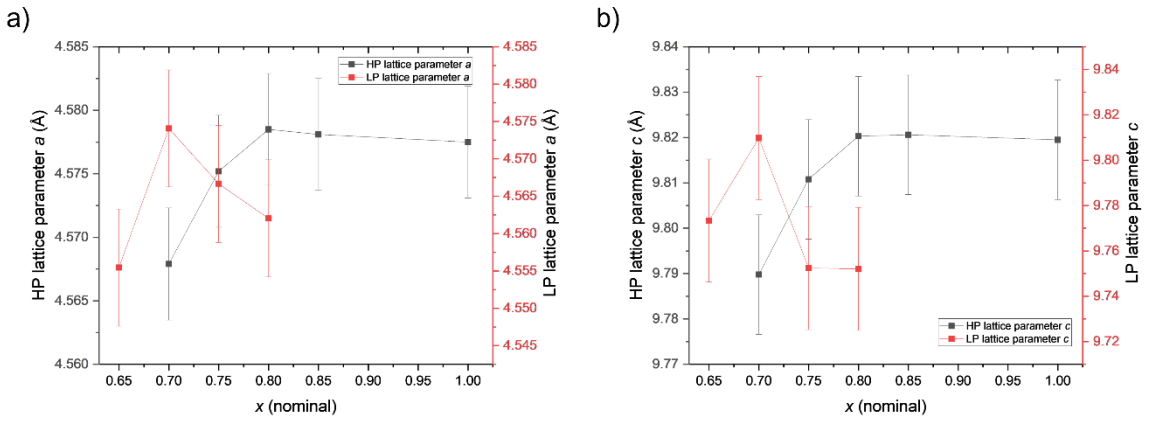


**Figure 6.15** Variation of lattice parameter *a* (a) and *c* (b) of LP (red plot) and HP (black plot) $LaNi_xBi_2$ with nominal *x*.

Variation of the unit cell volume with *x* for HP-$LaNi_xBi_2$ with $0.7 \leq x \leq 1$ resembles the same trend as *a* and *c* parameters; the volume peaks at x = 0.8 and remains constant afterwards (Figure 6.16a). On the other hand, the *c/a* ratio for HP-$LaNi_xBi_2$ phases the initial increase the trend settles after x = 0.85. The LP-$LaNi_xBi_2$ do not show any trend in unit cell volume or *c/a* ratio.

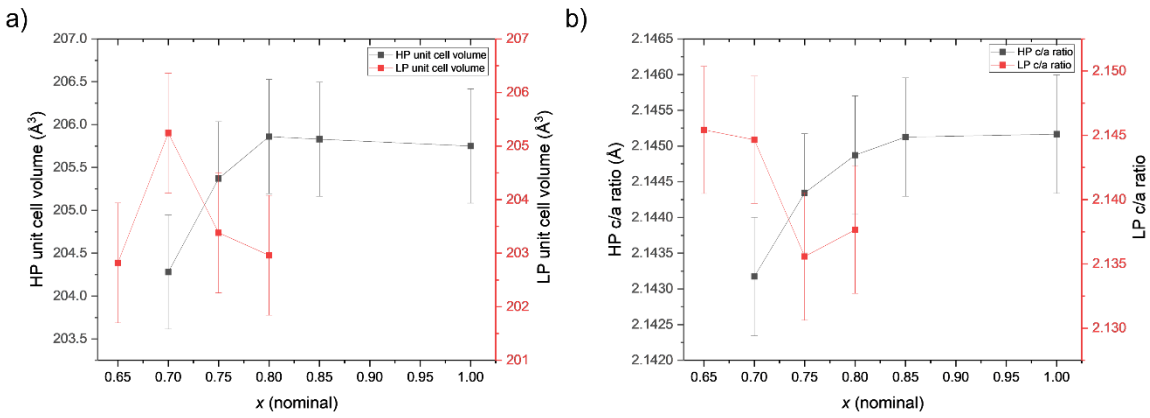


**Figure 6.16** Variation of the unit cell volume (a) and *c/a* ratio (b) of LP (red plot) and HP (black plot) $LaNi_xBi_2$ with nominal *x*.

Figure 6.17 shows the variation of lattice parameters with refined *x* for HP-$LaNi_xBi_2$ with $0.7 \leq x \leq 1$, and LP- $LaNi_{0.7}Bi_2$ is shown for reference. For refined *x* vs unit cell volume, the initial increase the trend settles after x = 0.85 (Figure 5.16a), and same is true for lattice parameters *a* and *c* (Figure

6.17b). On the other hand, for refined *x* vs *c/a* ratio (Figure 5.16c) the increase is linear between 0.7 ≤ x ≤ 1.

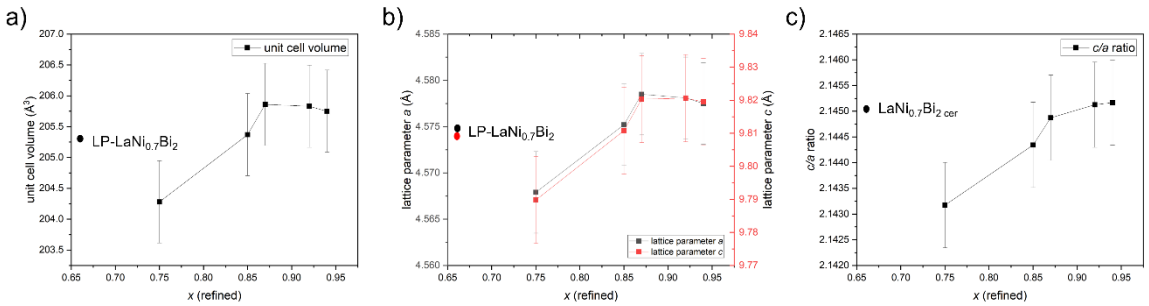


**Figure 6.17** Variation of a) unit cell volume, b) lattice parameters *a* (black plot) and *c* (red plot), and c) *c/a* ratio with refined x in HP-$LaNi_xBi_2$. LP-$LaNi_{0.7}Bi_2$ is shown for comparison.

Figure 6.18 shows the variation of bond lengths and tetrahedral angle ($\delta_{As\text{-}Fe\text{-}As}$) with nominal *x* from Synchrotron PXRD data. These do not follow any obvious trend with compositional changes, only the Ni-Ni distance follows the same trend as observed for lattice parameters (*a*, *c*, and *V*), where the distance peaks at x = 0.8 and levels off until x = 1.

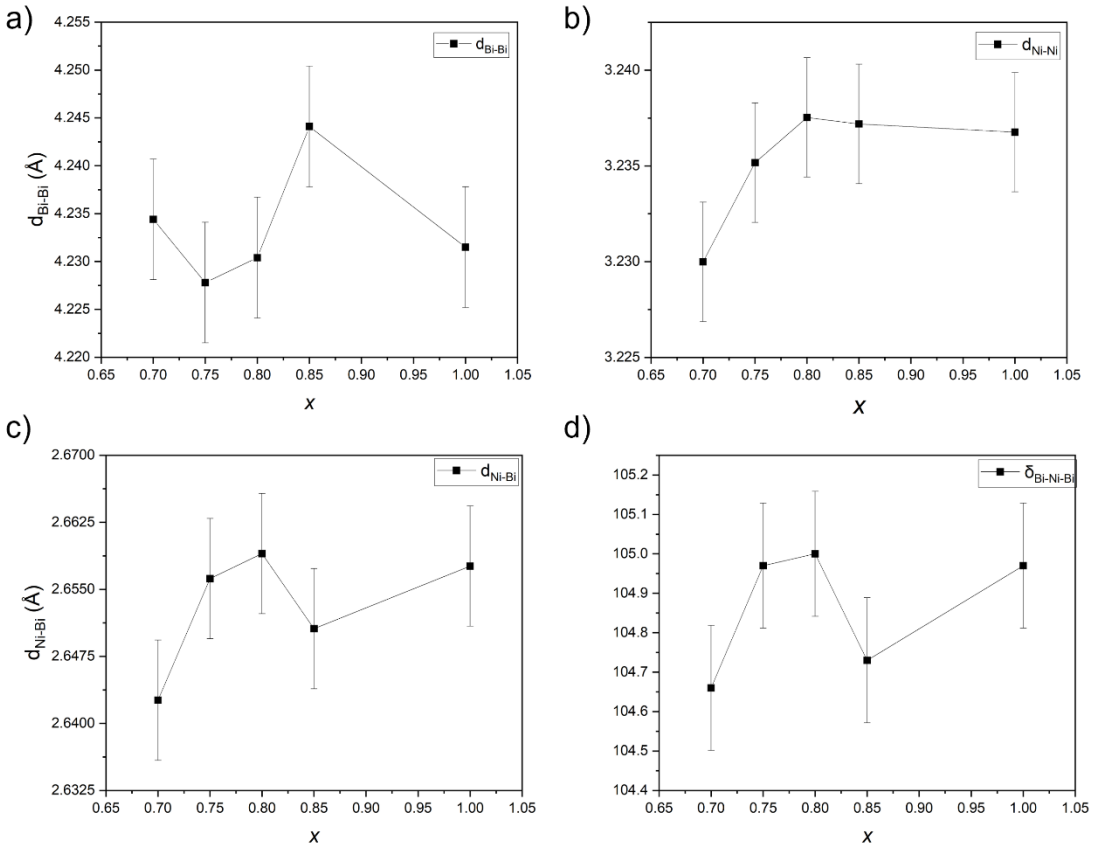


**Figure 6.18** Variation in bond lengths and tetrahedral angle across the HP-$LaNi_xBi_2$ series (*x* is nominal).

### *6.2.4 Variable Temperature SXRD*

Structural details of LP-$LaNi_{0.7}Bi_2$ were investigated as function of temperature between 100-300 K with high resolution PXRD, shown in Figure 6.19. The unit cell volume and lattice parameters *a* and *c* show a linear increase between 100 – 300 K. The Ni occupancy was refined and remained very close to the room temperature values, well within the error bar limit. There is no evidence for any structural phase transition in this range. Investigations at lower temperatures were not possible.

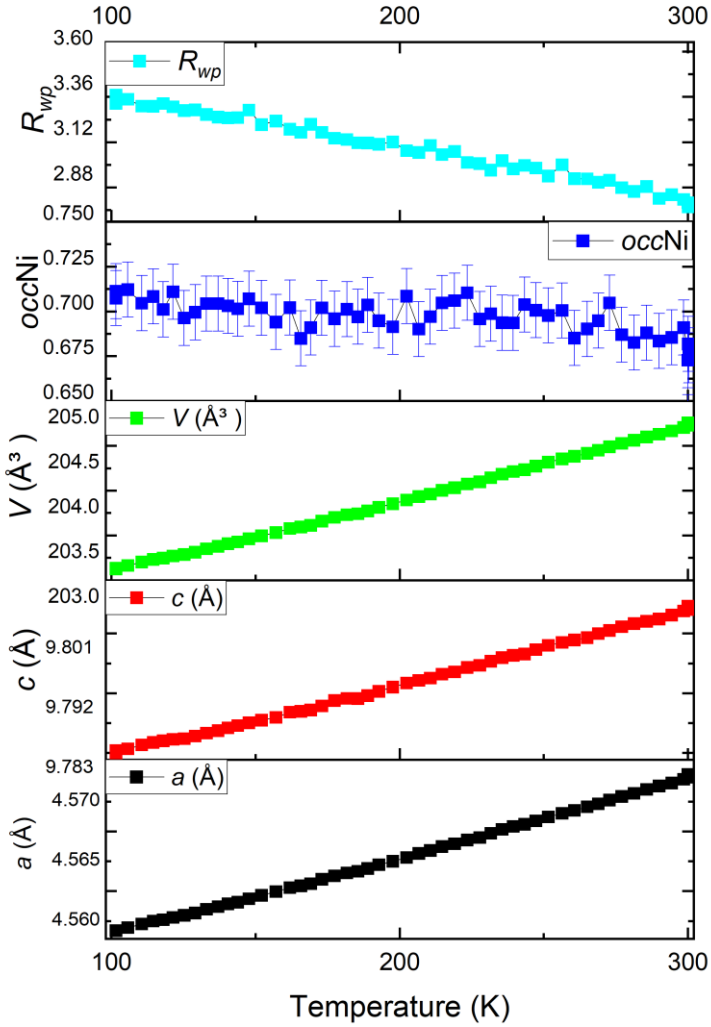


**Figure 6.19** Variable temperature (100-300 K) Synchrotron PXRD data of LP-$LaNi_{0.7}Bi_2$.

### *6.2.5 Magnetometry of $LaNi_xBi_2$*

The $T_c$ values for LP-$LaNi_xBi_2$ and the HP-$LaNi_xBi_2$ series with $0.7 \leq x \leq 1$ were measured by magnetometry on the MPMS-3 instrument at a small applied field of 20 Oe, between temperatures 1.8 – 20 K, as literature reports state the $T_c$ of $LaNi_xBi_2$ at ~4 K with a small *SVF* of < 3%.[5,8] A small applied field is important when studying $T_c$, as the critical fields $H_{c1}$ (the "lower critical field", where magnetic flux begins to penetrate the superconductor) and $H_{c2}$ (the "upper critical field", where magnetic flux fully penetrates the sample, destroying superconductivity) must not be exceeded. The lower critical field was estimated by a measurement of *M* (magnetisation) versus *H* (field) at 2 K (Figure 6.20). The data in Figure 6.20 show that a field of 20 Oe is not strong enough to penetrate

the superconductor, where $H_{c1}$ ~ 60 Oe. On the other hand, $H_{c2}$, the upper critical field, will be determined via resistivity measurements in Section 6.2.6, as no literature reports on this parameter were found in existing studies.

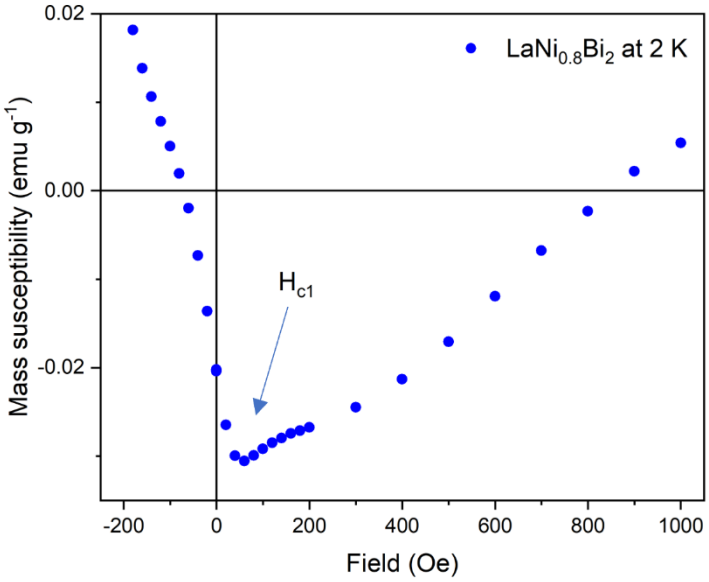


**Figure 6.20** Magnetisation isotherm at 2 K for HP-$LaNi_{0.7}Bi_2$. Measuring field used in scans of *M vs T* throughout this work was 20 Oe, which is below field $H_{c1}$ for this sample, which is identified at 60 Oe.

LP-$LaNi_xBi_2$ with x = 0.7, 0.75, and 0.8 were studied via magnetometry measurements. No signature of bulk superconductivity was found for any of these samples, as can be shown in their ZFC-FC magnetic susceptibility curves in Figure 6.21. The presence of a ferromagnetic impurity (likely Ni) in these samples can be observed by the divergence of the two curves.

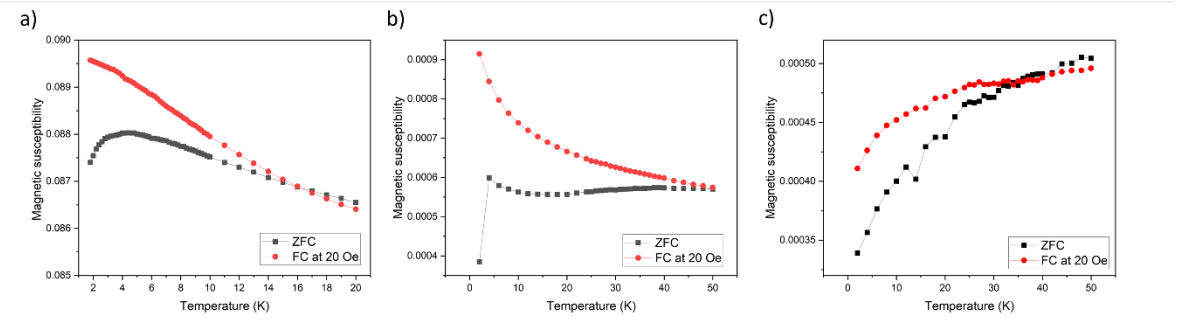


**Figure 6.21** ZFC-FC magnetic susceptibility curve measured at 20 Oe on $LaNi_xBi_2$ synthesised at ambient pressure with a) x = 0.7, b) x = 0.75, c) 0.8 (nominal compositions).

The amount of Ni ferromagnetic impurity can be estimated from the plot of *M v H* (Figure 6.22). The non-linear plot initially increases between 0 – 50,000 Oe, before saturating at 0.025 emu at 10,000 Oe. The estimated Ni impurity is calculated at 1.4%, which was not observed in PXRD.

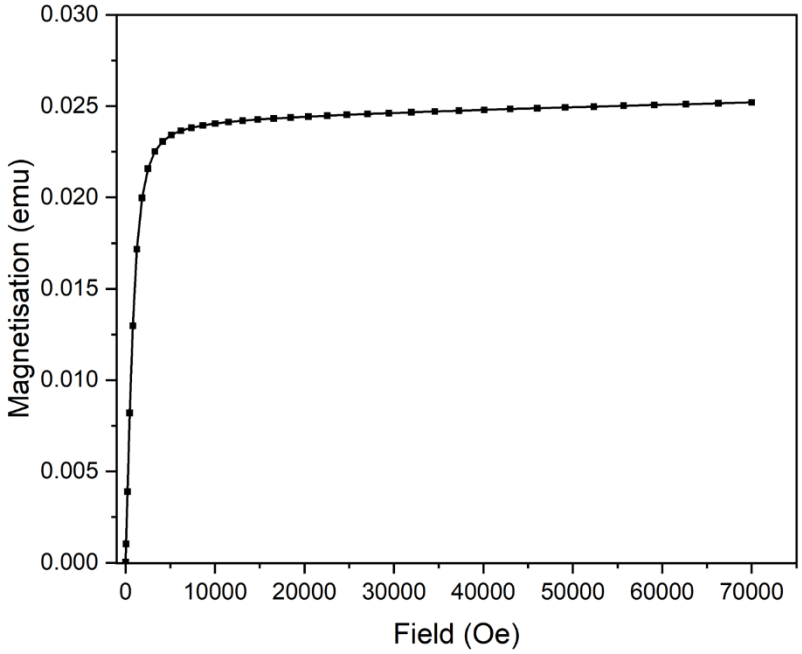


**Figure 6.22** *M vs H* plot of LP-$LaNi_{0.7}Bi_2$.

As the LP-$LaNi_xBi_2$ samples lacked any signature of bulk superconductivity, HP-$LaNi_xBi_2$ series was studied via magnetometry to determine whether the increased purity and crystallinity of the HP-$LaNi_xBi_2$ phases will have an effect on its properties. The synthesised non-stoichiometric samples were measured using magnetometry to probe any differences in their $T_c$ upon varying amount of Ni vacancies. It is worth noting that the doped samples have varying impurity content, with HP-$LaNi_{0.8}Bi_2$ sample being 99% phase pure from PXRD. The HP-$LaNi_xBi_2$ series shows a variation in $T_c$ and *SVF*. Figures 6.23-27 show the a) ZFC-FC magnetic susceptibility curves and b) *M vs H* plots of HP-$LaNi_xBi_2$ series with $0.7 \leq x \leq 1$.

In the ZFC-FC curve of HP-$LaNi_{0.7}Bi_2$ (Figure 6.23a) there are seemingly two superconducting transitions with $T_c$s of 7.3 K and 3.9 K. The *SVF* of these transitions is < 10%. From the *M vs H* curve in Figure 6.23b, the estimated Ni content was calculated at 0.09%.

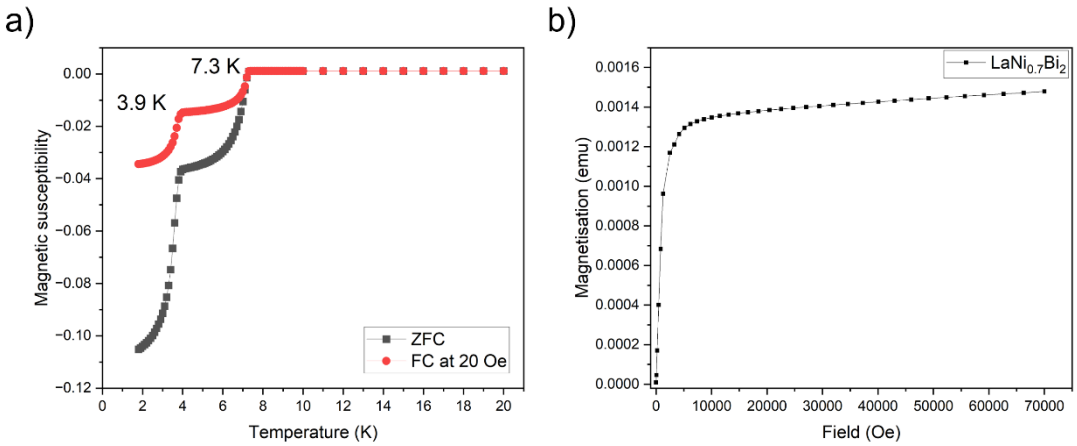


**Figure 6.23** a) ZFC-FC magnetic susceptibility curve measured at 20 Oe on HP-$LaNi_{0.7}Bi_2$, b) *M vs H* plot of $LaNi_{0.7}Bi_2$.

In the ZFC-FC curve of HP-$LaNi_{0.75}Bi_2$ (Figure 6.24a) the superconducting transition with $T_c$ of 4 K has an *SVF* of 9%. The two curves diverge only very little, and the *M vs H* curve in Figure 6.24b does not saturate even at high fields. HP-$LaNi_{0.75}Bi_2$ has higher susceptibility than HP-$LaNi_{0.7}Bi_2$.

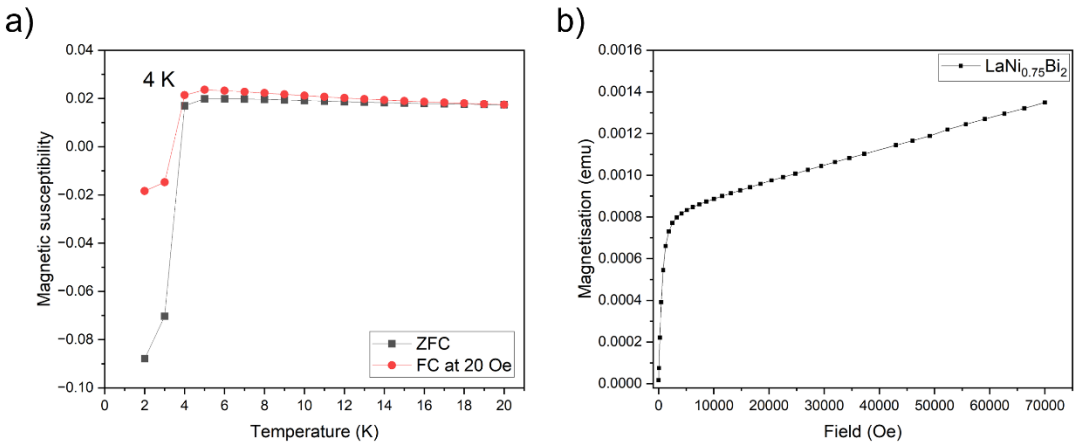


**Figure 6.24** a) ZFC-FC magnetic susceptibility curve measured at 20 Oe on HP-$LaNi_{0.75}Bi_2$, b) *M vs H* plot of $LaNi_{0.75}Bi_2$.

In the ZFC-FC curve of HP-$LaNi_{0.8}Bi_2$ (Figure 6.25a) the superconducting transition with $T_c$ of 4 K is again shown, but the *SVF* is here ~ 1%. From the *M vs H* curve in Figure 6.25b, the estimated Ni content was calculated at 0.7%.

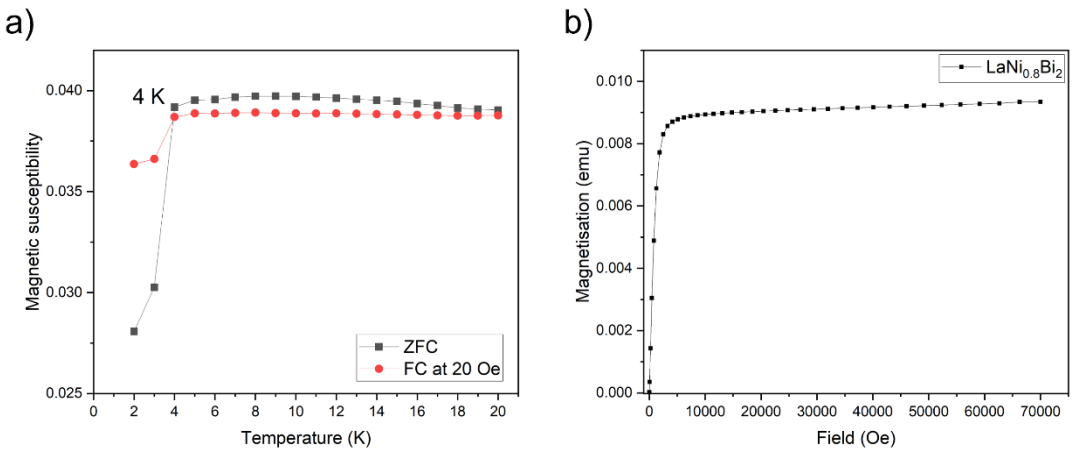


**Figure 6.25** a) ZFC-FC magnetic susceptibility curve measured at 20 Oe on HP-$LaNi_{0.8}Bi_2$, b) *M vs H* plot of $LaNi_{0.8}Bi_2$.

In the ZFC-FC curve of HP-$LaNi_{0.85}Bi_2$ (Figure 6.26a) there are seemingly two superconducting transitions with $T_c$s of 8.4 K and 4 K. The *SVF* of these transitions is difficult to determine, as the curves fail to reach negative magnetic susceptibility values, which could be due to the presence of the impurity. From the *M vs H* curve in Figure 6.26b, the estimated Ni content was found at 3.5%.

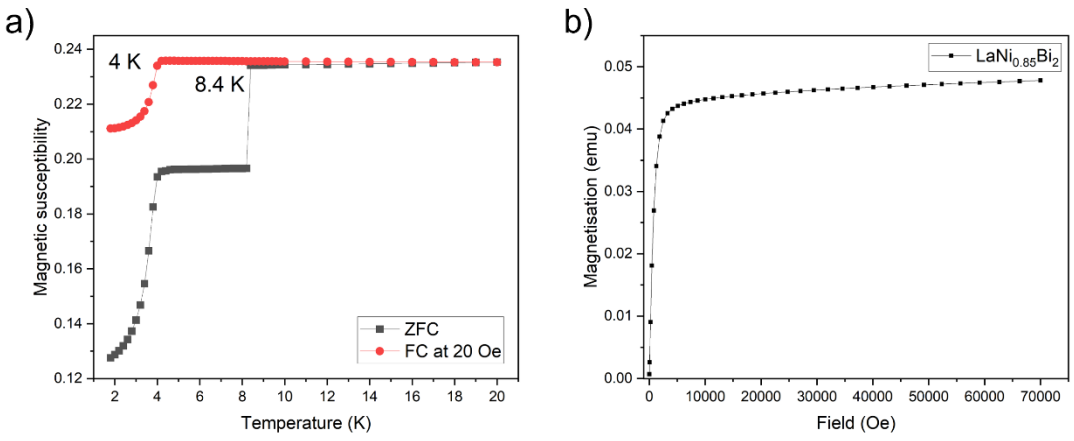


**Figure 6.26** a) ZFC-FC magnetic susceptibility curve measured at 20 Oe on HP-$LaNi_{0.85}Bi_2$, b) *M vs H* plot of $LaNi_{0.85}Bi_2$.

In the ZFC-FC curve of HP-$LaNiBi_2$ (Figure 6.27a) the superconducting transition with $T_c$ of 4 K is present, but the *SVF* is again difficult to determine due to the positive magnetic susceptibility values. From the *M vs H* plot in Figure 6.27b, the estimated Ni content was calculated at 0.6%.

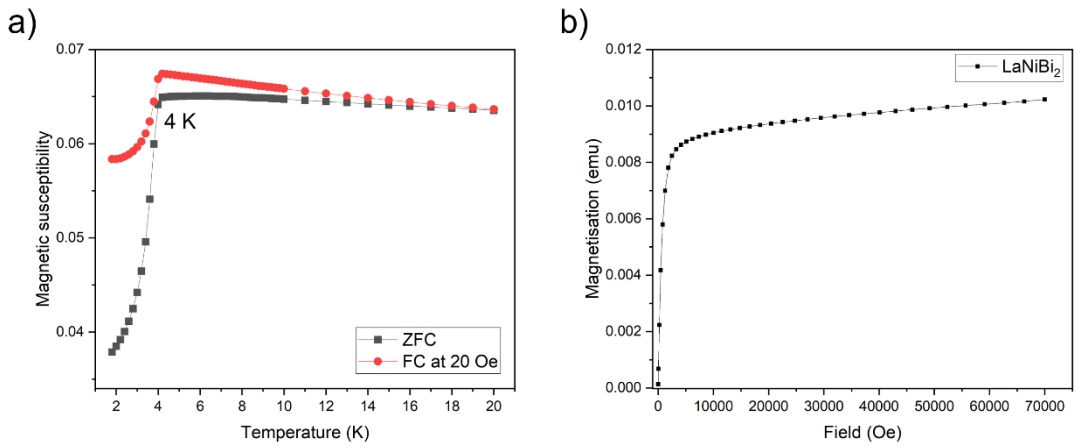


**Figure 6.27** a) ZFC-FC magnetic susceptibility curve measured at 20 Oe on HP-$LaNiBi_2$, b) *M vs H* plot of $LaNiBi_2$.

The superconductivity in HP-$LaNi_xBi_2$ series with $0.7 \leq x \leq 1$ is sample dependant and magnetometry results are not reproducible between samples. A superconducting transition with $T_c$ of ~4 K is present in all samples with varying *SVF*s, but two samples, namely, HP-$LaNi_{0.7}Bi_2$ and $LaNi_{0.85}Bi_2$ show a second transition with $T_c$ s of 7.3 and 8.4 K, respectively. This second transition likely arises from $LaBi_3$ which has a $T_c$ of 7.3 K,[12] but was not detected in PXRD. The origin of the 8.4 K transition is unclear, however, as the drop in magnetic susceptibility occurs over just one datapoint, it is possible that it was an instrumental artefact and it is not a real transition, especially since it is not visible in the FC dataset. Even HP-$LaNi_{0.8}Bi_2$ – synthesised to 99% purity from PXRD – does not show a signature of bulk superconductivity (Figure 6.25); though its magnetic susceptibility shows a sharp drop at 4 K, the SVF is ~1%, which agrees well with the amount of superconducting NiBi observed in PXRD ($T_c$ of NiBi is 4 K).[9] These results agree well with Lin *et al.*'s study which concluded that superconductivity in *R*$Ni_xBi_2$ arises from superconducting impurities. As it is agreed upon that $CeNi_xBi_2$ is a bulk superconductor (with 96% *SVF*, as opposed to small *SVF*s of the rest of the *R*$Ni_xBi_2$ series), the question arises what sets it apart from the rest of the *R*$Ni_xBi_2$ series. The reason

for this could be that Ce is present in a 4+ state – as opposed to the 3+ valence states of the rest of the series. Figure 6.28 shows the variation of the unit cell volume of $R\mathrm{Ni}_x\mathrm{Bi}_2$ phases with $R^{3+}$ ion. It can be noted that $Ce^{3+}$ is very slightly below the line, and this could indicate partial oxidation to $Ce^{4+}$, as it might be providing more electrons than 3. We have therefore compared this relationship with the variation of unit cell volume of $R_2O_3$ phases with $R^{3+}$ ion size, which shows a more consistent trend (Figure 6.29).

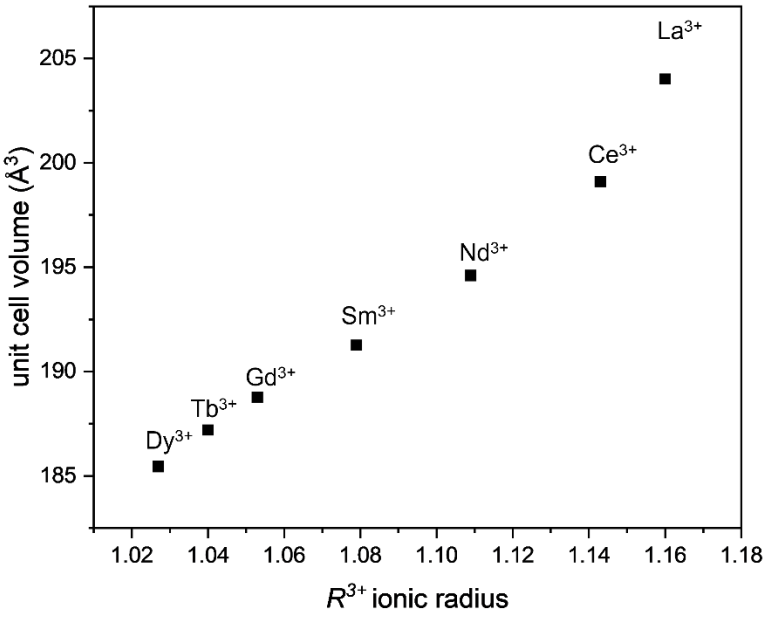


**Figure 6.28** Variation of unit cell volume vs ionic radius of $R^{3+}$ for 8 coordination number (CN = 8) in $R\mathrm{Ni}_x\mathrm{Bi}_2$ compounds. All values are taken from work of Lin *et al.* in Ref [7].

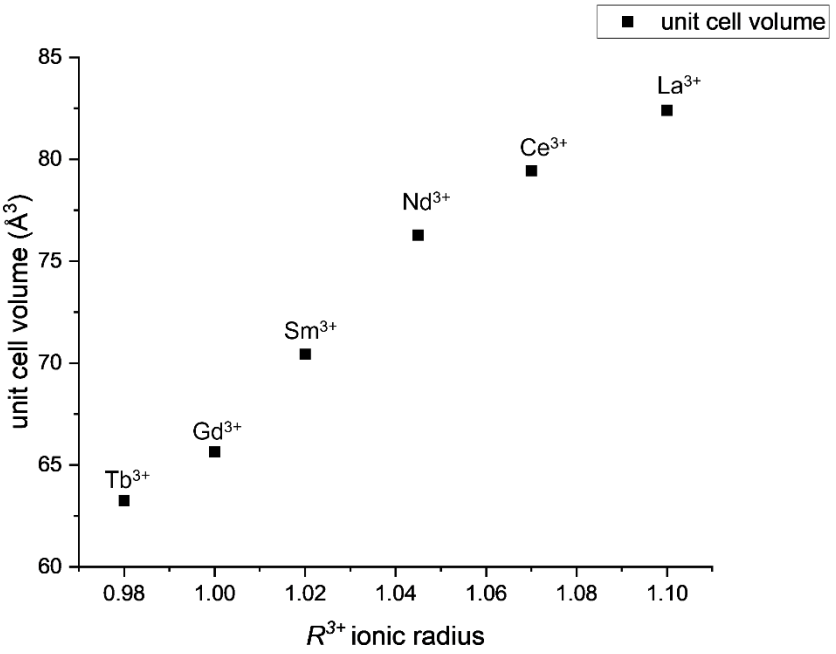


**Figure 6.29** Variation of unit cell volume vs ionic radius of $R^{3+}$ for 7 coordination number (CN = 7) in $R_2O_3$ compounds.

Mizoguchi *et al*. conclude that only $Ce^{3+}$ ($4f^1$) electrons contribute to superconductivity (if $Ce^{4+}$ $4f^0$, volume would be smaller).[5] Our impression after comparing the trends in unit cell volume in $R^{3+}Ni_xBi_2$ series with the data for $R^{3+}{}_2O_3$ phases is that the trends are not similar, and the possibility of $Ce^{4+}$ $4f^0$ present in $CeNi_xBi_2$ should not be ruled out. To draw definitive conclusions, further measurements are needed, such as XANES to probe the oxidation states of Ce in $CeNi_xBi_2$. We conclude that although superconductivity in $CeNi_xBi_2$ has bulk signature, in $LaNi_xBi_2$ superconductivity arises from Ni-Bi impurities.

### *6.2.6 Resistivity*

Resistivity ($\rho$) was measured on a sintered pellet of the best HP sample with composition $LaNi_{0.8}Bi_2$ connected to four copper wires using silver paint and mounted on a probe on a PPMS instrument which measured its resistivity between 2 – 22 K upon cooling at fields 0-5 Tesla. Resistivity at 0 T remains constant from 22 K down to 4.24 K, at which point a sharp drop in resistivity occurs to 0 Ωcm, indicative of a superconducting transition (Figure 6.30a). Upon application of external field

of 1 Tesla, the loss of resistivity occurs at lower $T_c$ of 3.73 K and the transition is complete at 0 Ωcm at 2 K (Figure 6.30b). With an external field of 2 Tesla, the $T_c$ lowers further to 3.36 K (Figure 6.30c).

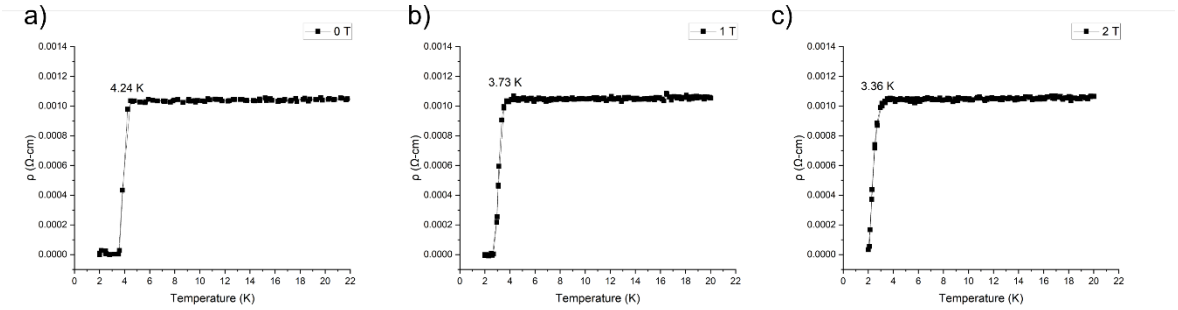


**Figure 6.30** Resistivity (ρ) as a function of temperature for HP-$LaNi_{0.8}Bi_2$ at a) 0 T, b) 1 T, c) 2 T.

Upon application of an external field of 3 T, the $T_c$ is lowered to 2.73 K and the loss of resistivity (and by extension, the superconducting behaviour of $LaNi_{0.8}Bi_2$) is beginning to fade as the transition is incomplete and does not reach 0 Ωcm at 2 K (Figure 6.31).

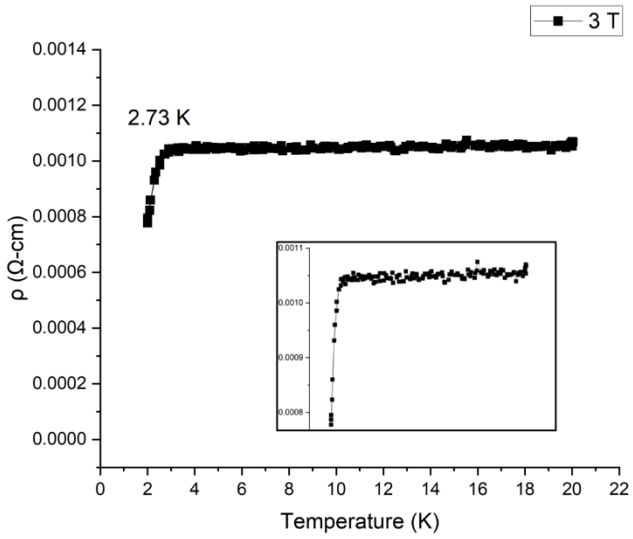


**Figure 6.31** Resistivity (ρ) as a function of temperature for HP-$LaNi_{0.8}Bi_2$ at 3 T. Inset is showing the transition at a smaller scale.

Figure 6.32 shows the resistivity as a function of temperature as an almost straight line and the superconducting transition is visible in the inset, which shows a very small drop in resistivity at 2.35 K. This transition occurs at a $10^{-5}$ Ωcm scale.

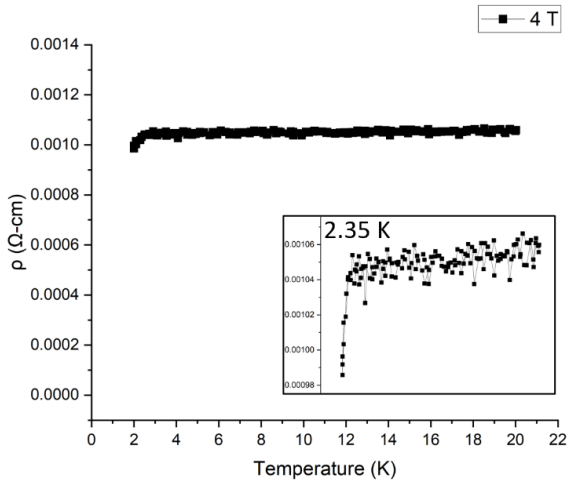


**Figure 6.32** Resistivity (ρ) as a function of temperature for HP-$LaNi_{0.8}Bi_2$ at 4 T. Inset is showing the transition at a smaller scale.

At 5 Tesla, there is no signature of superconducting behaviour in the sample of $LaNi_{0.8}Bi_2$, as resistivity remains constant as a function of temperature down to 2 K (Figure 6.33). $H_{c2}$, the upper critical field, at which magnetic flux penetrates sample and destroys superconductivity, is determined as 5 Tesla (50,000 Oe). This finding, however, does not agree well with other literature $H_{c2}$ values of $NiBi_3$, which range from 0.7 T [9] to 1.4 T [10].

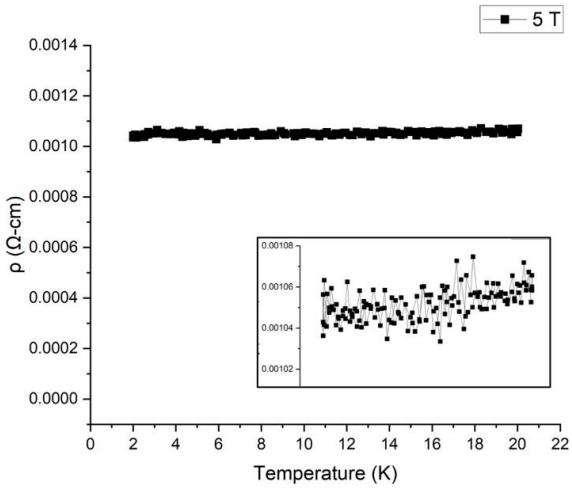


**Figure 6.33** Resistivity (ρ) as a function of temperature for HP-$LaNi_{0.8}Bi_2$ at 5 T. Inset is showing loss of resistivity at a smaller scale.

The changes in $T_c$ of HP-$LaNi_{0.8}Bi_2$ upon application of external field are summarised in Table 6.1. $T_c$ decreases gradually with applied field, which a typical behaviour of type-II BCS superconductors.

**Table 6.1** Variation of $T_c$ (K) with applied field (T) from resistivity measurements.

| **Field (T)** | **$T_c$ (K)** |
|---|---|
| 0 | 4.24 |
| 1 | 3.73 |
| 2 | 3.36 |
| 3 | 2.73 |
| 4 | 2.35 |

### *6.2.7 SEM-EDX*

Elemental analysis by SEM-EDX reveals an even distribution of La, Ni, and Bi across a portion of the polycrystalline HP-$LaNi_{0.8}Bi_2$ (Figure 6.34).

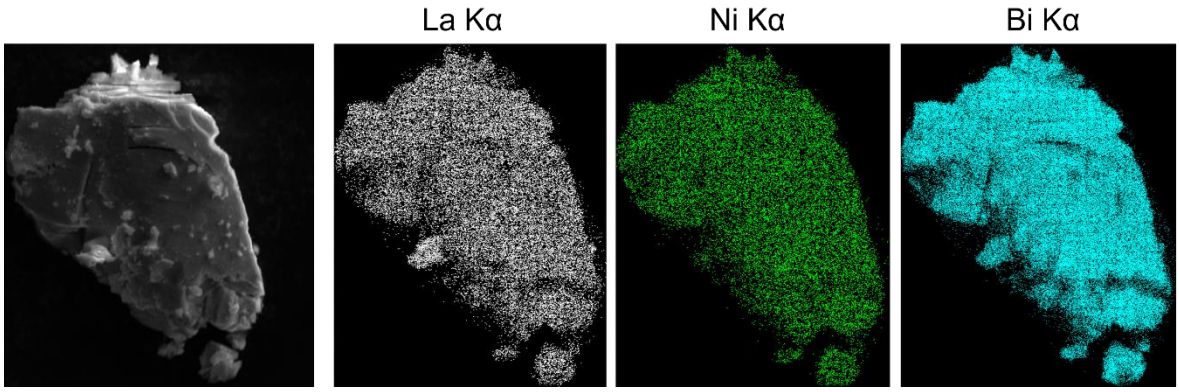


**Figure 6.34** An image of a polycrystalline sample of HP-$LaNi_{0.8}Bi_2$ sample under SEM, showing an even distribution of the constituent elements.

Its composition from EDX is $La_{1.00(1)}Ni_{1.03(1)}Bi_{1.78(8)}$, which shows Ni site fully occupied, contrary to previous literature reports of Ni deficiency being necessary for electronic structure stabilisation.[5,6] It is worth noting that the uncertainties here are reasonably large. No other compositions were found from SEM. However, as SEM-EDX is a surface technique, there is quite a high uncertainty on the

real composition of the bulk. Two other HP samples were studies in SEM-EDX; $LaNi_{0.7}Bi_2$ is shown as $La_{1.00(1)}Ni_{0.76(6)}Bi_{1.9(1)}$, and $LaNi_{0.75}Bi_2$ as $La_{1.00(4)}Ni_{0.90(9)}Bi_{1.9(1)}$, both Ni- and Bi-deficient (Table 6.2). Bi-deficiency was found in some single crystalline samples of $RNi_xBi_{2+y}$ Lin *et al.*'s study, namely for *R* = Pr, Gd, Tb, Dy, but not La.[8]

**Table 6.2** Nominal and observed compositions from SEM-EDX on HP $LaNi_xBi_2$.

| Nominal composition | Composition from SEM-EDX |
|---|---|
| $LaNi_{0.7}Bi_2$ | $La_{1.00(1)}Ni_{0.76(6)}Bi_{1.9(1)}$ |
| $LaNi_{0.75}Bi_2$ | $La_{1.00(4)}Ni_{0.90(9)}Bi_{1.9(1)}$ |
| $LaNi_{0.8}Bi_2$ | $La_{1.00(1)}Ni_{1.03(1)}Bi_{1.78(8)}$ |

## 6.3 Conclusion

Motivated by previous studies on superconductivity in $CeNi_xBi_2$,[2,5,7] we synthesised polycrystalline samples of $LaNi_xBi_2$ via ceramic ($0.65 \leq x \leq 0.8$) and high-pressure routes ($0.7 \leq x \leq 1$). As low-pressure ceramic synthesis yielded $LaNi_xBi_2$ with low purity, detailed magnetometry and resistivity analyses were performed on high-pressure samples of $LaNi_xBi_2$. Previous reports of bulk superconductivity in $LaNi_xBi_2$ showed its $T_c$ as 4 K and SVF as < 3%.[5,8] The $T_c$ coincides with that of Bi, NiBi, and $NiBi_3$, and the latter two form as secondary phases in all synthesised samples in this study. Lin *et al.* suggested that superconductivity in $RNi_xBi_2$ is extrinsic and arises from secondary superconducting phases as *SVF* for these phases is between 3-20%.[8] Our magnetometry studies reveal that superconductivity is sample-dependant with varying SVF (<10%). $H_{c1}$ was determined as 60 Oe for $LaNi_{0.7}Bi_2$, which coincides with that of $NiBi_3$.[9] Upper critical field, $H_{c2}$, was determined as 5 Tesla (50,000 Oe), which however does not agree with that of $NiBi_3$.[9,10] Our investigations conclude that superconductivity in $LaNi_xBi_2$ is extrinsic and arises from secondary Ni-Bi phases, with $T_c$ of 4 K.

## References

[1] Mizoguchi, H., Kamiya, T., & Hosono, H. (2012). Superconducting compounds with metallic square net. *Solid State Communications*, *152*(8), 666–670. https://doi.org/10.1016/j.ssc.2011.12.016

[2] Katayama, N., Kudo, K., Onari, S., Mizukami, T., Sugawara, K., Sugiyama, Y., Kitahama, Y., Iba, K., Fujimura, K., Nishimoto, N., Nohara, M., & Sawa, H. (2013). Superconductivity in Ca1-xLaxFeAs2: A novel 112-type iron pnictide with arsenic zigzag bonds. *Journal of the Physical Society of Japan*, *82*(12), 123702. https://doi.org/10.7566/JPSJ.82.123702

[3] Ota, H., Kudo, K., Kimura, T., Kitahama, Y., Mizukami, T., Ioka, S., & Nohara, M. (2017). Site-selective antimony doping in arsenic zigzag chains of 112-type Ca1-xLaxFeAs2. *Journal of the Physical Society of Japan*, *86*(2), 025002. https://doi.org/10.7566/JPSJ.86.025002

[4] Klemenz, S., Lei, S., & Schoop, L. M. (2019). Topological Semimetals in Square-Net Materials. *Annual Review of Materials Research*, *49*, 185-206 https://doi.org/10.1146/annurev-matsci-070218-010114.

[5] Mizoguchi, H., Matsuishi, S., Hirano, M., Tachibana, M., Takayama-Muromachi, E., Kawaji, H., & Hosono, H. (2011). Coexistence of light and heavy carriers associated with superconductivity and antiferromagnetism in $CeNi_{0.8}Bi_2$ with a Bi square net. *Physical Review Letters*, *106*(5), 057002. https://doi.org/10.1103/PhysRevLett.106.057002.

[6] Jung, M. H., Lacerda, A. H., & Takabatake, T. (2002). Magnetic and transport properties of the antiferromagnetic Kondo-lattice compound $CeNiBi_2$. *Physical Review B - Condensed Matter and Materials Physics*, *65*(13), 1324051–1324053. https://doi.org/10.1103/PhysRevB.65.132405

[7] Rosa, P. F. S., Jesus, C. B. R., Adriano, C., Fisk, Z., & Pagliuso, P. G. (2014). The role of Ni vacancies on the physical properties of $CeNi_xBi_{2-y}$ single crystals. *Journal of Physics: Conference Series*, *592*(1), 012063. https://doi.org/10.1088/1742-6596/592/1/012063.

[8] Lin, X., Straszheim, W. E., Bud'Ko, S. L., & Canfield, P. C. (2013). Anisotropic magnetization and resistivity of single crystalline RNi 1-xBi2±y (R = La-Nd, Sm, Gd-Dy). *Journal of Alloys and Compounds*, *554*, 304–311. https://doi.org/10.1016/j.jallcom.2012.11.138

[9] Shang, T., Meng, J., Zhu, X. Y., Zhang, H., Yu, B. C., Zhen, Z. X., Wang, Y. H., Xu, Y., Zhan, Q. F., Gawryluk, D. J., & Shiroka, T. (2023). Fully gapped superconductivity with preserved time-reversal symmetry in NiBi3 single crystals. *Physical Review B*, *107*(17), 174513. https://doi.org/10.1103/PhysRevB.107.174513

[10] Siva, V., Senapati, K., Satpati, B., Prusty, S., Avasthi, D. K., Kanjilal, D., & Sahoo, P. K. (2015). Spontaneous formation of superconducting NiBi3 phase in Ni-Bi bilayer films. *Journal of Applied Physics*, *117*(8), 083902. https://doi.org/10.1063/1.4913267

[11] Yakita, H., Ogino, H., Sala, A., Okada, T., Yamamoto, A., Kishio, K., Iyo, A., Eisaki, H., & Shimoyama, J. (2015). Dependences on RE of superconducting properties of transition metal co-doped (Ca, RE)$FeAs_2$ with RE = La-Gd. *Physica C: Superconductivity and Its Applications*, *518*, 14–17. https://doi.org/10.1016/j.physc.2015.02.041.

[12] Ray, S. J., & Alff, L. (2017). Superconductivity and Dirac fermions in 112-phase pnictides. *Physica Status Solidi (B) Basic Research*, *254*(1), 1600163. https://doi.org/10.1002/pssb.201600163.

[13] Kinjo, T., Kajino, S., Nishio, T., Kawashima, K., Yanagi, Y., Hase, I., Yanagisawa, T., Ishida, S., Kito, H., Takeshita, N., Oka, K., Eisaki, H., Yoshida, Y., & Iyo, A. (2016). Superconductivity in LaBi3 with AuCu3-type structure. *Superconductor Science and Technology*, *29*(3), 0953-2048. https://doi.org/10.1088/0953-2048/29/3/03LT02

# Chapter 7. Summary

This thesis explored the synthesis and magnetic and electronic characterisation of new layered transition metal chalcogenides and pnictides, namely the magnetically-ordered solid solutions $A$Co$_{2-x}$Ni$_x$$Ch_2$ ($A$ = K, Rb, Cs; $Ch$ = S, Se), high-$T_c$ superconductors CaKFe$_4$As$_4$ and SrRbFe$_4$As$_4$, and low-$T_c$ superconductor LaNi$_x$Bi$_2$. These materials have a number of similarities; firstly, their crystal structures are quasi-2-dimensional, leading to a similarly 2-dimensional electronic structure, which offers a rich playground for exotic magnetic phenomena. Secondly, the magnetic properties exhibited by the chalcogenide- and pnictide-based materials can be sensitively tuned with composition, which is a common theme across the four thesis chapters.

Chapter 3 discussed the effect of Ni substitution in $A$Co$_2$$Ch_2$ ($A$ = K, Rb, Cs; $Ch$ = S, Se) and the changes in magnetic properties of the formed solid solutions between $A$Ni$_2$$Ch_2$ and $A$Co$_2$$Ch_2$. The end members crystallise in the BaZn$_2$P$_2$ variant of the ThCr$_2$Si$_2$-type structure (*i.e.* no chalcogen-chalcogen bonding) but differ in terms of their magnetic properties. Upon substitution of Co in ferromagnetic $A$Co$_2$$Ch_2$ by Ni, an electron is added to the 3d bands per Ni ion, which drastically alters the magnetic properties across the whole series. Four solid solutions were synthesised and examined using magnetometry and neutron powder diffraction, namely KCo$_{2-x}$Ni$_x$Se$_2$, KCo$_{2-x}$Ni$_x$S$_2$, RbCo$_{2-x}$Ni$_x$Se$_2$ and CsCo$_{2-x}$Ni$_x$Se$_2$. The $A$Ni$_2$$Ch_2$ show paramagnetism down to low temperatures and superconductivity at temperatures below 0.4 – 2.7 K depending on composition. The $A$Co$_2$$Ch_2$ phases all show ferromagnetism with the sole exception of CsCo$_2$Se$_2$, which behaves antiferromagnetically below 66 K, suggesting that interlayer separation favours antiferromagnetic arrangement of magnetic moments. Magnetometry revealed that upon substitution with small amounts of Ni into ferromagnetic $A$Co$_2$$Ch_2$, antiferromagnetic coupling becomes prevalent, while the strength of the interactions was found to peak at x = 1 in every $A$Co$_{2-x}$Ni$_x$$Ch_2$ synthesised solid solution, demonstrated by $T_N$ peaking at this composition. At high substitution levels (1.5 < x < 2), antiferromagnetic coupling disappears and paramagnetism is evident from magnetometry, however no superconducting signal was detected for any $A$Ni$_2$$Ch_2$ down to 2 K. These phases all display non-Curie-Weiss behaviour.

Neutron powder diffraction was used to probe the three antiferromagnetic members of the $KCo_{2-x}Ni_xSe_2$ and $KCo_{2-x}Ni_xS_2$ solid solutions with x = 0.5, 1, and 1.5. Bragg peaks, which are systematically absent from the nuclear structure and are indicative of long-range magnetic ordering, were observed in the low temperature neutron diffraction patterns of each solid solution for x = 0.5 and 1, while in x = 1.5 no Bragg peaks were evident down to 3.5 K, although an antiferromagnetic transition, albeit a broad one, was evident from magnetometry. The Bragg magnetic peaks were indexed on a $\sqrt{2}a \times \sqrt{2}a \times c$ expansion of the nuclear unit cell and the refined magnetic model corresponds to ferromagnetic coupling between Co/Ni ions within the $(Co/Ni)_2Se_2$ sheets and an antiferromagnetic interaction between the adjacent $(Co/Ni)_2Se_2$ sheets along the stacking axis, also known as A-type antiferromagnetism. The magnetic anisotropy is consistent with the changes of lattice parameters observed at low temperatures; lattice parameter *a* contracts faster below $T_N$, and *c* remains approximately flat below $T_N$ instead of undergoing continued thermal contraction. The mechanisms responsible for the different types of magnetic coupling are direct ferromagnetic interactions between transition metal ions within the plane, while the RKKY mechanism is responsible for the between-the-plane antiferromagnetic coupling, as the distance between the planes is too large (~5 Å) for any kind of direct interaction. This refined magnetic moment per transition metal ion is 1.18 $\mu_B$ in $KCoNiSe_2$ and 1.22 $\mu_B$ in $KCoNiS_2$; this finding can be understood in light of the resistivity measurements in these phases which reveal metallic behaviour, hence the rest of the electrons behave as conduction electrons facilitating the RKKY mechanism. The magnetic-plus-nuclear structure can be described with the orthorhombic space group *Cmcm*, as opposed to the tetragonal symmetry (*I*4/*mmm*) of the nuclear-only structure of the $KCo_{2-x}Ni_xCh_2$ series (*Ch* = S, Se). The PND results show that there is no long-range chemical order of the Ni and Co species within the chalcogenide layers, and the chemical disorder within these layers does not suppress long-range magnetic order.[1]

In addition to the two $KCo_{2-x}Ni_xCh_2$ series, the x = 1 member of the $CsCo_{2-x}Ni_xSe_2$ series was also studied by neutron powder diffraction, similarly revealing A-type antiferromagnetism, while the refined magnetic moment was even lower than in the K-analogues: 0.80(1) $\mu_B$. Here, an interesting

finding was observed from Synchrotron PXRD which revealed a subtle structural distortion in $CsCo_{2-x}Ni_xSe_2$ series between $1.1 \leq x \leq 1.4$; systematic peak splitting at room temperature revealed symmetry lowering from tetragonal to orthorhombic with the *Fmmm* space group and a larger cell. Furthermore, there appears to be a two-phase-region forming at high temperatures (750-900 K) from Synchrotron PXRD data. As this Ni-rich region of compositions is where antiferromagnetic order was observed from magnetometry but no long-range order was evident from neutron powder diffraction in the K-analogues, it will be important to study these orthorhombic $CsCo_{2-x}Ni_xSe_2$ members using neutron diffraction as future work. The origin of the distortion could lie in an electronic instability of these compositions or perhaps in an ordering of Cs and the vacancies along the stacking axis, as these phases are all Cs-deficient from SEM-EDX and PND. Further experiments beyond the scope of this thesis are required to understand the behaviour of $CsCo_{2-x}Ni_xSe_2$ series.

The origin of the drastic changes in magnetism in $ACo_{2-x}Ni_xCh_2$ (*A* = K, Rb, Cs; *Ch* = S, Se) phases is likely due to the addition of an extra electron per Ni to the 3d band of the system. First-principles calculations performed in a previous study of $KCo_2Se_2$ and $KNi_2Se_2$ phases reveal complex electronic structures for both, with metallic character confirmed by a gapless $E_F$ which is crossed by flat and highly dispersive bands.

Chapter 4 discusses the effect of non-stoichiometry on $CaKFe_4As_4$, a member of the 1144 family of iron-based superconductors. These have the optimal electron count for high-temperature superconductivity and the perfect ordering of the electropositive metals means that there is no chemical disorder on any sublattice. From a crystallographic perspective, the 1144 is a superstructure of the 122 structure type due to ordering of the *Ae : A* ions along the stacking axis. Disorder was introduced by chemical substitution on Ae/A sites by varying the *Ae : A* ratios between $0 \leq x \leq 0.25$ in $Ca_{1+x}K_{1-x}Fe_4As_4$, and doping with phosphorus on arsenic site between $0 \leq x \leq 0.8$ in $CaKFe_4As_{4-x}P_x$. The attempted non-stoichiometry resulted in a non-linear behaviour of lattice parameters in both cases, which suggests that instead of incorporation of excess Ca into $CaKFe_4As_4$, Ca may be intergrown at a very small scale into the 1144 as $CaFe_2As_2$. The small compositional changes have subtle effects on the superconducting properties of the stoichiometric $CaKFe_4As_4$; the

$T_c$ and the *SVF* of substituted samples slightly differ from the stoichiometric $CaKFe_4As_4$ with observed $T_c$ varying between 30 – 34 K in $Ca_{1+x}K_{1-x}Fe_4As_4$, and 31 – 34 K in $CaKFe_4As_{4-x}P_x$. This finding of slightly supressed $T_c$ could be due to intergrowths of $CaFe_2As_2$ coherently grown in the $CaKFe_4As_4$ matrix, however this reasoning would need to be confirmed by an accurate microscopy technique such as STEM, where individual sublattices can be distinguished.

Chapter 5 explored the effect of applied pressure on a related 1144 iron-based superconductor: $SrRbFe_4As_4$. Both temperature- and pressure-induced structural phase transitions are common for a related type of compounds – the previously discussed 122 phases with the $ThCr_2Si_2$-type structure – but they were also observed in $CaAFe_4As_4$ (*A* = K, Rb); here, the structure undergoes two collapses – a half-collapse and full-collapse - marked by a sudden decrease in *a* and *c* lattice parameters. This is concomitant with suppression of superconductivity; firstly, a notable decrease in $T_c$ is observed and upon full-collapse superconductivity disappears completely. The phase transitions are driven by formation of *As-As* bonds along the stacking axis. During half-collapse of the unit cell (first structural phase transition upon application of pressure), the *As-As* bonds form across the smaller Ca layer, while the full-collapse is driven by formation of *As-As* bonds form across the larger *A* layer (*A* = K, Rb). In the case of $SrRbFe_4As_4$, both the alkali metal and alkaline earth metal are larger than the constituent elements of previously reported collapsed $CaKFe_4As_4$ and $CaRbFe_4As_4$, therefore higher pressures (up to 26 GPa) were applied during a high-pressure and room-temperature PXRD experiment at the BL10XU beamline of the SPring-8 Synchrotron in Japan. The collected PXRD patterns between 0-16 GPa were indexed according to the parent *P*4/*mmm* space group, and no sudden decrease in lattice parameters could be observed in this pressure region. However, above 16 GPa, the data analysis became increasingly difficult due to the pressure medium used in the DAC – the presence of daphne oil as pressure medium rendered the PXRD peaks too broad to assign any peak shape function, and neither Rietveld nor Pawley refinement could be used to definitively resolve the diffraction patterns above 16 GPa. For the data below 16 GPa, the variation of unit cell parameters (volume and lattice parameter *c*) with pressure were fitted to a third-order Birch−Murnaghan equation of state. However, lattice parameter *a* deviated from this behaviour and a third-order Birch-

Murnaghan equation of state fitting resulted in anomalous $K_0$ and $K_{0'}$ values, and a fourth-order Birch-Murnaghan equation of state was found to provide a better fit. This could be indicative of a structural reorganisation in the *ab* plane, however the data obtained from the high-pressure PXRD experiment were not of optimal quality to determine this with certainty.

Chapter 6 discusses the origin of low-$T_c$ superconductivity in $LaNi_xBi_2$, a 112 intermetallic phase with the $HfCuSi_2$-type structure. Here, the structure of $LaNi_xBi_2$ is characterised by a metallic square net of $Bi^{1-}$ ions, alternately stacked with tetrahedral layer of $Ni_xBi^{3-}$ and 9-coordinated La. In the Ce-analogue of this phase, the superconductivity is believed to originate from Ni vacancies, as the parent stoichiometric $CeNiBi_2$ is not a superconductor. However, there is a stark difference between the superconducting properties of $CeNi_xBi_2$ and the La-analogue, as the superconducting volume fraction for the former is 96% and for the latter it is reported as <1%. An intriguing similarity across the superconducting $RNi_xBi_2$ ($R$ = La - Dy) is that all phases have a $T_c$ of ~ 4 K, which when combined with the low *SVF* of $LaNi_xBi_2$ suggests that the superconducting features of this phase do not originate in the bulk, but possibly from secondary phases, such as NiBi, $NiBi_3$, and Bi, all of which share similar $T_c$s. As none of the previously studied $LaNi_xBi_2$ phases were synthesised to high purity, our investigations used high-pressure synthesis to obtain 99% pure product. However, even at high purity levels, the *SVF* is found to be <10%. Furthermore, magnetometry measurements revealed the lower critical value, $H_{c1}$, to be coincidental with that of $NiBi_3$. The upper critical field, $H_{c2}$, was determined from resistivity measurements at 5 T, and $T_c$ was found to decrease steadily with increasing field, revealing type-II superconductivity. Our investigations conclude that superconductivity in $LaNi_xBi_2$ is extrinsic and arises from secondary Ni-Bi phases, with $T_c$ of 4 K.

This thesis has shown that sensitive tuning of structure and composition can result in drastic changes in magnetic and electronic properties in layered chalcogenides and pnictides. Correlation of structure-composition-property relationships is detrimental to understanding the chemistry of these materials. The work presented here outlines an avenue for future research, especially the origin of subtle distortions in the $CsCo_{2-x}Ni_xSe_2$ series. Overall, this thesis has explored the effect of chemical substitution and pressure on the structures and properties of superconducting and magnetic materials.

## References

[1] Taskesen, L., Smyth, R.D., Crentsil, L.E., Murrell, J.I., Suard, E., Manuel, P. and Clarke, S.J. (2025). Competing Magnetism in Layered Mixed Transition Metal Chalcogenides $KCo_{2-x}Ni_xSe_2$, $KCo_{2-x}Ni_xS_2$, and $CsCo_{2-x}Ni_xSe_2$. *Chemistry of Materials*, 37(14), pp.5300–5311. doi:https://doi.org/10.1021/acs.chemmater.5c00996.

# Appendices

## Appendix A: Crystal and magnetic structure details for $ACo_{2-x}Ni_xCh_2$ phases ($A$ = K, Rb, Cs; $Ch$ = S, Se)

### A.1 Structural details of $KCo_{2-x}Ni_xSe_2$

**Table A.1.1** Structural parameters for $KNiCoSe_2$ from Rietveld refinement against I11 RT data (Diamond Light Source) and D2B RT data (ILL).

| Diffractometer | I11 | D2B |
|---|---|---|
| Radiation | X-ray | Neutron |
| Wavelength (Å) | 0.824619 | 1.594 |
| Temperature (K) | 298 | 300 |
| $R_{wp}$ (%) | 1.778 | 3.03914 |
| $\chi^2$ | 4.39 | 1.46(3) |
| Space group | *I*4/*mmm* | *I*4/*mmm* |
| *a* (Å) | 3.88427(1) | 3.88292(4) |
| *c* (Å) | 13.6133(1) | 13.6177(3) |
| *V* (Å$^3$) | 205.391(1) | 205.318(7) |
| *z(Se)* | 0.35404(6) | 0.35411(6) |
| $\rho$ (g cm$^{-3}$) | 5.08779 | 5.05672 |
| Ni/Co–Se (Å) | 2.4038(5) | 2.4036(9) |
| Se–Se (Å) | 3.974(1) | 3.975(3) |
| Ni/Co–Ni/Co (Å) | 2.74657(1) | 2.74565(1) |
| Se–Ni/Co–Se (°) | 107.87(2) | 107.80(2) |
| $U_{11}$ (K) (Å$^2$) | 0.00473(9) | 0.026(2) |
| $U_{33}$ (K) (Å$^2$) | 0.020(1) | 0.016(3) |
| $U_{11}$ (Ni) (Å$^2$) | 0.0002(4) | 0.0163(1) |
| $U_{33}$ (Ni) (Å$^2$) | 0.0038(7) | 0.015(1) |
| $U_{11}$ (Co) (Å$^2$) | 0.0002(4) | 0.0163(1) |
| $U_{33}$ (Co) (Å$^2$) | 0.0038(7) | 0.015(1) |
| $U_{11}$ (Se) (Å$^2$) | 0.00014(3) | 0.0098(6) |
| $U_{33}$ (Se) (Å$^2$) | 0.00165(5) | 0.0093(1) |

**Table A.1.2** Unit cell parameters, interatomic distances and angles in $KCo_{2-x}Ni_xSe_2$ series.

| | $x$ = 0 | $x$ = 0.25 | $x$= 0.5 | $x$ = 0.75 | $x$ = 1 | $x$ = 1.25 | $x$ = 1.5 | $x$ = 1.75 | $x$ = 2 |
|---|---|---|---|---|---|---|---|---|---|
| $a$ (Å) | 3.8443(1) | 3.8413(1) | 3.8539(1) | 3.8578(1) | 3.8843(1) | 3.8903(1) | 3.8969(1) | 3.8925(1) | 3.9066(1) |
| $c$ (Å) | 13.7722(4) | 13.8176(1) | 13.7555(1) | 13.7436(2) | 13.6133(1) | 13.5707(2) | 13.5326(1) | 13.4457(2) | 13.4324(4) |
| $V$ (Å$^3$) | 203.534(5) | 203.881(6) | 204.304(4) | 204.549(3) | 205.391(1) | 205.389(2) | 205.510(5) | 205.511(3) | 205.000(9) |
| $d_{X\text{-}X}$ (Å) | 4.021(3) | 4.034(5) | 4.016(3) | 4.013(1) | 3.974(1) | 3.962(2) | 3.951(9) | 3.9261(7) | 3.9223(2) |
| $d_{T\text{-}X}$ (Å) | 2.3971(4) | 2.3987(4) | 2.3999(1) | 2.4008(3) | 2.4038(5) | 2.4038(5) | 2.4036(6) | 2.3965(9) | 2.4014(4) |
| $d_{T\text{-}T}$ (Å) | 2.7183(1) | 2.7181(3) | 2.7251(2) | 2.7279(8) | 2.7466(1) | 2.7509(2) | 2.7556(3) | 2.7524(4) | 2.7624(3) |
| $\delta_{X\text{-}T\text{-}X}$(°) | 106.62(4) | 106.39(2) | 106.82(5) | 106.92(5) | 107.87(2) | 108.07(7) | 108.32(1) | 108.61(3) | 108.86(1) |

## A.2 Structural details of $RbCo_{2-x}Ni_xSe_2$

**Table A.2.1** Unit cell parameters, interatomic distances and angles in $RbCo_{2-x}Ni_xSe_2$ series.

| | **x = 0** | **x = 0.25** | **= 0.5** | **x = 0.75** | **x = 1** | **x = 1.25** | **x = 1.5** | **x = 1.75** | **x = 2** |
|---|---|---|---|---|---|---|---|---|---|
| **a (Å)** | 3.8342(0) | 3.8442(0) | 3.8707(0) | 3.8767(0) | 3.8727(0) | 3.8811(0) | 3.8905(0) | 3.9225(0) | 3.9390(0) |
| **c (Å)** | 14.4529(1) | 14.4276(5) | 14.2738(6) | 14.2859(5) | 14.2742(2) | 14.2751(3) | 14.1593(1) | 14.0048(1) | 13.8821(3) |
| **V ($Å^3$)** | 212.475(1) | 213.213(2) | 213.858(1) | 214.698(1) | 214.081(5) | 215.02(1) | 214.316(4) | 215.478(4) | 215.394(5) |
| **$d_{X-X}$ (Å)** | 4.4226(7) | 4.3860(7) | 4.3393(7) | 4.3424(7) | 4.3394(7) | 4.2882(7) | 4.2761(7) | 4.2070(7) | 4.2007(17) |
| **$d_{T-X}$ (Å)** | 2.375(9) | 2.3861(9) | 2.3880(9) | 2.3911(9) | 2.3888(9) | 2.4074(9) | 2.3977(9) | 2.4083(9) | 2.3992(7) |
| **$d_{T-T}$ (Å)** | 2.7112(15) | 2.7183(15) | 2.7370(15) | 2.7412(15) | 2.7384(15) | 2.7444(15) | 2.7510(15) | 2.7736(15) | 2.7853(10) |
| **$\delta_{X-T-X}$(°)** | 107.65(3) | 107.32(3) | 108.28(3) | 108.32(3) | 108.31(3) | 107.43(3) | 108.45(3) | 109.05(3) | 110.35(3) |

## A.3 Structural details of $CsCo_{2-x}Ni_xSe_2$

**Table A.3.1** Unit cell parameters, interatomic distances, and angles in $CsCo_{2-x}Ni_xSe_2$ series.

| | **x = 0.25** | **= 0.5** | **x = 0.75** | **x = 1** | **x = 1.15** | **x = 1.2** | **x = 1.25** | **x = 1.3** | **x = 1.4** | **x = 1.45** | **x = 1.5** | **x = 1.75** |
|---|---|---|---|---|---|---|---|---|---|---|---|---|
| **a (Å)** | 3.8273(1) | 3.8474(1) | 3.8570(3) | 3.8765(5) | 3.8764(5)<br>**b** = 3.8767(5) | 3.8905(5)<br>**b** = 3.8907(5) | 3.8839(5)<br>**b** = 3.8842(5) | 3.8867(2)<br>**b** = 3.8907(5) | 3.8899(5)<br>**b** = 3.8902(5) | 3.9051(4) | 3.9075(9) | 3.9271(8) |
| **c (Å)** | 15.3007(9) | 15.2584(9) | 15.1856(2) | 15.1221(3) | 15.0962(3) | 15.0278(3) | 15.065(3) | 15.0277(3) | 15.0321(3) | 14.9147(3) | 14.9244(4) | 14.8017(4) |
| **V (Å$^3$)** | 224.13(2) | 225.86(2) | 225.907(5) | 227.242(8) | 226.854(8) | 227.463(1) | 227.265(1) | 227.251(1) | 227.475(1) | 227.450(1) | 227.87(1) | 228.27(1) |
| **$d_{X\text{-}X}$ (Å)** | 4.7140(7) | 4.6996(7) | 4.7513(7) | 4.7314(7) | 4.7068(7) | 4.7581(7) | 4.6504(7) | 4.7581(7) | 4.7068(7) | 4.8714(7) | 4.6863(7) | 4.6477(7) |
| **$d_{T\text{-}X}$ (Å)** | 2.4128(9) | 2.4179(9) | 2.3953(9) | 2.3997(9) | 2.3440(9) | 2.3608(9) | 2.3683(9) | 2.3833(9) | 2.3999(9) | 2.3418(9) | 2.3966(9) | 2.3980(9) |
| **$d_{T\text{-}T}$ (Å)** | 2.7066(15) | 2.7205(15) | 2.7273(15) | 2.7411(15) | 2.7398(12) | 2.7431(12) | 2.7459(12) | 2.7631(12) | 2.7458(12) | 2.7613(15) | 2.7630(15) | 2.7769(15) |
| **$\delta_{X\text{-}T\text{-}X}$(°)** | 104.97(3) | 105.42(3) | 107.24(3) | 107.74(3) | 110.06(3) | 110.98(3) | 110.54(3) | 109.84(3) | 110.25(3) | 107.74(3) | 109.22(3) | 109.93(3) |

**Table A.3.2** Structural parameters for $CsNiCoSe_2$ from Rietveld refinement against I11 RT data (Diamond Light Source) and D2B RT data (ILL).

| Diffractometer | I11 | D2B |
|---|---|---|
| Radiation | X-ray | Neutron |
| Wavelength (Å) | 0.823918 | 1.594 |
| Temperature (K) | 298 | 300 |
| $R_{wp}$ (%) | 1.18 | 4.52 |
| $\chi^2$ | 2.43 | 1.77 |
| Space group | *I*4/*mmm* | *I*4/*mmm* |
| *a* (Å) | 3.87649(5) | 3.92276(9) |
| *c* (Å) | 15.1221(3) | 14.8594(6) |
| *V* (Å$^3$) | 227.242(8) | 228.65(1) |
| *z(Se)* | 0.3454(1) | 0.34394(1) |
| $\rho$ (g cm$^{-3}$) | 5.379 | 5.576 |
| Ni/Co–Se (Å) | 2.3997(9) | 2.4036(9) |
| Se–Se (Å) | 4.7314(7) | 3.975(3) |
| Ni/Co–Ni/Co (Å) | 2.7411(15) | 2.74565(1) |
| Se–Ni/Co–Se (°) | 107.74(3) | 107.80(2) |
| $U_{11}$ (Cs) (Å$^2$) | 0.0062(7) | 0.0206(1) |
| $U_{33}$ (Cs) (Å$^2$) | 0.004(1) | 0.010(3) |
| $U_{11}$ (Ni) (Å$^2$) | 0.0008(8) | 0.0128(9) |
| $U_{33}$ (Ni) (Å$^2$) | 0.010(1) | 0.028(1) |
| $U_{11}$ (Co) (Å$^2$) | 0.0008(8) | 0.0128(9) |
| $U_{33}$ (Co) (Å$^2$) | 0.010(1) | 0.028(1) |
| $U_{11}$ (Se) (Å$^2$) | 0.0001(6) | 0.0076(6) |
| $U_{33}$ (Se) (Å$^2$) | 0.0001(1) | 0.006(1) |

## A.4 Structural details of $KCo_{2-x}Ni_xS_2$

**Table A.4.1** Unit cell parameters, interatomic distances and angles in $KCo_{2-x}Ni_xS_2$ series.

| | $x = 0$ | $x = 0.25$ | $x = 0.5$ | $x = 0.75$ | $x = 1$ | $x = 1.25$ | $x = 1.5$ | $x = 1.75$ | $x = 2$ |
|---|---|---|---|---|---|---|---|---|---|
| $a$ (Å) | 3.712(1) | 3.7342(1) | 3.7429(1) | 3.7481(1) | 3.7583(1) | 3.7637(1) | 3.7681(1) | 3.7784(1) | 3.7870(1) |
| $c$ (Å) | 13.1820(4) | 13.1250(1) | 13.0717(1) | 13.0640(2) | 13.0194(1) | 12.9994(2) | 12.9729(1) | 12.9677(2) | 12.8271(4) |
| $V$ (Å$^3$) | 181.661(5) | 183.008(6) | 183.121(4) | 183.524(3) | 183.804(1) | 184.141(2) | 184.199(5) | 185.13(3) | 183.957(9) |
| $d_{X\text{-}X}$ (Å) | 4.0205(7) | 4.0031(7) | 3.9869 (7) | 3.9845(7) | 3.9709(7) | 3.9648(7) | 3.9567(7) | 3.9551(7) | 3.9123(7) |
| $d_{T\text{-}X}$ (Å) | 2.2576 (9) | 2.2635(9) | 2.2642(9) | 2.2659(9) | 2.2677(9) | 2.2689(9) | 2.2693(9) | 2.2732(9) | 2.2692(9) |
| $d_{T\text{-}T}$ (Å) | 2.6248(15) | 2.6404(15) | 2.6466(15) | 2.6503(15) | 2.6575(15) | 2.6613(15) | 2.6644(15) | 2.6717(4) | 2.6778(15) |
| $d_{X\text{-}T\text{-}X}$(°) | 110.60(4) | 111.15(3) | 111.49(3) | 111.59(3) | 111.92(3) | 112.08(3) | 112.25(3) | 112.42(3) | 113.11 (3) |

## Appendix B: Variable temperature PXRD measurements of orthorhombic $CsCo_{0.8}Ni_{1.2}Se_2$

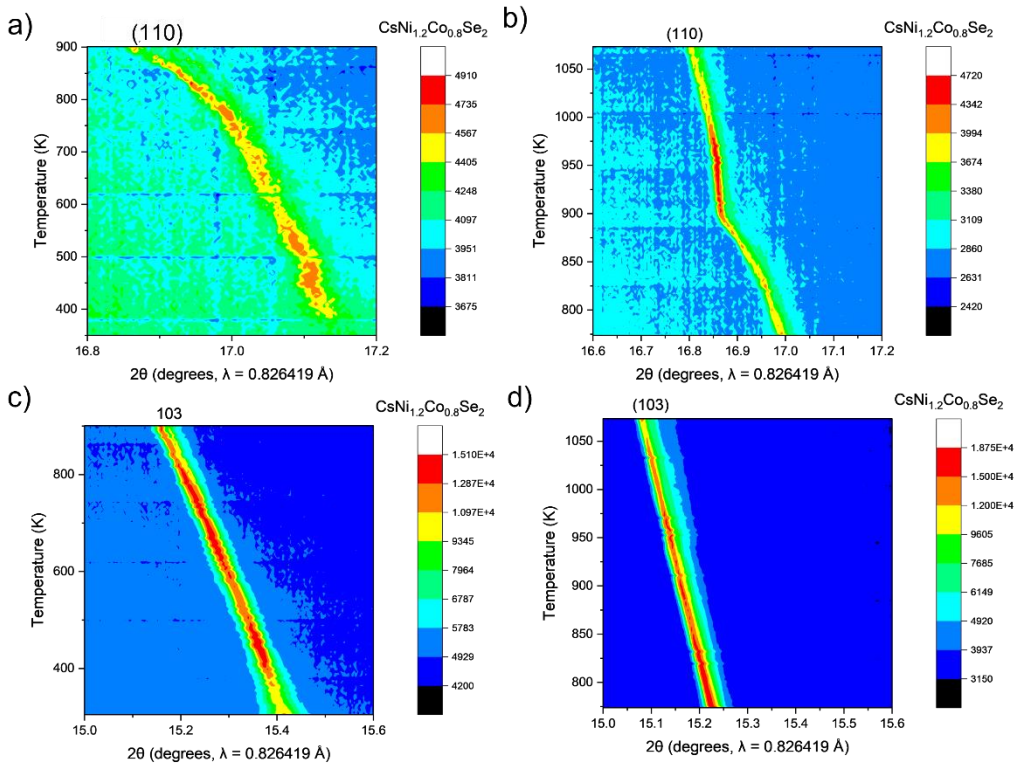


**Figure B.1**: Contour plot of $CsCo_{0.8}Ni_{1.2}Se_2$ showing the evolution of a) (110) peak between 300-900 K, b) (110) peak between 773-1073 K, c) (103) peak between 300-900 K, and d) (103) peak between 773-1073 K.

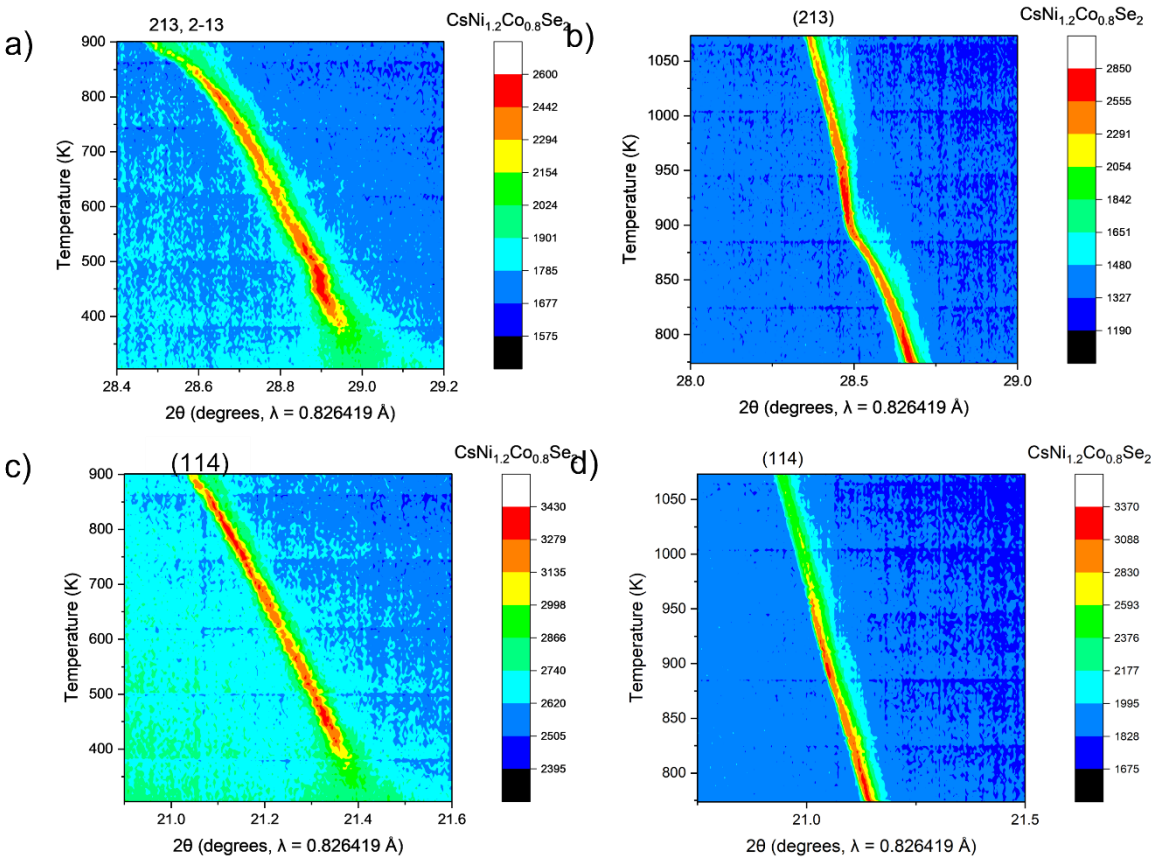


**Figure B.2**: Contour plot of $CsCo_{0.8}Ni_{1.2}Se_2$ showing the evolution of a) (213) peak between 300-900 K, b) (213) peak between 773-1073 K, c) (114) peak between 300-900 K, and d) (114) peak between 773-1073 K.

## Appendix C: Attempted Curie-Weiss fitting of $ACo_{2-x}Ni_xCh_2$ phases ($A$ = K, Rb, Cs; $Ch$ = S, Se)

### C.1 Curie-Weiss fitting of $KCo_{2-x}Ni_xSe_2$ ($0.5 \leq x \leq 1.5$)

For the antiferromagnetic members of $KCo_{2-x}Ni_xSe_2$ ($0.5 \leq x \leq 1.5$) the linear portion of the plot of the variation of $1/\chi$ with temperature above the Néel temperature was fitted to the Curie-Weiss law, $\chi = C/(T-\theta)$ for $KCoNiSe_2$ (Figure C.1.1), $KCo_{1.5}Ni_{0.5}Se_2$ (Figure C.1.2), and $KCo_{0.5}Ni_{1.5}Se_2$ (Figure C.1.3).

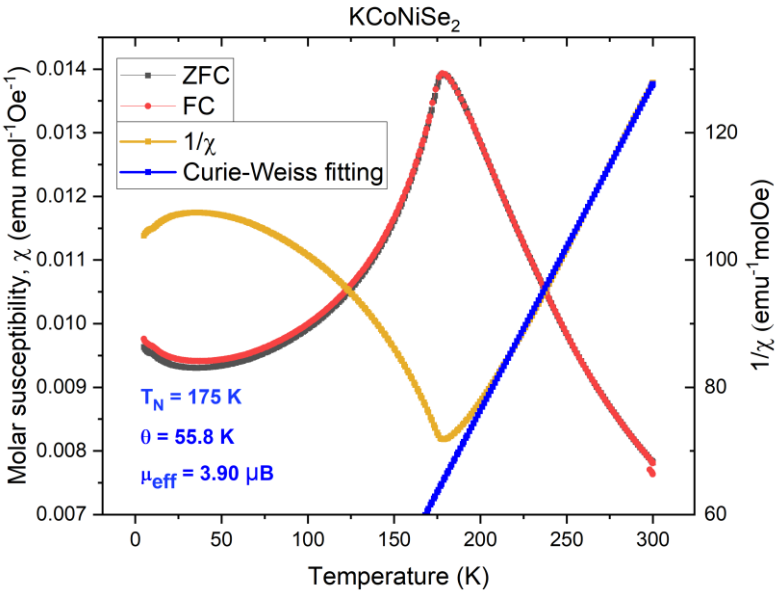


**Figure C.1.1** Curie-Weiss fitting of $KCoNiSe_2$.

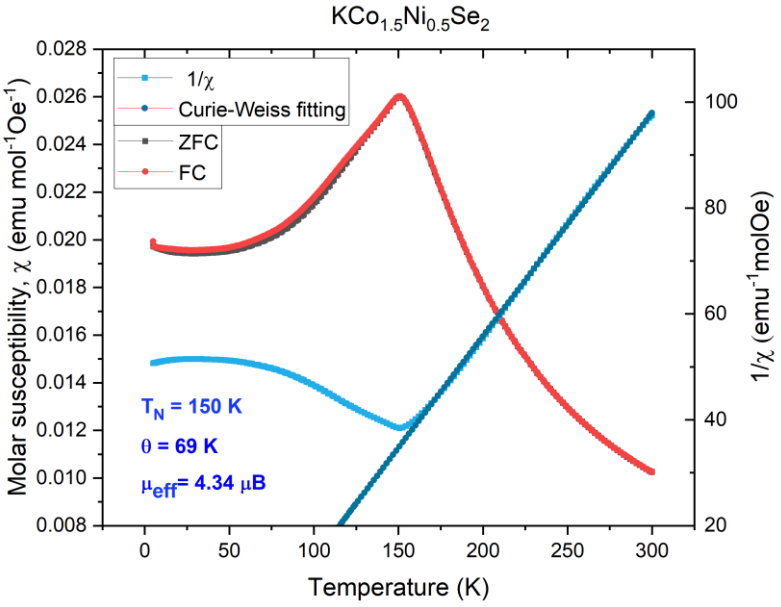


**Figure C.1.2** Curie-Weiss fitting of $KCo_{1.5}Ni_{0.5}Se_2$.

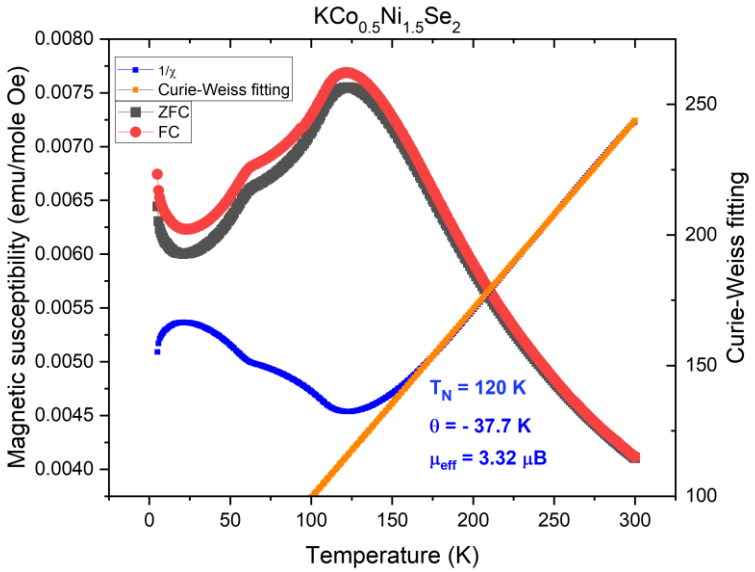


**Figure C.1.3** Curie-Weiss fitting of $KCo_{0.5}Ni_{1.5}Se_2$.

Using this treatment, the effective moment per transition metal ion, $\mu_{eff}^2 = 8C_m$, was calculated for the antiferromagnetic members of the series, listed in Table C.1.1, together with values of $T_N$ and $\theta$ (although see note below about the validity of this approach). Figure C.1.4 shows modified Curie-Weiss fits for the two paramagnetic members of the series: $KNi_2Se_2$ (Figure C.1.4a) and

$KCo_{0.25}Ni_{1.75}Se_2$ (Figure C.1.4b). These fits include a temperature-independent contribution to paramagnetism (fitting equation: $\chi = \chi_0 + C/(T-\theta)$), as the high temperature part of the $1/\chi$ vs $T$ plot was not linear and deviated from the Curie-Weiss law, therefore the values reported in Table C.1.1 for these two compounds come from the modified fitting.

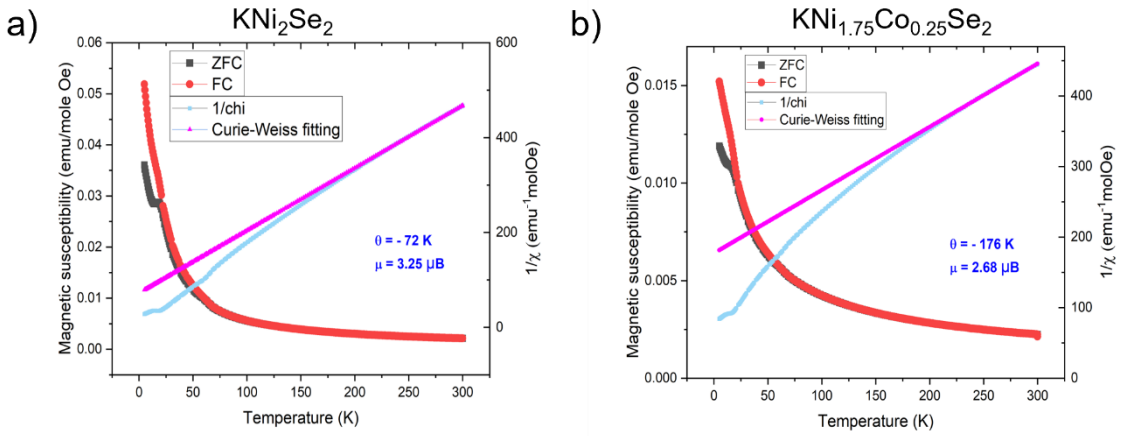


**Figure C.1.4** Curie-Weiss fitting of a) $KNi_2Se_2$ and b) $KCo_{0.25}Ni_{1.75}Se_2$. The fitting was constructed using a temperature-independent contribution ( $\chi = \chi_0 + C/(T-\theta)$).

**Table C.1.1** Physical properties of $KCo_{2-x}Ni_xSe_2$ obtained from magnetometry ($T_N$, $\theta$, and $\mu_{eff}$) and neutron powder diffraction.

| **Composition** | ***x*** | **$T_N$ (K)** | **θ(K)** | **$\mu_{eff}$ (μB)** | **Long-range ordered moment per T ion ($\mu_B$)** |
|---|---|---|---|---|---|
| $KCo_2Se_2$ | $x = 0$ | 90 (FM) | - | - | - |
| $KCo_{1.75}Ni_{0.25}Se_2$ | $x = 0.25$ | 65 (FM) | - | - | - |
| $KCo_{1.5}Ni_{0.5}Se_2$ | $x = 0.5$ | 150 | 69 | 4.34 | 1.07 |
| $KCo_{1.25}Ni_{0.75}Se_2$ | $x = 0.75$ | 145 | 49 | 4.85 | - |
| $KCoNiSe_2$ | $x = 1$ | 175 | 55.8 | 3.90 | 1.18 |
| $KCo_{0.75}Ni_{1.25}Se_2$ | $x = 1.25$ | 166 | 29.5 | 3.18 | - |
| $KCo_{0.5}Ni_{1.5}Se_2$ | $x = 1.5$ | 120 | -37.7 | 3.32 | - |
| $KCo_{0.25}Ni_{1.75}Se_2$ | $x = 1.75$ | - | -176 | 2.68 | - |
| $KNi_2Se_2$ | $x = 2$ | - | -72 | 3.25 | - |

The Weiss temperature, $\theta$, obtained in this treatment, which gives an estimate of the average strength of the coupling between magnetic moments, is positive for antiferromagnetic members of the series,

which is consistent with the strong in-plane ferromagnetism and the weaker coupling between the layers. For the members of the series with higher Ni contents which do not show evidence for magnetic long-range order, the Weiss temperatures are negative, suggesting that antiferromagnetic interactions dominate. It is important to note here that the Weiss temperatures are not much smaller than the temperatures in the range chosen for the fitting, so the results obtained from this treatment, especially the large values of the effective magnetic moments should be interpreted with a level of caution, as these compounds appear to be non-Curie-Weiss.

### C.2 Curie-Weiss fitting of $RbCo_{2-x}Ni_xSe_2$ ($0.25 \leq x \leq 1.75$)

For the antiferromagnetic samples the linear portion of the plot of the variation of $1/\chi$ with temperature above the Néel temperature was fitted to the Curie-Weiss law, $\chi = C/(T-\theta)$ for $RbCoNiSe_2$ (Figure C.2.1), $RbCo_{1.5}Ni_{0.5}Se_2$ (Figure C.2.2), and $RbCo_{0.5}Ni_{1.5}Se_2$ (Figure C.2.3). As in the case of the K-analogue, the Weiss temperatures are not much smaller than the temperatures in the range chosen for the fitting, so the results obtained from this treatment, especially the large values of the effective magnetic moments should be interpreted with some caution.

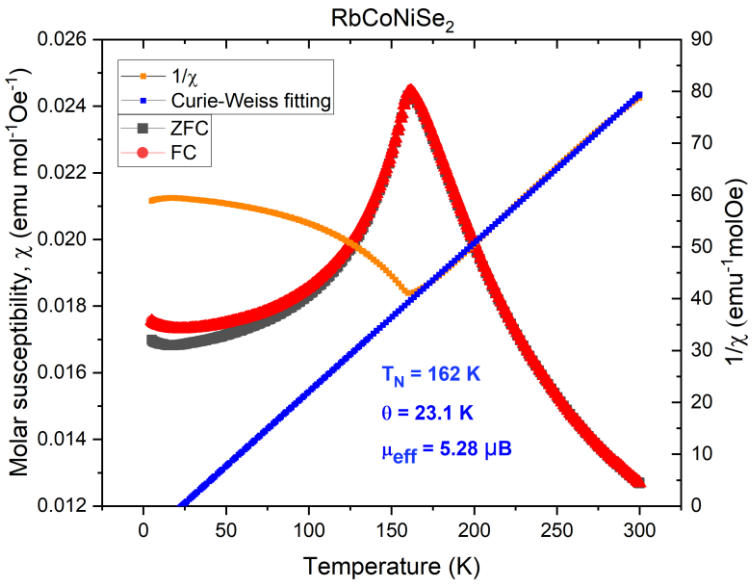


**Figure C.2.1** Curie-Weiss fitting of $RbCoNiSe_2$.

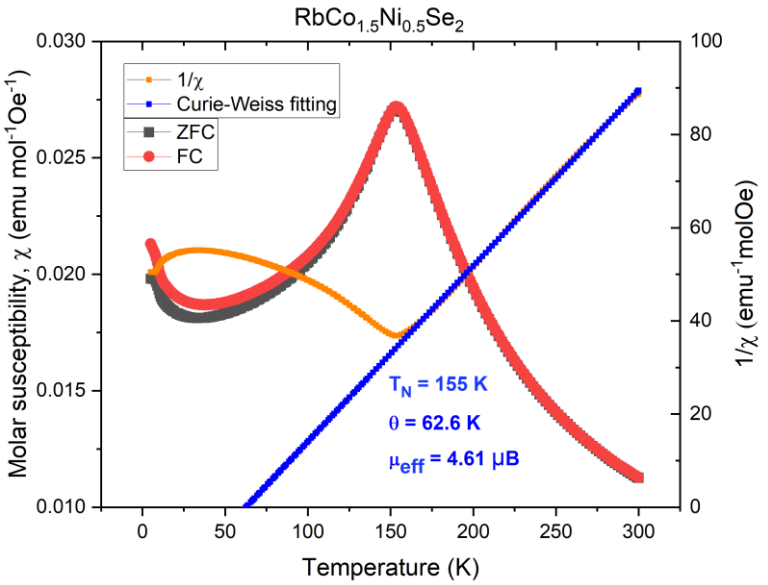


**Figure C.2.2** Curie-Weiss fitting of $RbCo_{1.5}Ni_{0.5}Se_2$.

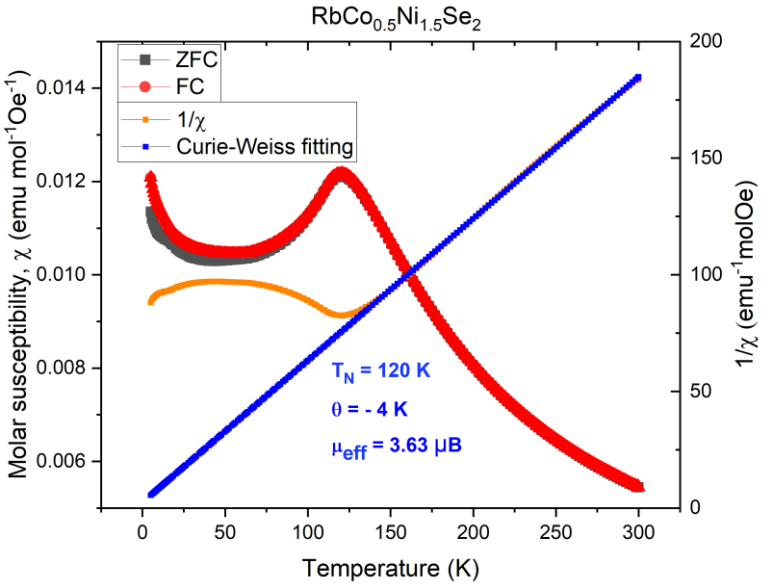


**Figure C.2.3** Curie-Weiss fitting of $RbCo_{0.5}Ni_{1.5}Se_2$.

**Table C.2.1** Physical properties of $RbCo_{2-x}Ni_xSe_2$ obtained from magnetometry ($T_N$, $\theta$, and $\mu_{eff}$).

| Composition | *x* | $T_N$ (K) | θ(K) | $\mu_{eff}$ (μB) |
|---|---|---|---|---|
| $RbCo_2Se_2$ | $x = 0$ | 75 (FM) | - | - |
| $RbCo_{1.75}Ni_{0.25}Se_2$ | $x = 0.25$ | 110 | 1.98 | 1.88 |
| $RbCo_{1.5}Ni_{0.5}Se_2$ | $x = 0.5$ | 155 | 62.6 | 4.61 |
| $RbCo_{1.25}Ni_{0.75}Se_2$ | $x = 0.75$ | 167 | 71.2 | 4.27 |
| $RbCoNiSe_2$ | $x = 1$ | 162 | 23.1 | 5.28 |
| $RbCo_{0.75}Ni_{1.25}Se_2$ | $x = 1.25$ | 145 | 41.5 | 3.94 |
| $RbCo_{0.5}Ni_{1.5}Se_2$ | $x = 1.5$ | 120 | -4 | 3.63 |
| $RbCo_{0.25}Ni_{1.75}Se_2$ | $x = 1.75$ | 30 | 99.5 | 2.50 |
| $RbNi_2Se_2$ | $x = 2$ | - | - | - |

## C.3 Curie-Weiss fitting CsCo2−xNixSe2 (0.25 ≤ x ≤ 1.75)

For the antiferromagnetic samples the linear portion of the plot of the variation of $1/\chi$ with temperature above the Néel temperature was fitted to the Curie-Weiss law, $\chi = C/(T-\theta)$ for $CsCoNiSe_2$ (Figure C.3.1b), $CsCo_{1.5}Ni_{0.5}Se_2$ (Figure C.3.1a), and $CsCo_{0.5}Ni_{1.5}Se_2$ (Figure C.3.1c). As in the case of the K- and Rb- analogues, the Weiss temperatures are not much smaller than the temperatures in the range chosen for the fitting, so the results obtained from this treatment, especially the large values of the effective magnetic moments should be interpreted with some caution. The results of this treatment suggests that these compositions are non-Curie-Weiss compounds, as their magnetic susceptibilities exhibit a complex temperature-dependent behaviour.

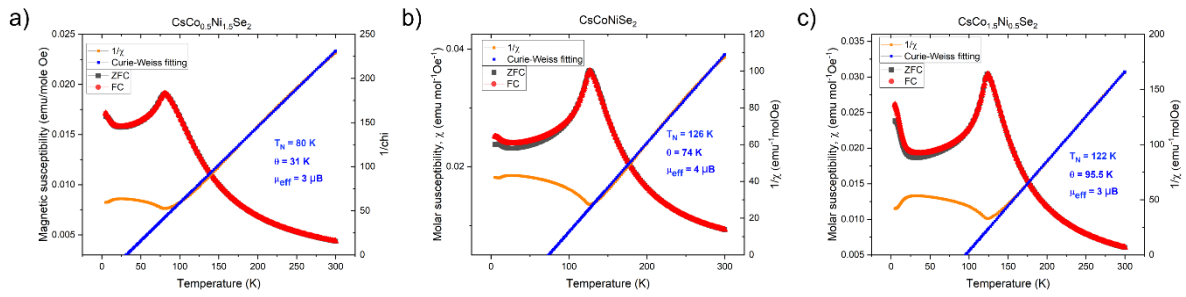


**Figure C.3.1** Curie-Weiss fitting of a) $CsCo_{1.5}Ni_{0.5}Se_2$, b) $CsCoNiSe_2$, c) $CsCo_{0.5}Ni_{1.5}Se_2$.

**Table C.3.1** Physical properties of $CsCo_{2-x}Ni_xSe_2$ obtained from magnetometry ($T_N$, $\theta$, and $\mu_{eff}$) and neutron powder diffraction.

| **Composition** | ***x*** | **$T_N$ (K)** | **θ(K)** | **$\mu_{eff}$ (μB)** | **Long-range ordered moment per T ion ($\mu_B$)** |
|---|---|---|---|---|---|
| $CsCo_2Se_2$ | $x = 0$ | 66 | - | - | |
| $CsCo_{1.75}Ni_{0.25}Se_2$ | $x = 0.25$ | 82 | Non-CW | | |
| $CsCo_{1.5}Ni_{0.5}Se_2$ | $x = 0.5$ | 122 | 95.5 | 3 | |
| $CsCo_{1.25}Ni_{0.75}Se_2$ | $x = 0.75$ | 120 | 90 | 3.7 | |
| $CsCoNiSe_2$ | $x = 1$ | 126 | 74 | 4 | 0.8 |
| $CsCo_{0.75}Ni_{1.25}Se_2$ | $x = 1.25$ | 110 | 77.5 | 3.1 | |
| $CsCo_{0.5}Ni_{1.5}Se_2$ | $x = 1.5$ | 80 | 31.5 | 3.03 | |
| $CsCo_{0.25}Ni_{1.75}Se_2$ | $x = 1.75$ | 25 | Non-CW | | |
| $CsNi_2Se_2$ | $x = 2$ | - | - | - | |

## C.4 Curie-Weiss fitting of $KCoNiS_2$

For the antiferromagnetic samples the linear portion of the plot of the variation of $1/\chi$ with temperature above the Néel temperature was fitted to the Curie-Weiss law, $\chi = C/(T-\theta)$ for $KCoNiS_2$ (Figure C.4.1). Only one fitting was performed as an example (for $KCoNiS_2$ shown in Figure C.4.1), as the Weiss temperatures extracted from this treatment for the selenide analogues were shown to be within the temperature range used for the fitting, meaning that they have to be interpreted with a lot of caution. Ideally, the fitting would be done at much higher temperatures to reach the linear portion of the $\chi^{-1}$ *vs* $T$ plot.

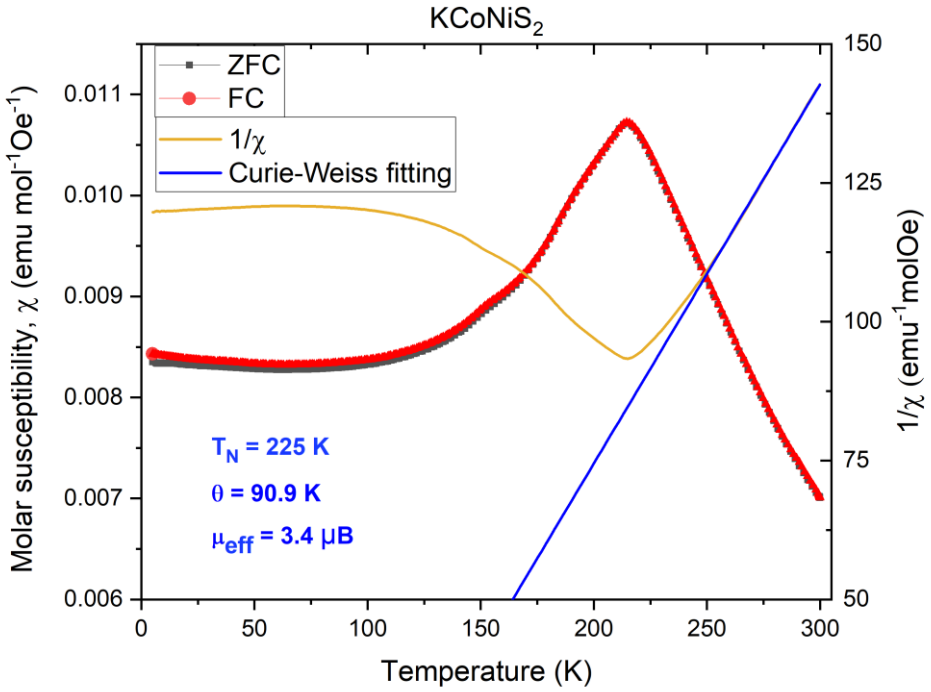


**Figure C.4.1** Curie-Weiss fitting of $KCoNiS_2$.

## Appendix D: Room-temperature Powder Neutron Diffraction of $ACo_{2-x}Ni_xSe_2$ phases (A = K, Cs)

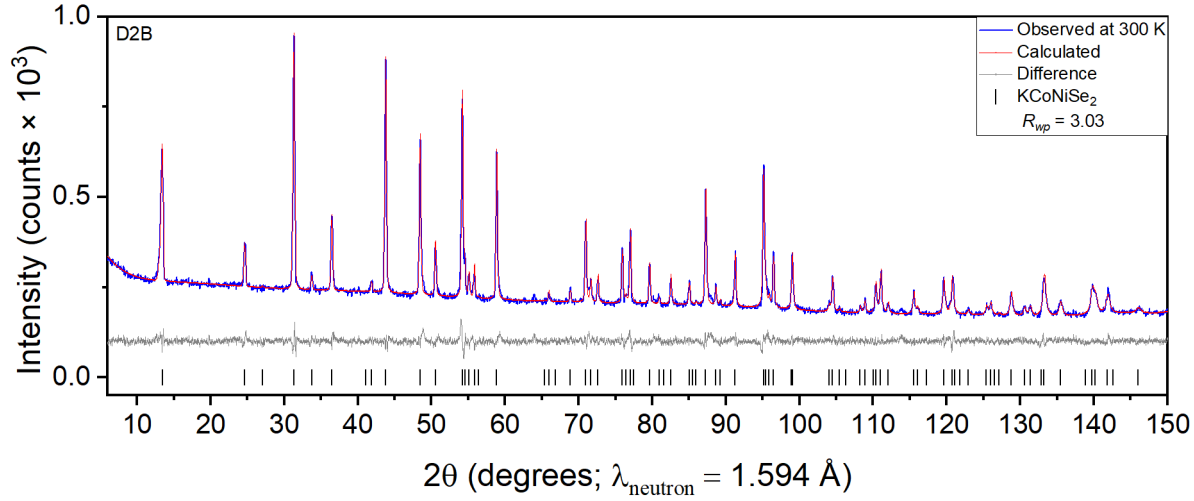


**Figure D.1** Rietveld refinement of $KCoNiSe_2$ against PND data measured at 300 K, $R_{wp}$ = 3.02% and $\chi^2$ = 1.45.

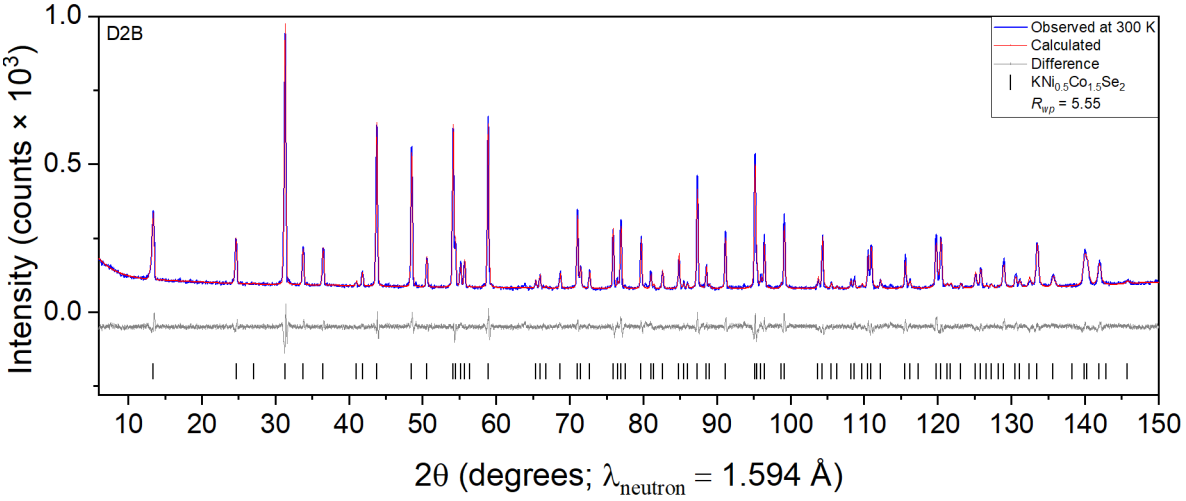


**Figure D.2** Rietveld refinement of $KCo_{1.5}Ni_{0.5}Se_2$ against PND data measured at 300 K, $R_{wp}$ = 5.55% and $\chi^2$ = 1.81.

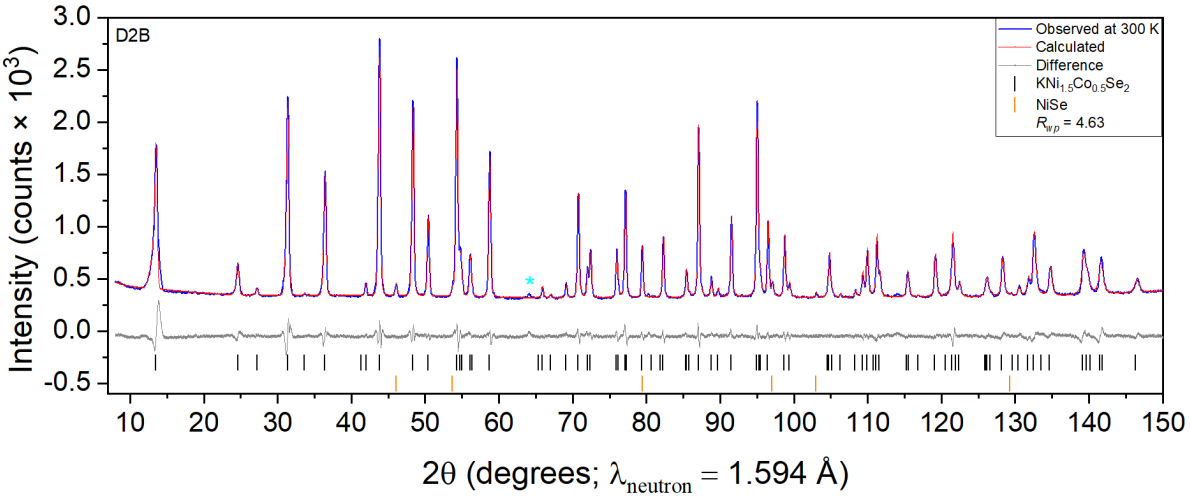


**Figure D.3** Rietveld refinement of $KCo_{0.5}Ni_{1.5}Se_2$ against PND data measured at 300 K, $R_{wp}$ = 4.63% and $\chi^2$ = 1.79.

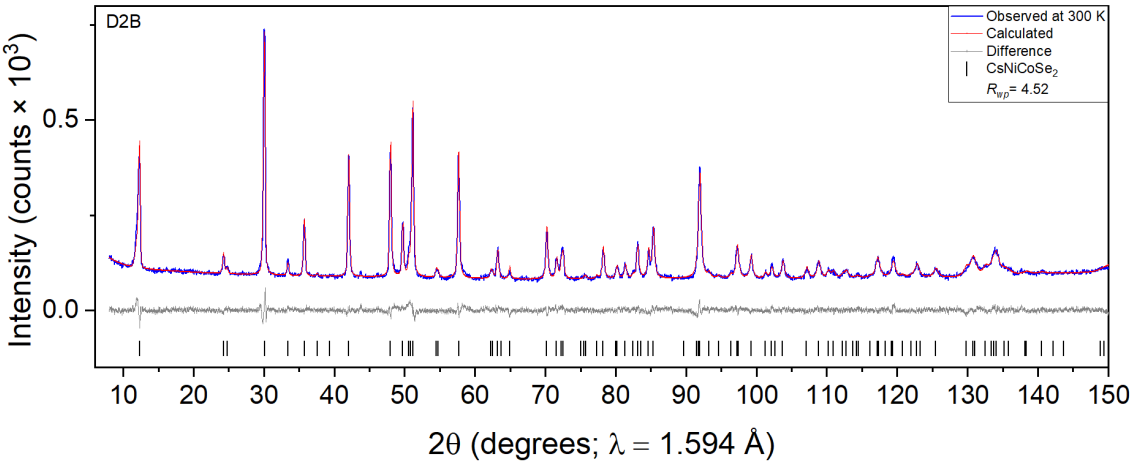


**Figure D.4** Rietveld refinement of $CsCoNiSe_2$ against PND data measured at 300 K, $R_{wp}$ = 4.52% and $\chi^2$ = 2.14.

## Appendix E: SEM-EDX details for $KCo_{2-x}Ni_xSe_2$

**Table E.1** Atomic occupancies of $KCo_{2-x}Ni_xSe_2$ series before scaling up from $K_2Se$ standard, where both K and TM (Co/Ni) were scaled up.

| **Nominal Composition** | **Observed composition** | **K** | **Co** | **Ni** | **Se** |
|---|---|---|---|---|---|
| $KCo_2Se_2$ | $K_{0.78(6)}Co_{1.90(7)}Se_{2.0(1)}$ | 0.78 ± 0.06 | 1.9 ± 0.07 | - | 2.0 ± 0.01 |
| $KCo_{1.75}Ni_{0.25}Se_2$ | $K_{0.76(2)}Co_{1.55(7)}Ni_{0.17(2)}Se_{2.0(1)}$ | 0.76 ± 0.02 | 1.55 ± 0.07 | 0.17 ± 0.02 | 2.00 ± 0.01 |
| $KCo_{1.5}Ni_{0.5}Se_2$ | $K_{0.79(3)}Co_{1.31(8)}Ni_{0.42(3)}Se_{2.0(1)}$ | 0.79 ± 0.03 | 1.31 ± 0.08 | 0.42 ± 0.03 | 2.00 ± 0.01 |
| $KCo_{1.25}Ni_{0.75}Se_2$ | $K_{0.79(2)}Co_{1.1(1)}$ $Ni_{0.70(5)}Se_{2.0(1)}$ | 0.79 ± 0.02 | 1.10 ± 0.01 | 0.7 ± 0.05 | 2.00 ± 0.01 |
| $KCoNiSe_2$ | $K_{0.79}Co_{1.05(6)}Ni_{0.91(6)}Se_{2.0}$ | 0.79 ± 0.05 | 1.05 ± 0.06 | 0.91 ± 0.06 | 2.00 ± 0.01 |
| $KCo_{0.75}Ni_{1.25}Se_2$ | $K_{0.87(2)}Co_{0.74(6)}Ni_{1.09(7)}Se_{2.0(1)}$ | 0.87 ± 0.02 | 0.74 ± 0.06 | 1.09 ± 0.07 | 2.00 ± 0.01 |
| $KCo_{0.5}Ni_{1.5}Se_2$ | $K_{0.90(4)}Co_{0.40(4)}$ $Ni_{1.3(1)}Se_{2.0(2)}$ | 0.90 ± 0.04 | 0.40 ± 0.04 | 1.30 ± 0.01 | 2.00 ± 0.02 |
| $KNi_2Se_2$ | $K_{0.85(6)}Ni_{1.79(9)}Se_{2.00(9)}$ | 0.85 ± 0.06 | - | 1.79± 0.09 | 2.00 ± 0.09 |

## Appendix F: Room temperature SXRD of $RbCoNiSe_2$ and $CsCoNiSe_2$

The Rietveld refinement of room temperature Synchrotron PXRD pattern of $RbCoNiS_2$ is shown in Figure F.1. This is the only member of the possible $RbCo_{2-x}Ni_xS_2$ solid solution synthesised in this work. The successful synthesis demonstrates that the rest of the solid solution may be synthesised, but this was beyond the scope of this work due to time constraints. The Rietveld refinement is not of an excellent quality, and the peak shapes for (002) and (103) peaks of the *I*4/*mmm* tetragonal cell were difficult to fit. The fit improved significantly when Rb occupancy was refined and it shows a deficiency of 29% (i.e. occupancy of 0.71(1)) on the alkali metal site. The lattice parameters, interatomic distances, and angles for $RbCoNiS_2$ are listed in Table F.1.

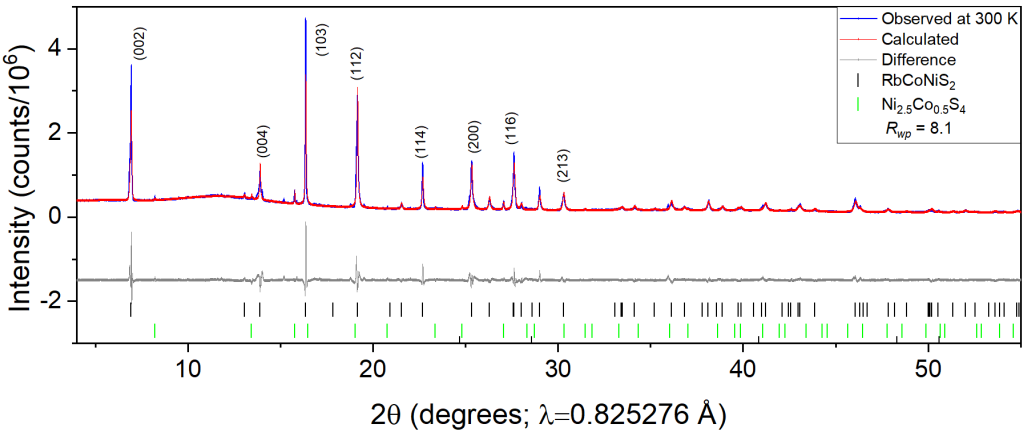


**Figure F.1.** Room-temperature Rietveld refinement of $RbCoNiS_2$ against Synchrotron PXRD.

**Table F.1** Lattice parameters, interatomic distances, and angles for $RbCoNiS_2$.

| | ***a*** **(Å)** | ***c*** **(Å)** | ***V*** **(Å$^3$)** | $d_{X\text{-}X}$ **(Å)** | $d_{T\text{-}X}$ **(Å)** | $d_{T\text{-}T}$ **(Å)** | $\delta_{X\text{-}T\text{-}X}$**(°)** |
|---|---|---|---|---|---|---|---|
| $RbCoNiS_2$ | 3.76402(7) | 13.6407(4) | 193.26(1) | 4.1975(0) | 2.2938(0) | 2.6615(7) | 110.26(0) |

The Rietveld refinement of room temperature Synchrotron PXRD pattern of $CsCoNiS_2$ is shown in Figure F.2. This is the only member of the possible $CsCo_{2-x}Ni_xS_2$ solid solution synthesised in this work. The successful synthesis again demonstrates that the rest of the solid solution may be

synthesised, but this was beyond the scope of this work due to time constraints. The Rietveld refinement is not of an excellent quality, and the peak shapes for (112) and (103) peaks of the *I*4/*mmm* tetragonal cell were difficult to fit. The fit to the PXRD pattern suffers from impurities, including $Ni_{2.5}Co_{0.5}S_4$ and $Cs_2Ni_3S_4$. The fit also improved significantly when Cs occupancy was refined and it shows a deficiency of 30% (occupancy 0.70(1)) on the alkali metal site. The lattice parameters, interatomic distances, and angles for $CsCoNiS_2$ are listed in Table F.2.

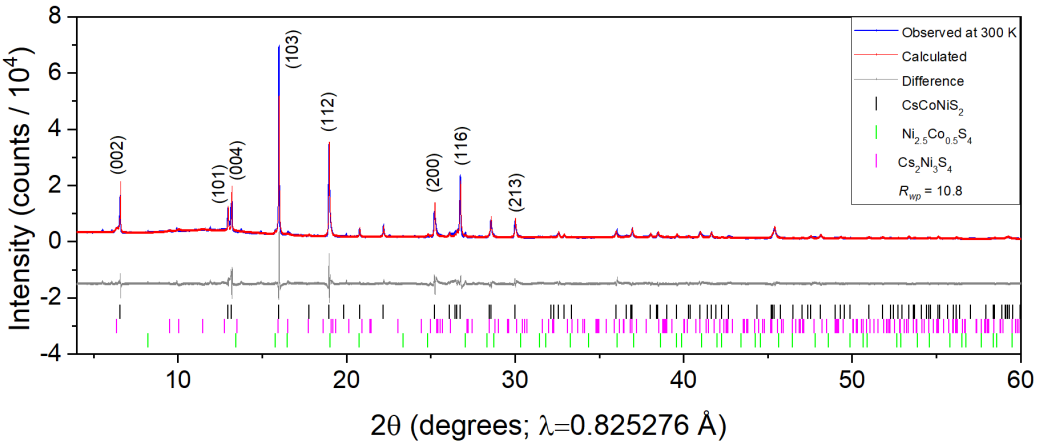


**Figure F.2** Room-temperature Rietveld refinement of $CsCoNiS_2$ against Synchrotron PXRD.

**Table F.2** The lattice parameters, interatomic distances, and angles for $CsCoNiS_2$.

| | ***a* (Å)** | ***c* (Å)** | ***V* (Å$^3$)** | $d_{X\text{-}X}$ **(Å)** | $d_{T\text{-}X}$ **(Å)** | $d_{T\text{-}T}$ **(Å)** | $\delta_{X\text{-}T\text{-}X}$**(°)** |
|---|---|---|---|---|---|---|---|
| $CsCoNiS_2$ | 3.77878 (5) | 14.37964(3) | 205.329(8) | 4.6547(7) | 2.2755(9) | 2.708(12) | 107.19(3) |

## Appendix G: Magnetic structure details of $KCo_{2-x}Ni_xS_2$

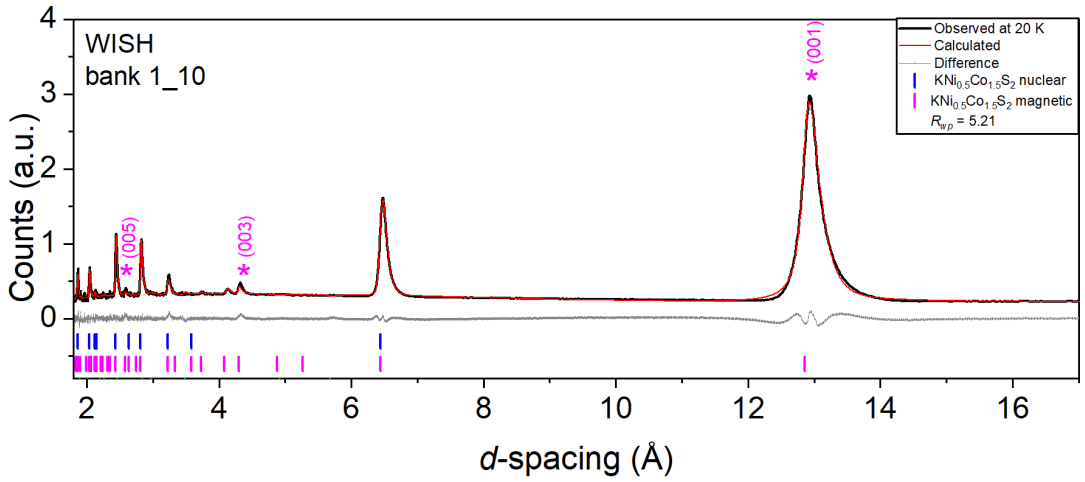


**Figure G.1** Rietveld refinement of $KCo_{1.5}Ni_{0.5}S_2$ against PND data measured at 20 K, $R_{wp}$ = 5.21%, with magenta asterisks denoting magnetic Bragg peaks (bank 1_10).

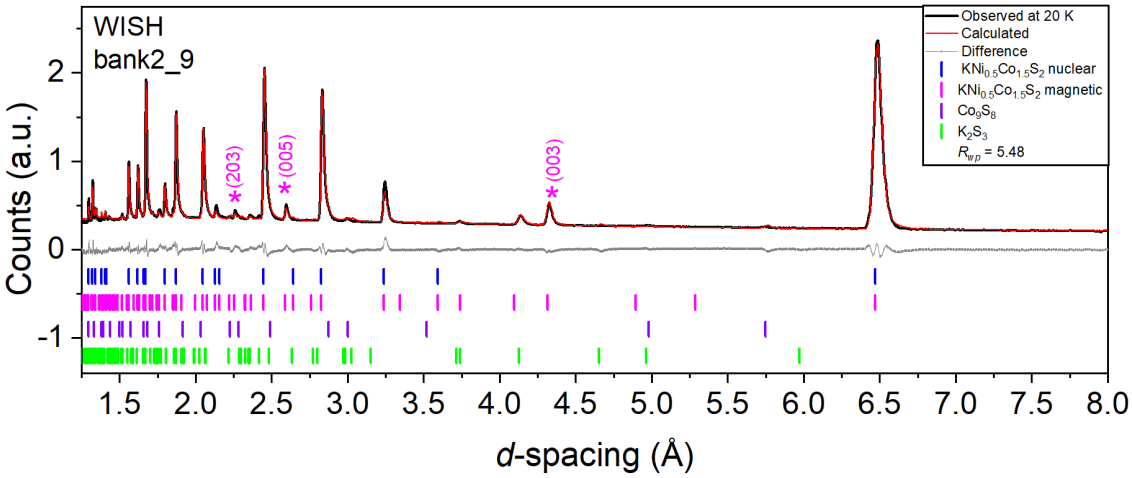


**Figure G.2** Rietveld refinement of $KCo_{1.5}Ni_{0.5}S_2$ against PND data measured at 20 K, $R_{wp}$ = 5.48%, with magenta asterisks denoting magnetic Bragg peaks (bank 2_9).

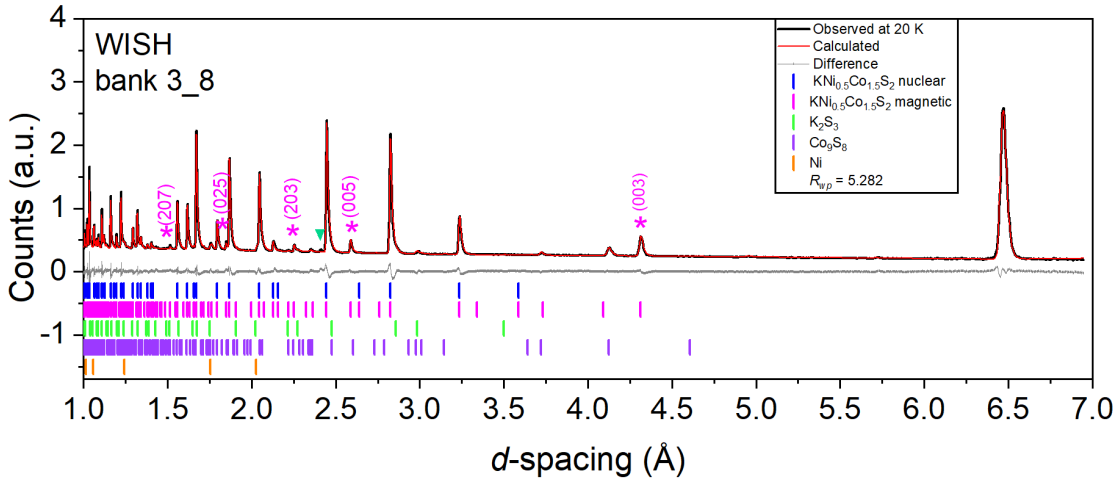


**Figure G.3** Rietveld refinement of $KCo_{1.5}Ni_{0.5}S_2$ against PND data measured at 20 K, $R_{wp}$ = 5.28%, with magenta asterisks denoting magnetic Bragg peaks (bank 3_8).

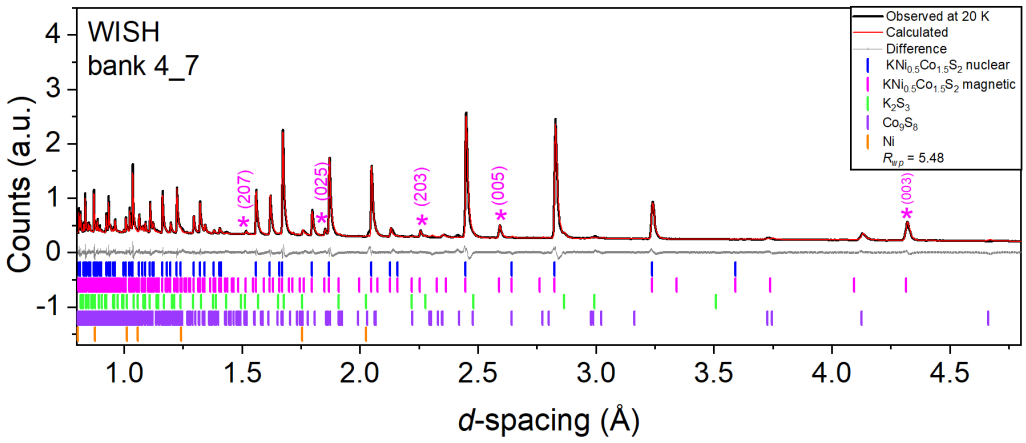


**Figure G.4** Rietveld refinement of $KCo_{1.5}Ni_{0.5}S_2$ against PND data measured at 20 K, $R_{wp}$ = 5.48%, with magenta asterisks denoting magnetic Bragg peaks (bank 4_7). The green triangle indicates an unknown impurity.

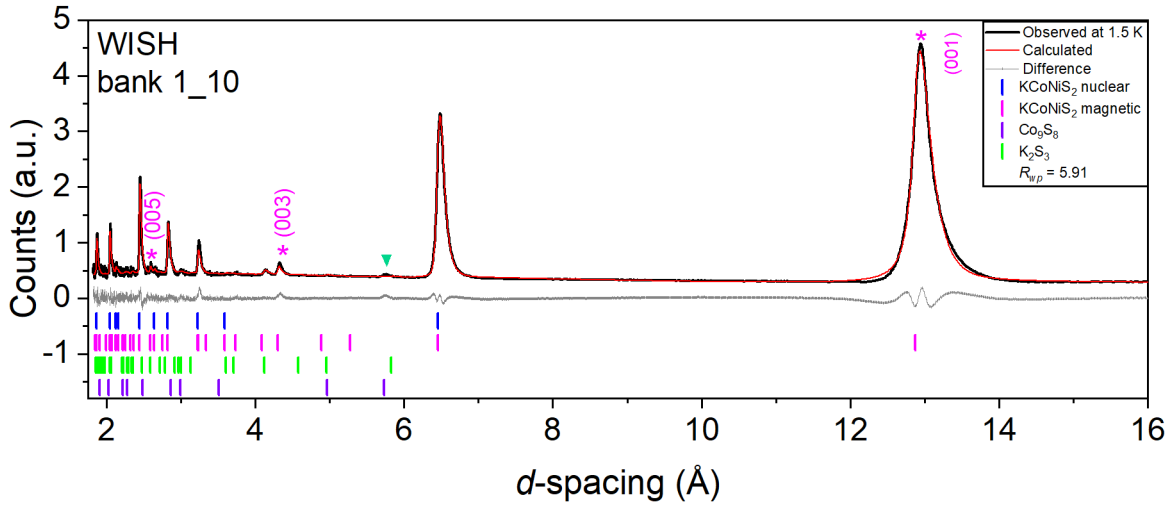


**Figure G.5** Rietveld refinement of $KCoNiS_2$ against PND data measured at 20 K, $R_{wp}$ = 5.91%, with magenta asterisks denoting magnetic Bragg peaks (bank 1_10). The green triangle indicates an unknown impurity.

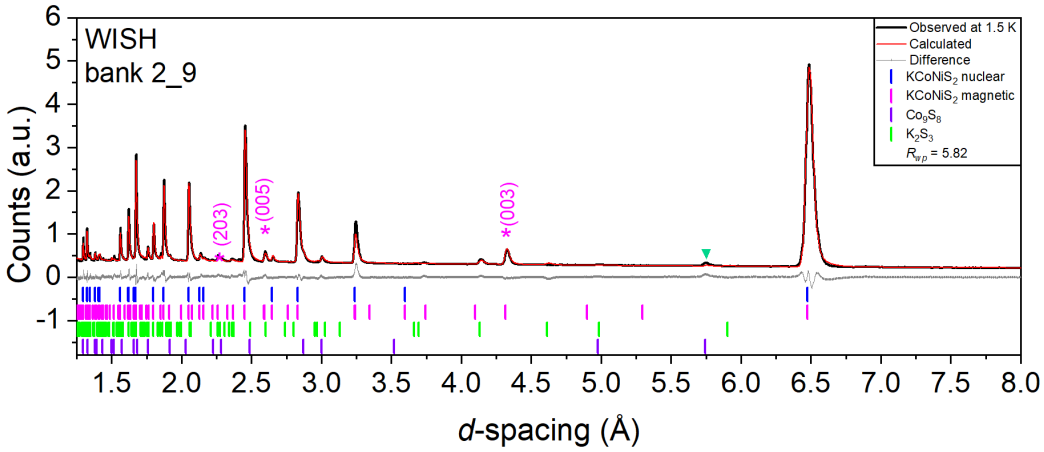


**Figure G.6** Rietveld refinement of $KCoNiS_2$ against PND data measured at 20 K, $R_{wp}$ = 5.82%, with magenta asterisks denoting magnetic Bragg peaks (bank 2_9). The green triangle indicates an unknown impurity.

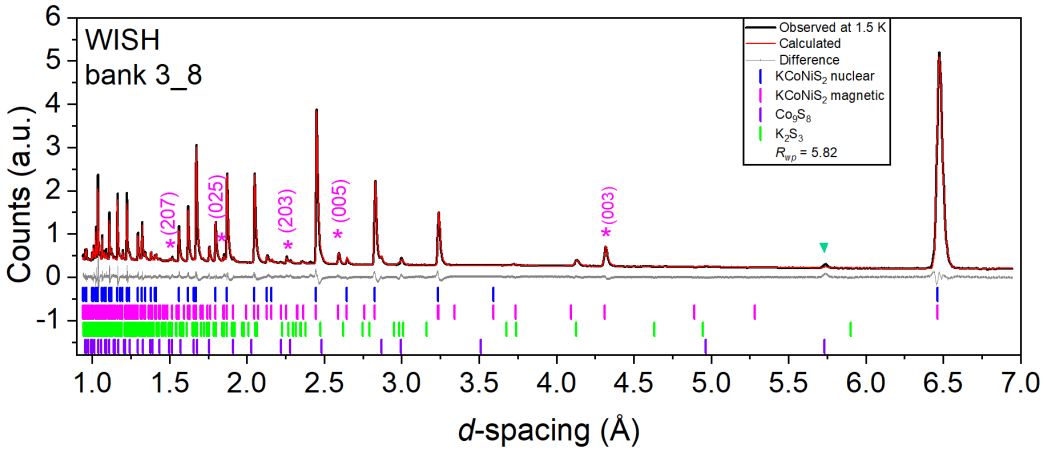


**Figure G.7** Rietveld refinement of $KCoNiS_2$ against PND data measured at 20 K, $R_{wp}$ = 5.82%, with magenta asterisks denoting magnetic Bragg peaks (bank 3_8).

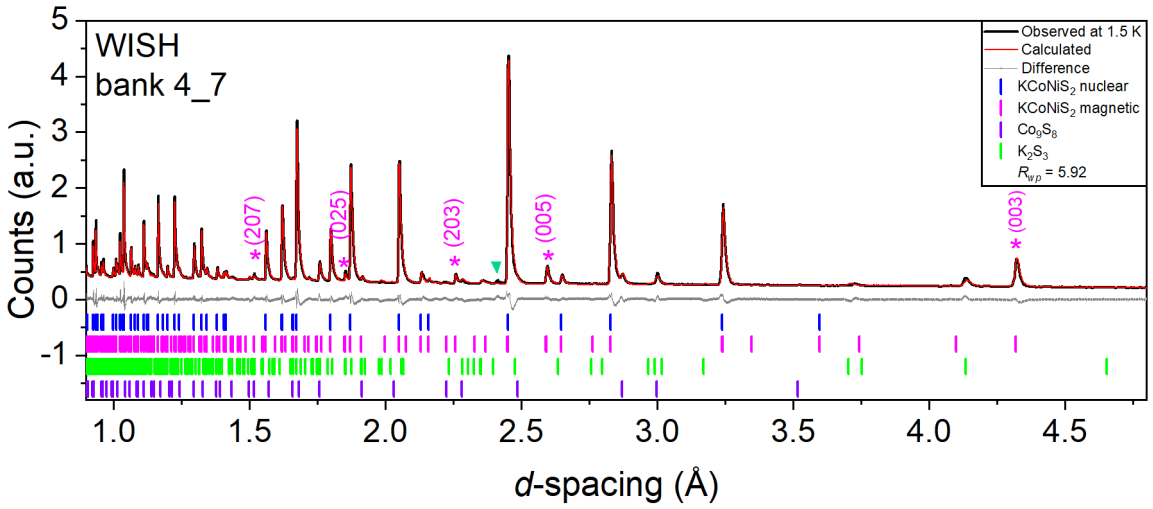


**Figure G.8** Rietveld refinement of $KCoNiS_2$ against PND data measured at 20 K, $R_{wp}$ = 5.92%, with magenta asterisks denoting magnetic Bragg peaks (bank 4_7). The green triangle indicates an unknown impurity.

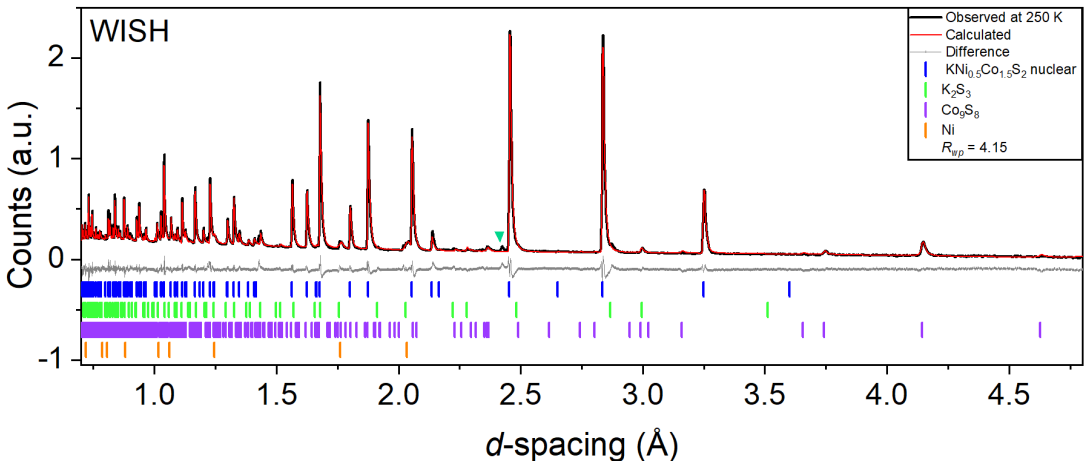


**Figure G.9** Rietveld refinement of $KCo_{1.5}Ni_{0.5}S_2$ against PND data measured at 250 K, $R_{wp}$ = 4.15%. The green triangle indicates an unknown impurity.

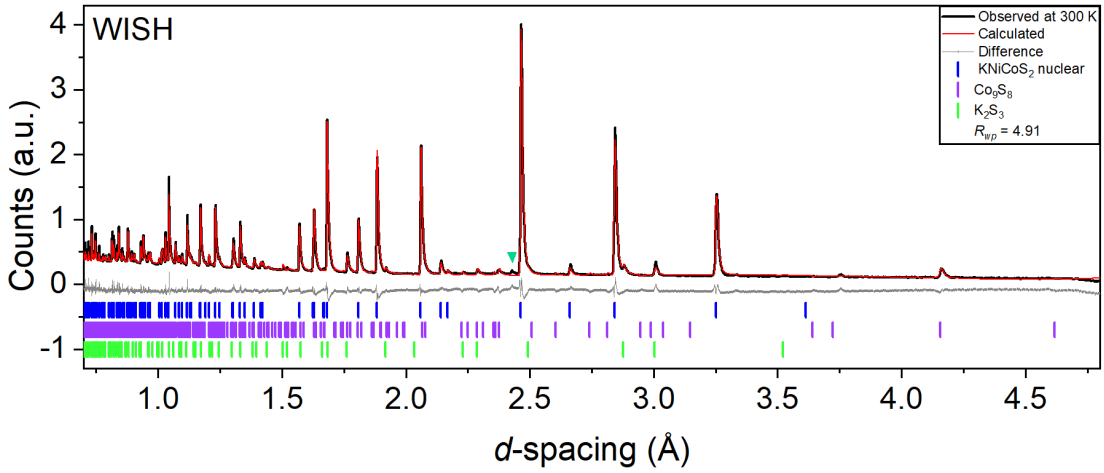


**Figure G.10** Rietveld refinement of $KCoNiS_2$ against PND data measured at 300 K, $R_{wp}$ = 4.91%. The green triangle indicates an unknown impurity.

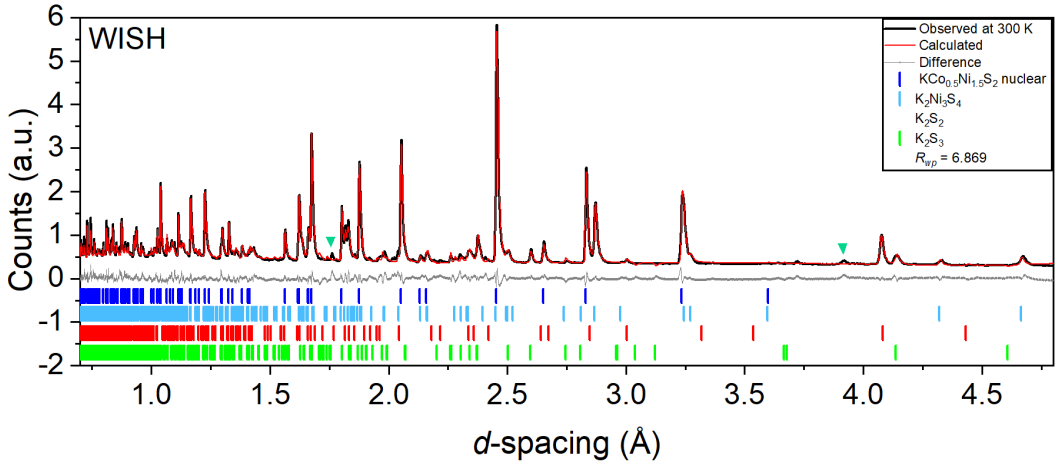

**Figure G.11** Rietveld refinement of $KCo_{0.5}Ni_{1.5}S_2$ against PND data measured at 300 K, $R_{wp}$ = 6.87%. The green triangle indicates an unknown impurity.

## Appendix H: Magnetometry of $RbCoNiS_2$ and $CsCoNiS_2$

Magnetometry measurements of $RbCoNiS_2$ are consistent with previous Ni-substituted $ACo_2Ch_2$-type systems (*A* = K, Rb, Cs; *Ch* = S, Se) presented in this chapter. $RbCo_2S_2$ displays ferromagnetism below 87 K, while $RbCoNiS_2$ shows an antiferromagnetic transition at 150 K from magnetic susceptibility plot of ZFC-FC vs T (Figure H.1a). The magnetisation isotherm (*M vs H*) at 2 K shows no saturation at 7 T and there is no hysteresis loop visible upon close inspection (Figure H.1b).

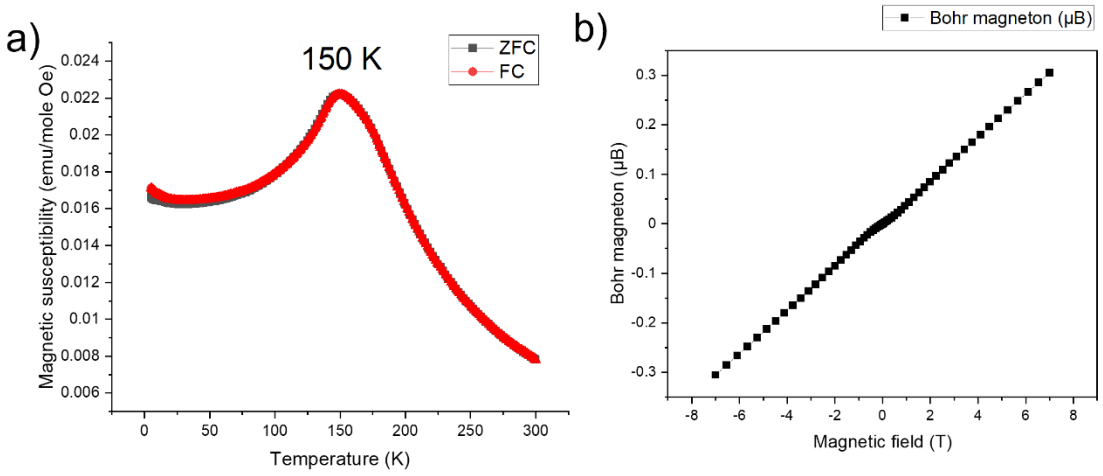


**Figure H.1** a) ZFC-FC magnetic susceptibility plots for $RbCoNiS_2$, b) Magnetisation isotherm measured at 2K.

On the other hand, magnetometry results for $CsCoNiS_2$ do not follow the same trend upon Ni-substitution in ferromagnetic $CsCo_2S_2$; ZFC-FC plot in Figure H.2a shows a ferromagnetic transition at ~ 25 K and the magnetisation isotherm at 2 K in Figure H.2b does not saturate at 7 T and displays a hysteresis loop between ±1 T.

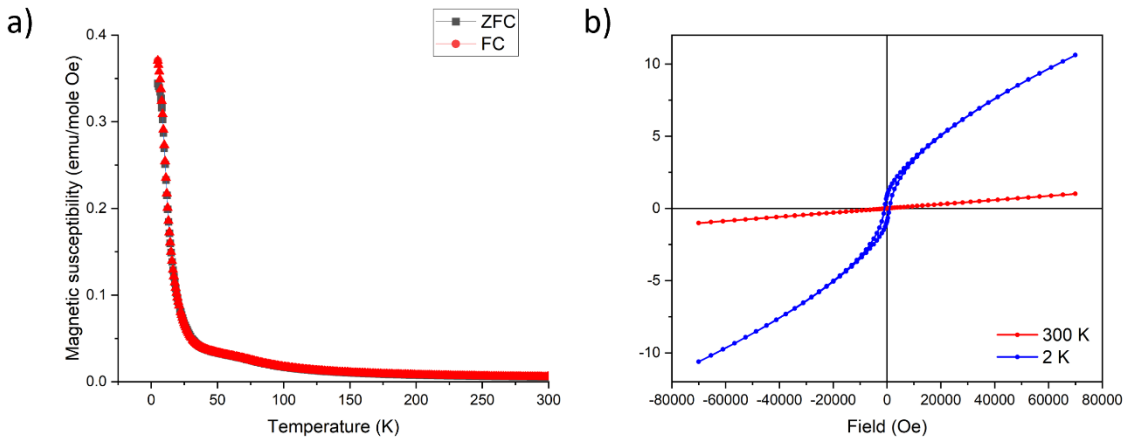


**Figure H.2** a) ZFC-FC magnetic susceptibility plots for $CsCoNiS_2$, b) Magnetisation isotherm measured at 2 K.